Philipps Universität Marburg

Adsorption Dynamics and Bonding Analysis of Organic Molecules on Silicon(001) Surfaces

Dissertation

zur Erlangung des
Doktorgrades der Naturwissenschaften
(Dr. rer. nat.)

dem Fachbereich Chemie
der Philipps-Universität Marburg
vorgelegt von

M. Sc.
Lisa Pecher
aus Höxter

Marburg an der Lahn, 2017

Erstgutachter: PD Dr. Ralf Tonner
Zweitgutachter: Prof. Dr. Robert Berger

Abgabedatum: 08.09.2017
Tag der mündlichen Prüfung: 27.10.2017

Vom Fachbereich Chemie der
Philipps-Universität Marburg (Hochschulkennziffer 1180)
als Dissertation angenommen am 25.10.2017

Für alle Menschen, die mich in den letzten Jahren
begleitet und mein Leben verschönert haben.

Zusammenfassung

Diese kumulative Dissertation behandelt die Untersuchung der Adsorption vier organischer Moleküle auf Si(001)-Oberflächen mittels quantenchemischer Methoden. Bei den Molekülen handelt es sich um Ethen, Tetrahydrofuran (THF), Cyclooctin und 5-Ethoxymethyl-5-Methylcyclooctin (EMC). Ethen und THF können hierbei als Modellsysteme angesehen werden, mit denen ein Verständnis über die Adsorption ungesättigter C-C-Bindungen und Ethergruppen auf Si(001) erlangt werden kann. Im Gegensatz dazu kann die Adsorption von Cyclooctin und EMC potenziell für Anwendungen im Elektronikbereich genutzt werden: Da Cyclooctin, wie kürzlich gezeigt wurde, auf Si(001) stabile und geordnete Strukturen bildet, bietet es sich für den Aufbau von Organik/Halbleiter-Grenzflächen und die Funktionalisierung von Halbleitern an. Wenn eine zweite funktionelle Gruppe am Molekül angebracht ist, es aber dennoch selektiv über die Dreifachbindung adsorbiert, kann es als kovalenter „Linker“ genutzt werden, um andere Moleküle oder Materialien mit der Halbleiteroberfläche zu verbinden. Die Ethergruppe im EMC-Molekül ist hierbei eine von mehreren möglichen funktionellen Gruppen. Beim Vergleich zwischen Cyclooctin und EMC kann zudem ermittelt werden, wie die Ethergruppe die Adsorption der Dreifachbindung beeinflusst und ob selektives Binden an die Oberfläche erreicht werden kann.

Im Gegensatz zu Metalloberflächen, deren elektronische Zustände delokalisiert sind, weist die elektronische Struktur der Si(001)-Oberfläche einen lokaleren Charakter auf. Sie lässt sich dabei angenähert beschreiben durch ein leeres *p*-Orbital am Lewis-sauren Si_{down}-Atom sowie ein nichtbindendes Elektronenpaar am Lewis-basischen Si_{up}-Atom. Beide Atomtypen sind durch eine kovalente Bindung verknüpft und bilden die für diese Oberfläche charakteristischen Dimere. Diese chemisch motivierte Beschreibung der elektronischen Struktur der Oberfläche erlaubt es, ihre Reaktivität gegenüber organischen Molekülen mit Hilfe von Konzepten aus der Molekülchemie zu verstehen. Das hat zur Folge, dass theoretische Modelle, die sich in der Molekülchemie etabliert haben, für diese Systeme angewandt werden können, um die Entstehung chemischer Bindungen zwischen Molekül und Oberfläche zu verstehen. In dieser Arbeit liegt der Fokus dabei auf der kürzlich entwickelten periodischen Energiedekompositionsanalyse (pEDA).

Neben dem Aspekt der Bindungsanalyse liegt der zweite Fokus dieser Arbeit in der theoretischen Beschreibung der Adsorptionsdynamik. Dafür gibt es zwei Ansätze: Der erste Ansatz basiert auf statistischer Thermodynamik und findet Anwendung, wenn ein Intermediat im Adsorptionsprozess vorhanden ist, das so langlebig ist, dass sich thermodynamisches Gleichgewicht einstellen kann. Falls die Lebensdauer dafür zu kurz ist oder gar kein Intermediat vorhanden ist, findet der zweite Ansatz Anwendung, nämlich die explizite Berechnung der zeitlichen Entwicklung des Systems mittels Ab-initio-Moleküldynamik (AIMD). Durch den Einblick, den die Dynamikrechnungen

liefern, können die Bedingungen (z.B. Temperatur oder Druck) vorhergesagt werden, unter denen sich bestimmte Adsorptionsstrukturen bilden. Da sowohl Adsorptionsdynamik als auch Bindungsanalyse mit der Potentialenergielandschaft verknüpft sind, erlaubt die Fokussierung auf diese beiden Schwerpunkte, ein allgemeines Verständnis über den Adsorptionsprozess zu erlangen.

Für Ethen ist bekannt, dass der Adsorptionsprozess auf Si(001) über ein Intermediat verläuft. Die Ergebnisse der Bindungsanalyse zeigen hier, dass sich in diesem Zustand eine dative Bindung zwischen dem π-System des Moleküls und einem Si_{down}-Atom ausbildet. Da es sich dabei um eine gerichtete Bindung handelt, ist das Molekül im Intermediat nicht mobil, was berechnete Diffusionsenergiebarrieren bestätigen. Diese Ergebnisse stehen im Widerspruch zu bisherigen Studien, in denen das Intermediat oft als physisorbiert und mobil beschrieben wurde. In einer zweiten Studie wird die Reaktivität zum Endzustand der Adsorption, einem [2+2]-Cycloaddukt, untersucht. Dabei liegt der Fokus insbesondere darauf, welchen Einfluss die Vorbedeckung der Oberfläche durch andere Atome und Moleküle auf die Reaktivität des Ethen-Moleküls hat. Die Ergebnisse zeigen, dass eine volle Bedeckung umgebender Dimere durch Wasserstoffatome keinen Einfluss auf die Reaktivität, insbesondere die Energiebarriere, hat. Eine partielle Vorbedeckung einzelner Dimere führt allerdings zu einer erhöhten Reaktivität zu einem verbrückenden Nebenprodukt an diesen Stellen der Oberfläche. Falls ein Dimer von adsorbierten Ethen-Molekülen eingeschlossen ist, wird das Intermediat aufgrund von Pauli-Repulsion so stark destabilisiert, dass es bei Raumtemperatur instabiler als das System im desorbierten Zustand ist.

Die Untersuchung von THF auf Si(001) zeigt, dass die Reaktivität in diesem System die säurekatalysierte Spaltung von Ethern in Lösung widerspiegelt: Im ersten Schritt bildet sich eine dative Bindung zwischen dem Sauerstoffatom und einem Si_{down}-Oberflächenatom aus, während im zweiten Schritt ein nukleophiler Angriff eines Si_{up}-Atoms in der näheren Umgebung erfolgt. Beim zweiten Schritt handelt es sich um eine kinetisch kontrollierte Reaktion. Die niedrigste Barriere wird dabei für den Angriff erreicht, bei dem die Übergangszustandsstruktur derjenigen von S_N2-Reaktionen in Lösung am ähnlichsten ist. Die Anwendung der pEDA liefert zudem wichtige Einblicke in den Mechanismus der Reaktion: Zunächst wird die Art der O-Si-Bindung im ersten Schritt als dativ bestätigt und zusätzlich zeigt die Visualisierung der Umstrukturierung der Elektronendichte während des nukleophilen Angriffs, dass dieser Schritt analog zu molekularen S_N2-Reaktionen verläuft.

Für Cyclooctin zeigen die Ergebnisse, dass das Cycloaddukt mit zwei Bindungen zwischen Molekül und Oberfläche deutlich stabiler ist als das mit vier Bindungen. Die Gründe dafür liegen sowohl in erhöhten Deformationsenergien von Molekül und Oberfläche als auch in schwächeren individuellen Bindungen im vierfach gebundenen Zustand. Weiterhin sorgt die Größe des Moleküls dafür, dass Dispersionskräfte einen ausgeprägten Einfluss auf En-

ergie und Struktur bekommen. Dies macht sich insbesondere in einer Verkippung des Rings in den Adsorptionszuständen bemerkbar. Im Vergleich zu Ethin zeigen pEDA-Ergebnisse, dass die erhöhte Reaktivität des Cyclooctins primär durch die Ringspannung verursacht wird und das Molekül somit als vorgeformt für Cycloadditionen angesehen werden kann. Die Art und Stärke der kovalenten Bindungen zwischen Molekül und Oberfläche wird hierdurch jedoch nicht beeinflusst.

Die Studien zur Adsorptionsdynamik des Cyclooctin-Moleküls zeigen, dass zwei verschiedene Pfade möglich sind: Direkte Adsorption in den Cycloaddukt-Endzustand und Adsorption über einen sehr kurzlebigen Zwischenzustand, der dem Intermediat des Ethen-Systems ähnelt. Eine Untersuchung des Einflusses der Molekülorientierung auf die Adsorption zeigt, dass die meisten Pfade über diesen Zwischenzustand verlaufen, was ebenfalls durch AIMD-Simulationen bestätigt wird. Die Lebensdauer dieses Zustandes ist allerdings so gering (50 K: Nanosekunden, 300 K: Picosekunden), dass eine Isolierung unter gewöhnlichen experimentellen Bedingungen nicht möglich ist. Dies wird durch zwei Methoden bestätigt: Die Evaluierung von AIMD-Trajektorien und die Anwendung der Theorie des Übergangszustands in der harmonischen Näherung. Die Adsorption kann demnach als direkt oder pseudo-direkt verstanden werden.

Die abschließende Untersuchung der Adsorption von EMC zeigt, dass die Ethergruppe die Reaktivität und Adsorptionsdynamik der Dreifachbindung nicht beeinflusst und auch die Art der chemischen Bindung zwischen Molekül und Oberfläche in den Cycloaddukten unverändert bleibt. Somit lassen sich die Ergebnisse von Cyclooctin auf diesen Teil des Systems übertragen. Die Adsorption der Ethergruppe wird jedoch durch den Rest des Moleküls beeinflusst, da der große Ring einen hohen sterischen Anspruch hat. Dies führt z.B. zu einer erhöhten Energiebarriere für den C-O-Bindungsbruch. Die Art der dativen O-Si-Bindung als auch des nukleophilen Angriffs wird allerdings nicht signifikant beeinflusst. Auch wenn doppelt gebundene Zustände, bei denen sich zusätzlich zur Cycloaddition die dative O-Si-Bindung ausbildet, vorkommen, liefern sie keinen signifikanten Energiegewinn gegenüber dem reinen Cycloaddukt. Die Gründe dafür sind einerseits eine hohe Deformationsenergie des Moleküls im doppelt gebundenen Zustand und andererseits eine Verringerung der Konformationsentropie, da das Molekül mehr strukturellen Einschränkungen unterliegt. Die geringe Energiedifferenz wird zusätzlich durch AIMD-Simulationen bestätigt. Somit kann angenommen werden, dass sich ein Gleichgewicht mit in etwa gleicher Verteilung zwischen diesen beiden Zuständen einstellen wird.

Im Ganzen zeigen die Studien dieser Arbeit, dass die Anwendung chemischer Konzepte und Methoden einen wertvollen Beitrag zum Forschungsfeld der Adsorption auf Oberflächen leisten kann. Insbesondere die pEDA ermöglicht es, die Art der Bindung zwischen Molekül und Oberfläche sowohl qualitativ als auch quantitativ zu beschrieben und die relativen Energien ver-

schiedener Adsorptionsstrukturen zueinander zu verstehen. Weiterhin erlauben die Dynamik-Untersuchungen Vorhersagen darüber, wie sich die Systeme auf verschiedenen Zeitskalen entwickeln und welche Strukturen sich bevorzugt ausbilden. Die Ansätze dieser Arbeit lassen sich voraussichtlich auch auf andere Systeme übertragen (z.B. Adsorption auf Metalloberflächen) und können somit neue Einblicke für verschiedene Forschungsgebiete in den Oberflächen- und Materialwissenschaften liefern.

Abstract

In this thesis, the adsorption of four organic molecules on Si(001) surfaces is studied using computational methods. The investigated molecules are ethylene, tetrahydrofuran (THF), cyclooctyne and 5-Ethoxymethyl-5-methylcyclooctyne (EMC). While ethylene and THF act as model systems that allow to understand how unsaturated carbon-carbon bonds and ether groups interact with these surfaces, the other two molecules are more application-oriented: Since cyclooctyne was previously shown to form stable and ordered structures on clean Si(001), it is a potential candidate for the formation of organic/semiconductor interfaces or the functionalization of semiconductor surfaces. If a second functional group is present and the bifunctional molecule bonds selectively via the triple bond, it can be used as a covalent linker to attach other molecules or materials to the semiconductor surface. EMC is an example of such a bifunctional molecule, since it has an ether group covalently attached to the cyclooctyne ring. Comparing cyclooctyne and EMC additionally allows to gain insight into how the ether group influences the adsorption of the triple bond and if selective bonding to the surface can be achieved.

In contrast to metal surfaces, where electronic states are delocalized, the surface states on Si(001) are more localized and can well be approximated by an empty p orbital at the Lewis acidic surface atom Si_{down} and a non-bonding electron pair at the Lewis basic surface atom Si_{up}. These two types of surface atoms form the characteristic tilted dimers of the Si(001) surface reconstruction. The reactivity between organic molecules and this surface can therefore often be understood with molecular chemistry concepts. As a consequence, bonding between molecule and surface can be analyzed using established computational methodology from molecular chemistry. In this thesis, this is done using the recently developed periodic Energy Decomposition Analysis (pEDA).

In addition to the aspect of bonding analysis, the second focus of this thesis is on the theoretical description of adsorption dynamics. There are two complementary approaches for this: The first is based on statistical thermodynamics and can be applied if there is an intermediate state in the adsorption process with a lifetime long enough so that thermodynamic equilibrium can be achieved. If the lifetime is not long enough or if there is no intermediate at all, the second approach is applied, i.e. explicitly calculating the evolution of the system over time using ab initio molecular dynamics (AIMD). The insight gained from understanding the dynamics can be used to predict the conditions (e.g. temperature, pressure) at which certain adsorption structures form. Since both adsorption dynamics and bonding analysis are connected to the potential energy landscape, focussing on these two aspects allows to achieve a general understanding of the adsorption process.

For ethylene, which is known to adsorb on Si(001) via an intermediate state, the results show that in this intermediate, a dative bond between the molecu-

lar π system and a Si_{down} atom is formed. Due to the localized nature of this bond, the molecule shows no mobility in this state, which is supported by calculated diffusion energy barriers that turn out to be considerably higher than the reaction energy barrier to the final state, a [2+2] cycloadduct. This is in contast to previous studies which stated that the intermediate is physisorbed and mobile. The influence of surface coverage on the reactivity towards the cycloadduct is investigated in a second study. Here, the results show that full hydrogen coverage on surrounding surface dimers has no effect on the reactivity (i.e. energy barrier), whereas partial hydrogenation of a dimer results in an increased reactivity towards a bridging byproduct. In contrast to this, if an isolated dimer is enclosed by chemisorbed ethylene molecules, the resulting Pauli repulsion leads to a high destabilization of the intermediate at room temperature. As a result, it becomes less stable than the reference of the separated molecule and surface.

The study of THF on clean Si(001) reveals that the adsorption mirrors the acid-catalyzed cleavage of ethers in solution: In a first step, a dative bond between the ether oxygen and a Si_{down} atom is formed, while in a second step, a nearby Si_{up} atom can initiate a nucleophilic attack at the molecule and break a C-O bond. This cleavage reaction is shown to be under kinetic control and the lowest energy barrier is achieved for the attack of the Si_{up} that is able to establish a transition state (TS) structure that most closely resembles the TS structure of S_N2 reactions in solution. Furthermore, pEDA confirms the nature of the O-Si bond as dative and the electron rearrangement during the nucleophilic attack is visualized. This confirms that the same process that breaks the C-O bond also forms the C-Si bond and that the mechanism is equivalent to a molecular S_N2 reaction.

For cyclooctyne, it is found that the cycloadduct with two molecule-surface bonds is much more stable than the one with four of these bonds. The reasons for this are large deformation energies within both molecule and surface in the four-bond configuration as well as weaker individual bonds compared to the two-bond configuration. Additionally, it is shown that dispersion interactions have a pronounced effect on the energy and structure of the adsorbed molecules and lead to a bending of the molecules. Comparing the system to acetylene, pEDA results show that the ring strain in cyclooctyne is responsible for its enhanced reactivity towards the surface and that the triple bond is pre-formed for cycloaddition. The character of the molecule-surface bonds, however, does not change significantly between the two systems.

Investigations of the adsorption dynamics of cyclooctyne on Si(001) show that while there are direct adsorption pathways into the cycloadduct states (i.e. not proceeding via an intermediate), adsorption via a datively bonded transient state similar to the ethylene intermediate is also possible. By sampling the influence of the molecular orientation on the adsorption, it is revealed that most pathways proceed via the transient state, which is also confirmed by AIMD simulations. However, the lifetime of this state is so low

(50 K: nanoseconds, 300 K: picoseconds) that isolation at usual experimental conditions is not possible. This is determined by two methods which are complementary to each other: Evaluation of AIMD trajectories and application of harmonic transition state theory. The adsorption of this molecule can therefore be described as direct or pseudo-direct.

Conclusively, EMC is studied, which combines the previously investigated functionalities of cyclooctyne and ethers. The results show that the second functional group does not affect the reactivity and bonding of the triple bond and that the insight gained from the adsorption studies of cyclooctyne can be transferred to this system. On the contrary, the reactivity of the ether functionality is enhanced, since the large ring residue has a high steric demand, which leads to, e.g., a higher energy barrier for the C-O bond cleavage. The nature of the O-Si dative bond and the nucleophilic attack, however, is unchanged in comparison to the model system. A state where both functional groups are bonded to the surface is shown to feature almost no energy gain compared to the state where only the triple bond is bonded. The reasons for this are found to be a high molecular deformation energy as well as a decrease of conformational entropy. This decrease is the result of structural constraints in the doubly bonded state. AIMD simulations confirm that there is essentially no energy gain in the doubly bonded state and that the system will most probably interconvert between this state and the triple bond cycloadduct.

Overall, the studies in this thesis show that the application of chemical concepts and methods can bring in valuable contributions to the field of surface science. The pEDA in particular allows to describe the bonding between molecule and surface both qualitatively and quantitatively, and therefore enables an understanding of the relative energies between different adsorption structures. Furthermore, the investigation of the dynamics allows to predict how the system evolves on different time scales and which structures form preferably. The approaches presented in this thesis can most likely be transferred to other systems as well (e.g. adsorption on metal surfaces) and allow to deliver new insight into different fields of research in surface science and material science.

Publications

Parts of this work have been published in scientific journals and presented at conferences. The articles and conference contributions are listed below.

Articles

(References updated on 23.11.2017)

L. Pecher, S. Schmidt, R. Tonner, *Modeling the complex adsorption dynamics of large organic molecules: Cyclooctyne on Si(001)*, *J. Phys. Chem. C* **2017**.
DOI: 10.1021/acs.jpcc.7b09538

L. Pecher, S. Laref, M. Raupach, R. Tonner, *Ethers on Si(001): A prime example for the common ground between surface science and molecular organic chemistry*, *Angew. Chem. Int. Ed.* **2017**, *56*, 15150.

J. Pecher, C. Schober, R. Tonner, *Chemisorption of a strained but flexible molecule: Cyclooctyne on Si(001)*, *Chem. Eur. J.* **2017**, *23*, 5459.

J. Pecher, G. Mette, M. Dürr, R. Tonner, *Site-selective reactivity of ethylene at dangling-bond configurations on Si(001)*, *ChemPhysChem* **2017**, *18*, 357.

J. Pecher, R. Tonner, *Precursor states of organic adsorbates on semiconductors are chemisorbed and immobile*, *ChemPhysChem* **2017**, *18*, 34.

P. Rosenow, A. Stegmüller, **J. Pecher**, R. Tonner, *Interfacial properties and growth dynamics of semiconductor interfaces*, in *High Performance Computing in Science and Engineering '15*, Eds. W. E. Nagel, W. Jäger, M. Resch, Springer (Berlin, Heidelberg) **2016**, 199.

Conference contributions

Oral presentations

L. Pecher, R. Tonner, *Adsorption dynamics and spectroscopic characterization of large molecules on surfaces using density functional theory*, 13th ETSF Young Researchers' Meeting, London (UK) **2016**.

Poster presentations

L. Pecher, F. Pieck, R. Tonner, *Chemical bonding and adsorption dynamics of cyclooctynes in the creation of organic/inorganic interfaces*, 11th Triennial Congress of the World Association of Theoretical and Computational Chemists, München **2017**.

L. Pecher, R. Tonner, *Answering chemically motivated questions in surface science using periodic Energy Decomposition Analysis (pEDA)*, FemEx Netherlands, Putten (The Netherlands) **2017**.

L. Pecher, S. Schmidt, R. Tonner, *Modelling the complex adsorption dynamics of cyclooctyne on Si(001) using computational chemistry*, 9th Meeting: From the witches cauldrons in materials science, Goslar **2017**.

L. Pecher, R. Tonner, *Establishing new concepts on molecular adsorption on semiconductor surfaces using computational chemistry*, 52nd Symposium Theoretische Chemie, Bochum **2016**.

L. Pecher, F. Pieck, J.-N. Luy, R. Tonner, *Bifunctional cyclooctyne molecules on Si(001): Investigating their suitability as interface building blocks using DFT*, 17th Workshop on Dynamical Phenomena at Surfaces, Milano (Italy) **2016**

L. Pecher, R. Tonner, *Revealing the unusual reactivity of organic molecules on Si(001) surfaces leading towards internal interfaces*, Theory and Applications of Computational Chemistry, Seattle (USA) **2016**.

L. Pecher, F. Pieck, R. Tonner, *Computational study on the suitability of a bifunctional cyclooctyne molecule as a building block for growing interfaces on Si(001)*, International Conference on Internal Interfaces, Marburg **2016**.

L. Pecher, R. Tonner, *Adsorption and surface dynamics of organic molecules on Si(001) for growing internal interfaces - a theoretical investigation*, Workshop: Simulation of chemistry-driven growth phenomena for metastable materials, Rauischholzhausen **2015**.

L. Pecher, R. Tonner, *Uncovering S_N2 reactions of tetrahydrofuran with Si(001) surface atoms using density functional theory*, 51st Symposium Theoretische Chemie, Potsdam **2015**.

L. Pecher, R. Tonner, *Computational investigation of adsorption and dynamics of molecules for organic/semiconductor interfaces on Si(001)*, 31st European Conference on Surface Science, Barcelona (Spain) **2015**.

L. Pecher, R. Tonner, *Analysis of kinetic and thermodynamical aspects of cyclooctyne binding to the Si(001) surface*, 1st European Conference on Theory, Modelling and Computational Methods for Semiconductors, Granada (Spain) **2015**.

L. Pecher, R. Tonner, *Thermodynamics and kinetics of adsorption processes for unsaturated hydrocarbons on the Si(001) surface*, 50th Symposium Theoretische Chemie, Wien (Austria) **2014**.

L. Pecher, R. Tonner, *Adsorption thermodynamics and kinetics of cyclooctyne and derivatives on silicon via DFT*, International Summer School on Semiconductor Interfaces: Methods and Model Systems, Donostia-San Sebastián (Spain) **2014**.

Contents

1 Introduction

Our modern society is heavily shaped by technology based on electronic devices. The circuitry in these devices is mainly composed of semiconducting materials, since they allow to control the conductivity externally via, e.g., temperature, exposure of light, or electric and magnetic fields. Silicon is the chemical element that is most commonly used here. The reasons for this are, among other things, that it is easy to modify (e.g. via doping) and its high abundance in the Earth's crust. As devices become more and more miniaturized, a level has been reached where the size of the active elements is approaching molecular dimensions.[1] This has lead to the emergence of chemically motivated approaches to enhance the application range of these devices, one of them being the functionalization of semiconductors by organic molecules. Here, the functionality of individual molecules is used to influence the properties of the device. Two exemplary applications are dye sensitized solar cells, where organic monolayers are able to increase the power output,[2] and biosensors that can detect binding events to certain biomolecules.[3]

In order to be able to link molecules and surfaces and form a hybrid organic/inorganic interface, knowledge about the chemical reactivity is crucial. Since electronic states on silicon and other semiconductor surfaces are mostly localized in space (see also Section 1.3),[4] they often behave like molecular reagents and chemical expertise becomes indispensable for describing their reactivity with organic molecules.[5] Most reaction types identified to date can be accurately described in terms of textbook organic chemistry: These include dative bond formation, dissociative addition, electrophilic aromatic substitution, elimination and multiple types of cycloaddition.[5–8]

Often, there are several ways a molecule can bond to a surface, e.g. at different sites or with a different number of chemical bonds being formed. Control-

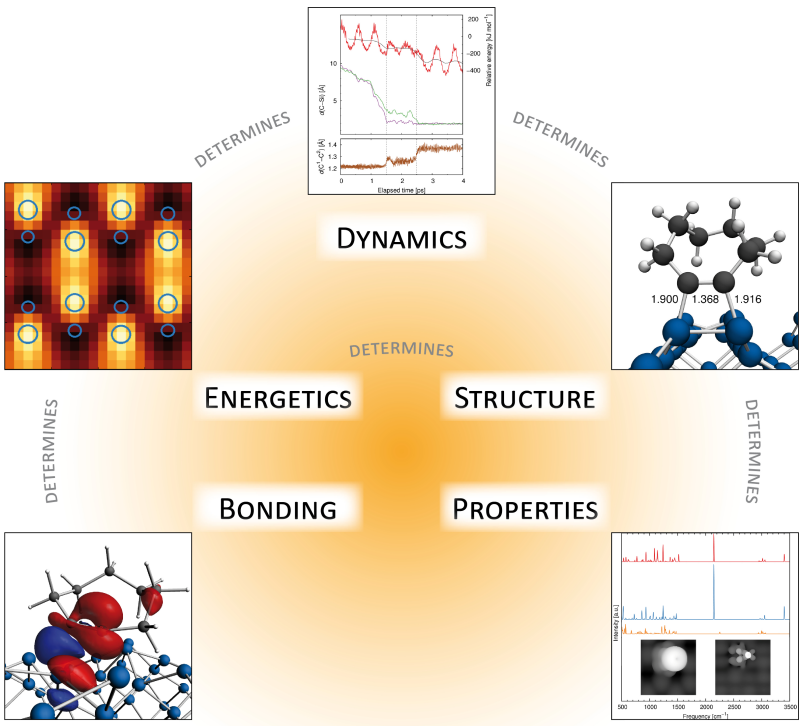

Figure 1.1. Scheme showing the interconnection between the five central aspects of adsorption.

ling the chemoselectivity, i.e. in which state the system will end up, is therefore a central task in adsorption studies. The main endeavor of theory in this is being able to predict the conditions (e.g. temperature, pressure) at which certain structures form. In order to be able to do these predictions, the five central aspects of adsorption have to be understood (Figure 1.1): The most fundamental aspect is **bonding**, i.e. what types of bonds can be formed between molecule and surface and how strongly they bind. This determines the **energetics**, i.e. the shape of the potential energy surface (PES), bonding energies of different adsorption states and energy barriers for interconversion between states. This again determines the **dynamics** of the system, which includes reaction and adsorption rates, and, the most central point, structural selectivity. The dynamics lead to a preference of certain adsorption **structures**, which can be identified from observable **properties**.

In experiment, observable properties like absorption spectra or microscopy topographies can be measured and allow to draw conclusions about the structure.[7] The adsorption dynamics can also be measured, e.g., using molecular beam techniques,[9] and analysis of the data allows to retrieve certain features of the PES. Certain aspects of bonding like electron binding energies

are accessible via, e.g., x-ray or ultraviolet photoelectron spectroscopy, while non-observable properties like the character of a chemical bond can rarely be determined from experimental data alone. While in the case of small adsorbates on metal surfaces, physisorbed (bound by van-der-Waals forces) and chemisorbed states (bound by the formation of covalent bonds)[10,11] are generally distinguished by their respective adsorption energies, this indicator is not reliable for larger molecules, where the adsorption energy of a physisorbed state can be in a range where chemisorbed states are usually expected.[12] This makes the computational method of bonding analysis an indispensable tool for understanding adsorption phenomena, since it allows to explain the causes for differences in adsorption energies and therefore enables to draw a comprehensive picture. In this thesis, one main focus of investigation is on bonding analysis.

Theory can also make valuable contributions to the other four aspects. Since methods like density functional theory (DFT) are known to be reliable in the prediction of structures,[13] the computation of adsorption structures can deliver a quantiative insight that might aid in the interpretation of experiments or even deliver data that is currently too difficult to determine from measurements, e.g. individual bond lengths in large and complex systems. Based on calculated structures, spectra and topographies can be predicted as well, with an accuracy similar to modern experimental methods. However, inaccuracies are introduced in DFT calculations due to the inherent weaknesses contained in these methods (this will be discussed in more detail in Chapter 2).[13]

The second main focus of investigation in this thesis is on adsorption dynamics. Using the same methodology as for the determination of structures, energy differences can be computed, which allow to predict the evolution of the systems down the time scale of nuclear motions (femtoseconds to picoseconds). Since, as already pointed out in Figure 1.1, dynamics and bonding are at least indirectly connected, the focus on these two aspects gives a complementary insight into adsorption in the investigated systems. In the following, a more detailed introduction to adsorption dynamics and bonding analysis is given, while afterwards, the characteristics of adsorption of organic molecules on Si(001) will be discussed and the investigated systems will be introduced.

1.1 Adsorption Dynamics

Understanding the adsorption dynamics of a system allows to predict rates of adsorption, desorption and reaction, structural selectivity, and the dependence on properties like temperature and pressure.[14,15] The fundamental concepts were introduced in 1932 by Lennard-Jones for the adsorption of atoms and diatomics on metal surfaces.[10] Even though in this thesis, the adsorption of larger organic molecules on semiconductor surfaces is studied, many of Lennard-Jones' concepts can be transferred.

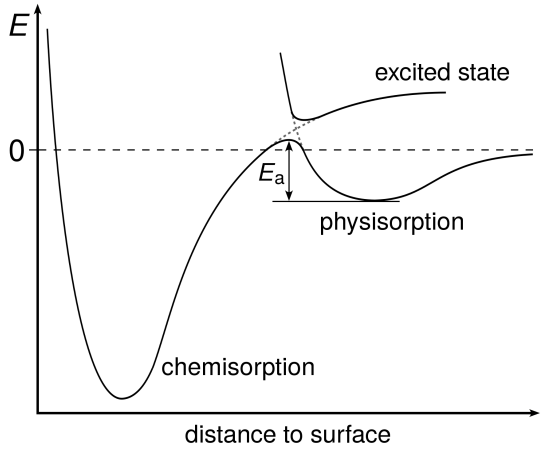

Figure 1.2. Schematic potential energy curve for adsorption on metal surfaces, adapted from Ref. [10].

There are two distinct types of adsorption on metal surfaces: Physisorption and chemisorption (Figure 1.2). While physisorption takes place at larger distances and is dominated by weak isotropic van-der-Waals (dispersive) forces, chemisorption sees the formation of strong directional covalent bonds to the surface and takes place at shorter distances. Due to the change in electronic structure upon chemisorption, the system often does not dissociate into the electronic ground state from this minimum, but an excited state. However, if the ground and excited state are of the same symmetry, an avoided crossing takes place and the minima of physisorption and chemisorption are connected by a transition state (TS). Unless the impinging adsorbate contains enough energy to overcome the corresponding energy barrier E_a (see Figure 1.2) upon arrival, it will stay in the physisorption minimum until it acquires enough energy to overcome the barrier and convert to the chemisorbed state.

If the adsorbate stays long enough in the physisorbed state (also called precursor in this case) to get into thermodynamic equilibrium, it can be described by statistical thermodynamics and kinetics that is based on this approach, e.g. Boltzmann statistics and the Arrhenius equation. Since chemisorbed states are, in most cases, more stable than physisorbed states, the equilibrium will usually heavily favor chemisorption, and after a certain amount of time, the majority of adsorbates will have become chemisorbed. This time can be calculated, e.g., from the Arrhenius equation for the reaction rate k (Equation 1.1):

$$k(T) = A_0 \cdot \exp\left(-\frac{E_a}{k_B T}\right) \tag{1.1}$$

$$\tau = k^{-1} \tag{1.2}$$

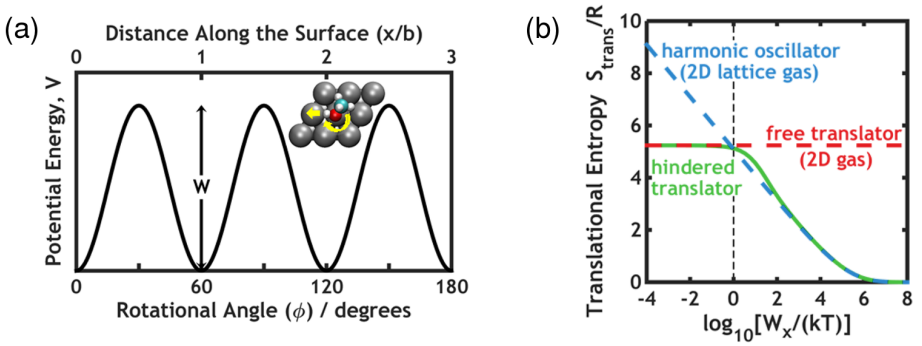

Figure 1.3. (a) Periodic potential for hindered translation or rotation of an adsorbate on a surface. (b) Entropy of a hindered translational mode in the harmonic oscillator, free translator and hindered translator approximations for a fixed temperature T and variable energy barrier W_x. Figures reproduced with permission from Ref. [17]. Copyright American Chemical Society.

τ is called the lifetime and is defined as the time when the fraction $\frac{1}{e} \approx 0.368$ of the system is still in the initial state. This property is a function of E_a, the temperature T and a pre-exponential factor A_0, which will be discussed later on.

Physisorbed adsorbates are mobile in general.[11,16] The reason for this is the absence of a directional bond to the surface, which causes a low energy barrier W for translation to equivalent adsorption sites (Figure 1.3(a)). If there is enough thermal energy available to overcome this barrier ($k_B T \gg W$), the atom will essentially behave as a 2D ideal gas.[17] This can lead to a drastic entropy change in the physisorbed state (Figure 1.3(b)), which will affect the reaction rate.[18] On the contrary, if the available thermal energy is significantly lower than the energy barrier ($k_B T \ll W$), the atom will oscillate in the potential well most of the time and is best described as a harmonic oscillator. If both energies are in the same order of magnitude ($k_B T \approx W$), there are two options: One is to use the partition function of a cosine potential,[17] the most accurate solution at the moment, or alternatively, all properties are calculated in both the harmonic oscillator and 2D ideal gas approximations to get an upper and lower limit.[19]

Often, there is not only one, but multiple chemisorbed states. This has severe consequences for the adsorption dynamics: The potential energy profile (Figure 1.2) is getting more complex, a 1D representation of the adsorbate position is not sufficient anymore and a 2D representation becomes necessary (Figure 1.4). In this case, all chemisorbed states might be reached from the physisorbed state and additionally be able to convert to each other. Hence, not only is the physisorbed state in thermodynamic equilibrium with all chemisorbed states, but these are also in equilibrium with each other. The initial reaction from the physisorbed state is under kinetic control, i.e. the path with the lowest energy barrier will most likely be taken first. Depending on the en-

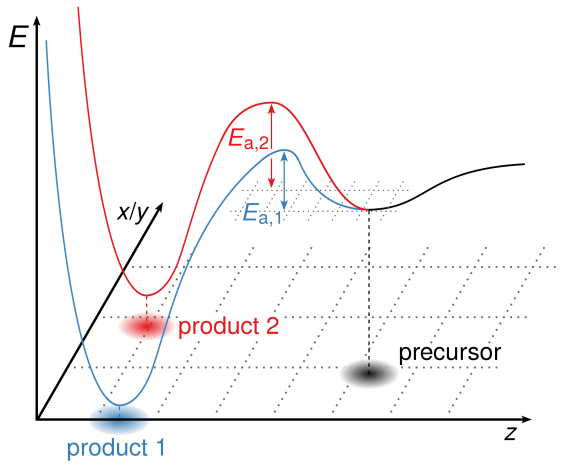

Figure 1.4. Schematic energy profile for an adsorption with two possible chemisorbed product states as a function of the adsorbate position (x/y: parallel to the surface, z: perpendicular to the surface).

ergy differences and barriers, the long-term product on an experimental time scale will either be the thermodynamically most stable one or the one with the lowest reaction energy, i.e. the kinetic product.[5]

The adsorption dynamics gets more complicated for molecular adsorbates. In the most simple case of diatomics (e.g. H_2, N_2, CO), the adsorption is not only dependent on the position, but also the orientation of the molecule and the bond length. To accurately describe these systems, explicit calculation of the dynamics is often necessary. This is usually done by calculating a high-dimensional PES[20] and simulating the propagation of nuclei either classically[21] or by quantum dynamical mehods like the time-dependent wave packet method.[22,23]

For larger molecules, this process might become even more complicated, since for each additional atom, three additional internal degrees of freedom are introduced. However, the adsorption is often determined by a single reactive site in the molecule (an atom, a bond or another type of functional group), while the rest of the molecule is not participating in the reaction with the surface and only interacts via weak van-der-Waals forces. In these cases, the dynamics mainly follows the adsorption of atoms with some minor corrections applied (van-der-Waals influence of the non-reacting groups, free or hindered rotation in adsorption states).

In this thesis, both types of systems are present: The type where the dynamics is dominated by a reactive site and statistical thermodynamics can be applied and the type where explicit dynamics is necessary, because the influence of the orientation becomes a determining factor. This allows the reader to view the two approaches side by side, compare the respective effort, reliability and necessity, and gain a general overview on the theoretical treatment

of adsorption dynamics.

1.2 Bonding Analysis on Surfaces

One of the most fundamental concepts in the field of chemistry is the chemical bond.[24] Chemical bonds are usually divided into the following classes: The covalent bond, where atoms are sharing one or more pairs of electrons, the ionic bond, which is formed by electrostatic attraction between charged parts of a molecule, and the metallic bond, where the valence electrons are delocalized. In case of the covalent bond, further differentiation can be made between shared-electron bonds, where each of the two bonding partners contributes a single electron to the bond, and dative (donor-acceptor) bonds, where both electrons originate from a single bonding partner. Recently, more broad definitions of the chemical bonds have also been proposed, which include bonding by dispersion and further subclasses of covalent bonds like correlated, charge shift, and charge transfer bonds.[25]

There are several computational methods available to determine the character of a chemical bond in periodic systems (surfaces, solids). These include the Crystal Overlap Hamilton Population (COHP),[26–28] the Electron Localization Index (ELI),[29–31] Energy Decomposition Analysis (EDA),[32,33] Natural Bond Orbital (NBO) analysis,[34,35] and the Quantum Theory of Atoms In Molecules (QTAIM).[36–38] This thesis will focus on application of the periodic EDA (pEDA). In the following, a brief introduction to the basic concepts of this method will be given. The mathematical formalism is explained in Section 2.6.1.

The EDA decomposes the interaction energy ΔE_{int} between two fragments of a system into three major expressions: The Pauli repulsion energy ΔE_{Pauli}, the electrostatic interaction energy ΔE_{elstat} and the orbital interaction energy ΔE_{orb}. These terms are well defined and allow interpretation in a chemically meaningful way, therefore providing a bridge between quantum chemistry and traditional models of chemical bonding.[32] Usually, EDA calculations are done within the framework of DFT. Since many DFT functionals are known to fail in describing dispersive interactions,[39,40] there are two ways this can be implemented in the analysis: If a functional is used which includes dispersion in the exchange-correlation term (see also Section 2.2), this interaction will become part of the three EDA terms. On the contrary, if a method is used which adds an explicit correction term for dispersion (see also Section 2.2.4), the corresponding energy will show up as an additional energy term. In this thesis, the latter approach is used. The way this energy is introduced into the decomposition process is presented in Section 2.6.1.

An illustrative example for application of the molecular EDA is given by the difference in dissociation energies between the isoelectronic molecules CO and N_2, which is more than 100 kJ mol^{-1} higher for CO.[32,41] Using the

EDA, this difference can be attributed to the weaker Pauli repulsion between the two atoms in the CO molecule. Even though electrostatic and orbital interaction could also lead to an increased stabilization, their absolute value is actually lower in the CO molecule. Additionally, decomposition of ΔE_{orb} by symmetry shows that the π bond character of the triple bond is much more pronounced in CO than it is in the N_2 molecule (CO: $E(\sigma)$: $E(\pi) \approx$ 50:50, N_2: $\approx$ 65:35).

The EDA is also able to quantitatively describe the interaction between transition metals and ligands in complexes in the Dewar-Chatt-Duncanson (DCD) model.[42,43] This model states how the interaction is stabilized by bonding from occupied orbitals of the ligand to unoccupied orbitals of the transition metal and occupied orbitals of the transition metal to unoccupied orbitals of the ligand. Examples are given in the review article by von Hopffgarten and Frenking.[32] The DCD model is also applicable in surface science, where it is named the Blyholder model.[44] The quantitative determination of bonding and back bonding contributions between molecule and surface will be a central point in the application of bonding analysis in this thesis.

The recent implementation of the EDA for periodic systems has extended its application range to molecule-surface systems. One notable example for pEDA application is the dissociative adsorption of H_2 on the surfaces Pd(001) and Cu(001).[33] Whereas on palladium, a non-activated process is observed, i.e. the TS energy for dissociation is below the zero-energy reference of the separated molecule and surface, adsorption on copper is an activated process (TS energy above the zero-energy reference). The analysis shows that at larger distances, the Pauli repulsion is higher for Cu(001), while electrostatic and orbital interaction are weakened at the same time. The reason for this lies in the differences in electronic structure on the two surfaces. Further examples in the introductory article by Raupach and Tonner are the adsorption of CO on Si(001), which sees the formation of a dative bond with properties very similar to the dative bond of CO to molecular Lewis acids, and the formation of two shared-electron covalent bonds between acetylene and Si(001).

The EDA and pEDA can be extended by applying the Extended Transition State–Natural Orbitals for Chemical Valence (ETS-NOCV) scheme.[45] This allows to further decompose ΔE_{orb} into independent contributions (e.g. σ/π symmetry or bonding/back bonding) and visualize the charge redistribution of each individual contribution in terms of deformation densities. Each densitiy has an assigned eigenvalue v_i, which gives the amount of charge being transferred, and an energy contribution ΔE_i. As with the pEDA, the mathematical formalism is presented in the next chapter (Section 2.6.2). The advantage of this scheme is that it allows a picture of chemical bond formation that is consistent with traditional bonding concepts, but quantitative at the same time. The prime example for application of the ETS-NOCV scheme is the formation of a dative bond in the aminoborane molecule (Figure 1.5). Here, the σ donation from the ammonia stabilizes the system by 284 kJ mol^{-1} (87% of

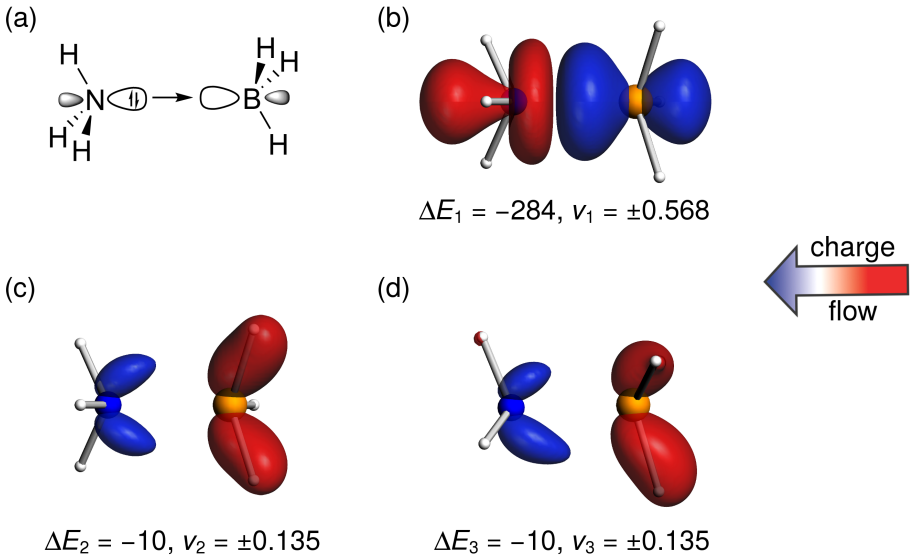

Figure 1.5. (a) Schematic drawing of the formation of the dative bond in aminoborane. (b) NOCV deformation density corresponding to the σ type donation. (c,d) NOCV deformation densities corresponding to the π type back donation. The view in (d) is rotated by 90° with respect to the N-B bond. Red: Depletion of electron density. Blue: Accumulation of electron density. Energies ΔE_i in kJ mol^{-1}, eigenvalues v_i in q_e. Calculated at PBE-D3/TZ2P.

ΔE_{orb}, Figure 1.5(b)). Additionally, there are two types of π back donation from σ(B-H) orbitals in the borane fragment to the ammonia which stabilize the system by 10 kJ mol^{-1} (3% of ΔE_{orb}, Figure 1.5(c,d)) each. The scheme is therefore consistent with the Lewis picture (Figure 1.5(a)), i.e. that the non-bonding electron pair at the nitrogen atom is donating charge into an empty orbital at the boron. At the same time, parts of the bonding that are not included in the Lewis picture, i.e. the π type back donation, become apparent and their contribution can be quantified.

The ETS-NOCV scheme can also be applied to reactions by performing an analysis at the initial state, the transition state and the product state.[46] Here, it is able to decompose the energy barrier and additionally show how electron density redistribution is evolving during the course of the reaction. Additionally, it has been implemented for application in periodic systems[47] and will be extensively applied in the work of this thesis.

1.3 Organic Molecules on Si(001)

Semiconductor surfaces often undergo a reconstruction, i.e. a structural rearrangement of the topmost layers.[48] This is because in contrast to metal surfaces, where the valence electrons are not bound to individual atoms, semiconductor crystals usually feature covalent bonds between pairs of atoms. If these bonds are cut, the unpaired electrons (dangling bonds) can not easily redistribute into the bulk and reconstruction is the best way to minimize the surface energy. In silicon, for example, each atom forms four covalent bonds to its next neighbors, leading to a local tetrahedral arrangement and the diamond bulk structure. If this crystal is cut along the (001) plane, there are two dangling bonds per surface atom (Figure 1.6, left). The first way to minimize the energy is through the formation of dimers, where one electron each per surface atom is used to form a covalent bond to a neighboring atom (Figure 1.6, center). The presence of dimers on Si(001) was experimentally confirmed in 1959 by Schlier and Farnsworth.[49] Additionally, a tilting (or buckling) of the dimer takes place (Figure 1.6, right).[50] This causes the two remaining dangling bond electrons to pair and localize at the upper Si dimer atom (Si_{up}), while the orbital at the lower Si dimer atom (Si_{down}) gets emptied. The buckling is in contrast to the reconstruction of the carbon(001) surface, where the dimers are horizontal. This is because on C(001), the distance between the two dimer atoms is low enough so that a proper π bond can form, while on Si(001), the overlap is too low and buckling becomes energetically more favorable.[51]

Due to interactions with each other, the dimers are not all oriented the same way, but alternating within and between the rows (Figure 1.7). This minimum reconstruction of the surface is called $c(4\times2)$.[4] In experiment, this structure is only apparent at temperatures below $\approx$ 200 K, since at higher temperatures, the flip-flop motion of the dimers is thermally excited so much that the arragement becomes random and the surface structure appears to be in a (2×1) reconstruction.[52,53] Nonetheless, the dimers stay buckled for most of the time even at high temperatures,[54] since the horizontal arrangement is not an energetic minimum, but a saddle point.[55]

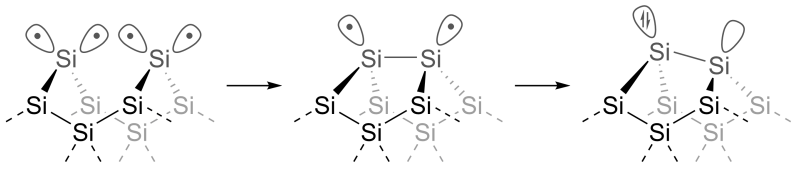

Figure 1.6. Schematic drawing of the surface reconstruction process on Si(001). Left: Unreconstructed surface. Center: Formation of dimers. Right: Buckling of dimers. Dots indicate unpaired electrons (dangling bonds).

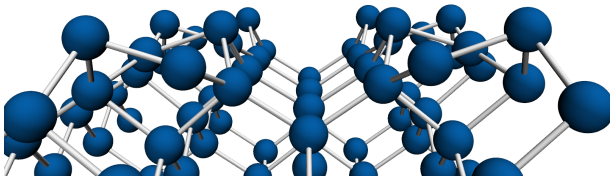

Figure 1.7. Structure of Si(001) in the most stable reconstruction, $c(4\times2)$.

The electronic structure of the Si(001) surface can be described in both real space and reciprocal space (Figure 1.8). In the real space picture, it is well approximated in terms of atom-centered orbitals (a), where the Si_{down} atom features an empty p type orbital and the Si_{up} atom a doubly occupied sp^3 type orbital. This picture is confirmed by theoretical calculations (b).[57] The advantage of the real space description is that the location and shape of the reactive sites can be determined. However, the energetic accessibility of the states is not apparent, since the real space description only gives a local view and long-range effects are not evident. This is covered in the reciprocal space description. The band structure (Figure 1.8(c))[56] shows that while the occupied states at the Si_{up} atoms (red lines below $E = 0$ eV) at the Γ point (center of the Brillouin zone, see also Section 2.2.1) are in a similar energy range as the bulk-like states, there is actually a wide range in k space where they are much

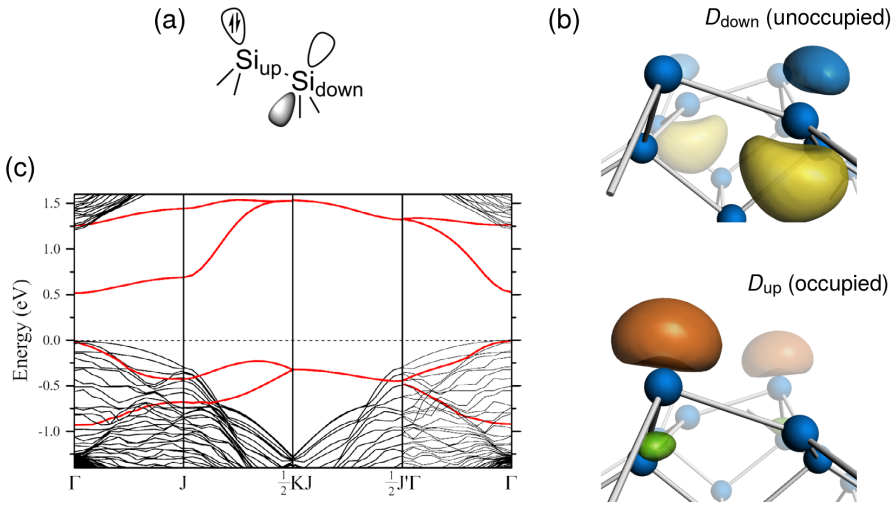

Figure 1.8. Electronic structure of the Si(001) surface. (a) Schematic drawing in terms of atom-centered orbitals. (b) Crystal orbitals (shown at the Γ point in k space) of a Si(001) slab corresponding to the D_{down} and D_{up} dimer states, calculated at PBE-D3/TZ2P. (c) Band structure, calculated using the HSE06 functional. The former dangling bond states are drawn in red lines. Reproduced with permission from Ref. [56]. Copyright IOP Publishing.

higher in energy than the other occupied states and therefore more accessible. The same applies to the unoccupied Si_{down} states (red lines above $E = 0$ eV), which are much lower in energy than the bulk-like states over a wide k range and hence more accessible as well.

The chemical reactivity of the dimer can therefore be considered to be both electrophilic (at Si_{down}) and nucleophilic (at Si_{up}).[4] This allows for a wide variety of reactions with molecules adsorbing on the surface. Four examples for this are given in Figure 1.9: If a Lewis acidic molecule like BH_3 approaches the surface, a dative bond will form between the Si_{up} atom and the Lewis acidic center in the molecule (a). Subsequently, a B-H bond can be broken, so that the dimer atoms are saturated with two covalent shared-electron bonds.[58] Alternatively, if a Lewis basic molecule like NH_3 approaches the surface, a similar interaction will take place, only that the dative bond will form between the Lewis basic center in the molecule and the Si_{down} atom (b).[59]

The reaction with unsaturated and aromatic molecules proceeds in a similar way to the reaction with Lewis basic molecules: In case of ethylene (Figure 1.9(c)), a π complex is formed with the Si_{down}, while afterwards, a [2+2] cycloaddition reaction takes place.[1] In contrast to usual [2+2] cycloadditions in organic chemistry, this reaction is not forbidden by the Woodward-Hoffmann rules[60] and has a very low energy barrier of ≤ 10 kJ mol^{-1} due to the asymmetric pathway via the π complex intermediate.[61–64] On C(001), which has a symmetric dimer with a pronounced π bond, this energy barrier is much higher (≈ 90 kJ mol^{-1}), since the Woodward-Hoffmann rules apply.[61] The final exemplary reaction of the dimer is with pyrrole (Figure 1.9(d)). Here, a π complex similar to ethylene is formed first, from which the system can undergo several reactions. The one depicted here is an electrophilic aromatic substitution. Other possible reactions are N-H dissociation (the most favorable reaction), and a [2+2] and [4+2] cycloaddition of the molecular π system.[65]

There are now several ways in which the investigation of adsorption dynamics and bonding can help to understand these systems: First, pEDA bonding analysis will allow to quantify the interactions that lead to chemical bond formation between the adsorbates and the Si(001) surface. Additionally, the ETS-NOCV scheme will confirm whether or not the orbital interaction occurs in the way of traditional chemical bonding models that is presented in Figure 1.9. The insight gained from this analysis will help to understand the importance of intermediate states in the adsorption dynamics and the differences in reaction barriers leading to the respective final states of adsorption. Calculation of the dynamics will then enable to predict structural selectivity and properties that can be measured in experiment.

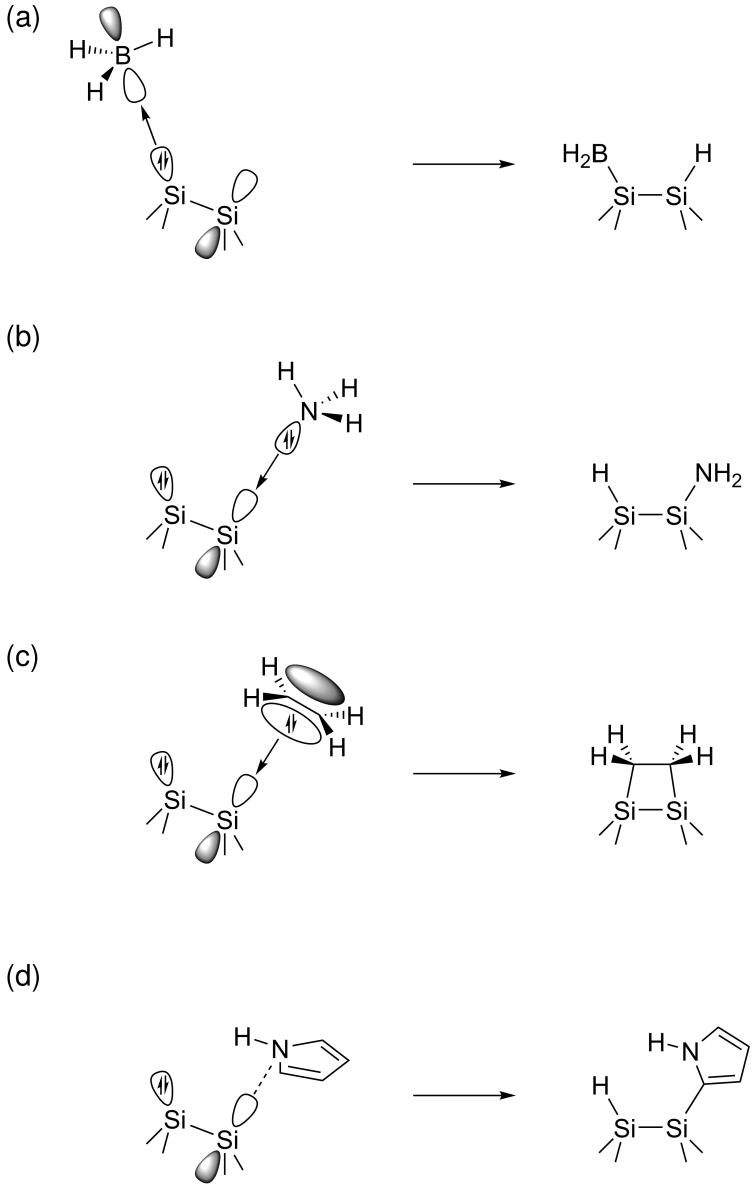

Figure 1.9. Four exemplary reactions of the Si(001) surface dimer with organic molecules. The selection highlights the different ways in which the dimer can form bonds and react. (a) Donor in a dative bond to BH_3 with subsequent B-H bond dissociation. (b) Acceptor in a dative bond to NH_3 with subsequent N-H bond dissociation. (c) π complex formation with ethylene and subsequent [2 + 2] cycloaddition. (d) π complex formation with pyrrole and subsequent electrophilic aromatic substitution.

1.4 Investigated Systems

In this thesis, the adsorption of four different organic molecules (Figure 1.10) on the Si(001) surface was studied: Ethylene and tetrahydrofuran (THF) act as model systems that allow to understand the adsorption and reactivity of unsaturated hydrocarbons and ether groups in organic molecules, respectively. The knowledge gained from the studies of these model systems was then applied to the more application-oriented systems of cyclooctyne and a bifunctional derivative. Cyclooctyne, the smallest cyclic alkyne stable under typical lab conditions, is an excellent choice for the functionalization of semiconductors and construction of organic/inorganic interfaces, which were introduced in the beginning of this chapter. The reasons for this are the following: First, unsaturated organic molecules form well-defined cycloadducts with the Si(001) surface, leading to very stable chemisorbed structures (see also the previous section).[66] Furthermore, the high ring strain of the cyclooctyne triple bond[67] leads to an increased stability of the cycloadducts compared to linear alkynes. This has already made the molecule a widely utilized building block in other fields of chemistry, like organic synthesis[68] or the *in vivo* modification of biological systems.[69–71] Additionally, different functional groups can be attached to the ring in synthesis[72,73] and, according to experiments, there is a direct (i.e. temperature-independent) adsorption pathway that leads to stable structures and well-ordered patterns at high coverage.[74] The adsorption of cyclooctyne was investigated to get an understanding how the strained triple bond adsorbs on Si(001) without interference of other functional groups. Afterwards, the adsorption of the bifunctional cyclooctyne was investigated. The second functionality was chosen since the ad-

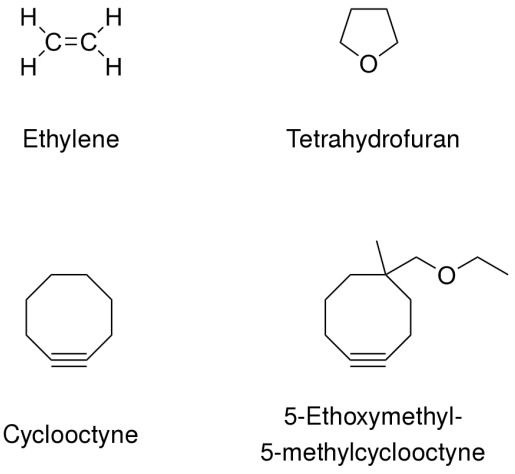

Figure 1.10. Structural formulae and names of the four molecules whose adsorption on Si(001) was investigated in this thesis.

sorption of ether molecules on Si(001) showed that the formation of strong (i.e. irreversible) covalent bonds can be controlled via temperature.[75–77] Therefore, combining a cyclooctyne triple bond with an ether group should yield a molecule that selectively binds via the triple bond, while the ether group remains available for coupling reactions. Recent experimental studies have shown that this selectivity is preserved over a wide temperature range.[72] Additionally, the knowledge gained from the study of THF can be transferred and the systems can be compared.

The main questions in this thesis therefore are:

- What is the exact adsorption mechanism of unsaturated hydrocarbons and ether groups on Si(001)?
- How can structural selectivity of surface reaction products be controlled?
- How does ring strain affect the adsorption of a carbon-carbon triple bond?
- What is the effect of subsitution in a cylooctyne molecule on the reactivity of the strained triple bond?
- Does a large side group affect the adsorption of ether molecules?
- How can selective adsorption be achieved if the molecule has two functional groups?

The answers to these questions will be provided in Chapter 3.

2

Theoretical Background

2.1 Basic Concepts of Quantum Chemistry

The following section will give a short introduction into the basic concepts of quantum chemistry and is based on textbooks about this subject.[78–80]

At the beginning of the twentieth century, it was discovered that the laws of Newton's classical mechanics are not able to properly describe very small particles like electrons or atomic nuclei. As a consequence, the theory of quantum mechanics was conceived. One striking feature of this theory is that electrons and photons have properties of both particles and waves and a wavelength can be assigned to each particle by the de Broglie relation.[81] Since the length scales of atoms and molecules are in the same order of magnitude as the de Broglie wavelength of electrons, a quantum mechanical description is inevitable for chemical phenomena.

Schrödinger suggested that the state of a quantum mechanical system is completely described by a wave function $\Psi(\mathbf{r}, t)$ which is dependent on the coordinates $\mathbf{r}$ of all particles and on time t. In order to gain information about specific properties of the system, a mathematical operator $\hat{O}$ can be assigned to a physical observable O, e.g. a property known from classical mechanics, and act on the wave function. This corresponds to a measurement of O and if Ψ is an eigenfunction of $\hat{O}$, the result will be an eigenvalue o:

$$\hat{O}\Psi = o\Psi \tag{2.1}$$

The total energy E is one of the most important properties of a system. By using the Hamilton operator $\hat{H}$, the energy operator in quantum mechanics,

in the above equation, the famous Schrödinger equation is obtained:

$$\hat{H}\Psi = E\Psi \tag{2.2}$$

In a molecule, $\hat{H}$ consists of operators for the kinetic energy of all particles and the Coulomb interaction between the particles (atomic units are used):

$$\begin{aligned}\hat{H} &= \hat{T}_\mathrm{N} + \hat{T}_\mathrm{e} + \hat{V}_\mathrm{NN} + \hat{V}_\mathrm{Ne} + \hat{V}_\mathrm{ee} \\ &= -\frac{1}{2}\sum_\alpha \nabla_\alpha^2 - \frac{1}{2}\sum_i \nabla_i^2 + \sum_{\alpha,\beta} \frac{Z_\alpha Z_\beta}{R_{\alpha\beta}} - \sum_{i,\alpha} \frac{Z_\alpha}{r_{i\alpha}} + \sum_{i,j} \frac{1}{r_{ij}}\end{aligned} \tag{2.3}$$

Here, $\hat{T}_\mathrm{N}$ is the nuclear and $\hat{T}_\mathrm{e}$ the electron kinetic energy, $\hat{V}_\mathrm{NN}$ is the Coulomb repulsion between nuclei, $\hat{V}_\mathrm{eN}$ the attraction between electrons and nuclei and $\hat{V}_\mathrm{ee}$ electron-electron repulsion. The indices α,β denote nuclei and i,j electrons, Z_α is the charge of nucleus α, while $R_{\alpha\beta}$, $r_{i\alpha}$ and r_{ij} are the distances between nuclei, electron-nucleus pairs and electrons, respectively. The sums go over all nuclei and electrons and all respective pairs.

In the Born-Oppenheimer approximation,[82] the motion of nuclei and electrons is treated separately and electrons act within a reference system of fixed nuclei. For most systems, this is a valid approximation, since the mass of the nuclei is three to five orders of magnitude larger than the electron mass, therefore the electrons move much faster and can instantaneously adapt to changes in nuclear geometry. This leads to $\hat{T}_\mathrm{N} = 0$ and $\hat{V}_\mathrm{NN} = \textit{constant}$ and $\hat{H}$ is reduced to:

$$\hat{H} = -\frac{1}{2}\sum_i \nabla_i^2 - \sum_{i,\alpha} \frac{Z_\alpha}{r_{i\alpha}} + \sum_{i,j} \frac{1}{r_{ij}} \tag{2.4}$$

So if the location of the nuclei, their charges, and the number of electrons is known, the Schrödinger equation (2.2) can be solved to yield the wave function and energy of a system. Unfortunately, an analytical solution for more than two particles is impossible, so several approximations have to be made. The first is the application of the variational principle: This states that a trial wave function Φ can be expanded by a set of basis functions $\{\chi_i\}$ using variable coefficients c_i:

$$\Phi = \sum_i c_i \chi_i \tag{2.5}$$

Calculating the energy expectation value of Φ yields an energy $\tilde{E}$ that is always equal to or higher than the true ground state energy E_0 of the true ground state wave function Ψ_0:

$$\frac{\langle\Phi|\hat{H}|\Phi\rangle}{\langle\Phi|\Phi\rangle} = \tilde{E} \geq E_0 \tag{2.6}$$

Therefore, by optimizing the coefficients c_i so that the energy is minimized, E_0 and Ψ_0 can be approximated as far as the size and nature of the basis set

allows. Another approximation that is made is the application of an independent-particle model which allows the wave function Ψ of an N-electron system to be expressed as a Hartree product of one-electron functions ϕ_i, also called orbitals (Equation (2.7)). Each orbital is a function of the spatial coordinates $\mathbf{r}_i$ and the spin coordinate σ_i of an individual electron i:

$$\Psi_{\text{Hartree}} = \phi_1(\mathbf{r}_1, \sigma_1)\, \phi_2(\mathbf{r}_2, \sigma_2)\, \ldots\, \phi_N(\mathbf{r}_N, \sigma_N) \tag{2.7}$$

Since Ψ_{Hartree} does not fulfil the Pauli principle, which states that Ψ must be antisymmetric upon exchange of two electron indices, the Hartree product must be antisymmetrized and normalized. The result is a Slater determinant Ψ_{SD}:

$$\Psi_{\text{SD}} = \frac{1}{\sqrt{N!}} \begin{vmatrix} \phi_1(\mathbf{r}_1, \sigma_1) & \phi_2(\mathbf{r}_1, \sigma_1) & \cdots & \phi_N(\mathbf{r}_1, \sigma_1) \\ \phi_1(\mathbf{r}_2, \sigma_2) & \phi_2(\mathbf{r}_2, \sigma_2) & \cdots & \phi_N(\mathbf{r}_2, \sigma_2) \\ \vdots & \vdots & \ddots & \vdots \\ \phi_1(\mathbf{r}_N, \sigma_N) & \phi_2(\mathbf{r}_N, \sigma_N) & \cdots & \phi_N(\mathbf{r}_N, \sigma_N) \end{vmatrix} \tag{2.8}$$

One requirement on the orbitals ϕ_i is orthonormality (Equation (2.9)). This ensures that the electrons are truly independent particles.

$$\langle \phi_i | \phi_j \rangle = \delta_{ij} \begin{cases} \delta_{ij} = 1,\ i = j \\ \delta_{ij} = 0,\ i \neq j \end{cases} \tag{2.9}$$

2.2 Density Functional Theory

There are two widely used approaches to calculate the ground state energy of a quantum chemical system. One is based on the wave function Ψ and the solution of the Schrödinger equation in different levels of approximation. The Hartree-Fock method belongs to this approach and accuracy can be systematically improved by applying electron correlation methods like Configuration Interaction (CI), Coupled Cluster (CC) or Møller-Plesset Perturbation Theory.[80] The other approach, DFT, is based on the electron density ρ. Its fundament is the first Hohenberg-Kohn theorem,[83] which states that the ground state energy E_0 of a system is completely determined by the electron density ρ and can be expressed by a functional $E_0[\rho]$. If a wave function Ψ is known, ρ is obtained by integrating the absolute square of Ψ over all coordinates except one set of spatial coordinates $\mathbf{r}$:

$$\rho(\mathbf{r}) = N \int |\Psi(\mathbf{r}, \sigma_1, \mathbf{r}_2, \sigma_2, \ldots, \mathbf{r}_N, \sigma_N)|^2\, \mathrm{d}\sigma_1 \mathrm{d}\mathbf{r}_2 \mathrm{d}\sigma_2 \ldots \mathrm{d}\mathbf{r}_N \mathrm{d}\sigma_N \tag{2.10}$$

If Ψ is a Slater determinant, ρ can also be written as the sum of the squared spin orbitals ϕ_i of all N occupied states:

$$\rho_{\mathrm{SD}} = \sum_{i}^{N} |\phi_i|^2 \tag{2.11}$$

Even if the wave function is unknown, all relevant information about a system can be obtained from the electron density ρ. This can be proven via *reductio ad absurdum* or, alternatively, the following relations: First, the integral of the density defines the number of electrons N:

$$\int \rho(\mathbf{r})\,\mathrm{d}\mathbf{r} = N \tag{2.12}$$

And second, the position of cusps in the density defines the position $\mathbf{R}_\alpha$ of the nuclei, while their height and the gradient of the density at small distances $r_{i\alpha}$ to the nucleus define the corresponding nuclear charge Z_α:

$$\lim_{r_{i\alpha}\to 0} \frac{\mathrm{d}\rho(\mathbf{r})}{\mathrm{d}r_{i\alpha}} = -2Z_\alpha\,\rho(r_{i\alpha}=0) \tag{2.13}$$

In the Born-Oppenheimer approximation, the total DFT energy of the system consists of three parts: The kinetic energy of the electrons T, the Coulomb attraction between nuclei and electrons V_{Ne}, and the electron-electron Coulomb repulsion V_{ee} (Equation (2.14)). The last term can further be divided into the classical Coulomb interaction J and an exchange-correlation energy E_{XC} (Equation (2.15)). All components are functionals of the density.

$$E[\rho] = T[\rho] + V_{\mathrm{Ne}}[\rho] + V_{\mathrm{ee}}[\rho] \tag{2.14}$$

$$V_{\mathrm{ee}}[\rho] = J[\rho] + E_{\mathrm{XC}}[\rho] \tag{2.15}$$

While V_{Ne} and J can be readily expressed by the Coulomb law as

$$V_{\mathrm{Ne}}[\rho] = -\sum_{\alpha}\int \frac{Z_\alpha\,\rho(\mathbf{r})}{|\mathbf{R}_\alpha - \mathbf{r}|}\,\mathrm{d}\mathbf{r} \tag{2.16}$$

$$J[\rho] = \frac{1}{2}\iint \frac{\rho(\mathbf{r}_i)\rho(\mathbf{r}_j)}{|\mathbf{r}_i - \mathbf{r}_j|}\,\mathrm{d}\mathbf{r}_i\mathrm{d}\mathbf{r}_j, \tag{2.17}$$

the exact expressions for T and E_{XC} are unknown, so they have to be approximated. There are two ways of doing this: In the numerical approach, the density is represented on a grid and T is evaluated by calculation of finite differences. Since the variational principle (Equations (2.5) and (2.6)) is applicable within DFT (second Hohenberg-Kohn theorem),[83] the values of ρ on the grid can be optimized iteratively until self-consistency is reached. In the other ap-

proach, which is more commonly used, orbitals are introduced in a formalism similar to the Hartree-Fock method to find an expression for T. This is called the Kohn-Sham method.[84] Here, T is divided into a part that can be calculated exactly, T_{SD} (SD: Slater determinant) and another part that is included in the exchange-correlation energy. This also leads to a redefinition of E_{XC}:

$$T_{\mathrm{SD}} = \sum_{i}^{N} \langle \phi_i | -\tfrac{1}{2}\nabla^2 | \phi_i \rangle \tag{2.18}$$

$$E_{\mathrm{XC}} = (T - T_{\mathrm{SD}}) + (V_{\mathrm{ee}} - J) \tag{2.19}$$

As in the numerical approach, the variational principle can be applied and the orbitals ϕ_i are optimized in an iterative and self-consistent way. The corresponding equation, also called Kohn-Sham equation, is:

$$\left[-\frac{1}{2}\nabla^2 - \sum_{\alpha} \frac{Z_\alpha}{|\mathbf{R}_\alpha - \mathbf{r}_i|} + \int \frac{\rho(\mathbf{r}_j)}{|\mathbf{r}_i - \mathbf{r}_j|}\, \mathrm{d}\mathbf{r}_j + v_{\mathrm{XC}} \right] \phi_i^{\mathrm{KS}} = \varepsilon_i\, \phi_i^{\mathrm{KS}} \tag{2.20}$$

The expression in brackets is also known as the one-electron Kohn-Sham operator $\hat{f}^{\mathrm{KS}}$ and the exchange-correlation potential v_{XC} is defined by:

$$v_{\mathrm{XC}} = \frac{\delta E_{\mathrm{XC}}[\rho]}{\delta \rho} \tag{2.21}$$

Furthermore, E_{XC} can be written in terms of the exchange energy ε_{X} and correlation energy ε_{C} per particle:

$$E_{\mathrm{XC}}[\rho] = E_{\mathrm{X}}[\rho] + E_{\mathrm{C}}[\rho] = \int \rho(\mathbf{r})\, \varepsilon_{\mathrm{X}}[\rho] \mathrm{d}\mathbf{r} + \int \rho(\mathbf{r})\, \varepsilon_{\mathrm{C}}[\rho] \mathrm{d}\mathbf{r} \tag{2.22}$$

Approaches that use the Kohn-Sham formalism only differ in their expression of E_{XC}. They are divided into different classes: The Local Density Approximation (LDA) makes the assumption that the density can locally be treated as a uniform electron gas, so that E_{XC} is only dependent on the local value of ρ. The corresponding exchange energy is given by the Dirac formula:[85]

$$E_{\mathrm{X}}^{\mathrm{LDA}} = -\frac{3}{4}\left(\frac{3}{\pi}\right)^{\frac{1}{3}} \int \rho^{\frac{4}{3}}(\mathbf{r})\, \mathrm{d}\mathbf{r} \tag{2.23}$$

E_{C} can be calculated in several ways. A notable example that is widely used is the functional by Vosko, Wilk and Nusair (VWN),[86] which was fitted to quantum Monte Carlo data calculated by Ceperley and Alder.[87] The LDA is appropriate for systems where ρ varies slowly with position. However, in chemical systems it is creating errors that lead to, e.g., an overestimation of bond strengths in molecules[80] and an underestimation of band gaps in semiconducting solids.[88] The performance can be improved by including the

gradient of the density, $\nabla\rho$, in the functional. This is called the Generalized Gradient Approximation (GGA). The general expression for the exchange-correlation energy of GGA functionals is given by:

$$E_{\mathrm{XC}}^{\mathrm{GGA}}[\rho] = \int \rho(\mathbf{r})\, \varepsilon_{\mathrm{XC}}[\rho, \nabla\rho]\mathrm{d}\mathbf{r} \tag{2.24}$$

As in Equation (2.22), it can be divided into contributions for correlation and exchange. Two of the most popular GGA functionals are those developed by Perdew and Wang (PW91)[89] and Perdew, Burke and Enzerhof (PBE).[90,91] The latter was extensively used in this work. While GGA functionals show a highly improved performance in comparison to the LDA in many tasks, they still produce significant errors. In molecules, reaction barriers are underestimated and polarizabilities overestimated,[13] while in solids, the band gaps of semiconductors are still significantly underestimated.[92] Inaccuracies in properties involving electronic excitation are comprehensible, since unoccupied orbitals are not considered in the Kohn-Sham equations. The functionals can be further improved by including the Laplacian of the density, $\nabla^2\rho$, which yields the class of meta-GGA functionals. An example is the functional by Tao, Perdew, Staroverov and Scuseria (TPSS).[93] Alternatively or additionally, the exact Hartree-Fock exchange can be included, which yields the class of hybrid functionals, e.g. B3LYP.[94,95] The B3LYP exchange-correlation energy contains several different terms: The LDA exchange energy $E_{\mathrm{X}}^{\mathrm{LDA}}$, the Hartree-Fock exchange energy $E_{\mathrm{X}}^{\mathrm{exact}}$, the Becke88 (GGA) exchange energy $E_{\mathrm{X}}^{\mathrm{B88}}$,[96] the VWN (LDA) correlation energy $E_{\mathrm{C}}^{\mathrm{VWN}}$[86] and the Lee-Yang-Parr (GGA) correlation energy $E_{\mathrm{C}}^{\mathrm{LYP}}$:[97]

$$\begin{aligned} E_{\mathrm{XC}}^{\mathrm{B3LYP}} =& (1 - a_0 - a_{\mathrm{X}}) E_{\mathrm{X}}^{\mathrm{LDA}} + a_0 E_{\mathrm{X}}^{\mathrm{exact}} + a_{\mathrm{X}} E_{\mathrm{X}}^{\mathrm{B88}} \\ &+ (1 - a_{\mathrm{C}}) E_{\mathrm{C}}^{\mathrm{VWN}} + a_{\mathrm{C}} E_{\mathrm{C}}^{\mathrm{LYP}} \end{aligned} \tag{2.25}$$

The parameters a_0, a_{X} and a_{C} have been determined by fitting to experimental data as 0.20, 0.72 and 0.81, respectively. Since the Hartree-Fock exchange operator is nonlocal, the calculation of $E_{\mathrm{X}}^{\mathrm{exact}}$ involves a high computational effort. This can be reduced by introducing a range separation into the functional, so that this exchange is only calculated for electron pairs at a short distance, while for larger distances, a GGA expression is used. One of these functionals is HSE06, which has been developed by Heyd, Scuseria and Enzerhof[98–100] and was applied in parts of this work.

A severe weakness of DFT in comparison to wave function methods is that the accuracy can not be systematically improved. While the functionals become more sophisticated by including the gradient, the Laplacian and Hartree-Fock exchange, this does not guarantee that the results become more accurate. In general, it is advisable to use a functional for the calculation of a property or system for which experience has shown that it gives reliable re-

sults. Additionally, all functionals suffer from two general weaknesses of DFT: First, the self-interaction error, which is apparent because the Coulomb potential acting on an electron (Equation (2.20)) includes the density of *all* electrons, and second, the inability to describe long range van-der-Waals (dispersion) interactions.[39,40] While the former issue has been partially compensated by changes in the functionals, the latter is usually treated by applying semiempirical corrections that are added to a converged DFT calculation. This will be discussed in detail in Section 2.2.4.

2.2.1 Extended Systems

Ordered solids are usually described as periodic crystals. This means that the system has a translational symmetry, which is defined by its lattice vectors $\mathbf{a}_i$ (i=1,2,3) and any two symmetry equivalent points in space are connected by the translation vector $\mathbf{R}$:[101]

$$\mathbf{R} = n_1\mathbf{a}_1 + n_2\mathbf{a}_2 + n_3\mathbf{a}_3 \quad n_i \in \mathbb{N} \tag{2.26}$$

The $\mathbf{a}_i$ vectors span the unit cell, which contains all information about the system, like the position of the nuclei or the electrostatic potential. In a calculation, only the unit cell is treated explicitly, while the rest of the system is represented by introducing periodic boundary (Born-von Karman) conditions (PBC). The volume V_{cell} of the unit cell is given by:

$$V_{\text{cell}} = \mathbf{a}_1 \cdot (\mathbf{a}_2 \times \mathbf{a}_3) \tag{2.27}$$

Due to the periodic nature of the crystal, some properties are better described in reciprocal (**k**) space rather than real (**r**) space. The unit cell in reciprocal space is spanned by the reciprocal lattice vectors $\mathbf{b}_i$, which can be obtained from the real space lattice vectors via the following relations:

$$\mathbf{b}_1 = \frac{2\pi}{V_{\text{cell}}}\,\mathbf{a}_2 \times \mathbf{a}_3 \qquad \mathbf{b}_2 = \frac{2\pi}{V_{\text{cell}}}\,\mathbf{a}_3 \times \mathbf{a}_1 \qquad \mathbf{b}_3 = \frac{2\pi}{V_{\text{cell}}}\,\mathbf{a}_1 \times \mathbf{a}_2 \tag{2.28}$$

This leads to the following relation between the two sets of lattice vectors:

$$\mathbf{a}_i\mathbf{b}_j = 2\pi\,\delta_{ij} \tag{2.29}$$

Analogous to the definition of **R**, symmetry equivalent points in reciprocal space are connected by the reciprocal translation vector **G** (Equation (2.30)). **R** and **G** are connected by the relation given in Equation (2.31).

$$\mathbf{G} = n_1\mathbf{b}_1 + n_2\mathbf{b}_2 + n_3\mathbf{b}_3 \quad n_i \in \mathbb{N} \tag{2.30}$$

$$e^{i\mathbf{GR}} = 1 \tag{2.31}$$

This description has consequences for the calculation of the electronic structure. A wave function ψ in PBC is not only a function of $\mathbf{r}$, but also of the wave vector $\mathbf{k}$. It has to obey the PBC and may only differ by a phase factor $e^{i\mathbf{kR}}$:

$$\psi_{\mathbf{k}}(\mathbf{r}+\mathbf{R}) = e^{i\mathbf{kR}}\,\psi_{\mathbf{k}}(\mathbf{r}) \tag{2.32}$$

An equivalent way to express $\psi_{\mathbf{k}}$ is in terms of Bloch's theorem,[102] i.e. as a modulated plane wave $e^{i\mathbf{kr}}$

$$\psi_{\mathbf{k}}(\mathbf{r}) = e^{i\mathbf{kr}}\,u_{\mathbf{k}}(\mathbf{r}) \tag{2.33}$$

where the function $u_{\mathbf{k}}(\mathbf{r})$ has the periodicity of the lattice:

$$u_{\mathbf{k}}(\mathbf{r}+\mathbf{R}) = u_{\mathbf{k}}(\mathbf{r}) \tag{2.34}$$

The fact that ψ is a function of $\mathbf{k}$ leads to a modification of the Kohn-Sham equation (2.20), where the energy ϵ of an individual orbital (or band) $\phi^{\mathrm{KS}}_{i,\mathbf{k}}$ is now a function of $\mathbf{k}$ as well:

$$\hat{f}^{\mathrm{KS}}\phi_{i,\mathbf{k}} = \epsilon_{i,\mathbf{k}}\,\phi_{i,\mathbf{k}} \tag{2.35}$$

Naturally, $\epsilon_{i,\mathbf{k}}$ shows the same periodicity as the reciprocal lattice:

$$\epsilon_{i,\mathbf{k}+\mathbf{G}} = \epsilon_{i,\mathbf{k}} \tag{2.36}$$

Because of this, calculations do not have to be performed over all of $\mathbf{k}$ space, but only a volume around the Γ point ($\mathbf{k} = \mathbf{0}$) called the first Brillouin zone, which contains all information on the electronic structure. It is defined by

$$0 \leq k_i \leq \frac{\pi}{|\mathbf{a}_i|}, \tag{2.37}$$

where k_i (i=1,2,3) are the elements of the $\mathbf{k}$ vector and $\mathbf{a}_i$ are the lattice vectors of the crystal. In practice, the periodic Kohn-Sham equation (2.35) is solved at a set of discreet points within the first Brillouin zone, the so-called $\mathbf{k}$ mesh and the energy of the bands in between is obtained by interpolation. Since the choice of the $\mathbf{k}$ mesh affects the accuracy of the calculation, it is a parameter that should always be chosen with care.

2.2.2 Basis Sets

As mentioned in Section 2.1, one-electron wave functions are usually expanded by a set of basis functions $\{\chi_i\}$. There are two major types: Atom-centered functions and plane waves. While atom-centered functions are usually used in molecular calculations, plane waves are a convenient choice for calculations in PBC, since they satisfy the conditions by definition (see also the previous subsection).

The advantage of an atom-centered basis in molecular calculations is apparent: In chemistry, a molecule is usually considered an assembly of atoms rather than of nuclei and electrons, so depiction of the electronic structure in terms of atomic orbitals (AO) suits this concept very well. Atom-centered basis sets are divided into two types: Slater type orbitals (STO) and Gaussian type orbitals (GTO). Slater type orbitals are of the form

$$\chi(r,\theta,\phi) = N\, Y_l^m(\theta,\phi)\, r^{n-1}\, \mathrm{e}^{-\zeta r}, \tag{2.38}$$

where r is the electron-nucleus distance, N a normalization constant, $Y_l^m(\theta,\phi)$ a spherical harmonic, n, l and m the orbital quantum numbers, and ζ a positive real number. The exponential decay of the function mirrors the exact solutions of the hydrogen atom and furthermore ensures the nuclear cusp, a local maximum of the wave function at the position of the nucleus with a discontinuous first derivative. However, the calculation of two-electron integrals, which is necessary in wave function methods, becomes overly complicated and in many cases analytically impossible. This problem does not arise when GTOs are used. They have the following form:

$$\chi(r,\theta,\phi) = N\, Y_l^m(\theta,\phi)\, r^{2n-2-l}\, \mathrm{e}^{-\zeta r^2} \tag{2.39}$$

The big disadvantage of GTOs is that s-type orbitals do not feature a nuclear cusp and even have a derivative of zero at the position of the nucleus. Since the derivative of a one-electron wave function is proportional to the velocity, this would mean that the electron slows down in close proximity to the nucleus. This is unphysical and contradicts the Coulomb law. To approximate the cusp, a fixed linear combination of GTOs is used in practice, which is also called a contracted basis function.

A plane wave basis is an excellent choice for metallic systems, where the electrons are usually delocalized in space. Nonetheless, all systems in PBC can be described by this basis, which has the following form:

$$\chi_{\mathbf{k}}(\mathbf{r}) = \mathrm{e}^{i\mathbf{k}\mathbf{r}} \tag{2.40}$$

Here, $\mathbf{k}$ is the wave vector of the basis function, whose absolute value represents the amount of oscillation in the function. To each $\mathbf{k}$ value, a kinetic

energy E_{kin} can be assigned by the following relation:

$$E_{\text{kin}} = \frac{1}{2}\mathbf{k}^2 \tag{2.41}$$

Although in principle, there is an infinite amount of basis functions available when using plane waves, the actual number of functions is limited by two criteria: First, only the wave functions of the same periodicity as the cell are used, and second, a cutoff to the kinetic energy is applied, so only functions with $\mathbf{k}$ values corresponding to an energy lower than E_{cutoff} are included in the basis set. This makes it very difficult to represent "sharp" features like the nuclear cusp by a plane wave basis. One way to avoid this problem is the use of pseudopotentials, which will be explained in the following subsection.

2.2.3 Pseudopotentials

Systems containing heavy elements can have a large number of core electrons that are uninvolved in bonding and reactivity. The corresponding core orbitals do not change significantly if the system undergoes changes in the valence region, e.g. chemical reactions, but are still calculated every time. This can heavily slow down the overall calculation of the electronic structure. One way to make this process more efficient is to replace the Coulomb potential between the valence electrons and the core region with a so-called pseudopotential (also called Effective Core Potential).[103,104] This potential includes an effective field representing the core electrons and nuclei, so only the valence electrons have to be treated explicitly in a calculation. For molecules, this is done for elements of the third period or higher, while for solids, elements of the second period are included as well. In addition to the general speedup in molecular and periodic calculations, they are particularly helpful if a plane wave basis set is used. This is because they remove the nuclear cusp of s-type orbitals and the oscillations of valence orbitals near the nuclei and therefore lower the kinetic energy cutoff necessary to describe the system properly.

Pseudopotentials are mainly classified by two criteria: Local vs. nonlocal and small core vs. large core. Local pseudopotentials act on all electrons in the same way, while non-local potentials depend on the orbital angular momentum (s, p, d, ...). The differentiation between small and large core depends on which electrons are defined to be in the core and valence region. For example, the large-core pseudopotential of a silver atom would only treat the $4d^{10}$ and $5s^1$ electrons explicitly, while a small-core potential would also exclude the $4s^2$ and $4p^6$ electrons. This enables a higher accuracy if the large-core potential is not performing well enough.

The Projector Augmented-Wave (PAW) method[105,106] allows to formally retain the core electrons while still benefiting from the computational speedup of pseudopotentials. The PAW wave function is divided into a valence region, which is expressed in a plane wave basis, and a core region, which is evalu-

ated on a grid or can be represented by atom-centered functions. This division is done in real space by defining a spherical augmentation region around each atom in terms of a "muffin-tin" model. In the first step of a PAW computation, a pseudo wave function $\widetilde{\Psi}$ is calculated similarly to the pseudopotential approach. Within the core region, this wave function can be expressed as the sum of smooth orbitals $\widetilde{\phi}_i$ that represent pseudo core states:

$$\widetilde{\Psi} = \sum_i c_i \widetilde{\phi}_i \tag{2.42}$$

Here, c_i are coefficients for the weight of each orbital $\widetilde{\phi}_i$. At the same time, the all-electron wave function Ψ is written as the sum of more accurate core states ϕ_i. These functions and their coefficients c_i can be determined, e.g., by calculating isolated atoms using an atom-centered basis.

$$\Psi = \sum_i c_i \phi_i \tag{2.43}$$

The all-electron wave function for the whole system is then obtained by substitution of all $\widetilde{\phi}_i$ functions by ϕ_i in the core region and using projector functions $\widetilde{p}_i$ which have to obey $\langle \widetilde{p}_i | \widetilde{\phi}_j \rangle = \delta_{ij}$:

$$|\Psi\rangle = |\widetilde{\Psi}\rangle + \sum_i \left(|\phi_i\rangle - |\widetilde{\phi}_i\rangle \right) \langle \widetilde{p}_i | \widetilde{\Psi} \rangle \tag{2.44}$$

This can also be written in the form of a transformation $\Psi = \hat{T}\,\widetilde{\Psi}$ by defining the linear transformation operator $\hat{T}$ as:

$$\hat{T} = 1 + \sum_i \left(|\phi_i\rangle - |\widetilde{\phi}_i\rangle \right) \langle \widetilde{p}_i | \tag{2.45}$$

2.2.4 Dispersion Correction

Since most density functionals are unable to describe dispersive forces,[39,40] corrections have to be applied in systems where this kind of interaction is relevant. While there are ways to modify functionals directly to include a proper description of these forces, semiempirical corrections that can be added to a finished DFT calculation will be presented here.

The DFT-D3 correction by Grimme et al.[107] describes dispersion as a sum of pairwise interaction energies:

$$E_{\text{disp}}^{\text{D3}} = -\sum_{A,B} \sum_{n=6,8} s_n \frac{C_n^{AB}}{R_{AB}^n} f_{\text{damp},n}(R_{AB}). \tag{2.46}$$

In this equation, s_n is a scaling factor for order n (the exponent of R_{AB} in the following denominator), C_n^{AB} the dispersion coeffient of atom pair AB,

R_{AB} the internuclear distance and $f_{\mathrm{damp},n}$ a damping function that is used to avoid unphysical behaviour at small distances. Summation is done over all pairs AB. The C_n^{AB} coefficients are parametrized for each atom pair with parameters taken from an ab initio time-dependent DFT calculation of the atomic polarizabilities. The D3 expression was later refined using a modified damping function by Becke and Johnson to yield the D3(BJ) expression:[108]

$$E_{\mathrm{disp}}^{\mathrm{D3(BJ)}} = -\sum_{A,B}\sum_{n=6,8} s_n \frac{C_n^{AB}}{R_{AB}^n + (\alpha_1 R_{0,AB} + \alpha_2)^n} \tag{2.47}$$

This damping function introduces three parameters: $R_{0,AB}$, a distance determining where the damping starts, and α_1 and α_2 which are determined by fitting, in a similar way to s_n. Alternatively, the dispersion coefficients and damping function can be calculated from the charge density of the system. This is done in the Tkatchenko-Scheffler method,[109] which is similar to the method by Grimme, but only uses terms of sixth order:

$$E_{\mathrm{disp}}^{\mathrm{TS}} = -\sum_{A,B} \frac{C_6^{AB}}{R_{AB}^6} f_{\mathrm{damp}}(R_{AB}) \tag{2.48}$$

2.3 Optimization Techniques

2.3.1 Structual Optimization

In many cases, one is interested in the geometry of a given set of atoms that represents an energy minimum. The process of finding the closest minimum to an initial guess of coordinates is called structural optimization. During this process, the force $\mathbf{F} = -\nabla E(\mathbf{R})$ acting on the nuclei is calculated, a stepwise displacement done by an optimization algorithm, and the procedure is repeated until the minimum structure is reached. There are several types of optimization algorithms:[79,110]

The steepest descent method displaces the nuclear coordinates by adding the force vector $\mathbf{F}_i$, scaled by a constant α, to the current structure $\mathbf{R}_i$:

$$\mathbf{R}_{i+1} = \mathbf{R}_i + \alpha \mathbf{F}_i \tag{2.49}$$

The issues, however, of this simple algorithm are a slow convergence close to a minimum and oscillation around the minimum path.[79] These problems are removed in the Conjugate Gradient method:[111] After an initial steepest descent step, all following structures $\mathbf{R}_{i+1}$ are generated by a displacement vector $\mathbf{d}_i$, which also contains part of the previous displacement $\mathbf{d}_{i-1}$ in addition to the current force $\mathbf{F}_i$:

$$\mathbf{R}_{i+1} = \mathbf{R}_i + \alpha \mathbf{d}_i \tag{2.50}$$

$$\mathbf{d}_i = \mathbf{F}_i + \beta_i \mathbf{d}_{i-1} \tag{2.51}$$

The β_i parameter can be calculated from the current and previous force vectors in the following way:

$$\beta_i = \frac{\mathbf{F}_i(\mathbf{F}_i - \mathbf{F}_{i-1})}{|\mathbf{F}_{i-1}|^2} \tag{2.52}$$

This removes the oscillation problem of the steepest descent method and ensures that the optimization closely follows the minimum path. Furthermore, the scaling factor α is optimized every second step using a line minimizer.

Close to a minimum, potentials often appear to be harmonic. Hence, information from second derivatives can be used to predict where the harmonic minimum would lie and to take the optimization step accordingly. This is done in quasi-Newton algorithms, for example the L-BFGS algorithm.[112] Here, the displacement vector is equal to the force vector $\mathbf{F}_i$ multiplied with the inverse Hessian $\mathbf{H}_i^{-1}$:

$$\mathbf{R}_{i+1} = \mathbf{R}_i + \mathbf{F}_i \mathbf{H}_i^{-1} \tag{2.53}$$

Since calculation of the inverse Hessian by second derivatives would be very expensive, it is constructed by an initial guess and further improved in each step by using changes in geometry and forces from previous iterations.

2.3.2 Nudged Elastic Band

Nudged Elastic Band (NEB)[113] is a chain-of-states method for determining the minimum energy path (MEP) between a pair of stable states, i.e. local minima on the PES. In this method, a set of geometries, also called images, connecting the two states is generated and structurally optimized. Once the calculation is finished, the images track out the MEP and properly describe the energy profile and reaction mechanism between the initial and final state (Figure 2.1).

The starting set of images is usually generated by linear interpolation of the cartesian coordinates. This works well very often, but can lead to complications e.g. if a group of atoms is rotating. In that case, the interpolation can also be done in internal coordinates.

To avoid that the images are optimized to the closest respective minimum structure, harmonic spring forces between the images are introduced. This force is added to the gradient of each structure, although not the full gradient is used, but only the force acting perpendicular to the spring. This is necessary, since using the full gradient would make the reliability of the calculation dependent on the spring force constant: With a value too low, the equidistance of the images could no longer be ensured and they would gather near the closest minima, while a too high force constant would cause corner-cutting effects and the converged calculation would not represent the minimum energy path, but a path higher in energy. Using the projection, the process becomes, in principle, independent of the force constant.

$$\begin{aligned} \mathbf{F}_i^{\mathrm{NEB}} &= \mathbf{F}_i^{\perp} + \mathbf{F}_i^{\mathrm{S}\parallel} \\ \mathbf{F}_i^{\perp} &= \mathbf{F}_i - \mathbf{F}_i^{\parallel} = -\nabla E(\mathbf{R}_i) + \nabla E(\mathbf{R}_i) \cdot \hat{\boldsymbol{\tau}}_i \hat{\boldsymbol{\tau}}_i \\ \mathbf{F}_i^{\mathrm{S}\parallel} &= k(|\mathbf{R}_{i+1} - \mathbf{R}_i| - |\mathbf{R}_i - \mathbf{R}_{i-1}|)\hat{\boldsymbol{\tau}}_i \end{aligned} \tag{2.54}$$

Equation (2.54) describes how the NEB force $\mathbf{F}_i^{\mathrm{NEB}}$ acting on image i is mathematically constructed: The force vector $\mathbf{F}_i = -\nabla E(\mathbf{R}_i)$ is projected onto the normalized tangent vector $\hat{\boldsymbol{\tau}}_i$, which is defined as the unit vector to the neighboring image of higher energy. This component is substracted from the force vector, which yields the perpendicular component $\mathbf{F}_i^{\perp}$. The spring force vector $\mathbf{F}_i^{\mathrm{S}\parallel}$ is defined as the force constant k multiplied by the difference of the coordinates $\mathbf{R}_i$ of image i to the coordinates of its neighbouring images, $\mathbf{R}_{i+1}$ and $\mathbf{R}_{i-1}$, again projected onto $\hat{\boldsymbol{\tau}}_i$. The sum of these two forces is the net force $\mathbf{F}_i^{\mathrm{NEB}}$. Although the original force along the MEP, $\mathbf{F}_i^{\parallel}$, is not accounted for dur-

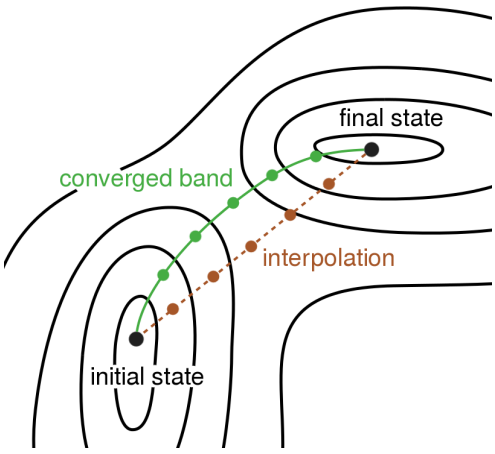

Figure 2.1. Illustration of the NEB method: A chain of states generated by interpolation is optimized to the minimum energy path (converged band).

ing optimization, it can still be used in a converged calculation to generate an interpolation in the energy profile.

In most NEB calculations, the transition state will lie between two optimized images and the exact structure and energy of it will be unknown. To solve this issue, a modification called Climbing Image (CI) was introduced.[114] In CI-NEB, the image of highest energy j feels no spring forces and instead of subtracting the original force along the tangent $\mathbf{F}_j^{S\parallel}$ once, it is subtracted twice (Equation (2.55)). This leads to an optimization process where the energy along the MEP is maximized, while it is minimized in all other directions. Image j therefore converges to the nearest first-order saddle point, the transition state.

$$\mathbf{F}_j^{\mathrm{CI}} = \mathbf{F}_j - 2\mathbf{F}_j^{\parallel} \tag{2.55}$$

2.3.3 The Dimer Method

In some cases, chain-of-states methods might not be an appropriate choice for finding transition states, for example if only the initial state, but not the final state of a reaction is known. Here, a minimum mode following algorithm, as often used in molecular calculations, is a suitable choice. This approach determines the vibrational mode of the lowest frequency at every optimization step and follows it until a transition state is reached. The underlying assumption is that this mode is the one that is most probable to invert its curvature and should therefore lead to the lowest-energy transition state close to the minimum. Unfortunately, calculating the Hessian at every step to determine the vibrational modes is very costly and while there are ways to reduce this cost in molecular calculations, the approach is not feasible for extended systems. The Dimer method[115] allows to determine the minimum mode without calculation of the Hessian. To do so, two structures, $\mathbf{R}_1$ and $\mathbf{R}_2$, are generated by positive and negative displacement of the current structure $\mathbf{R}$ in a normalized search direction $\hat{\mathbf{N}}$ by a separation distance ΔR:

$$\mathbf{R}_{1,2} = \mathbf{R} \pm \Delta R \cdot \hat{\mathbf{N}} \tag{2.56}$$

At each step of the calculation, the forces $\mathbf{F}_1$ and $\mathbf{F}_2$ of the dimer are evaluated (see Figure 2.2). Their components perpendicular to $\hat{\mathbf{N}}$ are added and the resulting perpendicular force $\mathbf{F}^{\perp}$ causes the dimer to rotate. Rotation steps are performed iteratively until $\mathbf{F}^{\perp}$ vanishes and, consequently, $\hat{\mathbf{N}}$ points in the direction of the minimum mode. To find an optimization (translation) direction which maximizes the energy along $\hat{\mathbf{N}}$, but minimizes it in all other directions, the modified force $\mathbf{F}^{\dagger}$ has to be introduced (Equation (2.57). To determine $\mathbf{F}^{\dagger}$, the net translational force $\mathbf{F}_R$, which is simply the average force $(\mathbf{F}_1 + \mathbf{F}_2)/2$, is taken and its component along $\hat{\mathbf{N}}$, the parallel force $\mathbf{F}^{\parallel}$, is subtracted twice:

$$\mathbf{F}^{\dagger} = \mathbf{F}_R - 2\mathbf{F}^{\parallel} \tag{2.57}$$

After each translational step, the rotation procedure is repeated, since the optimum search direction could have changed. The calculation is finished if the net force $\mathbf{F}_R$ is zero and the curvature of the energy profile of $\mathbf{R}_2$, $\mathbf{R}$ and $\mathbf{R}_1$ is positive so that $\mathbf{R}$ is a maximum in the search direction $\hat{\mathbf{N}}$.

2.4 Statistical Thermodynamics and Kinetics

2.4.1 Calculating Gibbs Free Energies

Chemical reactions are usually taking place at constant temperature and pressure. Therefore, the Gibbs energy G is the thermodynamical potential that determines how the system will evolve. Although energies from electronic structure calculations often cover most of the energetic differences, changes due to thermal excitation can sometimes be drastic and have to be considered to describe the system correctly. In the following, an approach to calculate thermodynamic corrections to the electronic energy using the concepts of statistical mechanics is described.

In systems where the electronic ground state is non-degenerate and other electronic states are not accessible via thermal excitation, only the motion of the nuclei is contributing to thermodynamic correction terms. There are two types of terms that have to be added to the electronic energy E_{el} to yield the Gibbs energy G: An enthalpy correction term H_{corr} that represents how far motions are thermally excited at a given temperature T, and an entropy term S that represents how many possibilities there are to distribute the available thermal energy into different excited states of the motions. The relation between these quantities is given by Equation (2.58). The enthalpy correction and entropy terms can be decomposed into contributions of vibration (vib), rotation (rot) and translation (trans) (Equations (2.59) and (2.60)). These are calculated using the partition functions of the harmonic oscillator, rigid rotor

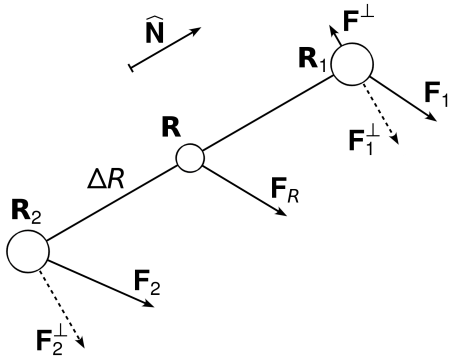

Figure 2.2. Illustration of the positions and force vectors in a Dimer calculation.

and ideal gas approximations (Equations (2.61) to (2.65)).[79,116]

$$G = E_{\mathrm{el}} + H_{\mathrm{corr}} - TS \tag{2.58}$$

$$H_{\mathrm{corr}} = H_{\mathrm{vib}} + H_{\mathrm{rot}} + H_{\mathrm{trans}} \tag{2.59}$$

$$S = S_{\mathrm{vib}} + S_{\mathrm{rot}} + S_{\mathrm{trans}} \tag{2.60}$$

$$H_{\mathrm{vib}} = R\sum_i \left(\frac{h\nu_i}{k}\left(\frac{1}{2} + \frac{1}{e^{h\nu_i/kT}-1}\right)\right) \tag{2.61}$$

$$H_{\mathrm{rot}} = \frac{3}{2}RT \qquad H_{\mathrm{trans}} = \frac{5}{2}RT \tag{2.62}$$

$$S_{\mathrm{vib}} = R\sum_i \left(\frac{h\nu_i}{kT}\frac{1}{e^{h\nu_i/kT}-1} - \ln\left(1-e^{-h\nu_i/kT}\right)\right) \tag{2.63}$$

$$S_{\mathrm{rot}} = R\left(\frac{3}{2} + \ln\left(\frac{\sqrt{\pi}}{\sigma}\left(\frac{8\pi^2 kT}{h^2}\right)^{\frac{3}{2}}\sqrt{I_1 I_2 I_3}\right)\right) \tag{2.64}$$

$$S_{\mathrm{trans}} = R\left(\frac{5}{2} + \ln\left(\frac{kT}{p}\left(\frac{2\pi mkT}{h^2}\right)^{\frac{3}{2}}\right)\right) \tag{2.65}$$

Here, ν_i are the computed harmonic frequencies, T is the temperature, σ the symmetry number of the molecule (i.e. the number of identical orientations), I_1, I_2 and I_3 the moments of inertia, p the pressure and m the molecular mass. Summation is done over all vibrational modes i and the zero-point vibrational energy is already included in H_{vib}. In case of a linear molecule, where there are only two rotational degrees of freedom and one more vibrational mode, the following modifications are made to H_{rot} and S_{rot}:

$$H_{\mathrm{rot}}(\mathrm{linear}) = RT \tag{2.66}$$

$$S_{\mathrm{rot}}(\mathrm{linear}) = R\left(1 + \ln\left(\frac{\sqrt{\pi}}{\sigma}\left(\frac{8\pi^2 kT}{h^2}\right)\sqrt{I_1 I_2}\right)\right) \tag{2.67}$$

In extended systems with periodic boundary conditions, rotation and translation of the bulk or surface slab are not considered and all nuclear motion is contained in the vibrations. Hence, rotation and translation only need to be considered in molecular calculations. Exceptions are weakly bound adsorbates where only a part of the motions of the free molecule are converted into vibrations and translation or rotation on the surface might only have a low energy barrier (see also Section 1.1). In those cases, the respecitve degrees of freedom can be calculated once as a vibration and once as a free translation or rotation to get upper and lower limits for their contribution to the Gibbs energy.

2.4.2 Reaction Rates

In chemical reactions, the reaction rate k determines how fast the system will convert from an initial state to a product state. It can be described by the Arrhenius equation (2.68), which is a function of the reaction energy barrier E_a, the temperature T, and a pre-exponential factor A_0. Since A_0 has the dimension of time^{-1}, it is usually interpreted as an attempt frequency, i.e. how frequently the system moves into the direction of the transition state. The exponential term gives the Boltzmann probability of the system to contain enough energy to overcome the energy barrier.

$$k(T) = A_0 \cdot \exp\left(-\frac{E_a}{k_B T}\right) \tag{2.68}$$

There are multiple ways to calculate A_0 from theory: In harmonic transition state theory (hTST), the vibrations of a system are approximated as harmonic oscillators and the classical rate equation is given by:[117]

$$k_{cl}^{hTST} = \frac{1}{Q_{trans}^{init} Q_{rot}^{init}} \frac{\prod_i \nu_i^{init}}{\prod_i \nu_i^{\ddagger}} \exp\left(-\frac{E_a}{k_B T}\right) \tag{2.69}$$

Here, Q_{trans}^{init} and Q_{rot}^{init} are the translational and rotational partition functions of the initial state (both are equal to 1 if all degrees of freedom are vibrations) and ν_i^{init} and $\nu_i^{\ddagger}$ are the vibrational frequencies in the initial and transition state, respectively. At the transition state, one mode has an imaginary frequency, which is not included in the product $\prod_i \nu_i^{\ddagger}$. The pre-exponential factor can therefore be viewed as an effective frequency that contains the initial frequency of the mode that inverts its curvature plus the changes in all other modes. In chemical systems, this expression is only valid at very high temperatures, since it is derived from classical mechanics and quantum effects only become negligible in the high-temperature limit. One way to correct this is to include the zero-point vibrational energy (ZPVE) in the activation energy E_a. However, this would only be valid at very low temperatures, when all vibrational modes are in their respective ground state. The quantum mechanical nature of the vibrations in the temperature range in between can be included by using the quantum mechanical partition functions for the vibrational modes in Equation (2.69). This is called quasi-quantum harmonic transition state theory (qq-hTST)[117,118] and the corresponding rate equation is

$$\begin{aligned} k_{qm}^{hTST} &= \frac{\prod_i \sinh(x_i^{init})/x_i^{init}}{\prod_i \sinh(x_i^{\ddagger})/x_i^{\ddagger}} \, k_{cl}^{hTST} \\ &= \frac{1}{Q_{trans}^{init} Q_{rot}^{init}} \frac{2k_B T}{h} \frac{\prod_i \sinh(x_i^{init})}{\prod_i \sinh(x_i^{\ddagger})} \exp\left(-\frac{E_a}{k_B T}\right) \end{aligned} \tag{2.70}$$

with $x_i = h\nu_i / 2k_\mathrm{B}T$. This can also be formulated as a temperature-dependent correction δE to the energy barrier E_a:

$$k_\mathrm{qm}^\mathrm{hTST} = \exp\left(\frac{\delta E}{k_\mathrm{B}T}\right) k_\mathrm{cl}^\mathrm{hTST} \tag{2.71}$$

$$\delta E = -k_\mathrm{B}T \ln\left[\frac{\prod_i \sinh(x_i^\mathrm{init})/x_i^\mathrm{init}}{\prod_i \sinh(x_i^\ddagger)/x_i^\ddagger}\right] \tag{2.72}$$

In the high-temperature limit, δE vanishes, while in the low-temperature limit, it is equivalent to the zero-point energy correction. It therefore adequately describes the system over the whole temperature range.

2.5 Ab Initio Molecular Dynamics

Sometimes, the representation of a system by a statistical ensemble, as presented in the last section, does not adequately describe its dynamics and effects of thermal excitation. In these cases, the evolution of the system over time has to be calculated explicitly. This is called molecular dynamics (MD). While there are ways to treat the dynamics of electrons and nuclei at the same time, e.g. Car-Parrinello MD,[119] it is often sufficient to treat the nuclei as classical particles that propagate on the potential energy surface $E(\mathbf{R})$, which can be calculated by ab initio methods. In this case, the trajectory is obtained by integration of Newton's second law of motion (Equations (2.73) and (2.74)).[79]

$$\mathbf{F} = m\mathbf{A} \tag{2.73}$$

$$-\nabla E(\mathbf{R}) = m\frac{\mathrm{d}^2\mathbf{R}}{\mathrm{d}t^2} \tag{2.74}$$

For a small time step Δt, the positions $\mathbf{R}_{i+1}$ of the nuclei at step $i+1$ can be represented by a Taylor expansion at $\mathbf{R}_i$:

$$\begin{aligned}\mathbf{R}_{i+1} &= \mathbf{R}_i + \frac{\mathrm{d}\mathbf{R}}{\mathrm{d}t}\Delta t + \frac{1}{2}\frac{\mathrm{d}^2\mathbf{R}}{\mathrm{d}t^2}(\Delta t)^2 + \ldots \\ &= \mathbf{R}_i + \mathbf{V}_i\Delta t + \frac{1}{2}\mathbf{A}_i(\Delta t)^2 + \ldots\end{aligned} \tag{2.75}$$

Here, $\mathbf{V}_i$ are the velocities and $\mathbf{A}_i$ the accelerations at step i. Although this series could, in principle, be continued, terms of higher than second order (hyperaccelerations) are usually not considered. While the accelerations are always obtained from the gradient via Equation (2.74), there are different ways to calculate the next set $(i+1)$ of coordinates and velocities. Two simple algorithms are the Verlet[120] and the leap-frog integrator.[121] Their disadvantages, however, are a high sensitivity towards finite precision errors (Verlet) and the use of "half steps" (leap frog), which is why the positions and veloci-

ties are never known at the same time.[79] Both disadvantages are removed in the velocity Verlet algorithm,[120,122] which was used in this work. The corresponding equations are:

$$\mathbf{R}_{i+1} = \mathbf{R}_i + \mathbf{V}_i \Delta t + \frac{1}{2}\mathbf{A}_i (\Delta t)^2 \tag{2.76}$$

$$\mathbf{V}_{i+1} = \mathbf{V}_i + \frac{1}{2}(\mathbf{A}_i + \mathbf{A}_{i+1})\, \Delta t \tag{2.77}$$

In general, MD simulations are very sensitive to the choice of the time step Δt. While a too small value increases the computational effort without further benefit, a too large value can lead to a trajectory where high-frequency vibrations are not properly sampled and energy conservation is violated. In systems containing organic molecules, the vibrations of highest frequency are the X-H (X=C,N,O,...) stretching modes with a period of ≈ 10 fs. Here, a Δt value of 1 fs is usually an appropriate choice.

2.5.1 Thermostats

The natural ensemble of a standard MD simulation is NVE, which means that the number of particles N, the volume of the system V and the total energy E are conserved. However, many chemical reactions take place at constant temperature. To account for this in a MD simulation, a thermostat is introduced, which adds or removes kinetic energy to or from the system.[123] Since the average kinetic energy $\langle E_{\text{kin}} \rangle$ of each single degree of freedom is proportional to the temperature

$$\langle E_{\text{kin}} \rangle = \frac{1}{2} k_{\text{B}} T, \tag{2.78}$$

one way to keep the temperature constant is to scale the velocities $\mathbf{V}$ by a scaling factor α if the actual temperature T_{act} deviates from the desired temperature T_{des}:

$$\frac{\mathrm{d}T}{\mathrm{d}t} = \frac{1}{\tau}\left(T_{\text{des}} - T_{\text{act}}\right) \tag{2.79}$$

$$\alpha = \frac{\Delta \mathbf{V}}{\mathbf{V}} = \sqrt{1 + \frac{\Delta t}{\tau}\left(\frac{T_{\text{des}}}{T_{\text{act}}} - 1\right)} \tag{2.80}$$

The rate of the heat transfer is controlled by a coupling parameter τ. While this thermostat produces correct averages of properties, it also shows incorrect fluctuations.[79] This deficiency is removed by using the Nosé thermostat.[124,125] Here, the heat bath is treated as an integral part of the system by introducing an additional degree of freedom s which couples to all $3N$ internal degrees of freedom and periodically adds and removes kinetic energy to

or from the system. The classical Hamiltonian in this approach is given by:

$$H = E(\mathbf{R}) + \sum_{\alpha} \frac{1}{2s^2} m_\alpha \mathbf{V}_\alpha^2 + \frac{1}{2} M_{\text{Nosé}} V_s^2 + (3N+1)\, k_\text{B} T \ln s \tag{2.81}$$

$E(\mathbf{R})$ is the electronic potential energy surface, which acts as a classical potential here, $\mathbf{V}_\alpha$ is the velocity of nucleus α, V_s the velocity of s, and $M_{\text{Nosé}}$ is the thermostat mass, which controls the energy oscillation frequency. It should be set to a value so that the frequency is approximately the same as the lowest internal vibrational frequencies in the system. This ensures a proper coupling and simulates the heat transport in a real system, which mainly takes place via long-range low-frequency phonons.

2.6 Bonding Analysis

2.6.1 Periodic Energy Decomposition Analysis

The EDA is a method that decomposes the interaction energy ΔE_int between two fragments A and B in a system into well defined terms that allow interpretation in a chemically meaningful way.[32] This approach was developed by Morokuma[126,127] as well as Ziegler and Rauk.[128] Recently, the EDA was adapted for application to periodic systems, e.g. surfaces and solids.[33] The formalism in this periodic EDA is identical to the molecular EDA, the only differences are in the treatment of the electronic structure due to the periodic boundary conditions (see also Section 2.2.1) and a separate treatment of dispersion interactions. Those will not be discussed here and can be found in the original article.

The interaction energy ΔE_int can be obtained by subtracting the preparation energy ΔE_prep from the bonding energy E_bond between the two fragments:

$$\Delta E_\text{int} = E_\text{bond} - \Delta E_\text{prep} \tag{2.82}$$

These three terms can be defined by the energy E_AB of the relaxed total system, the energies E_A^rel and E_B^rel of the relaxed isolated fragments and the energies E_A and E_B of the fragments in their "prepared" state:

$$\Delta E_\text{int} = E_\text{AB} - E_\text{A} - E_\text{B} \tag{2.83}$$

$$E_\text{bond} = E_\text{AB} - E_\text{A}^\text{rel} - E_\text{B}^\text{rel} \tag{2.84}$$

$$\Delta E_\text{prep} = E_\text{A} + E_\text{B} - E_\text{A}^\text{rel} - E_\text{B}^\text{rel} \tag{2.85}$$

The preparation of the fragments consists of structural deformation to achieve the geometry in the bound system and, optionally, electronic excitation. Since dispersion is usually not included in a DFT calculation and has to be added in a semiempirical way (see also Section 2.2.4), ΔE_int can furthermore be di-

vided into contributions stemming from dispersion (disp) and electronic effects (elec):

$$\Delta E_{\text{int}} = \Delta E_{\text{int}}(\text{disp}) + \Delta E_{\text{int}}(\text{elec}) \tag{2.86}$$

The actual EDA procedure then decomposes $\Delta E_{\text{int}}(\text{elec})$ into contributions from Pauli repulsion, electrostatics (elstat) and orbital interaction (orb):

$$\Delta E_{\text{int}}(\text{elec}) = \Delta E_{\text{Pauli}} + \Delta E_{\text{elstat}} + \Delta E_{\text{orb}} \tag{2.87}$$

These energies are calculated in the following way: First, a product wave function $\{\Psi_{\text{A}}\Psi_{\text{B}}\}$ with a corresponding energy E^0_{AB} is generated from the wave functions Ψ_{A} and Ψ_{B} of the fragments in their prepared state. The electron densities ρ_{A} and ρ_{B} of the fragments as well as the charge Z and location $\mathbf{R}$ of the nuclei can be used to calculate the quasiclassical Coulomb interaction ΔE_{elstat}:

$$\begin{aligned}\Delta E_{\text{elstat}} = &\sum_{\alpha\in\text{A}}\sum_{\beta\in\text{B}}\frac{Z_\alpha Z_\beta}{|\mathbf{R}_\alpha - \mathbf{R}_\beta|} - \sum_{\alpha\in\text{A}}\int\frac{Z_\alpha\,\rho_{\text{B}}(\mathbf{r})}{|\mathbf{R}_\alpha - \mathbf{r}|}\,\mathrm{d}\mathbf{r} \\ &- \sum_{\beta\in\text{B}}\int\frac{Z_\beta\,\rho_{\text{A}}(\mathbf{r})}{|\mathbf{R}_\beta - \mathbf{r}|}\,\mathrm{d}\mathbf{r} + \iint\frac{\rho_{\text{A}}(\mathbf{r}_i)\rho_{\text{B}}(\mathbf{r}_j)}{|\mathbf{r}_i - \mathbf{r}_j|}\,\mathrm{d}\mathbf{r}_i\mathrm{d}\mathbf{r}_j\end{aligned} \tag{2.88}$$

This quantity is attractive in most cases. In the second step, the product wave function is antisymmetrized by an operator $\hat{A}$ and renormalized by a constant N to fulfil the Pauli principle. The difference between the energy E^0 of this wave function Ψ^0 and E^0_{AB} is defined as the Pauli repulsion energy ΔE_{Pauli}:

$$\Psi^0 = N\hat{A}\{\Psi_{\text{A}}\Psi_{\text{B}}\} \tag{2.89}$$

$$\Delta E_{\text{Pauli}} = E^0 - E^0_{\text{AB}} \tag{2.90}$$

This energy is always repulsive, since constraints are put on the wave function. Once the wave function Ψ_{AB} and energy E_{AB} of the relaxed total system are determined, the orbital interaction energy ΔE_{orb} can be calculated as the energy difference to E^0:

$$\Delta E_{\text{orb}} = E_{\text{AB}} - E^0 \tag{2.91}$$

ΔE_{orb} is always attractive, because the wave function is optimized in this step. Since there are two attractive and stabilizing terms in the EDA, ΔE_{elstat} and ΔE_{orb}, the ratio between them is one way to characterize the bond. This is usually done by assigning percentage values.

2.6.2 Extended Transition State–Natural Orbitals for Chemical Valence

The orbital term of the EDA can further be decomposed by applying the ETS-NOCV scheme to the system.[45] Here, the density difference $\Delta\rho_{\text{orb}}$ between ρ_{AB} and ρ^0, which represents the change in electron density due to orbital interaction, is expressed by a set of orthonormal fragment spin-orbitals λ_i, which also form the basis of the deformation density matrix $\Delta\mathbf{P}^{\text{orb}}$:

$$\Delta\rho_{\text{orb}} = \rho_{\text{AB}} - \rho^0 = \sum_{\mu}\sum_{\nu} \Delta P^{\text{orb}}_{\mu\nu}\, \lambda_\mu \lambda_\nu \tag{2.92}$$

$\Delta P^{\text{orb}}_{\mu\nu}$ are the matrix elements of $\Delta\mathbf{P}^{\text{orb}}$. The NOCVs ψ_i are now defined as the eigenvectors that diagonalize $\Delta\mathbf{P}^{\text{orb}}$ and must satisfy Equation (2.93).

$$\Delta\mathbf{P}^{\text{orb}}\,\mathbf{C}_i = v_i\,\mathbf{C}_i \tag{2.93}$$

$$\psi_i = \sum_j C_{ij}\,\lambda_j \tag{2.94}$$

The eigenvalues v_i give the amount of charge that is transferred into or out of an NOCV, depending on the sign. These values pair, so there are always two eigenvalues v_k and v_{-k} of the same absolute value, but opposite sign. The corresponding pair of orbitals (ψ_{-k}, ψ_k) can then be used to express $\Delta\rho_{\text{orb}}$ in terms of deformation densities $\Delta\rho_k$ that are associated with the eigenvalues v_k:

$$\Delta\rho_{\text{orb}} = \sum_k v_k \left[-|\psi_{-k}|^2 + |\psi_k|^2\right] = \sum_k \Delta\rho_k \tag{2.95}$$

It is also possible to assign energy values to the deformation densities. This is done by using $\Delta\mathbf{P}^{\text{orb}}$ to decompose ΔE_{orb}:

$$\Delta E_{\text{orb}} = E[\rho_{\text{AB}}] - E[\rho^0] = \sum_{\mu}\sum_{\nu} \Delta P^{\text{orb}}_{\mu\nu}\, F^{\text{TS}}_{\mu\nu} \tag{2.96}$$

$F^{\text{TS}}_{\mu\nu}$ are matrix elements of the Kohn-Sham Fock matrix $\mathbf{F}^{\text{TS}}$ of a so-called transition state density ρ^{TS} which is defined as the average of ρ_{AB} and ρ^0:

$$\rho^{\text{TS}} = \frac{1}{2}\left(\rho_{\text{AB}} + \rho^0\right) \tag{2.97}$$

The trace of the product of $\Delta\mathbf{P}^{\text{orb}}$ and $\mathbf{F}^{\text{TS}}$ is equivalent to ΔE_{orb} and can also be connected to the eigenvalues v_i of $\Delta\mathbf{P}^{\text{orb}}$. This is done by unitary transformation of $\Delta\mathbf{P}^{\text{orb}}$ and $\mathbf{F}^{\text{TS}}$ from the basis of the fragment orbitals λ_i into the basis of the NOCVs ψ_i using the transformation operator $\mathbf{C}$. The diagonal matrix elements $F^{\text{TS}}_{i,i}$ of the transformed Fock matrix can then be used to assign energy values ΔE^{orb}_i to the eigenvalues v_i and their corresponding deformation

densities $\Delta\rho_i$:

$$\begin{aligned}\Delta E_{\text{orb}} &= \text{Tr}\Big(\Delta\mathbf{P}^{\text{orb}}\,\mathbf{F}^{\text{TS}}\Big) = \text{Tr}\Big(\mathbf{C}^{\dagger}\Delta\mathbf{P}^{\text{orb}}\mathbf{C}\,\mathbf{C}^{\dagger}\mathbf{F}^{\text{TS}}\mathbf{C}\Big) \\ &= \sum_k v_k\left[-F^{\text{TS}}_{-k,-k} + F^{\text{TS}}_{k,k}\right] = \sum_k \Delta E^{\text{orb}}_k \end{aligned} \tag{2.98}$$

2.7 Simulating Experimentally Observable Properties

2.7.1 Scanning Tunneling Microscopy

Scanning Tunneling Microscopy (STM) allows to map the topography of surfaces by exploiting the tunneling of electrons between a tip and the surface.[129] In order to have a measurable current, the tip has to be sufficiently close to the surface; typical distances are in the same order of magnitude as interatomic distances (several Angstroms). The theory of STM was first described by Tersoff and Hamann in the following way:[130,131]

The current I of electrons tunneling between electronic states ψ_μ of the tip and electronic states ψ_ν of the surface can be calculated by first-order perturbation theory as:

$$I = \frac{2\pi e}{\hbar}\sum_{\mu,\nu} f(E_\mu)\left[1 - f(E_\nu + eU)\right] \times |M_{\mu\nu}|^2\,\delta(E_\mu - E_\nu) \tag{2.99}$$

Here, $f(E_i)$ is the Fermi function at the energy E_i of state ψ_i, U is the applied voltage and $M_{\mu\nu}$ the tunneling matrix element between the two states, which was shown to be:[132]

$$M_{\mu\nu} = \frac{\hbar^2}{2m_{\text{e}}}\int (\psi^*_\mu \nabla\psi_\nu - \psi_\nu\nabla\psi^*_\mu)\,\text{d}\mathbf{S} \tag{2.100}$$

Integration is done over any surface lying entirely in the vacuum between the tip and the surface. In the limit of low temperatures (room temperature or below) and small voltages, Equation (2.99) is reduced to:

$$I = \frac{2\pi e}{\hbar}\,e^2U\sum_{\mu,\nu}|M_{\mu\nu}|^2\,\delta(E_\nu - E_{\text{F}})\,\delta(E_\mu - E_{\text{F}}) \tag{2.101}$$

In the most simple approximation, the tip is replaced by a probing point charge. This represents the ideal case of maximum resolution and nonintrusive measurement. The current is then proportional to the local density of states (LDOS) at the Fermi energy E_{F} and the position $\mathbf{r}_0$ of the probe:

$$I \propto \sum_\nu |\psi_\nu(\mathbf{r}_0)|^2\,\delta(E_\nu - E_{\text{F}}) \tag{2.102}$$

Hence, the measured topography represents a contour map of constant density (the LDOS) and only this quantity has to be calculated to simulate STM topographies in this approximation. While there are more sophisticated ways to calculate the topography that also consider electronic states of the tip, in many cases this approach is sufficient.

2.7.2 Vibrational Spectroscopy

Vibrational frequencies can be calculated at any stationary point, e.g. a minimum or saddle point of the PES. They are obtained from the Hessian **H**, the matrix of second derivatives with respect to the nuclear coordinates, which can be determined either by density functional perturbation theory[133–135] or by numerical construction using finite differences. Diagonalization of **H** yields the harmonic frequencies as eigenvalues and the vibrational modes as eigenvectors. Often, a scaling factor is applied to the frequencies to compensate for inaccuracies in the electronic structure calculation and the harmonic approximation. A list of scaling factors for several approximate methods can be found, e.g., at the Computational Chemistry Comparison and Benchmark Database (CCCBDB).[136]

The intensities of vibrations in infrared (IR) spectroscopy can be calculated in the following way:[137] First, the transition dipole moment $\boldsymbol{\mu}_{n\to m}$ of vibrational states ψ_n and ψ_m has to be calculated, since the adsorption intensity I is proportional to the square of this quantity:

$$I \propto |\boldsymbol{\mu}_{n\to m}|^2 \tag{2.103}$$

$$\boldsymbol{\mu}_{n\to m} = \langle \psi_m | \boldsymbol{\mu} | \psi_n \rangle \tag{2.104}$$

The dipole operator $\boldsymbol{\mu}$ can be written as a first-order Taylor expansion of the dipole moment in normal coordinates $\boldsymbol{Q}_i$,

$$\boldsymbol{\mu} = \boldsymbol{\mu}_0 + \sum_i \left(\frac{\partial \boldsymbol{\mu}}{\partial \boldsymbol{Q}_i} \right)_0 \boldsymbol{Q}_i \tag{2.105}$$

where the subscript 0 denotes the equilibrium structure. Inserting this expression into Equation (2.104) yields:

$$\boldsymbol{\mu}_{n\to m} = \boldsymbol{\mu}_0 \langle \psi_m | \psi_n \rangle + \sum_i \left(\frac{\partial \boldsymbol{\mu}}{\partial \boldsymbol{Q}_i} \right)_0 \langle \psi_m | \boldsymbol{Q}_i | \psi_n \rangle \tag{2.106}$$

The first integral is zero, since in the harmonic approximation, all vibrational states are orthogonal to each other. The second integral is only non-zero if the change in the vibrational quantum number v_i for the vibration along $\boldsymbol{Q}_i$ is one ($\Delta v_i = \pm 1$). Furthermore, $\boldsymbol{\mu}$ has to change during this vibration. So essentially, the IR intensity of a vibrational mode i is proportional to the square of the

change in $\boldsymbol{\mu}$ with respect to the direction of the mode, $\boldsymbol{Q}_i$:

$$I_i \propto \left(\frac{\partial \boldsymbol{\mu}}{\partial \boldsymbol{Q}_i} \right)^2 \tag{2.107}$$

Hence, a calculation of the change in dipole moment, as it can be done during numerical construction of the Hessian, is sufficient to calculate the intensities of the vibrational modes.

3

Results and Discussion

3.1 Computational Setup

All calculations except bonding analysis were performed in the Vienna Ab Initio Simulation Package (VASP),[138–141] version 5.3.5, using the PAW formalism[105,106] (E_{cutoff} = 400 eV), the PBE[90,91] and HSE06[98–100] functionals and the D3(BJ) dispersion correction by Grimme and co-workers.[107,108] The Si(001) surface was modeled as a six-layer slab in the frozen double layer approximation (i.e. the positions of the atoms in the two lowest layers were kept fixed) with the bottom layer saturated with hydrogen atoms pointing in the direction of the next bulk layer at a distance of d(Si-H) = 1.480 Å, the experimental equilibrium Si-H bond length in silane.[142] The $c(4\times2)$ reconstruction was applied to the surface and sizes of 4×2 and 4×4 atoms per layer were chosen, which corresponds to coverages of θ = 0.25 (4×2) and 0.125 (4×4) molecules per surface dimer. The cell constants a and b were set to 15.324 and 7.662 (4×2) or 15.324 Å (4×4), respectively, derived from an optimized bulk lattice parameter of 5.418 Å.[143] Electronic k space was sampled using a Γ-centered Monkhorst-Pack grid: Γ(241) for cells of size 4×2 and Γ(221) for cells of size 4×4. Additionally, a vacuum of at least 10 Å in z direction was ensured to minimize interactions with periodically repeated images of the slab.

The convergence criterion for the self-consistent field (SCF) calculations was set to 10^{-5} eV, while structural optimization was done to an accuracy of 10^{-2} eV Å^{-1} using the Conjugate Gradient algorithm[111] Reaction pathways and transition states were calculated using the NEB method,[113,114] while occasionally, the Dimer method[115] was used to refine the structure of transition states. Vibrational frequencies were calculated by numerical construction of the Hessian using Cartesian displacements of 0.01 Å and a SCF convergence

criterion of 10^{-8} eV. Additionally, structures for frequency calculations were more strictly converged down to $5 \cdot 10^{-3}$ eV Å^{-1} or lower. Gibbs energies were calculated at T = 300 K, p = 1 bar unless stated otherwise. All obtained minimum and transition state structures are given in the Appendix.

Ab initio MD trajectories were calculated using the velocity Verlet algorithm[120,122] with a time step of $\Delta t = 1$ fs. A canonical NVT ensemble was simulated using the Nosé thermostat[124,125] with a thermostat mass set to a value so that the energy oscillation had the same periodicity λ as the lowest energy vibrations in the system ($\lambda \approx 600$ fs $\widehat{=}$ 55 cm^{-1}). Initially, molecule and slab were simulated separately for 20 ps starting in their respective minimum geometry. This was done to get both independently of each other into thermodynamic equilibrium. Afterwards, the coordinates and velocities were written out every 3 ps to obtain qualitatively different states of thermal excitation. At this point, sets for molecule and surface were arbitrarily paired and the molecular center of mass was displaced randomly in x and y direction using a true number generator,[144] while in z direction, it was placed 5.5 Å above the equilibrium position of the highest surface atom. Additionally, the effect of gas escaping a nozzle into UHV was simulated by adding a thermal translational velocity vector to the molecule. The vector's absolute value was chosen as the mean speed of a Maxwell-Boltzmann distribution (Equation 3.1), where T is the temperature and m the molecular mass, while the direction was again chosen randomly using a true number generator. As a restriction, the z component of the vector was ensured to point towards the surface.

$$\langle v \rangle = \sqrt{\frac{8 k_\mathrm{B} T}{\pi m}} \tag{3.1}$$

Bonding analysis was performed using the pEDA method[33] as implemented in ADF-BAND 2016[145,146] at the PBE-D3(BJ)/TZ2P level of theory and a Γ only sampling of k space. STM topographies were calculated in the Tersoff-Hamann approximation.[130,131]

3.2 General Remarks

In the following, results on the adsorption of four different organic molecules on the Si(001), as introduced in Section 1.4, will be presented and discussed. The majority of the results has already been published as articles in peer-reviewed journals and these are included as part of the main body of this thesis. For sections that are treated in an article, the respective citation, abstract and author contribution is given here, while the article itself can be found in the Appendix.

3.3 Model Systems

3.3.1 Precursor States of Organic Adsorbates on Semiconductor Surfaces are Chemisorbed and Immobile

J. Pecher and R. Tonner, *ChemPhysChem* **2017**, *18*, 34.

Abstract
Intermediate states to covalent attachment of molecules on surfaces, so called precursors, are usually considered to be physisorbed and mobile. We show that this view should be reconsidered and provide evidence for a chemisorbed precursor for ethylene on Si(001). The character of the molecule-surface bond as a π complex is determined and quantified using our recently developed method for energy and charge analysis in extended systems. In contrast to previous assumptions, the precursor should thus be immobile, which is underlined by computation of high diffusion energy barriers. This has important implications for understanding and modelling of adsorption kinetics. Our analysis highlights that taking the viewpoint of molecular chemistry helps uncover important aspects in the adsorption process on surfaces. Previous experimental results that appear to be in contrast to our model are examined and reinterpreted.[147]

Contributions
The author performed all calculations leading to the results presented in this article. Interpretation of the results was initially done by the author and discussed with the supervisor. The first version of the manuscript was written by the author and subsequently refined in collaboration with the supervisor.

3.3.2 Site-Specific Reactivity of Ethylene at Distorted Dangling-Bond Configurations on Si(001)

J. Pecher, G. Mette, M. Dürr and R. Tonner, *ChemPhysChem* **2017**, *18*, 357.

Abstract
Differences in adsorption and reaction energetics for ethylene on Si(001) are reported with respect to distorted dangling bond configurations induced by hydrogen precoverage, as obtained by DFT calculations. This can help to understand the influence of surface defects and precoverage on the reactivity of organic molecules on semiconductor surfaces in general. The results show that the reactivity of surface dimers fully enclosed by hydrogen-covered atoms is essentially unchanged compared to the clean surface. This is confirmed by scanning tunneling microscopy measurements. On the contrary, adsorption sites with partially covered surface dimers show a drastic increase in reactivity. This is due to a lowering of the reaction barrier by more than 50% relative

to the clean surface, which is in line with previous experiments. Adsorption on dimers enclosed by molecule (ethylene)-covered surface atoms is reported to have a strongly decreased reactivity, as a result of destabilization of the intermediate state due to steric repulsion; this is quantified through periodic energy decomposition analysis. Furthermore, an approach for the calculation of Gibbs energies of adsorption based on statistical thermodynamics considerations is applied to the system. The results show that the loss in molecular entropy leads to a significant destabilization of adsorption states.[148]

Contributions
The study was motivated by experimental results from GM and a discussion between the four authors and Prof. Ulrich Höfer. The author performed all theoretical calculations and derived the approach to calculate Gibbs energies of adsorption, while the experimental data was obtained by GM. Results were discussed with the supervisors (MD and RT) and the first version of the theoretical part of the manuscript was written by the author, while GM wrote the experimental methods and experimental results sections. The author additionally wrote the first version of the abstract, introduction and conclusions sections. The manuscript was subsequently refined in collaboration between all four authors.

3.3.3 Ethers on Si(001): A Prime Example for the Common Ground Between Surface Science and Molecular Organic Chemistry

L. Pecher, S. Laref, M. Raupach and R. Tonner, *Angew. Chem. Int. Ed.* **2017**, *56*, 15150. (Reference updated on 23.11.2017)

Abstract
Using computational chemistry, we show that the adsorption of ether molecules on Si(001) under ultra-high vacuum conditions can be understood with textbook organic chemistry. The two-step reaction mechanism of (1) dative bond formation between the ether oxygen and a Lewis acidic surface atom and (2) a nucleophilic attack of a nearby Lewis basic surface atom is analyzed in detail and found to mirror the acid-catalyzed cleavage of ethers in solution. The O-Si dative bond is furthermore found to be the strongest of its kind and reactivity from this state defies the Bell-Evans-Polanyi (BEP) principle by having the lowest energy barrier leading to the product of highest energy. Electron rearrangement during the C-O bond cleavage is visualized using a newly developed bonding analysis method, which verifies that the reaction occurs as a single-step nucleophilic attack. This confirms that the mechanism of nucleophilic substitutions on semiconductor surfaces, which have been occasionally reported in recent years, is identical to molecular chemistry S_N2 reactions. Our findings thus illustrate how the fields of surface science and molecular chemistry can mutually benefit and unexpected insight can be

gained.[149]

Contributions
The study was motivated by discussions with Prof. Ulrich Koert, Prof. Ulrich Höfer and Prof. Michael Dürr as well as previous experimental and theoretical results.[75] SL performed preliminary work on structural optimization of the dative bond intermediate and reaction product states as well as transition state search, while MR performed preliminary pEDA calculations of the dative bond intermediate. Building on this, the author performed all other calculations, including structural optimizations of all states in all possible conformations, determination of transition states for all possible conformational changes and reactions, and all remaining pEDA calculations. The data was subsequently interpreted by the author and the supervisor, and a first version of the manuscript was written by the author. Afterwards, the manuscript was refined by the author and the supervisor.

3.4 Adsorption of Cyclooctyne on Si(001)

3.4.1 Chemisorption of a Strained but Flexible Molecule: Cyclooctyne on Si(001)

J. Pecher, C. Schober and R. Tonner, *Chem. Eur. J.* **2017**, *23*, 5459.

Abstract
The adsorption characteristics of a promising system for hybrid organic–inorganic interfaces, cyclooctyne on Si(001), is analyzed using density functional theory. The chemisorbed 'on-top' configuration, where a cycloadduct is formed between the ring triple bond and a surface dimer, is shown to be most stable. Less stable are 'bridge' and 'sublayer' modes featuring two molecule-surface bonds and the 'pedestal' mode with four bonds. Investigations with our recently proposed periodic energy decomposition analysis (pEDA) reveal that the four-bond configuration is destabilized by large deformation energies needed within molecule and surface as well as rather weak molecule-surface bonds. Dispersion interactions show significant influence on energy and structure of the configurations leading to an increased bending of the rather flexible molecules. Thus, features found in previous scanning tunneling microscopy experiments are conclusively explained with bent 'on-top' configurations and the 'pedestal' mode can be ruled out. A comparison to acetylene shows that the ring structure and the resulting strain of cyclooctyne are responsible for an increased reactivity of the larger adsorbate due to a preforming of the ring triple bond for surface bonding. In contrast, ring strain leads only to negligible electronic effects on the adsorbate-surface bonds. The computations highlight the need for in-depth theoretical analysis to understand adsorption characteristics of large, flexible molecules.[143]

Contributions
The study was motivated by discussions with Prof. Ulrich Koert, Prof. Ulrich Höfer and Prof. Michael Dürr as well as previous experimental results.[74] CS performed the molecular calculations, convergence studies of the bulk, preliminary work on structural optimization of the *on-top* and *bridge* states, and calculated the STM topography. Building on this, the author performed all other calculations, including convergence studies of the slab, identification of the covalently bonded *sublayer* and *pedestal* structures, structural optimization of all structures, and pEDA calculations. Results were discussed and interpreted with the supervisor and a first version of the manuscript was written by the author. Subsequently, the manuscript was refined in collaboration with the supervisor.

3.4.2 Modeling the Complex Adsorption Dynamics of Large Organic Molecules: Cyclooctyne on Si(001)

L. Pecher, S. Schmidt and R. Tonner, *J. Phys. Chem. C* **2017**.
DOI: 10.1021/acs.jpcc.7b09538 (Reference updated on 23.11.2017)

Abstract
We present a computational protocol for the description of the adsorption dynamics of large molecules (i.e. more than two non-hydrogen atoms) on surfaces at the example of the system cyclooctyne/Si(001). The system size prohibits the use of established accurate methods and approximations have to be made and validated. Our approach combines potential energy surface scans, reaction path determination methods, statistical thermodynamics and *ab initio* molecular dynamics simulations based on density functional theory (DFT). This leads to a conclusive picture of adsorption dynamics in this system in the limits of DFT accuracy. Surprising insight is gained regarding the adsorption pathways which are shown to be either direct or pseudo-direct in contrast to common precursor-mediated surface reactions. This shows how a thoughtful selection of DFT methods can comprehensively describe the adsorption dynamics of a system that might seem too complex for *ab initio* approaches at first glance.[150]

Contributions
The study was motivated by discussions with Prof. Ulrich Koert, Prof. Ulrich Höfer and Prof. Michael Dürr as well as previous experimental results.[72,74] All calculations were performed by the author except the PES scans, which were performed by SS under supervision by the author. Results were initially interpreted by the author and furthermore discussed with the supervisor. The first version of the manuscript was written by the author and subsequently refined in collaboration with the supervisor.

3.5 Adsorption of a Bifunctional Cyclooctyne on Si(001)

3.5.1 Introduction

In this section, results on the adsorption of a bifunctional cyclooctyne on Si(001) will be presented and discussed. The molecule, 5-Ethoxymethyl-5-methylcyclooctyne (EMC, Figure 3.1), combines the previously investigated functionalities of cyclooctyne and ethers. This opens up the opportunity to investigate two major topics: First, determination of how the substitution affects bonding and reactivity of the two functionalities (strained triple bond, ether group) in comparison to the parent systems (Sections 3.3.3 and 3.4.1). And second, chemoselectivity in the adsorption process: Since the chemisorption of the two functional groups is competitive and furthermore, adsorption modes where both groups are bonded to the surface are possible, it is important to be able to predict which structures will form at a given set of conditions. Since the datively bonded (DB) state of diethylether is much more weakly bonded to the surface than chemisorbed cyclooctyne (see Sections 3.3.3 and 3.4.1 as well as experimental studies[72,77]) and furthermore, the irreversible C-O bond cleavage from the DB state can be controlled via temperature, the premise of this system is that adsorption via the triple bond should be highly preferred. Experimental studies have confirmed this by showing that the molecule reacts exclusively via the triple bond at 50 and 300 K, and that C-O bond cleavage only occurs at higher temperatures.[72]

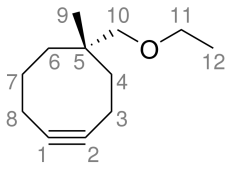

Figure 3.1. Lewis structure of (*S*)-5-Ethoxymethyl-5-methylcyclooctyne (EMC) with carbon numbering used subsequently.

In the following, results on the adsorption modes bonding via the triple bond (Figure 3.2 (a)) and the ether oxygen (b) will be presented and discussed separately. Since EMC is lacking the rotational symmetry of its parent molecules cyclooctyne and diethylether, there are two distinct versions each of the *Bridge* mode (*B1*, *B2*), the DB state (*DB1*, *DB2*) and the most probable C-O bond cleavage product (*C1*, *C2*). Afterwards, results on doubly bonded states and their reactivity will be presented. To conclude the study, results on the adsorption dynamics of the molecule will be presented and implications for chemoselective bonding to the surface discussed.

Additional Notes

(a) EMC is a chiral molecule (Figure 3.1), but since the Si(001) surface is achiral, the choice of enantiomer does not affect the results. In this study, the (*S*) enantiomer was used.

(b) The description of hindered internal rotations of the methyl and ethoxymethyl groups as harmonic vibrations might not be accurate. For example, in the calculation of Gibbs energies, entropies might be underestimated. However, if the corresponding energy profiles are not drastically affected by the adsorption, most of the errors will cancel out in the calculation of Gibbs bonding energies. Since these are the only calculated properties in this study that are affected by the treatment of these motions, the assumption of error cancellation is made and the harmonic approximation is applied exclusively.

(c) Preliminary work on structural optimization and bonding analysis of adsorption modes *OT*, *B2*, *DB2* and *C2* was done by Jan-Niclas Luy in an internship under supervision by the author.

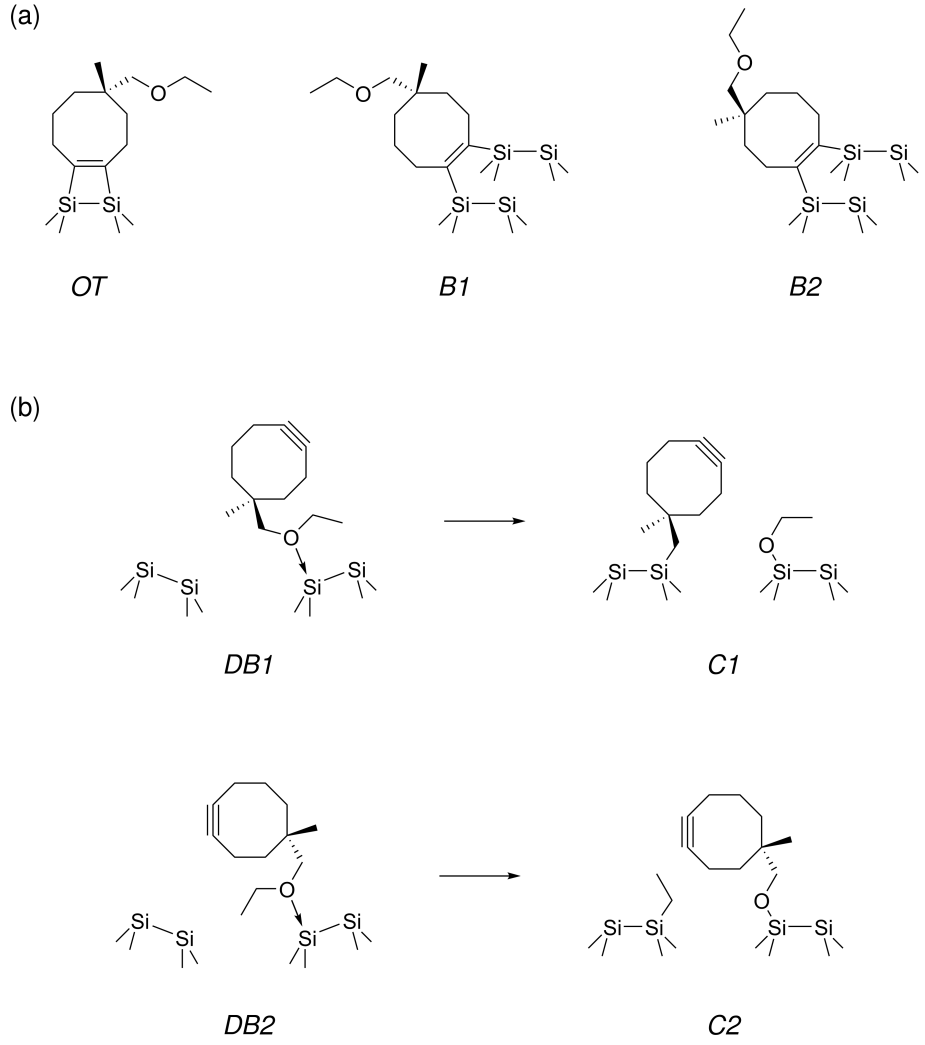

Figure 3.2. Selected adsorption modes of EMC on Si(001): (a) Cycloadducts *On-top* (*OT*), *Bridge 1* (*B1*) and *Bridge 2* (*B2*). (b) Dative bond formation in two possible orientations (*DB1*, *DB2*) and the corresponding C-O bond cleavage products (*C1*, *C2*). For clarity, the electronic structure of the surface is not depicted.

3.5.2 The Isolated Molecule

As with cyclooctyne, conformational analysis was performed to ensure that the lowest energy conformer is used in the adsorption studies. The ring scaffold can adopt the chair and twist boat conformations similar to cyclohexane (see Section 3.4.1), but due to the symmetry reduction caused by the introduction of substituents, there are not two, but six stable conformers in total (Figure 3.3). The four twist boat conformations can be seen as intermediates in two distinct ring inversion paths connecting the two chair conformations. Path 1 proceeds via twist boat conformations 1 and 2, where the ethoxymethyl group is in spatial proximity to the ring, while path 2 proceeds via twist boat conformations 3 and 4, where the methyl group is close to the ring. The energies of all conformers and the connecting transition states are given in Figure 3.4.

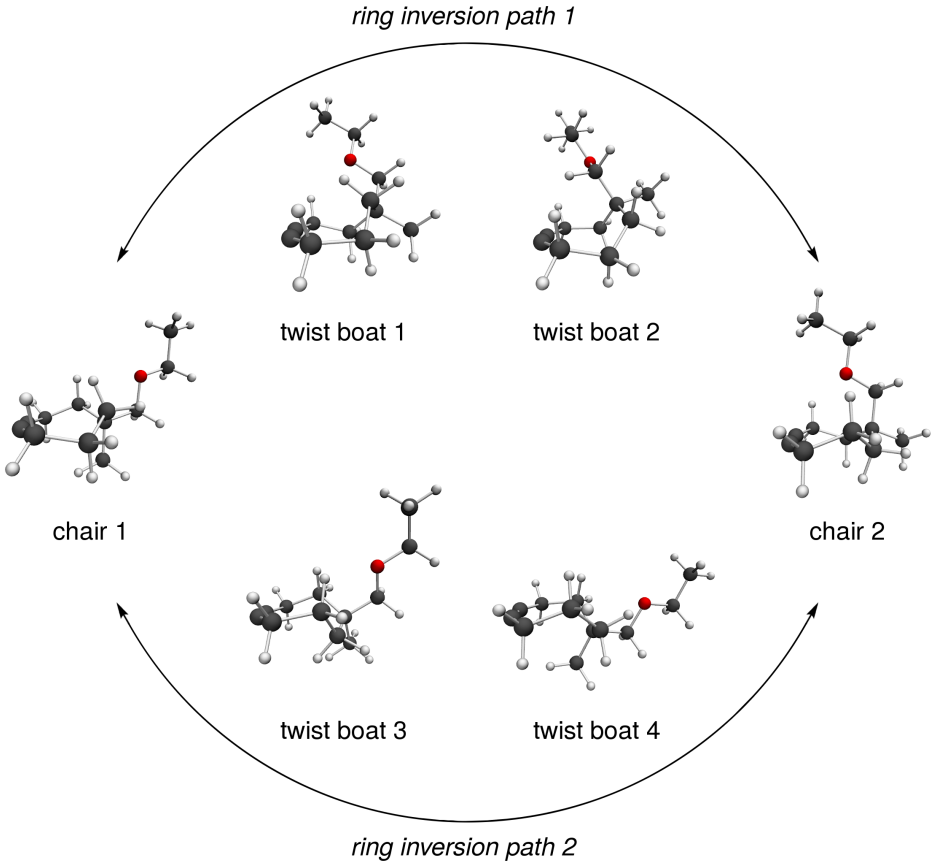

Figure 3.3. Optimized (PBE-D3/def2-TZVPP) structures of the six conformers of EMC.

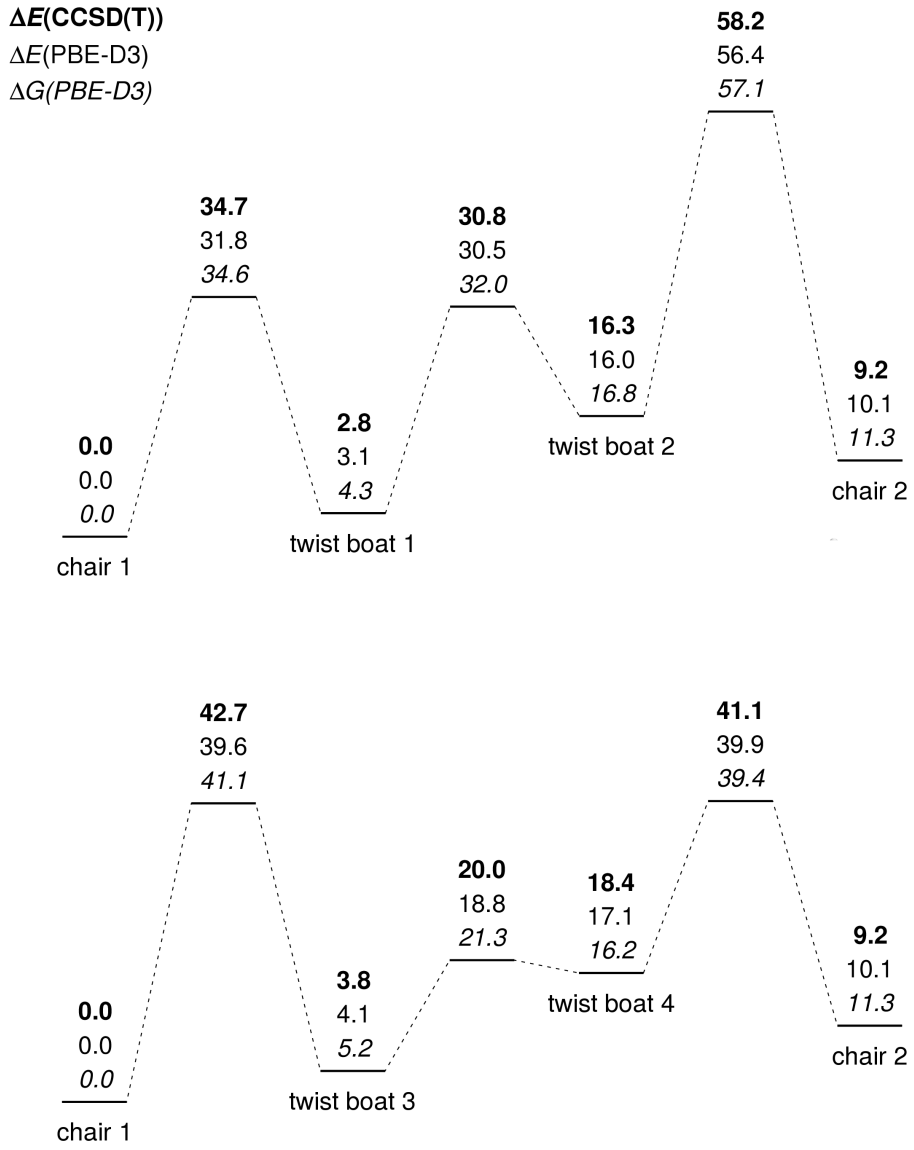

Figure 3.4. Relative energies of the six conformers of EMC and the connecting transition states. Energies (in kJ mol^{-1}) calculated at DLPNO-CCSD(T)/def2-TZVPP[151–153] and PBE-D3/def2-TZVPP on the PBE-D3 structures. Gibbs energies calculated at T = 300 K, p = 1 bar.

The results show that the location of the substituents has a pronounced effect on the energy: In cyclooctyne, the chair conformation is 11 to 13 kJ mol^{-1} lower in energy than the twist boat conformation.[143] Here, the chair 1 conformation is also the most stable one, but chair 2 is not the second lowest, but actually the conformer third highest in energy at values relative to chair 1 of 10.1 (DFT := PBE-D3/def2-TZVPP) and 9.2 kJ mol^{-1} (CC := DLPNO-CCSD(T)/def2-TZVPP) in electronic energies and 11.3 kJ mol^{-1} (DFT) in Gibbs energies at T = 300 K and p = 1 bar. This energy difference is caused by the axial position of the ethoxymethyl group, which leads to a higher 1,3-diaxial strain than in chair 1, where the smaller methyl group is in axial position. This strain is reduced in the twist boat conformations, where only one 1,3-diaxial interaction is present. For twist boat 1 and 3, this lowers the energy difference to chair 1 (ΔE(DFT): 3.1/4.1, ΔE(CC): 2.8/3.8, ΔG(DFT): 4.3/5.2 kJ mol^{-1}) with respect to the parent molecule, while for twist boat 2 and 4, the energy difference increases (ΔE(DFT): 16.0/17.1, ΔE(CC): 16.3/ 18.4, ΔG(DFT): 16.8/16.2 kJ mol^{-1}). This increase, however, is not an effect of diaxial interactions, but the spatial proximity of the subtituent groups to the triple bond (Figure 3.3), which leads to steric repulsion that is not apparent in the other four conformers. The repulsion also affects the height of the energy barriers, which are increased up to 56.4 (ΔE(DFT)), 58.2 (ΔE(CC)) and 57.1 kJ mol^{-1} (ΔG(DFT)) for the conversion between twist boat 2 and chair 2, while in cyclooctyne, the energy barrier for conversion from chair to twist boat is 20 to 23 kJ mol^{-1}.[143]

The substituent effects have relevant implications for the occurrence of the conformers assuming thermodynamic equilibrium: In a Boltzmann distribution at 300 K using ΔG(DFT) values, 76% of the molecules are in the chair 1 conformation, 14% in twist boat 1, 9% in twist boat 3, and 1% in chair 2. This is in stark contrast to cyclooctyne, where at this temperature, 99% of the molecules are in chair conformation and the twist boat conformation can be neglected.[143] However, since most experimental adsorption studies are performed at room temperature or lower and additionally, conversion into the twist boat conformations might be kinetically hindered due to the high barriers, it can be assumed that the chair 1 conformation is the most relevant one for adsorption. Furthermore, the computational effort, which is already large due to the size of the molecule, increases when considering multiple conformers. Hence, only chair 1 was used in the adsorption studies.

Selected structural parameters of the minimum conformation are given in Table 3.1. Comparison is done to equivalent parameters in cyclooctyne, where the applied methodology showed good agreement with theoretical and experimental literature data.[143] Bond lengths r in EMC are very similar to cyclooctyne and most values deviate by less than 0.005 Å. The only exceptions are r_{45} and r_{56}, which are longer in EMC by 0.013 and 0.019 Å, respectively. These elongations reduce the previously mentioned 1,3-diaxial strain that is caused by the large substituents at C^5. Angles α are very similar to cyclooctyne as well

with differences below 2° except again the parameters involving C^5, α_{345}, α_{456} and α_{567}, which have slightly larger deviations of +2.2, –3.4 and +3.2°, respectively. Due to the asymmetric substitution with respect to the C_2 axis in cyclooctyne, pairs of bond lengths and angles that are identical in that molecule, like r_{34}/r_{78} or $\alpha_{234}/\alpha_{781}$, do not have the exact same value in EMC. However, the differences are minor (up to 0.002 Å or 2°) except for the aforementioned parameters involving C^5. Therefore, it can be concluded that the substitution does not change the minimum structure of the molecule in a significant way, especially at the reactive triple bond.

Table 3.1. Structural parameters of the carbon frame of optimized (PBE-D3/def2-TZVPP) EMC and cyclooctyne (see Section 3.4.1) in their respective minimum conformation. Numbering according to Figure 3.1.[a]

Molecule	Structural parameter								
EMC	r_{12}	r_{23}	r_{34}	r_{45}	r_{56}	α_{123}	α_{234}	α_{345}	α_{456}
	1.214	1.452	1.549	1.560	1.579	158.1	107.7	117.8	115.0
		r_{18}	r_{78}	r_{67}		α_{812}	α_{781}	α_{678}	α_{567}
		1.454	1.551	1.547		156.0	106.3	115.4	121.6
Cyclooctyne	1.215	1.455	1.553	1.547	1.560	157.5	107.0	115.6	118.4

[a] Bond lengths r in Å, angles α in degrees.

3.5.3 Triple Bond Cycloadducts

The optimized structures of the cycloadducts *OT*, *B1* and *B2* (see Figure 3.2) in their minimum conformation are given in Figure 3.5. In all cases, the molecule favors an orientation where the ethoxymethyl group is facing the surface, as opposed to the methyl group. This enhances the amount of dispersion

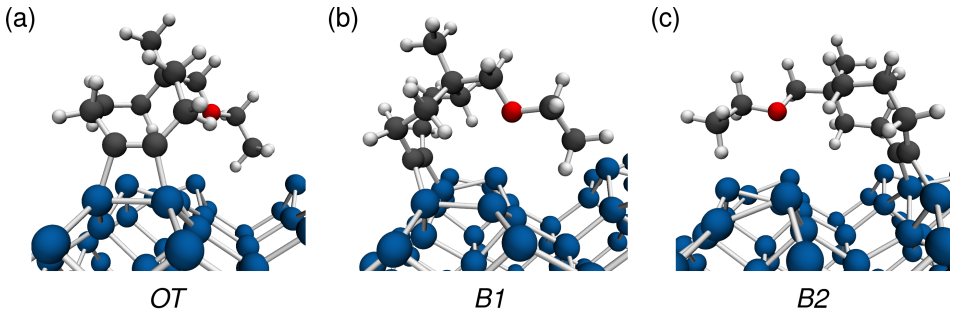

Figure 3.5. Optimized (PBE-D3/PAW) cycloadduct adsorption modes of EMC on Si(001).

Table 3.2. Structural parameters of EMC and cyclooctyne (see Section 3.4.1) bonded to Si(001) in the *OT* and *B* modes.[a]

	$d(C^1\text{-}C^2)$	$d(C^1\text{-Si})$	$d(C^2\text{-Si}')$
EMC			
OT	1.368	1.918	1.895
B1	1.365	1.935	1.913
B2	1.366	1.932	1.932
Cyclooctyne			
OT	1.368	1.916	1.900
B	1.365	1.943	1.921

[a] Interatomic distances *d* given in Å.

interaction between molecule and surface compared to orientations where the smaller methyl group faces the surface. Selected structural parameters of these structures are given in Table 3.2. There are no qualitative differences to the *OT* and *B* modes of cyclooctyne. The bond length of the former C-C triple bond, $d(C^1\text{-}C^2)$, is even quantitatively unchanged, while the d(C-Si) values in *OT* and *B1* are deviating by less than 0.01 Å in comparison to cyclooctyne. The only notable difference is in the *B2* mode, where the asymmetry of the C-Si bonds found for *B1* and *B*(cyclooctyne) is missing and the d(C-Si) value, 1.932 Å, corresponds exactly to the mean of the bond lengths in the *B* mode of cyclooctyne.

Bonding energies of these structures are given in Table 3.3. In general, they show that EMC is more strongly bonded to Si(001) than cyclooctyne by 23 to 44 kJ mol^{-1} (E_{bond}) and 16 to 38 kJ mol^{-1} (G_{bond}). The main reason for this is the increased dispersion contribution (E_{bond}(D3)), which is caused by the increased size of the molecule. This correlation between molecular size and dispersion contribution to the adsorption energy was previously found in a study of smaller organic adsorbates on Si(001) as well.[154] The largest dispersion contribution, –90 kJ mol^{-1}, is found in the *B1* mode. A view at the corresponding structures (Figure 3.5) reveals the reason for this: In *OT* and *B2*, a part of the molecule is located vertically above the lower surface atoms of the trench between the dimer rows, which leads to increased distances between molecule and surface atoms and low dispersion interaction. In *B1*, however, the molecule is "wrapped" around a dimer row, which leads to smaller distances and therefore high dispersion interaction.

Electronic bonding energies (E_{bond}(PBE)) are mostly unchanged with respect to cyclooctyne, although the *OT* value of EMC is more stabilized by 13 kJ mol^{-1}. This is mainly caused by a decrease in molecular deformation

Table 3.3. Gibbs bonding energies G_{bond}, electronic bonding energies E_{bond} and the PBE and D3 contributions to E_{bond} of EMC and cyclooctyne (see Section 3.4.1) bonded to Si(001) in the *OT* and *B* modes.[a]

	EMC			**Cyclooctyne**	
	OT	*B1*	*B2*	*OT*	*B*
G_{bond}(PBE-D3)	–276	–237	–214	–238	–198
E_{bond}(PBE-D3)	–352	–308	–286	–308	–263
E_{bond}(PBE)	–274	–218	–208	–261	–213
E_{bond}(D3)	–78	–90	–78	–47	–50

[a] All values in kJ mol^{-1}, calculated using PBE-D3/PAW. G_{bond} values calculated at T = 300 K, p = 1 bar.

energy, as pEDA results will show later. The E_{bond} difference between *OT* and *B* in cyclooctyne/Si(001), 45 kJ mol^{-1}, is qualitatively conserved in the EMC/Si(001) system (ΔE_{bond}(*OT-B1/B2*) = 44/66 kJ mol^{-1}). The larger value for *B2* mainly stems from the previously mentioned lower dispersion interaction in *B2* compared to *B1* and the electronic stabilization in the *OT* mode compared to the parent molecule. The G_{bond} values of EMC are higher by 70 to 80 kJ mol^{-1} than the respective E_{bond} values, which is in line with the numbers for cyclooctyne (65–70 kJ mol^{-1}). The slight increase for EMC can be attributed to entropy loss upon adsorption caused by constraints on the flexibility of the ethoxymethyl group, which will not be able to move around as freely as in the isolated molecule.

Further insight into the similarities and differences between the systems EMC/Si(001) and cyclooctyne/Si(001) can be gained by applying the pEDA scheme to the *OT* mode. The results (Table 3.4) show that, as previously discussed, the increased dispersion interaction for EMC is the main reason for the difference in bonding energies. The electronic interaction energy ΔE_{int}(elec) as well as the pEDA terms ΔE_{Pauli}, ΔE_{elstat} and ΔE_{orb} are very similar, albeit slightly increased in absolute value by 1–2% for EMC. This confirms that the character of the molecule-surface bonds is not affected by the substituents. The surface preparation energy ΔE_{prep}(Surf.) is almost identical in both systems, whereas the molecular preparation energy ΔE_{prep}(Mol.) is lower by 10 kJ mol^{-1} for EMC. This is caused by a difference in tilting (Figure 3.6), which was described for cyclooctyne in Section 3.4.1: Due to the interaction of the ethoxymethyl side chain with the surface, the ring of EMC (a) does not need to tilt as much to reach the equilibrium geometry as in cyclooctyne (b). This can be quantified by the vertical difference Δz between the topmost carbon atom of the ring and the equilibrium position of a Si_{up} atom, which yields values of 4.250 (EMC) and 4.024 Å (cyclooctyne). Hence, the EMC molecule is

closer to its gas phase geometry, leading to a reduced preparation energy.

Table 3.4. pEDA values of EMC and cyclooctyne (see Section 3.4.1) bonded to Si(001) in the OT mode.[a]

	EMC *OT*	Cyclooctyne *OT*
ΔE_{int}	–695	–658
ΔE_{int}(disp)[b]	–73 (10%)	–43 (7%)
ΔE_{int}(elec)[b]	–622 (90%)	–615 (93%)
ΔE_{Pauli}	1500	1468
ΔE_{elstat}[c]	–957 (45%)	–936 (45%)
ΔE_{orb}[c]	–1165 (55%)	–1148 (55%)
ΔE_{prep}(Mol.)	303	313
ΔE_{prep}(Surf.)	27	26
E_{bond}[d]	–365 (–352)	–319 (–308)

[a] All values in kJ mol^{-1}, calculated at PBE-D3/TZ2P. Fragments: Molecule and surface. Fragmentation: Triplet. [b] Percentage values give dispersion and electronic contributions to the total interaction energy ΔE_{int}. [c] Percentage values give the contribution to the sum of the attractive pEDA interaction terms ΔE_{elstat} and ΔE_{orb}. [d] PAW values (in parentheses) given for comparison.

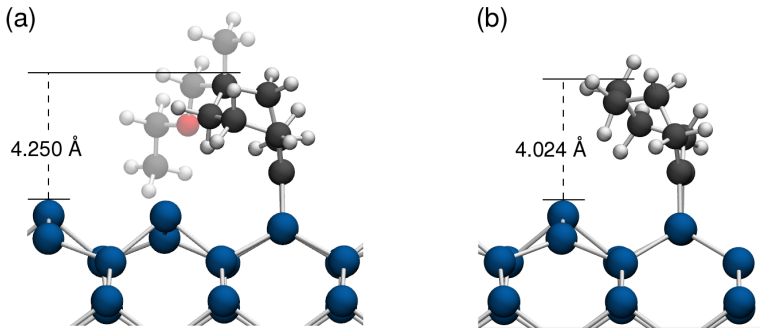

Figure 3.6. Tilting of adsorbed EMC (a) and cyclooctyne (b) in the *OT* mode. The given vertical distance is the difference Δz between the topmost carbon atom of the molecular ring and the equilibrium position of a Si_{up} atom.

3.5.4 Oxygen-Bonded States and Their Reactivity

The optimized structures of the oxygen-bonded states *DB1*, *DB2*, *C1* and *C2* (see Figure 3.2) in their minimum conformation are given in Figure 3.7. While *DB1* and *DB2* can interconvert via rotation around the O-Si bond axis, *C1* and *C2* are qualitatively different, since the nucleophilic attack leading to these structures occurs at a different carbon atom (*C1*: C^{10}, *C2*: C^{11}). In *C1*, the ethyl group remains at the oxygen and the ring residue attaches directly to the surface, while in *C2*, this is reversed. In both *DB* modes, the ethyl group has to rotate out of its gas phase equilibrium position to allow for a better exposure of the oxygen compared to the minimum conformation in the gas phase (Figure 3.3). The effects of this deformation will be discussed later.

Selected structural parameters of the four modes are given in Table 3.5. The length of the O-Si bond in *DB1* and *DB2* (1.921 and 1.939 Å, respectively) is significantly larger than the corresponding value in the diethylether/Si(001) system (1.908 Å). This is an effect of the steric demand of the ring residue, which leads to repulsive forces between molecule and surface that are not present for diethylether. The influence of substitution becomes even more apparent in the *C1* and *C2* modes: In *C1*, the ethyl group is still attached to the oxygen and the O-Si bond length (1.673 Å) is virtually identical to the value in the *C* mode of diethylether (1.674 Å), while the C-Si bond length (1.909 Å, ring residue attached) is elongated by 0.010 Å. On the contrary, in *C2*, the C-Si bond length (1.900 Å) is virtually identical to the value for diethylether (1.899 Å), while the O-Si bond length (1.665 Å) is shorter by 0.009 Å. This shows that once the bond cleavage is finished, the residue containing the ethyl group is no more influenced by the rest of the molecule. The longer C-Si bond length in *C1* can again be explained by steric repulsion between ring and surface. This, however, is not the case in *C2*, where the oxygen atom acts as a spacer between ring and surface and repulsion effects are far less pronounced. The shortening of the O-Si bond in comparison to diethylether is most likely a result of the inductive effect.

Bonding energies of the four structures are given in Table 3.6. The values show that *DB1* is more stable than *DB2* by 23 kJ mol^{-1} in electronic energies and 27 kJ mol^{-1} in Gibbs energies. The reason for this difference lies in the location of the ring residue: In *DB2*, it is located above the dimer row surface atoms and due to steric repulsion, the whole molecule has to increase its distance to the surface. This leads to an increased d(O-Si) value, a decrease of the O-Si interaction compared to *DB1* and a lower absolute value of E_{bond}(PBE). The decrease in E_{bond}(PBE) for both structures compared to diethylether, however, is not caused by the increased O-Si distance, but a higher molecular preparation energy, as pEDA results will show later. In *DB1*, the distance to the surface does not have to increase as much as in *DB2*, since the ring residue is located above the trench between the dimer rows, where the surface atoms have a lower vertical position, and therefore the absolute value of E_{bond}(PBE)

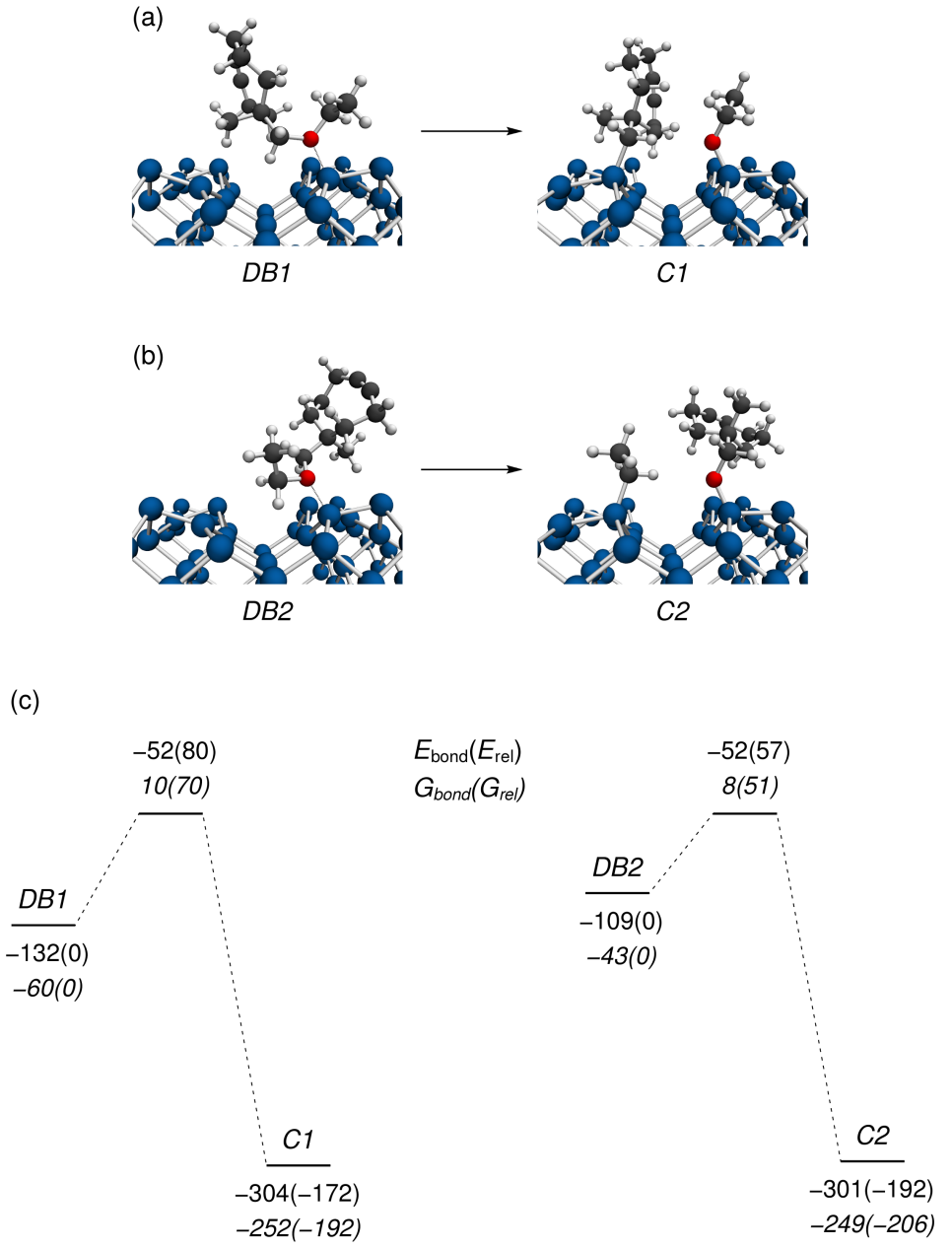

Figure 3.7. (a,b) Optimized (PBE-D3/PAW) datively bonded adsorption modes of EMC on Si(001) and the corresponding C-O bond cleavage products. (c) Energy diagrams of the two *DB*→*C* cleavage reactions. All energies in kJ mol^{-1}. Gibbs energies calculated at T = 300 K, p = 1 bar.

Table 3.5. Structural parameters of EMC and diethylether (see Section 3.3.3) bonded to Si(001) in the *DB* and *C* modes and at the TS(*DB*→*C*) geometry. C* denotes the carbon at which the nucleophilic attack takes place.[a]

	d(O-Si)	*d*(C*-O)	*d*(C*-Si′)	*α*(O-C*-Si′)
EMC				
DB1	1.921	1.480		
TS(*DB1*→*C1*)	1.780	1.998	2.981	141.0
C1	1.673		1.909	
DB2	1.939	1.486		
TS(*DB2*→*C2*)	1.788	1.927	2.809	155.1
C2	1.665		1.900	
Diethylether				
DB	1.908	1.475		
TS(*DB*→*C*)	1.774	1.931	2.800	153.2
C	1.674		1.899	

[a] Interatomic distances *d* in Å, angles *α* in degrees.

Table 3.6. Gibbs bonding energies G_{bond}, electronic bonding energies E_{bond} and the PBE and D3 contributions to E_{bond} of EMC and diethylether (see Section 3.3.3) bonded to Si(001) in the *DB* and *C* modes.[a]

	EMC				**Diethylether**	
	DB1	*DB2*	*C1*	*C2*	*DB*	*C*
G_{bond}(PBE-D3)	–60	–43	–252	–249	–59	–222
E_{bond}(PBE-D3)	–132	–109	–304	–301	–116	–274
E_{bond}(PBE)	–40	–27	–220	–233	–61	–235
E_{bond}(D3)	–92	–82	–84	–68	–56	–39

[a] All values in kJ mol^{-1}, calculated using PBE-D3/PAW. G_{bond} values calculated at T = 300 K, p = 1 bar.

does not decrease as much compared to diethylether as for *DB2*. Additionally, the large residue is enclosed by two dimer rows, leading to high dispersive interaction with both rows and a larger stabilization.

The differences of the *C1* and *C2* bonding energies in comparison to diethylether are also mostly dominated by the increased dispersion contribution. Again, this effect is more pronounced for *C1*, where the large ring residue is closer to the surface atoms than in *C2*. However, while E_{bond}(PBE) in *C2* is almost identical to diethylether, it is 13 kJ mol^{-1} weaker in *C1*. This is in line with the differences in O-Si and C*-Si bond lengths (Table 3.5, C* denotes the carbon (C^{10}/C^{11}) at which the nucleophilic attack takes place): While in *C2*, *d*(C*-Si) is essentially unchanged and *d*(O-Si) shortened in comparison to diethylether, in *C1*, *d*(O-Si) is essentially unchanged and *d*(C*-Si) longer. Hence, the orbital overlap is lower than in *C2*, which should lead to less stabilization in the process of chemical bond formation.

The differences between G_{bond} and E_{bond} (Table 3.6) are of similar size for *DB1* and *DB2* (72 and 66 kJ mol^{-1}, respectively) compared to the cycloadducts (70–80 kJ mol^{-1}, Table 3.3), while for *C1* and *C2*, the differences are significantly smaller (both: 52 kJ mol^{-1}). This can be attributed to a gain of intramolecular flexibility in the *C* states: Whereas in the free molecule and the *DB* states, steric repulsion between the ethoxy group and the ring prevents them to get close to each other (which also causes the high energy of the twist boat 2 conformation: See Figures 3.3 and 3.4), the ethyl/ethoxy group can move around more freely when it is separated from the rest of the molecule in *C1* and *C2*. As a consequence, the potential energy surface becomes more shallow, frequencies of vibrations corresponding to hindered rotations of this group become lower and the entropy increases, leading to a relative stabilization.

Bonding in the *DB* states can be analyzed and compared to diethylether using pEDA (Table 3.7). Apart from the increased dispersion contribution for EMC, the qualitative picture, i.e. the ratio between electrostatic and orbital interaction and the percentage of dative bond contributions to ΔE_{orb}, does not change significantly. However, the results also show that the comparison of bond lengths (Table 3.5) and bonding energies (Table 3.6) can lead to wrong conclusions: Since the O-Si distance in the two EMC/Si(001) modes is larger than in the corresponding diethylether structure, while at the same time, the E_{bond} value is less negative, one might assume that the O-Si dative bond is weaker for EMC. The pEDA results, however, show that the opposite is the case: Both stabilizing pEDA terms, ΔE_{elstat} and ΔE_{orb}, are more negative for the two EMC structures, which leads to a more negative ΔE_{int}(elec). NOCV analysis reveals that the orbital contribution due to dative bond formation (see also Figure 3.8(a) and (c)) is also stronger for EMC. However, the ΔE_{prep}(Mol.) value of EMC is twice as high as the value of diethylether in both structures. This reflects the results from the conformation study of the isolated molecule (Figures 3.3 and 3.4), which showed that the location of the ethoxy group with

Table 3.7. pEDA values of EMC and diethylether (see Section 3.3.3) bonded to Si(001) in the *DB* mode.[a]

	EMC *DB1*	EMC *DB2*	Diethylether *DB*
ΔE_{int}	–194	–179	–151
ΔE_{int}(disp)[b]	–85 (44%)	–78 (44%)	–54 (37%)
ΔE_{int}(elec)[b]	–109 (56%)	–101 (56%)	–97 (63%)
ΔE_{Pauli}	713	689	645
ΔE_{elstat}[c]	–443 (54%)	–422 (53%)	–409 (55%)
ΔE_{orb}[c]	–379 (46%)	–367 (47%)	–334 (45%)
ΔE_{orb}(dative)[d]	–299 (79%)	–297 (81%)	–284 (85%)
ΔE_{prep}(Mol.)	35	39	19
ΔE_{prep}(Surf.)	19	23	14
E_{bond}[e]	–140 (–132)	–117 (–109)	–118 (–116)
d(O-Si) [Å]	1.921	1.939	1.908

[a] All values in kJ mol^{-1}, calculated at PBE-D3/TZ2P. Fragments: Molecule and surface. Fragmentation: Closed-shell singlet. [b] Percentage values give dispersion and electronic contributions to the total interaction energy ΔE_{int}. [c] Percentage values give the contribution to the sum of the attractive pEDA interaction terms ΔE_{elstat} and ΔE_{orb}. [d] The percentage value gives the relative contribution to the total orbital energy ΔE_{orb}. [e] PAW values (in parentheses) given for comparison.

respect to the ring has a profound effect on the energy. On the contrary, the energy difference between conformers of diethylether is less than 10 kJ mol^{-1}, as experiments and theoretical calculations have shown.[155] Unless intramolecular bonds are broken or overly stretched, the preparation energy can not get significantly higher than this. It is therefore not surprising that the preparation energies of EMC are larger than the one of diethylether. Apart from what was already mentioned, pEDA results of EMC are very similar to diethylether, e.g. the ratio between electrostatic and orbital interaction, which confirms that the character of the chemical bond is the same. The increased strength of the O-Si dative bond interaction in EMC, even though the corresponding bond length is longer (Table 3.5) is most likely a result of the inductive effect.

The energy barriers of the bond cleavage reaction (Figure 3.7(c)) show an interesting behavior in EMC: While the value for the reaction *DB2*→*C2* (E_a: 57, G_a: 51 kJ mol^{-1}) is very similar to diethylether (E_a: 61 kJ mol^{-1}),[149] the corresponding *DB1*→*C1* value is much higher at E_a = 80 and G_a = 70 kJ mol^{-1}. The

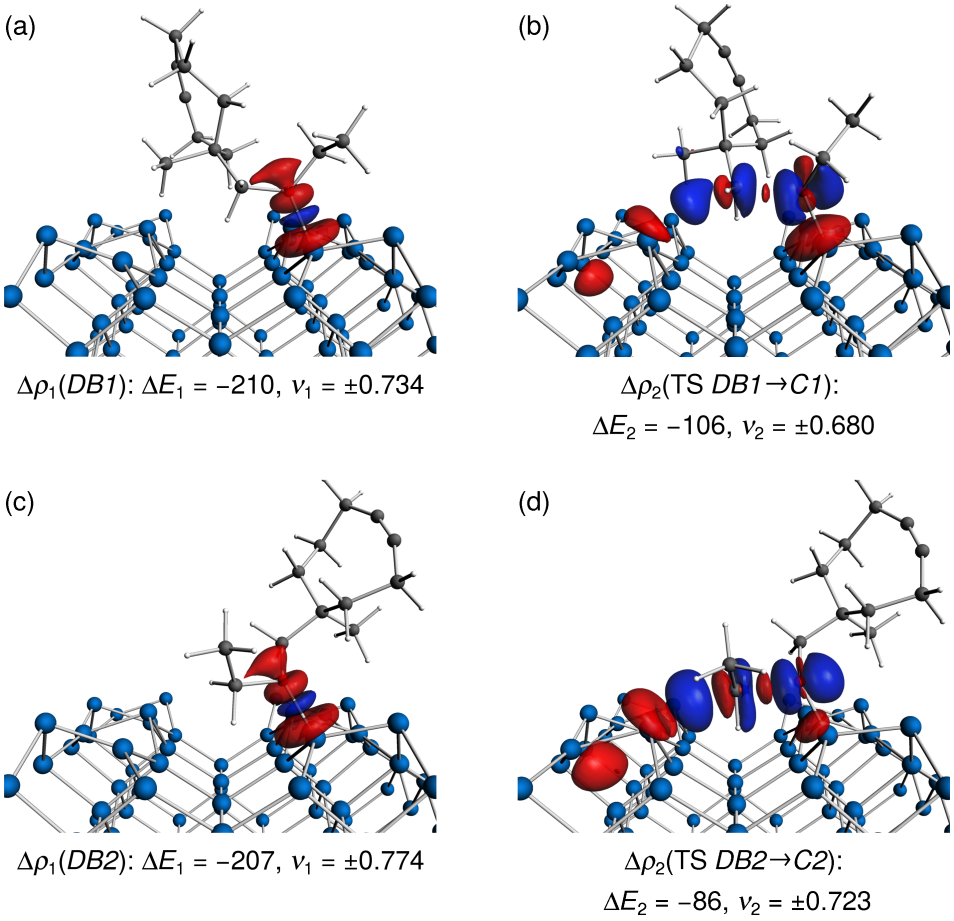

Figure 3.8. NOCV deformation densities showing (a,c) dative bond formation between the ether oxygen and a Si_{down} atom in the *DB* modes and (b,d) the nucleophilic attack in the TS(*DB*→*C*) geometries. Red: Depletion of electron density. Blue: Accumulation of electron density. Energies ΔE_i in kJ mol^{-1}, eigenvalues v_i in q_e.

two transition states even have the same E_{bond} value of –52 kJ mol^{-1} and an almost identical G_{bond} value of +10 (*DB1*→*C1*) and +8 kJ mol^{-1} (*DB2*→*C2*). While one might assume that the effects that stabilize *DB1* more than *DB2* (higher dispersion contribution, stronger O-Si bond) might simply be lost at the transition state, pEDA bonding analysis at the transition state geometries (Table 3.8) reveals that this is not entirely true: The ΔE_{int}(disp) value for TS(*DB1*→*C1*) is indeed slightly less negative than for TS(*DB2*→*C2*), but the ΔE_{int}(elec) value is significantly more negative. This is caused neither by a stronger dative bond, since the ΔE_{orb}(dative) interaction is weaker than in TS(*DB2*→*C2*), nor other stabilizing terms, but a lower Pauli repulsion energy ΔE_{Pauli}. This is compensated by the larger ΔE_{prep}(Mol.) value of 185 kJ mol^{-1} compared to TS(*DB2*→*C2*) (166 kJ mol^{-1}), leading to an equivalent E_{bond} value.

Table 3.8. pEDA values of EMC and diethylether (see Section 3.3.3) bonded to Si(001) at the TS(DB→C) geometry.[a]

	EMC		**Diethylether**
	TS(*DB1*→*C1*)	TS(*DB2*→*C2*)	TS(*DB*→*C*)
ΔE_{int}	–291	–271	–248
ΔE_{int}(disp)[b]	–80 (27%)	–85 (31%)	–58 (23%)
ΔE_{int}(elec)[b]	–211 (73%)	–186 (69%)	–190 (77%)
ΔE_{Pauli}	1011	1070	1001
ΔE_{elstat}[c]	–619 (51%)	–638 (51%)	–611 (51%)
ΔE_{orb}[c]	–603 (49%)	–618 (49%)	–580 (49%)
ΔE_{orb}(dative)[d]	–413 (68%)	–451 (73%)	–402 (69%)
ΔE_{orb}(S_N)[d]	–106 (18%)	–86 (14%)	–117 (20%)
ΔE_{prep}(Mol.)	185	166	160
ΔE_{prep}(Surf.)	51	52	32
E_{bond}[e]	–55 (–52)	–53 (–52)	–56 (–55)

[a] All values in kJ mol^{-1}, calculated at PBE-D3/TZ2P. Fragments: Molecule and surface. Fragmentation: Closed-shell singlet. [b] Percentage values give dispersion and electronic contributions to the total interaction energy ΔE_{int}. [c] Percentage values give the contribution to the sum of the attractive pEDA interaction terms ΔE_{elstat} and ΔE_{orb}. [d] The percentage value gives the relative contribution to the total orbital energy ΔE_{orb}. [e] PAW values (in parentheses) given for comparison.

The reason for the increased preparation energy in TS(*DB1*→*C1*) becomes apparent when comparing interatomic distances at the transition states (Table 3.5): For the *DB2*→*C2* reaction, the C*-O bond has to stretch from 1.486 Å in the *DB2* minimum to 1.927 Å at the TS, a difference of 0.441 Å. This is close to the values of diethylether, where the bond stretches from 1.475 to 1.931 Å (Δd = 0.456 Å). On the contrary, in the *DB1*→*C1* reaction, it stretches from 1.480 to 1.998 Å, a much larger difference of 0.518 Å. However, this does not mean that the C* atom is closer to the Si' atom, since this distance is 2.981 Å at the TS, which is also larger than the corresponding *DB2*→*C2* and diethylether values (2.809 and 2.800 Å, respectively). Since the O-Si' distance is fixed, this means that the angle α(O-C*-Si') has to be more acute. The corresponding numbers (Table 3.5) confirm this: In TS(*DB1*→*C1*), the value is 141.0°, while for TS(*DB2*→*C2*) and diethylether, it is 155.1 and 153.2 Å, respectively. Since this angle and the length of the C*-O bond were found to be the determin-

ing factors for the height of the energy barrier for THF and diethylether on Si(001),[149] this explains why TS(*DB1→C1*) is so high in energy. The reason for the acute angle can again be attributed to steric repulsion, since the large ring residue is not able to fit into the trench between the dimer rows as easily as the ethyl group (see also Figure 3.8(b) and (d)).

The mechanism of the nucleophilic attack in the EMC/Si(001) system is very similar to diethylether: While the O-Si dative bond is still the dominant contribution to the orbital interaction at the TS geometry with approximately 70% of ΔE_{orb}, the second largest contribution stems from the nucleophilic attack (Figure 3.8(b) and (d)). The corresponding energy contribution $\Delta E_{\mathrm{orb}}(\mathrm{S_N})$ is lower in absolute value for EMC compared to diethylether because of the aforementioned more acute angle α(O-C*-Si'). Interestingly, it is more negative for TS(*DB1→C1*) than for TS(*DB2→C2*), even though the angles and distances imply otherwise. This might, however, be a technical issue: The deformation density $\Delta\rho_2$(TS *DB1→C1*) (Figure 3.8(b)) appears to contain a larger amount of polarization at the O-Si bond than the corresponding densities for TS(*DB2→C2*) (d) and diethylether (see Section 3.3.3), which is apparent from the red lobes (electron depletion) at this bond. At the same time, the blue lobes (electron accumulation) are smaller for TS(*DB1→C1*). Since the location of the TS structures on the PES is between the *DB* modes, where a closed-shell singlet fragmentation is the best description of the electronic structure, and the *C* modes, where a triplet fragmentation is better, the choice of the fragmentation might not be unambiguous. Even though in both cases, a closed-shell singlet fragmentation was found to be the best description of the system at the TS structures, in case of *DB1→C1* it might be closer to the part of the PES that is best described in a triplet fragmentation. This would explain the increased amount of apparent polarization and the more negative energy contribution in comparison to TS(*DB1→C1*).

3.5.5 Doubly Bonded States and Their Reactivity

In addition to each functional group bonding to the surface, there are also configurations where both groups are bonded. The minimum structures are *OT+DB*, a combination of *OT* and *DB2*, and *OT+C*, a combination of *OT* and *C2*, are given in Figure 3.9(a). While combinations with the *B1* and *B2* modes instead of *OT* are also possible, they were not investigated due to the low relevance of *Bridge* structures in the adsorption of cyclooctyne (see Section 3.4.2 and experimental studies[74]) and experimental results on this system.[72]

The *OT+DB* mode can be reached from both *OT* and *DB1*: The path from *OT* (Figure 3.10(a)) proceeds via a doubly bonded intermediate *DI* (b), which is essentially a higher energy conformation of *OT+DB*. The transition state energies relative to *OT* for the two steps *OT→DI* and *DI→OT+DB* are at 8 and 4 kJ mol^{-1}, respectively, in electronic energies and 11 and 20 kJ mol^{-1} in Gibbs energies. Interestingly, while the doubly bonded modes are lower in electronic

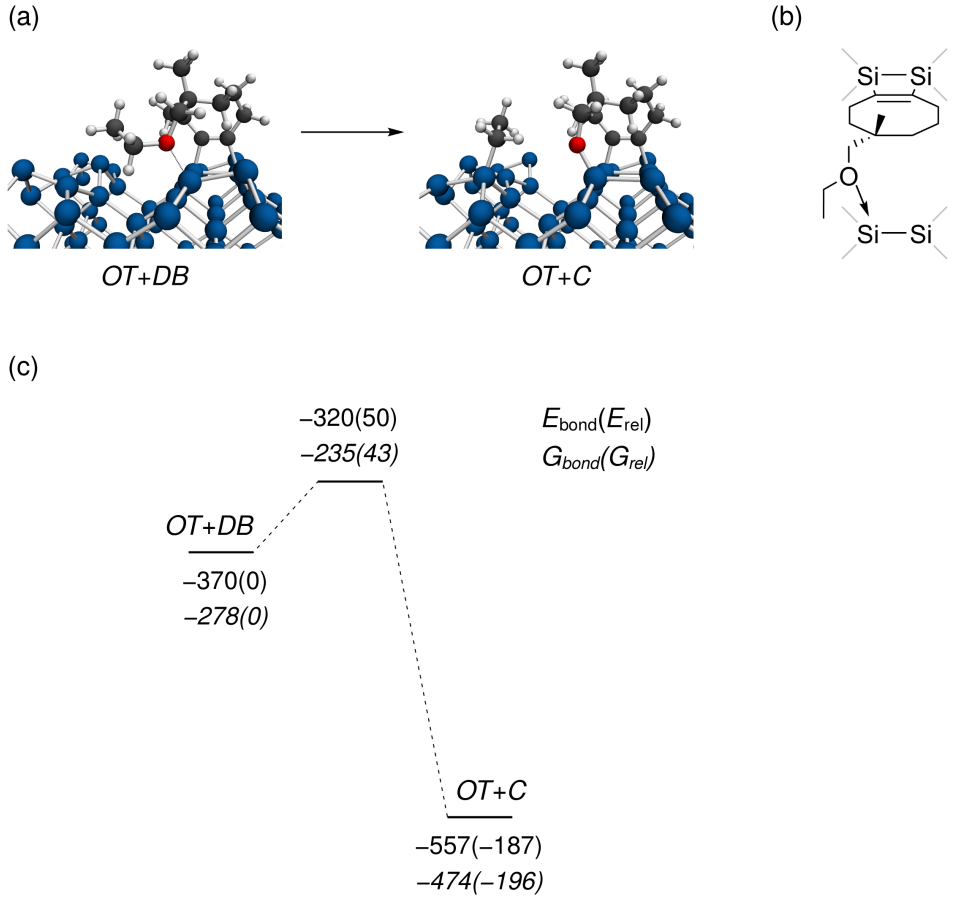

Figure 3.9. (a) Optimized (PBE-D3/PAW) doubly bonded (cycloaddition + dative bond) adsorption mode of EMC on Si(001) and corresponding C-O bond cleavage product. (b) Schematic depiction of *OT+DB*. (c) Energy diagram of the cleavage reaction. All energies in kJ mol^{-1}. Gibbs energies calculated at $T = 300$ K, $p = 1$ bar.

energy than *OT* by –9 (*DI*) and –18 kJ mol^{-1} (*OT+DB*), these values change significantly in Gibbs energies (*DI*: +6, *OT+DB*: –2 kJ mol^{-1}). This implies that in thermodynamic equilibrium, these two doubly bonded states are not necessarily more stable than *OT*. The reasons for this will be discussed later, when Gibbs energies are compared in more detail. The *OT+DB* mode can also be reached from the minimum *DB* configuration, *DB1* (Figure 3.10(c)): However, the energy barrier for this conversion is so high (E_a: 77, G_a: 79 kJ mol^{-1}) that at room temperature, it becomes more favorable for the molecule to desorb, react to *OT* and convert from there than undergo this pathway, since the Gibbs energy of the transition state is significantly higher (19 kJ mol^{-1}) than the zero-energy reference of the separated molecule and surface.

Selected structural parameters of the doubly bonded states are given in

Table 3.9. Structural parameters of EMC bonded to Si(001) in the *OT*+*DB* and *OT*+*C* modes and at the TS(*OT*+*DB*→*C*) geometry in comparison to the respective values in the singly bonded states.

	Structural parameter			
	d(C^1-C^2)	d(C^1-Si)	d(C^2-Si′)	
OT+*DB*	1.365	1.917	1.900	
TS(*OT*+*DB*→*C*)	1.366	1.915	1.901	
OT+*C*	1.367	1.909	1.904	
OT	1.368	1.918	1.895	
	d(O-Si″)	d(C^{11}-O)	d(C^{11}-Si‴)	α(O-C^{11}-Si‴)
OT+*DB*	1.961	1.483		
TS(*OT*+*DB*→*C*)	1.787	1.904	2.843	153.9
OT+*C*	1.659		1.901	
DB2	1.939	1.486		
TS(*DB2*→*C2*)	1.788	1.927	2.809	155.1
C2	1.665		1.900	

[a] Interatomic distances d in Å, angles α in degrees.

Table 3.10. Gibbs bonding energies G_{bond}, electronic bonding energies E_{bond} and the PBE and D3 contributions to E_{bond} of EMC bonded to Si(001) in the *OT*+*DB* and *OT*+*C* modes.[a]

	OT+*DB*	*OT*+*C*
G_{bond}(PBE-D3)	–278	–474
E_{bond}(PBE-D3)	–370	–557
E_{bond}(PBE)	–269	–474
E_{bond}(D3)	–101	–84

[a] All values in kJ mol^{-1}, calculated using PBE-D3/PAW. G_{bond} values calculated at T = 300 K, p = 1 bar.

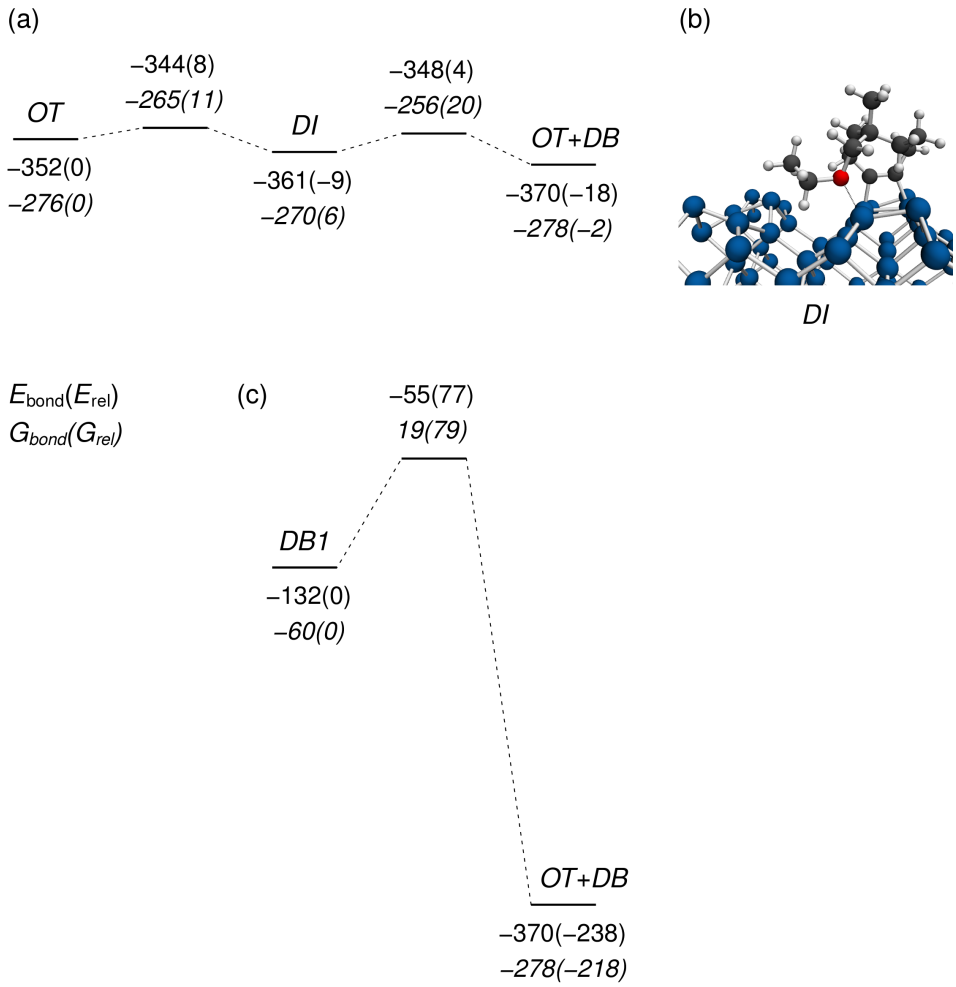

Figure 3.10. Pathways leading to *OT*+*DB*. (a) Energy diagram of the pathway *OT* → *OT*+*DB*. (b) Optimized (PBE-D3/PAW) structure of the doubly bonded intermediate *DI*. (c) Energy diagram of the pathway *DB1* → *OT*+*DB*. All energies in kJ mol^{-1}. Gibbs energies calculated at T = 300 K, p = 1 bar.

Table 3.9. In *OT*+*DB*, the cycloadduct bond parameters d(C^1-C^2), d(C^1-Si) and d(C^2-Si') differ by 0.005 Å or less compared to *OT*. During the course of the C^{11}-O bond cleavage, these values change slightly and most notably, the difference between d(C^1-Si) and d(C^2-Si') becomes smaller, but the differences to *OT* never exceed 0.01 Å. It can therefore be concluded that the bonding situation of the ether group does not affect the structure in this part of the system in a significant way. In contrast, the ether group shows more pronounced structural differences when compared to *DB2* and *C2*: The d(O-Si'') value in *OT*+*DB*, 1.961 Å, is significantly larger than the value in *DB2*, 1.939 Å, most likely an effect of strain within the molecule which counteracts against the for-

mation of the O-Si dative bond. On the contrary, the *d*(O-Si″) value in *OT+C*, 1.659 Å, has a smaller deviation to *C2* (1.665 Å) and is even slightly shorter. The *d*(C^{11}-Si‴) value in *OT+C* and *C2* is, as expected, virtually identical to diethylether, since the ethyl group is bonded to another dimer row and no longer attached to the rest of the molecule.

The transition state of the C^{11}-O bond cleavage reaction occurs earlier on the reaction coordinate for the doubly bonded system: This is reflected in a smaller stretching of the C-O bond with respect to *OT+DB* (1.483 to 1.904 Å, Δd = 0.421 Å) compared to the *DB2→C2* reaction (1.486 to 1.927 Å, Δd = 0.441 Å) and a larger *d*(C^{11}-Si‴) value (TS(*OT+DB→C*): 2.843, TS(*DB2→C2*): 2.809 Å). At the same time, the angle α(O-C^{11}-Si‴) does not differ significantly (TS(*OT+DB→C*): 153.9°, TS(*DB2→C2*): 155.1°). The reduction of the stretching of the C-O bond also leads to a reduced reaction energy barrier, which is 50 (E_a) and 43 kJ mol^{-1} (G_a) in the *OT+DB→C* reaction (Figure 3.9(c)) and 57 (E_a) and 51 kJ mol^{-1} (G_a) in the *DB2→C2* reaction (Figure 3.7). This will be discussed in more detail along with the pEDA results.

Bonding energies of *OT+DB* and *OT+C* are given in Table 3.10. While in a first approximation, one could assume the E_{bond}(PBE-D3) value of *OT+DB* to be the sum of the respective values for *OT* and *DB2* (–352 + –109 = –461 kJ mol^{-1}), the actual energy is much lower in absolute value at –370 kJ mol^{-1}. The main reason for this is an overestimation of the dispersion contribution E_{bond}(D3) in the sum of *OT* and *DB2* (–78 + –82 = –160 vs. –101 kJ mol^{-1}), since some interactions occur in both structures and are therefore counted twice. However, –101 kJ mol^{-1} is still the highest absolute value of E_{bond}(D3) of any mode in the system, which is due to the low vertical position of all molecule atoms (see Figure 3.9(a)). The E_{bond}(PBE) value, –269 kJ mol^{-1}, is also significantly smaller than the sum of *OT* and *DB2* (–274 + –27 = –301 kJ mol^{-1}) and even lower in absolute value than the respective *OT* value. As pEDA results will show later, this is mostly caused by the increased preparation energy of the molecule. The difference in bonding energies between *OT+DB* and *OT+C*, –187 (E_{bond}) and –196 kJ mol^{-1} (G_{bond}) is in the range of the two values for the singly bonded system (E_{bond}: –172 (*DB1/C1*), –192 (*DB2/C2*), G_{bond}: –192 (*DB1/C1*), –206 kJ mol^{-1} (*DB2/C2*), see also Table 3.6), so the energy gain by the formation of shared-electron bonds in this part of the molecule is energetically unaffected by the cycloaddition of the triple bond.

The most intriguing property of the doubly bonded states is the large difference between electronic and Gibbs bonding energies: While for singly bonded states, the difference is in the range of 50 to 80 kJ mol^{-1} (see Tables 3.3 and 3.6), the values for *OT+DB* and *OT+C* are slightly higher at 92 and 83 kJ mol^{-1}, respectively. This is caused by a loss of intramolecular flexibility leading to a decrease in entropy, since the double-bonding situation forces every part of the molecule except the ethyl group into a fixed position, while in the singly bonded states, the part of the molecule not bonded to the surface can move

around more freely. The actual energy difference due to this entropy loss might even be higher than the value given here, since the flexibility of the soft modes in the singly bonded states could be underestimated in the harmonic approximation. The same causes for destabilization are also apparent in the *OT*+*C* mode. However, due to the previously mentioned effects that entropically stabilize the *C* structures in comparison to the *DB* structures (see Table 3.6 and the corresponding discussion), the difference between E_{bond} and G_{bond} is 9 kJ mol^{-1} lower for *OT*+*C* than for *OT*+*DB*.

Table 3.11. pEDA values of EMC bonded to Si(001) in the OT + DB mode and the TS(OT + DB→C) geometry. For comparison, the sum of the OT and DB2 pEDA values is given as well.[a]

	E(*OT*)+*E*(*DB2*)	*OT*+*DB*	TS(*OT*+*DB*→*C*)
ΔE_{int}	–874	–792	–874
ΔE_{int}(disp)[b]	–151 (17%)	–93 (12%)	–98 (11%)
ΔE_{int}(elec)[b]	–723 (83%)	–699 (88%)	–776 (89%)
ΔE_{Pauli}	2189	2118	2589
ΔE_{elstat}[c]	–1379 (47%)	–1306 (46%)	–1536 (46%)
ΔE_{orb}[c]	–1532 (53%)	–1511 (54%)	–1829 (54%)
ΔE_{prep}(Mol.)	341	365	485
ΔE_{prep}(Surf.)	50	42	59
E_{bond}[d]	–483 (–461)	–385 (–370)	–330 (–320)

[a] All values in kJ mol^{-1}, calculated at PBE-D3/TZ2P. Fragments: Molecule and surface. Fragmentation: Triplet. [b] Percentage values give dispersion and electronic contributions to the total interaction energy ΔE_{int}. [c] Percentage values give the contribution to the sum of the attractive pEDA interaction terms ΔE_{elstat} and ΔE_{orb}. [d] PAW values (in parentheses) given for comparison.

The effect of double-bonding on the bonding of the individual functional groups can be analyzed using pEDA. Table 3.11 compares the pEDA values of *OT*+*DB* with the sum of the pEDA values of *OT* and *DB2*. This also helps to figure out why this state is not much more strongly bonded than *OT*. The results show that the electronic interaction energy ΔE_{int}(elec) actually conserves 97% of the sum of the *OT* and *DB2* values. The largest difference in the pEDA terms is apparent in ΔE_{elstat} (95% conservation), while ΔE_{orb} has the lowest difference (99% conservation). This shows that stabilization due to chemical bond formation in a bifunctional molecule is essentially additive, while the Pauli and electrostatic terms show some minor losses due to double counting of interactions between molecule and surface. The double counting is more strongly apparent in ΔE_{int}(disp), where the *OT*+*DB* value

(–93 kJ mol^{-1}) only conserves 62% of the sum of the *OT* and *DB2* values (–151 kJ mol^{-1}). These 58 kJ mol^{-1} make the largest contribution to the difference in E_{bond} (98 kJ mol^{-1}). The second largest contribution stems from a higher ΔE_{prep}(Mol.) value in *OT+DB* of 24 kJ mol^{-1}. This is as expected, since in addition to the deformation needed to form chemical bonds at each of the two sites, the distance between the sites puts further constraints on the molecular structure. Surprisingly, ΔE_{prep}(Surf.) is slightly lower than the sum of the *OT* and *DB2* values. Most likely, this is caused by the missing steric interaction between the non-bonding residue in the molecule and the surface, which is apparent in the singly bonded states (see also the increased O-Si bond length (Table 3.5) and surface preparation energy (Table 3.7) of *DB2* in comparison to the other *DB* structures).

The previously made assumption that the lower energy barrier of the *OT+DB*→*C* reaction is mainly caused by the shorter C^{11}-O bond length at the transition state is confirmed by the pEDA results: The ΔE_{prep}(Mol.) difference between the transition state and the *OT+DB* minimum, 120 kJ mol^{-1}, is 7 kJ mol^{-1} smaller than the corresponding difference for the *DB2*→*C2* reaction (127 kJ mol^{-1}, see Tables 3.7 and 3.8), the exact difference of the corresponding E_{a} values (*OT+DB*→*C*: 50, *DB2*→*C2*: 57 kJ mol^{-1}). However, there are other factors as well which cancel out, so the difference is not completely determined by the preparation energies. In contrast to the previous subsection, the strength of the O-Si dative bond and the orbital contribution due to the nucleophilic attack can not be quantified using the NOCV scheme here. This is because some NOCVs can not be clearly assigned to one bonding site, as an example in Figure 3.11 shows, and this prevents a distinct separation of energy contributions.

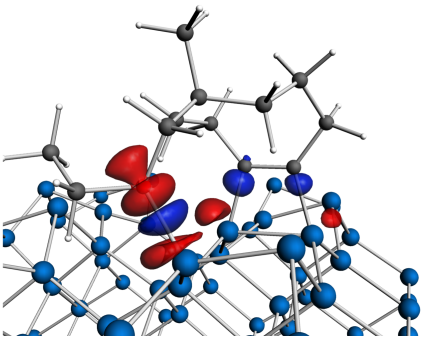

Figure 3.11. NOCV deformation density $\Delta\rho_{3\alpha}$ of the *OT* + *DB* mode. In this case, a clear assignment to a single bonding site is no longer possible. Red: Depletion of electron density. Blue: Accumulation of electron density.

3.5.6 Adsorption Dynamics

According to the approach outlined in Section 3.4.2, the adsorption dynamics of EMC was investigated as well. Since, as previously shown, the substituents do not have a significant influence on the bonding of the triple bond, the analysis is not performed in as much detail as for cyclooctyne, but reduced to certain key aspects. One of these aspects is the shape of the energy profile for direct adsorption into the *OT* and *B* states. By comparing the profiles to those of cyclooctyne, the effect of the subtituents on this part of the PES can be quantified. As for the parent molecule, the profiles were calculated via structural optimization using the Conjugate Gradient algorithm from certain starting points. These were set to be equivalent to positions 1, 4 and 5 in the study of cyclooctyne, i.e. triple bond atoms pointing in the direction of the surface at a vertical position so that $\Delta z(C_{triple}\text{-}Si_{up})$ = 4 Å, former C_2 axis oriented parallel to the z axis, triple bond oriented parallel to the y (position 1) or x axis (positions 4 and 5) and xy positioning of the triple bond center according to Section 3.4.2, Figures 2 and 5. While there are, due to the missing rotational symmetry in EMC, two inequivalent molecular orientations possible for each starting point, calculations were only done for one of them, since it can be assumed that the location of the substituents does not influence the results in a significant way. A schematic drawing of the chosen orientations along with the adsorption paths is given in Figure 3.12(a).

The resulting energy profiles are given in Figure 3.12(b–d). As for cyclooctyne, trajectory (b) proceeds directly to *OT*, while (d) ends up in *B2* and (c) in an intermediate-like state *TI* (triple bond intermediate), which will be discussed later. In general, the shape of the profiles of EMC is very similar to cyclooctyne. There are some minor differences, most notably the lower energy of the final states, which was already discussed in the beginning of this section. The reason for the smaller differences of the final state energies to cyclooctyne compared to the values given in Section 3.5.3 is that these trajectories do not end up in the respective mininum energy conformation. Additionally, the narrow drop in energy in the center of profiles (b) and (d) ((b): –140 to –220 kJ mol^{-1}, (d): –50 to –220 kJ mol^{-1}), which is where the formation of the shared-electrons takes place, shifts slightly in position for EMC. The reason for this is a change in the amount of structural relaxation (e.g. tilting, see Figure 3.6) after bond formation, which elongates or shortens the latter part of the path below –280 kJ mol^{-1}. Since the adsorption coordinate is normalized, this makes the location of the energy drop appear to shift.

The optimized structure of *TI* is given in Figure 3.13(a). It is virtually identical to the same mode in the cyclooctyne/Si(001) system (see Section 3.4.2) and the interatomic distances $d(C^1\text{-}C^2)$ = 1.261, $d(C^1\text{-Si})$ = 2.202 and $d(C^2\text{-Si})$ = 1.985 Å differ by less than 0.01 Å to the cyclooctyne values (1.263, 2.214 and 1.981 Å, respectively). The energy barriers for convergence into the *OT* and *B* states were not calculated, since the determination of a first-order saddle

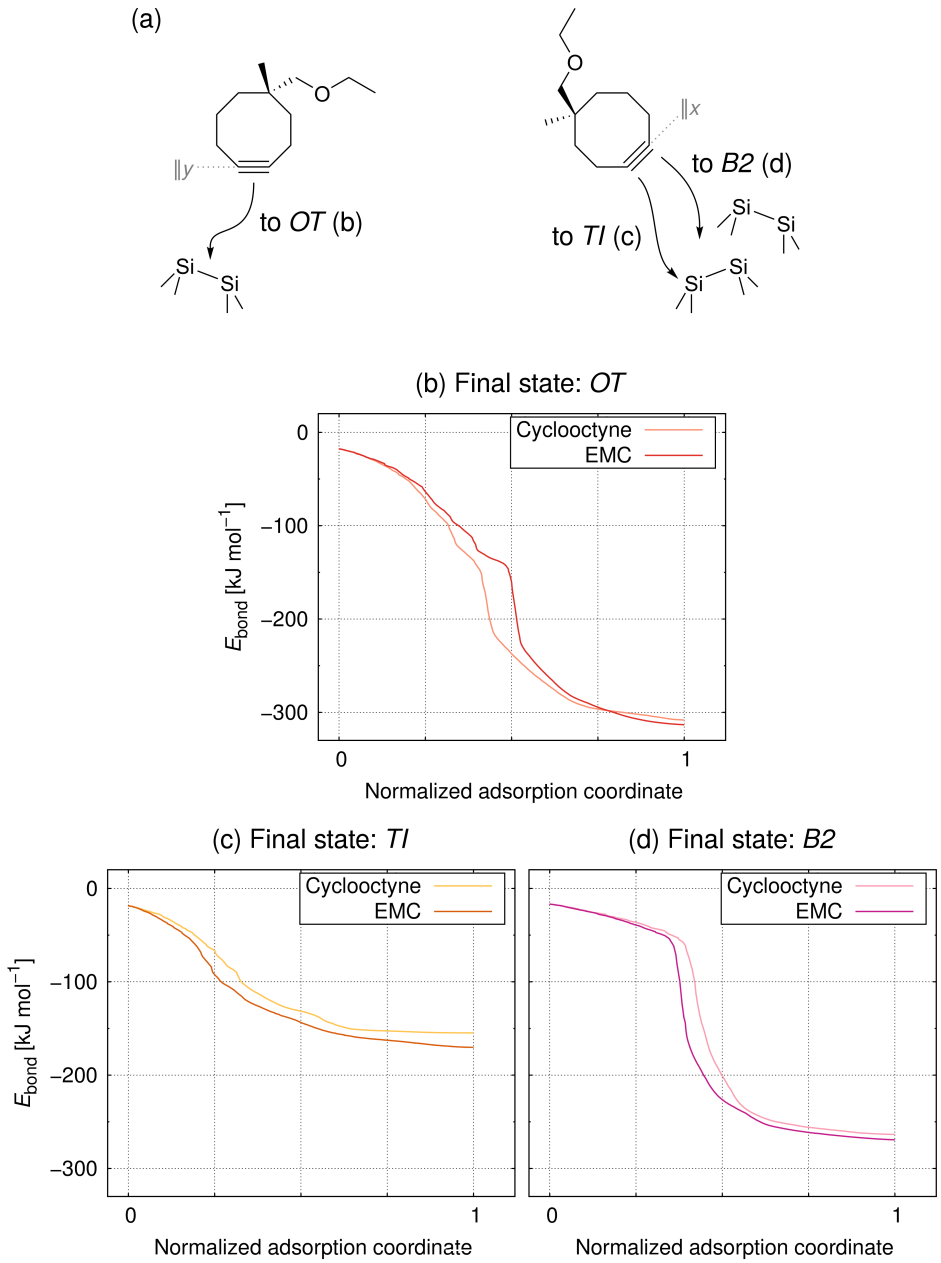

Figure 3.12. (a) Schematic depiction of the adsorption paths to which the energy profiles are given below. (b–d) Energy profiles of direct adsorption into the states *OT* (b), *TI* (c) and *B2* (d), obtained by Conjugate Gradient optimization. The definition of the starting structures is given in the text.

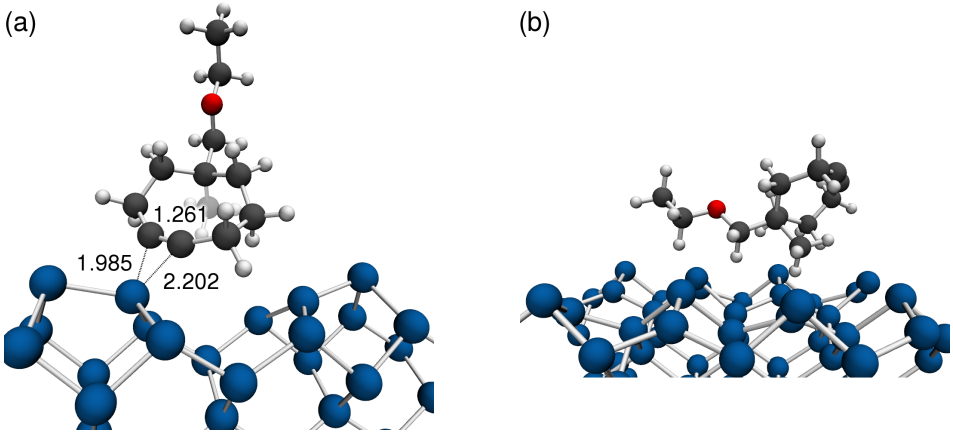

Figure 3.13. Optimized (PBE-D3/PAW) structures of *TI* (a) and *PH* (b). Bond lengths given in Å.

point is very difficult in such a shallow region of the PES (see Figure 3.12(c)) when there are additional low-frequency modes like hindered internal rotations within the molecule.[a] Since the interaction of the triple bond with the surface showed no significant differences to the adsorption of cyclooctyne in all other cases, it is assumed that the energy barrier is also unaffected by the substitution. As AIMD results will show later, this is a valid assumption.

In contrast to the previously investigated systems, a physisorbed structure (*PH*) is also possible (Figure 3.13(b)). But while there is always a physisorbed minimum in the adsorption on metal surfaces (Section 1.1), this one only occurs if the impinging molecule is in an orientation where both functional groups are pointing away from the surface. Although this could, in principle, also happen with the other molecules whose adsorption was investigated in this work, their reduced size prevents that those orientations are minima on the PES. However, the relevance of *PH* in the adsorption dynamics is limited, since the orientation of the molecule during first contact with the surface is most likely random and additionally, it can easily convert to a chemisorbed state via rotation. This will be discussed further along with the AIMD results.

Bonding energies of *TI* and *PH* are given in Table 3.12. The E_{bond} value of *TI*, –168 kJ mol^{-1}, is close to the value in the cyclooctyne system, –155 kJ mol^{-1} (Section 3.4.2), and the difference can again be attributed to the increased dispersion in EMC caused by the larger size of the molecule. Interestingly, the E_{bond}(PBE) and E_{bond}(D3) values of *TI* are almost equivalent, which is in contrast to the other chemisorbed states where either the electronic contri-

[a] Minimum mode following algorithms, such as the Dimer method, are based on the premise that there is only one low-frequency mode, i.e. the one that is going to invert its curvature. Climbing-image NEB, on the contrary, only works if the frequencies of the imaginary mode and the lowest real modes are large enough so that the computation is unsusceptible to numerical noise. Both methods failed to convert to first-order saddle points in this system.

Table 3.12. Gibbs bonding energies G_{bond}, electronic bonding energies E_{bond} and the PBE and D3 contributions to E_{bond} of EMC bonded to Si(001) in the *TI* and *PH* modes.[a]

	TI	*PH*
G_{bond}(PBE-D3)	–109	–31
E_{bond}(PBE-D3)	–168	–83
E_{bond}(PBE)	–89	8
E_{bond}(D3)	–79	–91

[a] All values in kJ mol^{-1}, calculated using PBE-D3/PAW. G_{bond} values calculated at T = 300 K, p = 1 bar.

bution is dominating (*OT*, *B1/2*, *C1/2*) or the dispersion contribution (*DB1/2*). The reason for this is an absence of both the electronic stabilization due to shared-electron bond formation (as in, e.g., *OT*) and the destabilization due to molecule deformation (as in *DB1/2*), so that only a moderately strong dative bond interaction between the π system and the Si_{down} is left (see Sections 3.3.1 and 3.4.2) in addition to the comparatively large dispersion contribution that this molecule shows in general. In contrast, the *PH* mode is exclusively stabilized by dispersion, while the electronic contribution is even positive. This confirms that the state is purely physisorbed. The differences between the electronic and Gibbs bonding energy in *TI*, 59 kJ mol^{-1}, is comparable to the values obtained for *OT*, *B1/2* and *DB1/2*, while the difference in *PH* is slightly lower at 52 kJ mol^{-1}. This difference can be explained by the presence of a directional bond in *TI*, which puts constraints on the flexibility of the molecule, while in *PH*, these constraints are missing and the state is entropically stabilized.

As with cyclooctyne, a series of AIMD simulations was performed to determine the effect of random orientation and thermal excitation on the adsorption dynamics. Due to the increased computational demand, only 10 trajectories were simulated in total. The trajectories were evaluated according to Section 3.4.2 and the results are given in Table 3.13, while data of an exemplary simulation can be found in Figure 3.14 (the data of all ten simulations is given in the Appendix). In contrast to cyclooctyne, where only the duration of stay in *TI* was extracted from the data using the criteria given in the respective section, here the duration of stay in *PH* and *OT* is given as well, since the system can convert from *PH* to other modes and from *OT* to *OT+DB*. The results show that four trajectories end up in *OT*, three in *OT+DB* via *OT* and one each in *B1*, *B2* and *PH*. In case of *OT* as a final state, the simulation time was extended to at least 10 ps after the formation of the shared-electron bonds to allow for conversion into *OT+DB*. Analogously, the simulation time in simulation 7 was extended to 20 ps to allow for conversion into any other state.

Table 3.13. Final state and, if applicable, duration of stay Δt (in ps) in the states *PH*, *TI* and *OT*.

Simulation	Final state	$\Delta t(PH)$	$\Delta t(TI)$	$\Delta t(OT)$
1	*OT*	–	1.00	>10.00
2	*OT*	≈1.5	0.66	>10.00
3	*OT+DB*	–	0.73	1.09
4	*B1*	–	–	–
5	*B2*	–	0.15	–
6	*OT+DB*	≈6.0	0.65	1.29
7	*PH*	>20.0	–	–
8	*OT*	≈2.0	2.12	>10.00
9	*OT+DB*	–	0.86	7.99
10	*OT*	–	3.61	>10.00

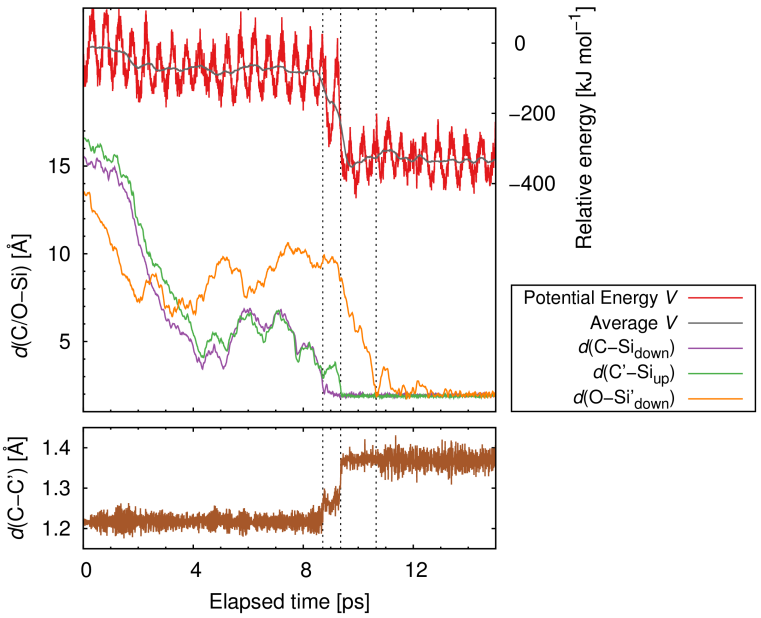

Figure 3.14. Evolution of the potential energy V and selected interatomic distances over time in simulation 6. Vertical lines denote a change in the adsorption mode: *PH* (until 8.71 ps), *TI* (8.71–9.36 ps), *OT* (9.36–10.65 ps), *OT* + *DB* (from 10.65 ps).

In both cases, conversion could not be observed. Interestingly, none of the trajectories ended up in *DB1* or *DB2*. This is in line with the high molecular preparation energies (Table 3.7) which means that the molecule would have to be out of its equilibrium conformation to enable the formation of the O-Si dative bond.

In contrast to cyclooctyne, where 15 of 17 trajectories ending up in *OT* proceeded via *TI* and all three trajectories ending up in *B* skipped the intermediate, the adsorption of EMC into *OT* proceeds exclusively via *TI* and one of the simulations ending up in a *B* states features the *TI* intermediate, albeit with a very low duration of stay of $\Delta t(TI) = 0.15$ ps (simulation 5). The average duration of stay in *TI* for reactions to *OT* can be determined as 1.38 ± 1.11 ps. This is slightly larger than the cyclooctyne value (1.0 ± 0.7 ps), albeit both are in the error bars of each other. However, while the statistical relevance of this average value was already limited for cyclooctyne, where 15 values were used, it is even more limited here, since only seven values are available. In any case, the low difference between the two values reinforces the previously made assumption that the energy barrier for this reaction does not change significantly between the two systems.

Three of the seven trajectories resulting in the *OT* mode also converted to *OT+DB*. The corresponding durations of stay in *OT* are 1.09, 1.29 and 7.99 ps (Table 3.13). Here, the starting point of residence in *OT+DB* was defined as the time when the first contact of the oxygen to a surface atom is made (d(O-Si) < 2.00 Å). The data from the trajectories also reveals that there is no significant change in potential energy in the transition from *OT* to *OT+DB* (see Figure 3.14). This is in line with the the results from the former parts of this section, which showed very low energy differences between the two states at 300 K. Presumably, continuous interconversion between these two states would be observed for all trajectories that ended up in either of the states if the simulations were allowed to run longer.

The physisorbed *PH* mode can be identified by an average potential energy of –50 to –100 kJ mol^{-1} (see Figure 3.14, t = 2 to 8 ps). There are four simulations in which the duration of stay Δt in this state is longer than 1 ps: Simulations 2, 6, 7 and 8 (Table 3.13). While the system stays in this mode for more than 20 ps in simulation 7, it quickly converts to a chemisorbed state in the other three cases. This confirms the previously made assumption that the system can easily convert from *PH* via rotation and that the state is of limited significance for the adsorption dynamics.

3.5.7 Conclusions

In this section, the bonding, energetics, dynamics, structure and properties of EMC on Si(001) were studied. The results have shown that the substituents have virtually no effect on the reactivity of the triple bond, since the properties in bonding and adsorption dynamics show no significant differences to cyclooctyne. While there are some minor differences in energetics and structure, these are caused by interaction between the substituents and the surface (dispersive attraction, steric repulsion). This means that if the reactivity of the triple bond in a functionalized cyclooctyne with substituents at the 5 and/or 6 position (see Figure 3.1) is to be simulated, it is sufficient to do the calculations with the unsubstituted parent molecule. However, this is not transferable to cyclooctynes substituted at another position: As previous studies have shown, the introduction of electron-withdrawing groups at the 3 position increases the reactivity of the triple bond in a significant way.[156–159]

In contrast to this, the reactivity of the ether functionality is more markedly affected by the substitution, since the large ring puts constraints on the structure, but also increases the O-Si bond strength via the inductive effect. The most pronounced change here is in the reaction barrier for C-O bond cleavage: While the minimum conformation of the datively bonded structure for EMC, *DB1*, is more stable in comparison to diethylether, the transition state in EMC is destabilized, leading to a high energy barrier of 70–80 kJ mol^{-1} as opposed to 61 kJ mol^{-1} in diethylether. Additionally, at T = 300 K and p = 1 bar, the Gibbs bonding energy of the transition state in EMC is higher in energy than the separated molecule and surface, which means that the molecule is more likely to desorb from *DB1* than undergo this reaction. However, due to the deformation needed to form the O-Si dative bond in the first place, it is unlikely that datively bonded structures form at all, as the absence of the *DB* modes in the AIMD simulations has also underlined. This is important for the applicability of the molecule as a building block for internal interfaces, since dative bond formation and C-O bond cleavage are unwanted reaction types.

While the formation of doubly bonded structures is possible, they bring in almost no gain in adsorption energy compared to the cycloadduct *OT*. At 300 K, the *OT*+*DB* mode is only 2 kJ mol^{-1} more stable than *OT* and the energetic order of the states might even inverse in the real system, since the entropic stabilization of *OT* could be underestimated in the applied methodology. While the doubly bonded structure was found in some of the AIMD trajectories, it can be expected that systems in this state are constantly interconverting with *OT* and that at experimental time scales, *OT* could even be more stable. All these results are in line with the experimental observations, which showed a predominance of *OT* at 300 K.[72] While the C-O bond cleavage reaction from a doubly bonded state was observed at 450 K, this is also in line with our results: The split double bonded structure is the global thermodynamic minimum, so if the system is interconverting between *OT*

and *OT+DB* and there is enough internal energy available for overcoming the bond cleavage reaction barrier, then the system will eventually end up in the split state.

Bibliography

[1] S. F. Bent, *Surf. Sci.* **2002**, *500*, 879.

[2] A. V. Teplyakov, S. F. Bent, *J. Vac. Sci. Technol. A* **2013**, *31*, 050810.

[3] C. Heitzinger, G. Klimeck, *J. Comput. Electron.* **2007**, *6*, 387.

[4] J. Yoshinobu, *Prog. Surf. Sci.* **2004**, *77*, 37.

[5] M. A. Filler, S. F. Bent, *Prog. Surf. Sci.* **2003**, *73*, 1.

[6] Z. Ma, F. Zaera, *Surf. Sci. Rep.* **2006**, *61*, 229.

[7] R. J. Hamers, *Annu. Rev. Anal. Chem.* **2008**, *1*, 707.

[8] T. R. Leftwich, A. V. Teplyakov, *Surf. Sci. Rep.* **2008**, *63*, 1.

[9] D. A. King, M. G. Wells, *Surf. Sci.* **1972**, *29*, 454.

[10] J. E. Lennard-Jones, *Trans. Faraday Soc.* **1932**, *28*, 333.

[11] M. Bowker, *J. Phys.: Condens. Matter* **2010**, *22*, 263002.

[12] R. Tonner, P. Rosenow, P. Jakob, *Phys. Chem. Chem. Phys.* **2016**, *18*, 6316.

[13] A. J. Cohen, P. Mori-Sánchez, W. Yang, *Chem. Rev.* **2012**, *112*, 289.

[14] C. T. Rettner, D. J. Auerbach, J. C. Tully, A. W. Kleyn, *J. Phys. Chem.* **1996**, *100*, 13021.

[15] *Dynamics of Gas-Surface Interactions*, Eds.: R. Díez Muiño, H. F. Busnengo, Springer, Berlin/Heidelberg, **2013**.

[16] D. A. King, *Crit. Rev. Solid State Mater. Sci.* **1978**, *7*, 167.

[17] L. H. Sprowl, C. T. Campbell, L. Árnadóttir, *J. Phys. Chem. C* **2016**, *120*, 9719.

[18] C. T. Campbell, L. H. Sprowl, L. Árnadóttir, *J. Phys. Chem. C* **2016**, *120*, 10283.

[19] A. Antony, A. Asthagiri, J. F. Weaver, *J. Chem. Phys.* **2013**, *139*, 104702.

[20] V. J. Bukas, J. Meyer, M. Alducin, K. Reuter, *Z. Phys. Chem.* **2013**, *227*, 1523.

[21] M. R. Tuckerman, *J. Phys.: Condens. Matter* **2002**, *14*, R1297.

[22] R. Kosloff, *J. Phys. Chem.* **1988**, *92*, 2087.

[23] G.-J. Kroes, *Prog. Surf. Sci.* **1999**, *60*, 1.

[24] *The Chemical Bond: Fundamental Aspects of Chemical Bonding*, Eds.: G. Frenking, S. Shaik, Wiley-VCH, Weinheim, **2014**.

[25] M. Rahm, R. Hoffmann, *J. Am. Chem. Soc.* **2016**, *138*, 3731.

[26] R. Dronskowski, P. E. Blöchl, *J. Phys. Chem.* **1993**, *97*, 8617.

[27] V. L. Deringer, A. L. Tchougréeff, R. Dronskowski, *J. Phys. Chem. A* **2011**, *115*, 5461.

[28] A. Nandula, Q. T. Trinh, M. Saeys, A. N. Alexandrova, *Angew. Chem. Int. Ed.* **2015**, *54*, 5312.

[29] M. Kohout, *Int. J. Quantum Chem.* **2004**, *97*, 651.

[30] A. I. Baranov, M. Kohout, *J. Comput. Chem.* **2011**, *32*, 2064.

[31] F. R. Wagner, A. I. Baranov, Y. Grin, M. Kohout, *Z. Anorg. Allg. Chem.* **2013**, *639*, 2025.

[32] M. von Hopffgarten, G. Frenking, *WIREs Comput. Mol. Sci.* **2012**, *2*, 43.

[33] M. Raupach, R. Tonner, *J. Chem. Phys.* **2015**, *142*, 194105.

[34] B. D. Dunnington, J. R. Schmidt, *J. Chem. Theory Comput.* **2012**, *8*, 1902.

[35] B. D. Dunnington, J. R. Schmidt, *J. Catal.* **2015**, *324*, 50.

[36] R. F. W. Bader, *Chem. Rev.* **1991**, *91*, 893.

[37] A. Otero-de-la-Roza, E. R. Johnson, V. Luaña, *Comput. Phys. Commun.* **2014**, *185*, 1007.

[38] J.-H. Lee, N. C. Bristowe, P. D. Bristowe, A. K. Cheetham, *Chem. Commun.* **2015**, *51*, 6434.

[39] A. Tkatchenko, L. Romaner, O. T. Hofmann, E. Zojer, C. Ambrosch-Draxl, M. Scheffler, *MRS Bull.* **2010**, *35*, 435.

[40] S. Grimme, *WIREs Comput. Mol. Sci.* **2011**, *1*, 211.

[41] C. Esterhuysen, G. Frenking, *Theor. Chem. Acc.* **2004**, *111*, 381.

[42] M. J. S. Dewar, *Bull. Soc. Chim. Fr.* **1951**, *18C*, 74.

[43] J. Chatt, L. A. Duncanson, *J. Chem. Soc.* **1953**, 2939.

[44] G. Blyholder, *J. Phys. Chem.* **1964**, *68*, 2772.

[45] M. P. Mitoraj, A. Michalak, T. Ziegler, *J. Chem. Theory Comput.* **2009**, *5*, 962.

[46] M. P. Mitoraj, M. Parafiniuk, M. Srebro, M. Handzlik, A. Buczek, A. Michalak, *J. Mol. Model.* **2011**, *17*, 2337.

[47] M. Raupach, *Ph.D. thesis*, Philipps-Universität Marburg, **2015**.

[48] C. Kittel, *Introduction to Solid State Physics*, 8th Ed., Wiley, Hoboken, **2005**.

[49] R. E. Schlier, H. E. Farnsworth, *J. Chem. Phys.* **1959**, *30*, 917.

[50] D. J. Chadi, *Phys. Rev. Lett.* **1979**, *43*, 43.

[51] P. Krüger, J. Pollmann, *Phys. Rev. Lett.* **1995**, *74*, 1155.

[52] Y. Murata, M. Kubota, *Phase Transitions* **1995**, *53*, 125.

[53] K. Terakura, T. Yamasaki, Y. Morikawa, *Phase Transitions* **1995**, *53*, 143.

[54] R. J. Hamers, R. M. Tromp, J. E. Demuth, *Phys. Rev. B* **1986**, *34*, 5343.

[55] J. Dabrowski, M. Scheffler, *Appl. Surf. Sci.* **1992**, *56–58*, 15.

[56] K. Sagisaka, J. Nara, D. Bowler, *J. Phys.: Condens. Matter* **2017**, *29*, 145502.

[57] E. Pehlke, M. Scheffler, *Phys. Rev. Lett.* **1993**, *71*, 2338.

[58] R. Konecny, D. J. Doren, *J. Phys. Chem. B* **1997**, *101*, 10983.

[59] S.-H. Lee, M.-H. Kang, *Phys. Rev. B* **1998**, *58*, 4903.

[60] R. B. Woodward, R. Hoffmann, *Angew. Chem. Int. Ed.* **1969**, *8*, 781.

[61] J.-H. Cho, L. Kleinman, *Phys. Rev. B* **2003**, *68*, 195413.

[62] J.-H. Cho, L. Kleinman, *Phys. Rev. B* **2004**, *69*, 075303.

[63] X. L. Fan, Y. F. Zhang, W. M. Lau, Z. F. Liu, *Phys. Rev. B* **2005**, *72*, 165305.

[64] Q. J. Zhang, X. L. Fan, W. M. Lau, Z. F. Liu, *Phys. Rev. B* **2009**, *79*, 195303.

[65] G. T. Wang, C. Mui, J. F. Tannaci, M. A. Filler, C. B. Musgrave, S. F. Bent, *J. Phys. Chem. B* **2003**, *107*, 4982.

[66] R. J. Hamers, S. K. Coulter, M. D. Ellison, J. S. Hovis, D. F. Padowitz, M. P. Schwartz, *Acc. Chem. Res.* **2000**, *33*, 617.

[67] R. D. Bach, *J. Am. Chem. Soc.* **2009**, *131*, 5233.

[68] D. Heber, P. Rösner, W. Tochtermann, *Eur. J. Org. Chem.* **2005**, 4231.

[69] N. J. Agard, J. A. Prescher, C. R. Bertozzi, *J. Am. Chem. Soc.* **2004**, *126*, 15046.

[70] S. T. Laughlin, J. M. Baskin, S. L. Amacher, C. R. Bertozzi, *Science* **2008**, *320*, 664.

[71] M. F. Debets, S. S. van Berkel, J. Dommerholt, A. J. Dirks, F. P. J. T. Rutjes, F. L. van Delft, *Acc. Chem. Res.* **2011**, *44*, 805.

[72] M. Reutzel, N. Münster, M. A. Lipponer, C. Länger, U. Höfer, U. Koert, M. Dürr, *J. Phys. Chem. C* **2016**, *120*, 26284.

[73] N. Münster, P. Nikodemiak, U. Koert, *Org. Lett.* **2016**, *18*, 4296.

[74] G. Mette, M. Dürr, R. Bartholomäus, U. Koert, U. Höfer, *Chem. Phys. Lett.* **2013**, *556*, 70.

[75] G. Mette, M. Reutzel, R. Bartholomäus, S. Laref, R. Tonner, M. Dürr, U. Koert, U. Höfer, *ChemPhysChem* **2014**, *15*, 3725.

[76] M. Reutzel, G. Mette, P. Stromberger, U. Koert, M. Dürr, U. Höfer, *J. Phys. Chem. C* **2015**, *119*, 6018.

[77] M. Reutzel, M. Lipponer, M. Dürr, U. Höfer, *J. Phys. Chem. Lett.* **2015**, *6*, 3971.

[78] W. Koch, M. C. Holthausen, *A Chemist's Guide to Density Functional Theory*, Wiley-VCH, Weinheim, **2001**.

[79] F. Jensen, *Introduction to Computational Chemistry*, 2nd Ed., Wiley-VCH, Weinheim, **2007**.

[80] I. N. Levine, *Quantum Chemistry*, 6th Ed., Pearson Education, London, **2009**.

[81] L. de Broglie, *Ann. Phys.* **1925**, *10*, 22.

[82] M. Born, R. Oppenheimer, *Ann. Phys.* **1927**, *389*, 457.

[83] P. Hohenberg, W. Kohn, *Phys. Rev.* **1964**, *136*, B864.

[84] W. Kohn, L. J. Sham, *Phys. Rev.* **1965**, *140*, A1133.

[85] P. A. M. Dirac, *Proc. Cambridge Phil. Roy. Soc.* **1930**, *26*, 376.

[86] S. J. Vosko, L. Wilk, M. Nusair, *Can. J. Phys.* **1980**, *58*, 1200.

[87] D. M. Ceperley, B. J. Alder, *Phys. Rev. Lett.* **1980**, *45*, 566.

[88] J. P. Perdew, *Int. J. Quantum Chem.* **1985**, *28*, 497.

[89] J. P. Perdew, J. A. Chevary, S. H. Vosko, K. A. Jackson, M. R. Pederson, D. J. Singh, C. Fiolhais, *Phys. Rev. B* **1992**, *46*, 6671.

[90] J. P. Perdew, K. Burke, M. Enzerhof, *Phys. Rev. Lett.* **1996**, *77*, 3865.

[91] J. P. Perdew, K. Burke, M. Enzerhof, *Phys. Rev. Lett.* **1997**, *78*, 1396.

[92] J. Heyd, J. E. Peralta, G. E. Scuseria, R. L. Martin, *J. Chem. Phys.* **2005**, *123*, 174101.

[93] J. Tao, J. P. Perdew, V. N. Staroverov, G. E. Scuseria, *Phys. Rev. Lett.* **2003**, *91*, 146401.

[94] A. D. Becke, *J. Chem. Phys.* **1993**, *98*, 5648.

[95] P. J. Stephens, F. J. Devlin, C. F. Chabalowski, M. J. Frisch, *J. Phys. Chem.* **1994**, *98*, 11623.

[96] A. D. Becke, *Phys. Rev. A* **1988**, *38*, 3098.

[97] C. Lee, W. Yang, R. G. Parr, *Phys. Rev. B* **1988**, *37*, 785.

[98] J. Heyd, G. E. Scuseria, M. Enzerhof, *J. Chem. Phys.* **2003**, *118*, 8207.

[99] J. Heyd, G. E. Scuseria, *J. Chem. Phys.* **2004**, *121*, 1187.

[100] J. Heyd, G. E. Scuseria, M. Enzerhof, *J. Chem. Phys.* **2006**, *124*, 219906.

[101] S. Elliott, *The Physics and Chemistry of Solids*, Wiley, West Sussex, **1998**.

[102] F. Bloch, *Z. Phys.* **1929**, *52*, 555.

[103] H. Hellmann, *J. Chem. Phys.* **1935**, *3*, 61.

[104] P. Schwerdtfeger, *ChemPhysChem* **2011**, *12*, 3141.

[105] P. E. Blöchl, *Phys. Rev. B* **1994**, *50*, 17953.

[106] G. Kresse, D. Joubert, *Phys. Rev. B* **1999**, *59*, 1758.

[107] S. Grimme, J. Antony, S. Ehrlich, H. Krieg, *J. Chem. Phys.* **2010**, *132*, 154104.

[108] S. Grimme, S. Ehrlich, L. Goerigk, *J. Comput. Chem.* **2010**, *32*, 1456.

[109] A. Tkatchenko, M. Scheffler, *Phys. Rev. Lett.* **2009**, *102*, 073005.

[110] D. Sheppard, R. Terrell, G. Henkelman, *J. Chem. Phys.* **2008**, *128*, 134106.

[111] M. R. Hestenes, E. Stiefel, *J. Res. Natl. Bur. Stand.* **1952**, *49*, 409.

[112] J. Nocedal, S. J. Wright, *Numerical Optimization*, Springer, New York, **2013**.

[113] H. Jónsson, G. Mills, K. W. Jacobsen, in *Classical and Quantum Dynamics in Condensed Phase Simulations*, (Editors: B. J. Berne, G. Ciccotti, D. F. Coker), World Scientific, **1998**, 385.

[114] G. Henkelman, B. P. Uberuaga, H. Jónsson, *J. Chem. Phys.* **2000**, *113*, 9901.

[115] G. Henkelman, H. Jónsson, *J. Chem. Phys.* **1999**, *111*, 7010.

[116] P. Atkins, J. de Paula, *Atkins' Physical Chemistry*, 9th Ed., Oxford, New York, **2010**.

[117] G. Henkelman, A. Arnaldsson, H. Jónsson, *J. Chem. Phys.* **2006**, *124*, 044706.

[118] L. Árnadottir, E. M. Stuve, H. Jónsson, *Surf. Sci.* **2012**, *606*, 233.

[119] R. Car, M. Parrinello, *Phys. Rev. Lett.* **1985**, *55*, 2471.

[120] L. Verlet, *Phys. Rev.* **1967**, *159*, 98.

[121] M. P. Allen, D. J. Tildesley, *Computer Simulation of Liquids*, Clarendon, Oxford, **1989**.

[122] W. C. Swope, H. C. Andersen, P. H. Berens, K. R. Wilson, *J. Chem. Phys.* **1982**, *76*, 637.

[123] H. J. C. Berendsen, J. P. M. Postma, W. F. van Gunsteren, A. DiNola, J. R. Haak, *J. Chem. Phys.* **1984**, *81*, 3684.

[124] S. Nosé, *Mol. Phys.* **1984**, *52*, 255.

[125] S. Nosé, *J. Chem. Phys.* **1984**, *81*, 511.

[126] K. Morokuma, *J. Chem. Phys.* **1971**, *55*, 1236.

[127] K. Kitaura, K. Morokuma, *Int. J. Quantum Chem.* **1976**, *10*, 325.

[128] T. Ziegler, A. Rauk, *Theor. Chim. Acta* **1977**, *46*, 1.

[129] G. Binnig, H. Rohrer, *Surf. Sci.* **1983**, *126*, 236.

[130] J. Tersoff, D. R. Hamann, *Phys. Rev. Lett.* **1983**, *50*, 1998.

[131] J. Tersoff, D. R. Hamann, *Phys. Rev. B* **1985**, *31*, 805.

[132] J. Bardeen, *Phys. Rev. Lett.* **1961**, *6*, 57.

[133] S. Baroni, P. Giannozzi, A. Testa, *Phys. Rev. Lett.* **1987**, *58*, 1861.

[134] X. Gonze, *Phys. Rev. A* **1995**, *52*, 1086.

[135] X. Gonze, *Phys. Rev. A* **1995**, *52*, 1096.

[136] NIST Computational Chemistry Comparison and Benchmark Database, NIST Standard Reference Database Number 101, Release 18, October **2016**, Ed. Russell D. Johnson III, http://cccbdb.nist.gov (accessed: 18.07.2017).

[137] F. Siebert, P. Hildebrandt, *Vibrational Spectroscopy in Life Science*, Wiley-VCH, Weinheim, **2008**.

[138] G. Kresse, J. Hafner, *Phys. Rev. B* **1993**, *47*, 558.

[139] G. Kresse, J. Hafner, *Phys. Rev. B* **1994**, *49*, 14251.

[140] G. Kresse, J. Furthmüller, *Phys. Rev. B* **1996**, *54*, 11169.

[141] G. Kresse, J. Furthmüller, *Comput. Mat. Sci.* **1996**, *6*, 15.

[142] D. R. J. Boyd, *J. Chem. Phys.* **1955**, *23*, 922.

[143] J. Pecher, C. Schober, R. Tonner, *Chem. Eur. J.* **2017**, *23*, 5459.

[144] *Random Decimal Fraction Generator*, http://www.random.org/decimal-fractions (accessed: 18.07.2017).

[145] G. te Velde, E. J. Baerends, *Phys. Rev. B* **1991**, *44*, 7788.

[146] BAND 2016, SCM, Theoretical Chemistry, Vrije Universiteit Amsterdam, The Netherlands, http://www.scm.com (accessed: 18.07.2017).

[147] J. Pecher, R. Tonner, *ChemPhysChem* **2017**, *18*, 34.

[148] J. Pecher, G. Mette, M. Dürr, R. Tonner, *ChemPhysChem* **2017**, *18*, 357.

[149] L. Pecher, S. Laref, M. Raupach, R. Tonner, *Angew. Chem. Int. Ed.* **2017**, doi:10.1002/anie.201707428.

[150] L. Pecher, S. Schmidt, R. Tonner, *submitted* **2017**.

[151] C. Riplinger, F. Neese, *J. Chem. Phys.* **2013**, *138*, 034106.

[152] C. Riplinger, B. Sandhoefer, A. Hansen, F. Neese, *J. Chem. Phys.* **2013**, *139*, 134101.

[153] F. Weigend, R. Ahlrichs, *Phys. Chem. Chem. Phys.* **2005**, *7*, 3297.

[154] S.-W. Kim, J.-H. Lee, H.-J. Kim, J.-H. Cho, *Chem. Phys. Lett.* **2013**, *557*, 159.

[155] N. Kuze, N. Kuroki, H. Takeuchi, T. Egawa, S. Konaka, *J. Mol. Struct.* **1993**, *301*, 81.

[156] D. H. Ess, G. O. Jones, K. N. Houk, *Org. Lett.* **2008**, *10*, 1633.

[157] F. Schoenebeck, D. H. Ess, G. O. Jones, K. N. Houk, *J. Am. Chem. Soc.* **2009**, *131*, 8121.

[158] K. Chenoweth, D. Chenoweth, W. A. Goddard III, *Org. Biomol. Chem.* **2009**, *7*, 5255.

[159] F. C. Pigge, *Curr. Org. Chem.* **2016**, *20*, 1902.

List of Abbreviations

AIMD Ab initio molecular dynamics

AO Atomic orbital

BEP Bell-Evans-Polanyi

bond Bonding

CC Coupled Cluster

CI Configuration Interaction

CI-NEB Climbing Image Nudged Elastic Band

cl Classical

COHP Crystal Orbital Hamilton Population

DB Datively bonded

DCD Dewar-Chatt-Duncanson

DFT Density functional theory

disp Dispersion interaction

EDA Energy Decomposition Analysis

elec Electronic

ELI Electron Localization Index

EMC 5-Ethoxymethyl-5-methylcyclooctyne

elstat Electrostatic

ETS Extended Transition State

GGA Generalized Gradient Approximation

GTO Gaussian type orbital

hTST Harmonic transition state theory

int Interaction

IR Infrared

KS Kohn-Sham

LDA Local Density Approximation

LDOS Local density of states

MD Molecular dynamics

MEP Minimum energy path

NBO Natural Bond Orbital

NEB Nudged Elastic Band

NOCV Natural Orbitals for Chemical Valence

orb Orbital

PAW Projector Augmented-Wave

PBC Periodic boundary conditions

pEDA Periodic Energy Decomposition Analysis

PES Potential energy surface

prep Preparation

qq-hTST Quasi-quantum harmonic transition state theory

QTAIM Quantum Theory of Atoms In Molecules

rel Relaxed

SCF Self-consistent field

SD Slater determinant

STO Slater type orbital

STM Scanning Tunneling Microscopy

THF Tetrahydrofuran

TS Transition state

UHV Ultra-high vacuum

XC Exchange-correlation

ZPVE Zero-point vibrational energy

Curriculum Vitae

Danksagung

Mit der Fertigstellung dieser Dissertation geht eine intensive und lehrreiche, gleichzeitig aber auch sehr schöne Zeit zu Ende. Da man so ein Projekt unmöglich alleine erfolgreich abschließen kann, möchte ich mich hier bei den Menschen bedanken, die mir das ermöglicht und mich in den letzten vier Jahren unterstützt haben.

In erster Linie gilt mein Dank meinem Betreuer, Dr. Ralf Tonner. Er hat mir ermöglicht, an einem spannenden Thema zu forschen, für eine sehr angenehme Arbeitsatmosphäre gesorgt und mich auch in schwierigen Zeiten motivieren und unterstützen können. Weiterhin bedanke ich mich bei Prof. Robert Berger für die Übernahme des Zweitgutachtens sowie bei Prof. Michael Gottfried und Prof. Ulrich Koert dafür, dass sie sich die Zeit genommen haben, Teil meiner Prüfungskommission zu sein.

Als Teil des Sonderforschungsbereichs 1083 "Structure and Dynamics of Internal Interfaces" wurde das Projekt von der Deutschen Forschungsgemeinschaft finanziert und auch dafür möchte ich mich bedanken. Die Arbeit im SFB hat auch zu Kooperationen und intensiven Diskussionen mit Personen der Fachbereiche Physik in Marburg und Gießen geführt. Diesbezüglich gilt mein Dank insbesondere Prof. Michael Dürr, Dr. Gerson Mette und Dr. Marcel Reutzel.

Einige Studierende haben in Forschungspraktika Ergebnisse für mich produziert, die mir wichtige Einblicke in Teilgebiete dieser Arbeit ermöglicht haben und zum Teil auch im Auswertungsteil verwendet wurden. Danke dafür an Monika Williams, Eike Dornsiepen, Jan-Niclas Luy, Fabian Pieck, Steffen Giesen, Sebastian Schmidt und Mira Diekmann. Dass zwei Publikationen dieser Arbeit es sogar auf das Frontcover des jeweiligen Journals geschafft haben, habe ich sicher dem großen Talent von Aaron Beller in Sachen 3D-Grafikgestaltung zu verdanken, der für uns die beiden Grafiken angefertigt hat.

Am Fachbereich Chemie in Marburg habe ich mich wirklich wohl gefühlt und das lag vor allem an den Mitgliedern der Arbeitsgruppen Tonner, Berger und Frenking. Besonderer Dank gilt dabei Andreas Stegmüller, Marc Raupach und Fabian Pieck, mit denen ich mir in den letzten Jahren das Büro geteilt habe, Phil Rosenow für die spannenden und unterhaltsamen Diskussionen sowie Anna Hansmann und Diego Andrada dafür, dass es immer etwas zu lachen gab. Weiterhin danke ich Reuti für den immer schnellen und zuverlässigen technischen Support sowie Andrea Tschirch und Annette Hoyer-Holtorf für Unterstützung im Verwaltungsbereich.

In Marburg haben sich außerhalb der Universität viele wertvolle Freundschaften gebildet, die mir seit Beginn dieser Arbeit jeden Tag den nötigen emotionalen Rückhalt geben konnten. Dazu gehörigen erst einmal natürlich die Mitbewohner meiner WG in dieser Zeit, insbesondere Caro und Jacqueline, die immer Zeit für tiefgehende Gespräche hatten. Weiterhin danke ich

Aaron, Clara, Erwin, Eva, Joana, Max, Paul und Tabea, die für mich zu einer zweiten Familie geworden sind, sowie Annika, Bine, Christian, Francisco, Hajo, Ida, Jasmin, Johanna, Jule, Moritz, Roman, Töbi und allen, die ich vergessen habe, für die vielen schönen Momente.

Auch außerhalb Marburgs gibt es viele wichtige Freundschaften, die ich nicht unerwähnt lassen möchte, da sie die letzten Jahre definitiv schöner gemacht haben. Dazu gehören die Jevi-Ritter David, Jonas und Peter in Hamburg, das Organisationsteam von *Friends & Bands*: André, Clara, Debbi, Fabi, Jonas, Robin und Schmitty sowie auf musikalischer Ebene Jan, Markus, Mike und Tim. Weiterhin danke ich allen OBS-Gängern für vier magische Pfingstwochenenden sowie Julia Schacht in Neuseeland für den niemals abbrechenden Kontakt.

Dass ich diese Arbeit im Fach Chemie in englischer Sprache erfolgreich schreiben konnte, habe ich auch zwei Lehrern aus meiner Schulzeit zu verdanken. Robert Korell hat es geschafft, mich in der Oberstufe für Chemie zu begeistern, obwohl ich vorher absolut nicht von dem Fach angetan war, und insbesondere konnte er mir zeigen, wie viel man dabei zu lachen hat. Hätte ich einen anderen Lehrer in der Oberstufe in Chemie gehabt, hätte ich mich mit Sicherheit nicht für das Chemiestudium entschieden und wäre heute nicht an diesem Punkt in meinem Leben angekommen. Maria Hillmann danke ich für ihren Englischunterricht, durch den ich ein intuitives Gefühl für die englische Sprache entwickeln konnte. Insbesondere ihre tolle Auswahl an Büchern und Filmen hat dafür gesorgt, dass man einen eigenen Antrieb entwickelt, solche Werke im englischen Original zu lesen oder anzuschauen. Das erleichtert natürlich jeglichen Umgang mit der englischen Sprache und hat mir für diese Dissertation sehr weitergeholfen.

Zu guter Letzt möchte ich mich bei meiner Familie bedanken, die mich seit jeher unterstützt und akzeptiert. Ich bin froh, dass alle meine vier Großeltern es noch erleben können, dass eines ihrer Enkelkinder eine Doktorarbeit abschließt und wünsche ihnen noch viele weitere gesunde und schöne Jahre. Meinem Bruder Jan danke ich, dass er immer für mich da ist, obwohl wir an zwei ganz unterschiedlichen Orten im Land wohnen. Abschließend möchte ich meinen Eltern danken, die mich großgezogen und einen Großteil meines Lebens unterstützt und gefördert haben. Ihr habt ohne Frage am meisten dazu beigetragen, dass ich das hier erreichen konnte.

A
Appendix

A.1 AIMD Data: EMC/Si(001)

Simulation 1, final state: *OT*

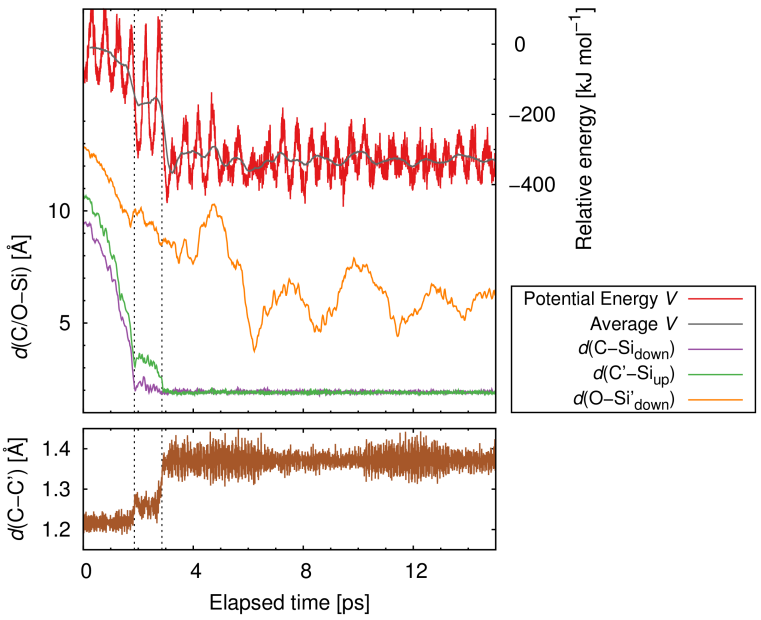

Simulation 2, final state: *OT*

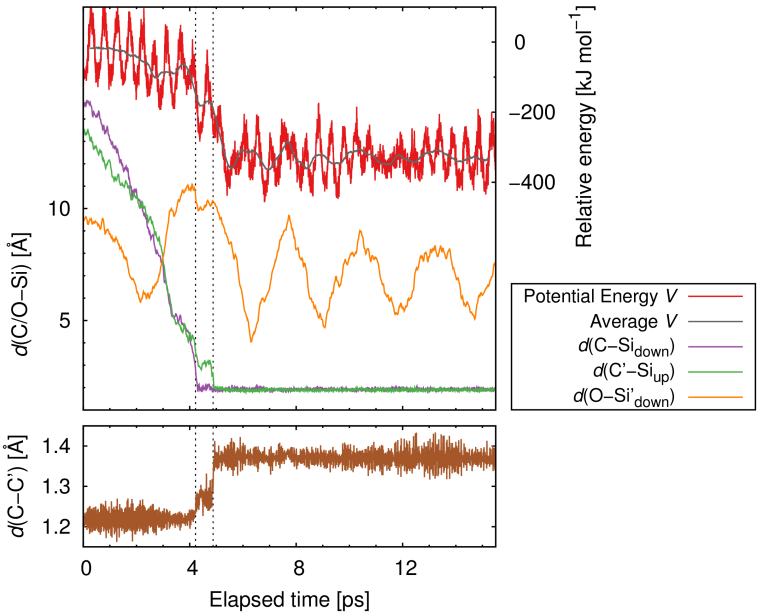

Simulation 3, final state: *OT+DB*

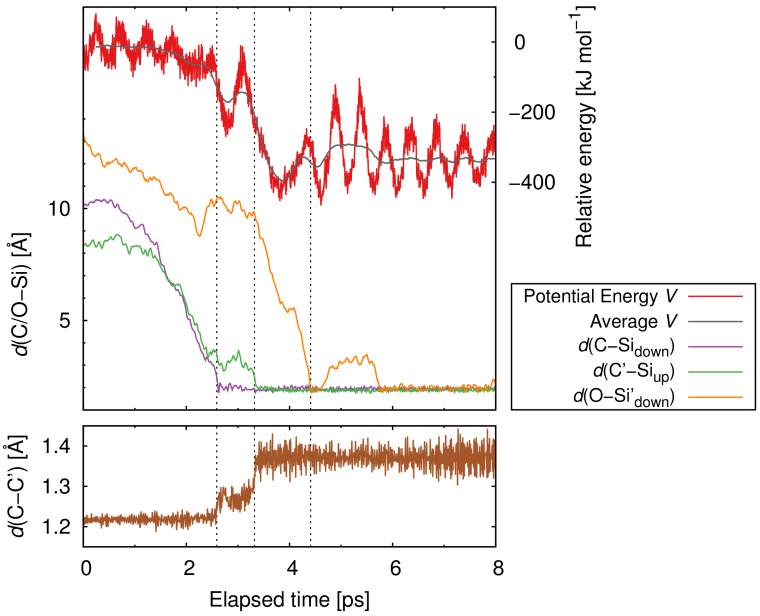

Simulation 4, final state: *B1*

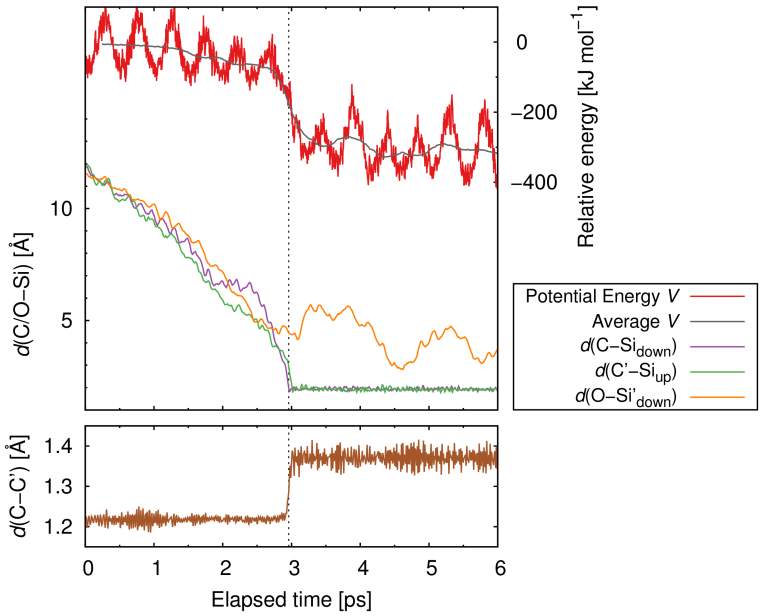

Simulation 5, final state: *B2*

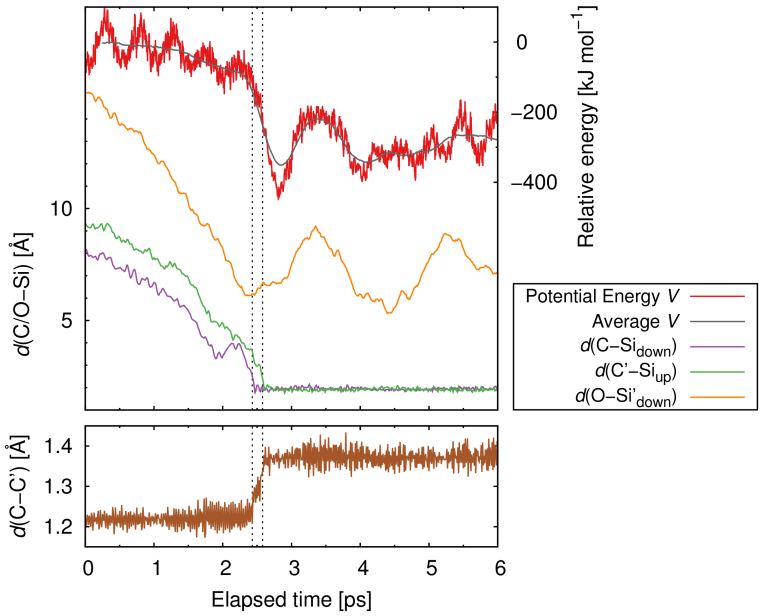

Simulation 6, final state: *OT+DB*

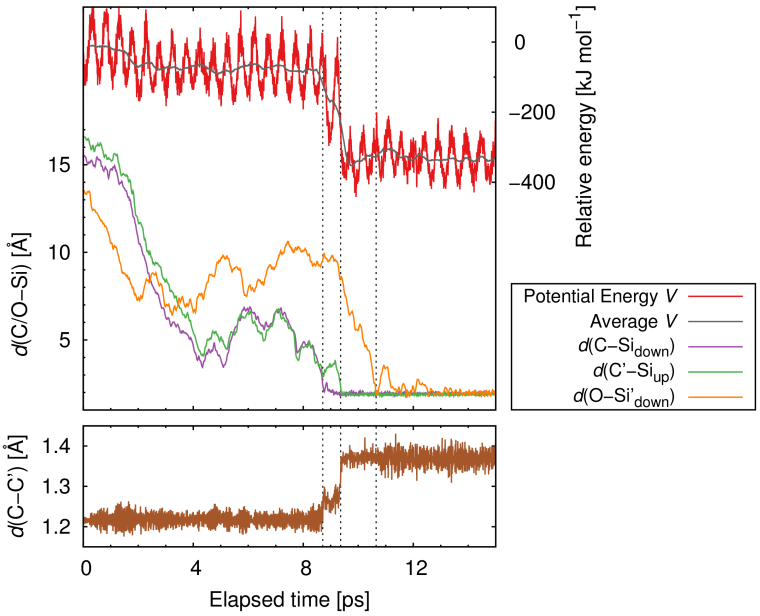

Simulation 7, final state: *PH*

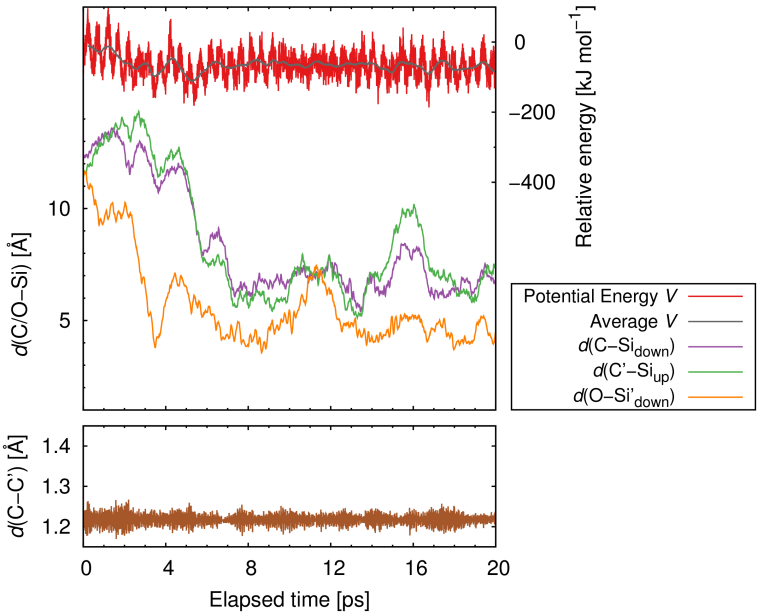

Simulation 8, final state: *OT*

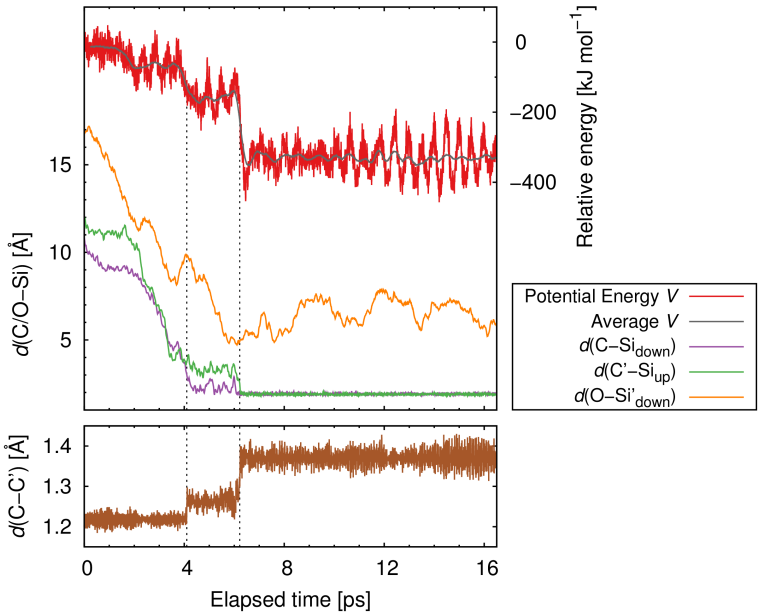

Simulation 9, final state: *OT+DB*

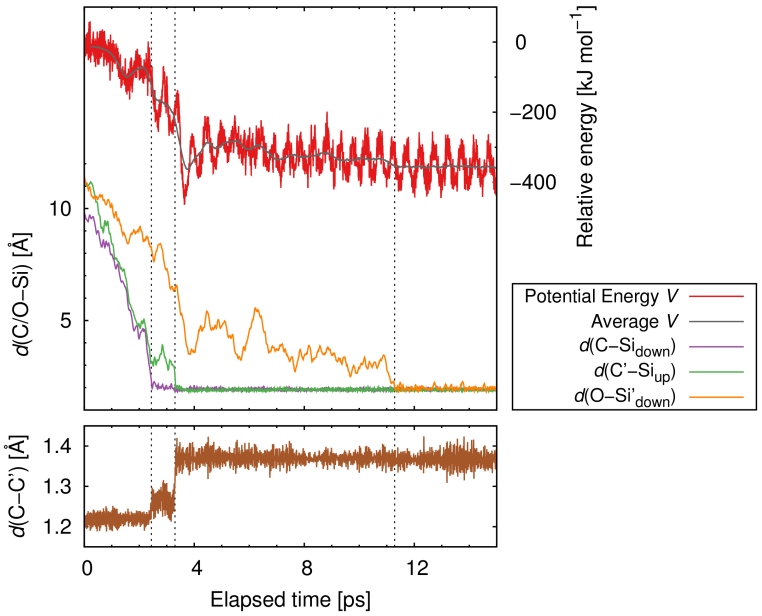

Simulation 10, final state: *OT*

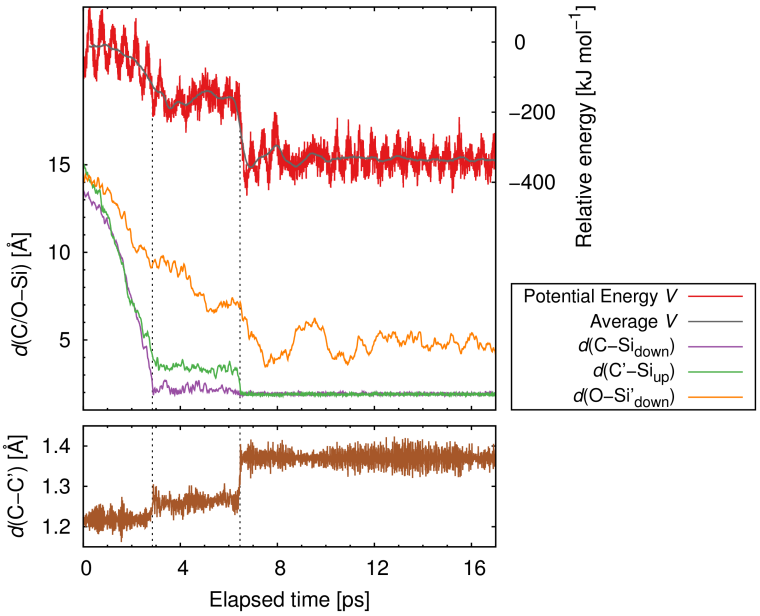

A.2 Cartesian Coordinates And Total Energies: EMC/Si(001)

The cartesian coordinates and corresponding total energies of all structures discussed in Section 3.5 can be found on the attached data medium.

A.3 Manuscripts

All manuscripts by the author that are part of the results and discussion in this thesis (Sections 3.3 and 3.4) are given in the following. Digital versions and the full Supporting Information of each publication can be found on the attached data medium. The published articles (*ChemPhysChem* **2017**, *18*, 34; *ChemPhysChem* **2017**, *18*, 357; *Chem. Eur. J.* **2017**, *23*, 5459) are reproduced with permission – Copyright 2017 Wiley-VCH. Due to a name change in 2017, the author is listed with the former first name Josua in these articles.

ChemPubSoc Europe

DOI: 10.1002/cphc.201601129

CHEMPHYSCHEM Communications

Precursor States of Organic Adsorbates on Semiconductor Surfaces are Chemisorbed and Immobile

Josua Pecher and Ralf Tonner*[a]

Dedicated to Professor Gernot Frenking on the occasion of his 70th birthday

Intermediate states to covalent attachment of molecules on surfaces, so called precursors, are usually considered to be physisorbed and mobile. We show that this view should be reconsidered and provide evidence for a chemisorbed precursor for ethylene on Si(001). The character of the molecule-surface bond as a π complex is determined and quantified using our recently developed method for energy and charge analysis in extended systems. In contrast to previous assumptions, the precursor should thus be immobile, which is underlined by computation of high diffusion energy barriers. This has important implications for understanding and modelling of adsorption kinetics. Our analysis highlights that taking the viewpoint of molecular chemistry helps uncover important aspects in the adsorption process on surfaces. Previous experimental results that appear to be in contrast to our model are examined and reinterpreted.

The mechanism for adsorption of covalently bound molecules on metal surfaces is well-established: attractive van der Waals forces between adsorbate and surface lead, in many cases, to a local energy minimum and conversion to the strongly bound final state occurs after overcoming an energy barrier (Scheme 1).[1] The local minimum, called precursor, sees many molecules mobile before conversion[1b,2] and its existence and the amount of mobility are essential for describing the kinetics of surface adsorption through rate equations.[1d,3] In addition, the change in molecular entropy is markedly different between mobile and immobile precursors, which is a determining factor in the Gibbs energy of adsorbed states.[4] Soon after this adsorption model had been established for metal surfaces, the concept of the mobile precursor was adapted to the adsorption of molecules on semiconductor surfaces as well,[5] assuming that it could be generalized. We show that this view should be reconsidered.

The two bonding regimes of the adsorption potential energy profile derived from the mechanism described above (Scheme 1 a) is usually characterized with the terms physisorption and chemisorption.[1a,6] Indications for physisorption are: weak surface–adsorbate interactions mainly stemming from isotropic dispersion (London) forces, hardly altered adsorbate structure and reversible adsorption. Chemisorption is associated with directional covalent bonding, strong interaction, changes in adsorbate structure up to dissociation and irreversible reactions.

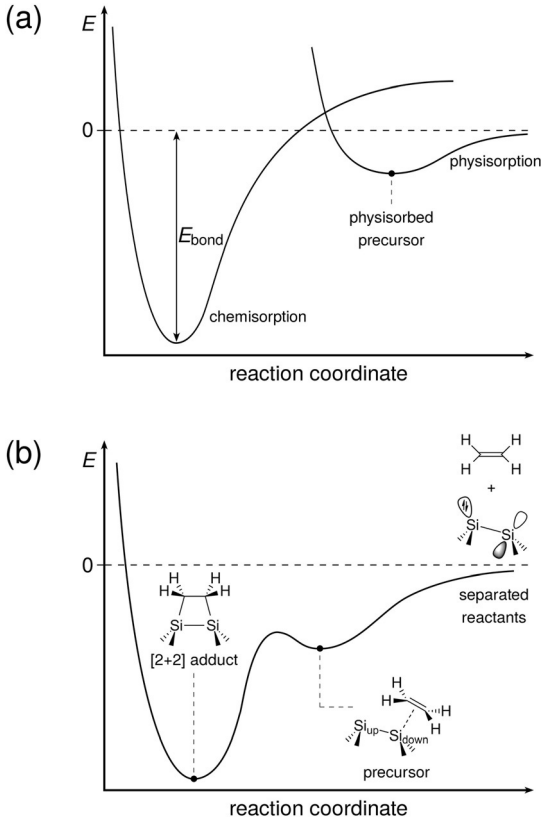

Scheme 1. Potential energy profile for a) surface adsorption model adapted from Ref. [1a] and b) for the adsorption of an organic molecule (ethylene) on a covalent semiconductor (Si(001)) surface.

Although these characteristics are generally agreed upon and approximate theories for chemisorption exist,[7] common descriptors, such as bonding energies and interatomic distances, are no reliable indicators for distinction. For example, the adsorption energy for a physisorbed state of a large organic molecule can well be in the usual range of chemisorption energies.[8] Here, we use a newly developed analytical method[9] that is able to clearly distinguish between the two bonding scenarios.

Silicon is the most thoroughly investigated covalent semiconductor from basic and applied science perspectives. The most interesting surface of this material is Si(001), showing

[a] J. Pecher, Dr. R. Tonner
Faculty of Chemistry and Material Sciences Centre
Philipps-Universität Marburg
Hans-Meerwein-Str. 4, 35032 Marburg (Germany)
E-mail: tonner@chemie.uni-marburg.de

Supporting Information and the ORCID identification number(s) for the author(s) of this article can be found under http://dx.doi.org/10.1002/cphc.201601129.

tilted Si–Si dimers. The electronic structure is well described by an empty p orbital at the Si_{down} atom and a non-bonding electron pair at the Si_{up} atom (Scheme 1 b), underlining the rather localized nature of unsaturated (dangling) bonds[10] in contrast to the delocalized states (bands) observed on metal surfaces. Seemingly in agreement with the general adsorption mechanism sketched in Scheme 1 a, an ethylene molecule approaches the surface via a weakly bound precursor, which, after overcoming an energy barrier, reacts further to the covalently bound final state that can be described as product of a [2+2] cycloaddition (Scheme 1 b). In contrast to common [2+2] cycloadditions, which are thermally forbidden by the Woodward–Hoffmann rules, this reaction is allowed due to the asymmetric approach of the molecule and the aforementioned electronic situation at the surface dimer as confirmed by experiment[5a,11] and theory.[12] We show that in contrast to previous assumptions, the precursor in Scheme 1 b is chemisorbed and thus immobile.

The precursor intermediate (Figure 1) shows a moderately strong bond with a dissociation energy of $E_{bond} = -74\ kJ\,mol^{-1}$, while the Gibbs energy is considerably smaller ($G_{bond} = -22\ kJ\,mol^{-1}$) due to the aforementioned loss of molecular entropy upon adsorption.[13] The bond is thus significantly

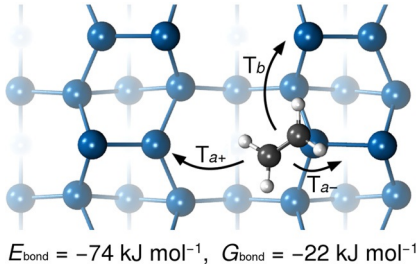

Figure 1. Optimized (PBE-D3) structure of the precursor for ethylene on Si(001). Hindered translations T in (diffusion) directions *a* and *b* parallel to the surface. Bond dissociation energy (E_{bond}) and Gibbs energy (G_{bond}) given with respect to the separated molecule and surface.

weaker compared to the [2+2] adduct ($E_{bond} = -201\ kJ\,mol^{-1}$, previous work: $E_{bond} = -180$ to $-216\ kJ\,mol^{-1}$[12,14]). But does this mean the precursor is physisorbed and mobile like those on metal surfaces? The localized nature of the interaction between the π system of ethylene and an empty p orbital at a Si_{down} atom indicates a significant bond strength and thus low mobility, yet several experiments claim this precursor to be mobile.[5a,11] Main arguments are the non-detection of adsorbed molecules in low temperature scanning tunnelling microscopy (STM) measurements,[11a] an unusually low pre-exponential factor of $10^2\ s^{-1}$ for an Arrhenius-type empirical rate equation of adsorption[11a] and an apparent sticking probability larger than unity at certain hydrogen coverage configurations that could only be explained by a mobile precursor.[11b]

Clarifying the origin of this disagreement and determining the type of molecule–surface interaction would highlight differences between the adsorption dynamics of molecules on metal and semiconductor surfaces, and help to improve understanding of surface adsorption processes in general. We chose to address this question with our recently developed periodic energy decomposition analysis (pEDA).[9,15] Extending the previous methods by Morokuma and Ziegler to systems computationally described with periodic boundary conditions (e.g. surfaces, solids), pEDA enables to quantitatively split up the molecule–surface interaction into Pauli repulsion, dispersion, electrostatics and orbital contributions. A chemisorbed state will show stabilization mainly by orbital interaction, that is, covalent bond formation, while a physisorbed state is dominated by dispersion and electrostatic interactions. The results for ethylene on Si(001) (Table 1) show that for the precursor, orbital interaction ΔE_{orb} makes up the largest contribution (52%) to the stabilizing components of the interaction energy ΔE_{int}. This is close to the value (56%) in the more stable and decisively covalently bound [2+2] adduct, which is uniformly agreed on to be chemisorbed.[5a,11a,b,12a,c,16] Therefore, although the precursor is clearly more weakly bound, it should still be considered chemisorbed, not physisorbed. Even prototype covalent bonds like the C–C bond in ethane show no more than 58% orbital contribution to the stabilizing terms.[15d]

Table 1. Bonding analysis (pEDA) of the molecule-surface interaction in the precursor and [2+2] adduct structures (see Scheme 1 b). All values in $kJ\,mol^{-1}$, calculated with PBE-D3/TZ2P.

	Precursor		[2+2] Adduct	
ΔE_{int}	−113		−605	
ΔE_{Pauli}	707		1278	
ΔE_{disp} [a]	−28	(3%)	−15	(1%)
ΔE_{elstat} [a]	−366	(45%)	−816	(43%)
ΔE_{orb} [a]	−426	(52%)	−1051	(56%)
ΔE_{prep}	31		398	
E_{bond}	−82		−207	
E_{bond}(PAW)[b]	−74		−201	

[a] Percentage values give the relative contribution to the sum of all stabilizing interactions $\Delta E_{disp} + \Delta E_{elstat} + \Delta E_{orb}$. [c] Bond dissociation energies computed with plane wave basis set for comparison.

The nature of this chemical bond already becomes apparent with the periodic equivalent of molecular orbital analysis. Figure 2 b shows the occupied crystal orbital[17] of the precursor with the most pronounced overlap of ethylene's π bond and the empty p orbital at Si_{down}. This is in line with the usual[10,12c,18] schematic representation of this π complex (Figure 2 a). Orbital overlap is a characteristic of chemisorption, whereas physisorption would show no or only weak overlap.[19] This qualitative picture can be quantified by applying the natural orbitals for chemical valence (NOCV) extension to the pEDA.[20] NOCV analysis allows the orbital interaction to be split up into few major contributions. The corresponding charge redistribution between fragments can then be visualized via deformation densities $\Delta\rho_i$. Visual inspection of these enables to distinguish between σ- and π-type bonding interactions.[20a] Furthermore, charge transfer (eigenvalues ν_i) and energy gain (ΔE_i) can be quantified. The most important deformation densities[21] (Figures 2 c–e) mainly show charge transfer from adsor-

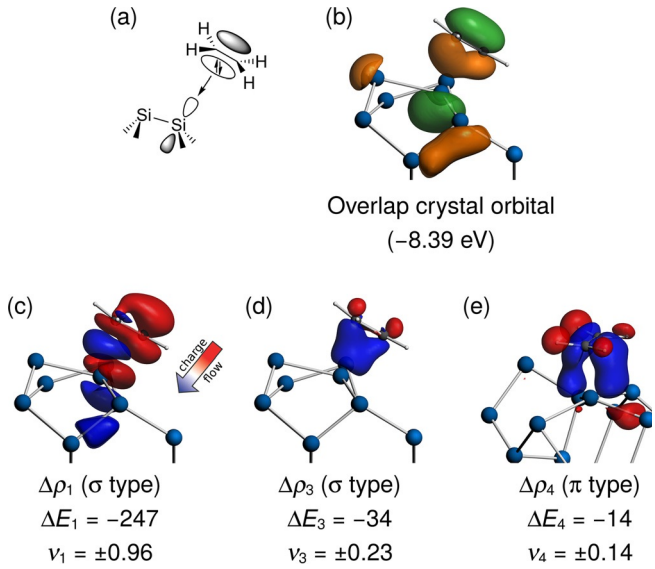

Figure 2. a) Schematic representation of the π complex between ethylene and the formally empty *p* orbital at Si_{down} and b) the corresponding computed crystal orbital. c)–e) Bonding analysis (pEDA) results in deformation densities ($\Delta\rho$) visualizing the charge flow mainly from the molecule (red lobes) to the molecule–surface bonding region (blue lobes). Energy contributions ΔE_i to the total orbital energy ΔE_{orb} are given in kJ mol^{-1}, eigenvalues ν of NOCVs in q_e.

bate orbitals into the bonding region between the molecule and the Si_{down} atom—the typical signature of a donor–acceptor bond.[22] The deformation density with the largest energy gain (Figure 2c) sees the transfer arising from a density at the molecule resembling the π bond (red lobes) into the bonding region between the carbon atoms and Si_{down}, with some additional charge redistribution within the surface (blue lobes). In total, the energy contributions of these deformation densities ($\Delta E_{1,3,4}$) dominate the orbital energy term (69% of ΔE_{orb}). The eigenvalues $\nu_{1,3,4}$, indicators of charge transfer, sum up to 1.33 q_e. The quantitative picture given by NOCV analysis thus fully supports and confirms the usual schematic description of a π complex for the precursor intermediate.

Since such a moderately strong donor–acceptor bond should significantly restrain mobility, we calculated the energy barriers for hindered translation (or diffusion) into symmetry-equivalent precursor structures (see Figure 1 for nomenclature). The results (Table 2) show that both diffusion barriers T_{a+} and T_b are significantly higher than the reaction barrier T_{a-} towards the [2+2] adduct final state. Therefore, the precursor is more likely to react than show any kind of surface mobility. This is underlined by low-temperature vibrational spectroscopy experiments that showed two hindered vibrational modes,[16] which agree very well with our computed harmonic frequencies of the translational motion T_c perpendicular to the surface (Table 2) and a hindered rotation (Supporting Information, Table S1). These modes would not show up if the precursor were mobile.

But how can the experimental observations supporting precursor mobility be explained? The invisibility of the precursor in previous STM measurements[11a] has a seemingly simple explanation: the negative bias voltage applied, $U = -1.5$ V, leads to the probing of occupied states, which are located at the Si_{up} atoms.[10] Since small molecules often lead to dark features on the Si(001) surface by quenching the bright signals from surface atoms,[11a,23] even an immobile precursor should be invisible in this measurement mode as it is located on a Si_{down} atom. To the contrary, it should be visible in positive bias voltage where the picture is known to be dominated by the bright spots of unoccupied states of Si_{down} atoms. This is confirmed in our STM simulations (Figure 3). At negative voltage, the presence of the molecule has virtually no effect on the simulated topography in comparison to a clean dimer row. But at positive voltage, the molecule is apparent by quenching the signal of the surface atom to which it is bound. Consequently, low-temperature STM measurements with positive bias voltage are good candidates to experimentally probe our hypothesis.

Table 2. Calculated energy (E_a) and Gibbs Energy (G_a) barriers and harmonic vibrational frequencies (ν) for hindered translational motions leading to equivalent precursor states (diffusion, T_{a+}, T_b), desorption (T_c) and reaction towards the final state (T_{a-}).[a]

Motion	E_a	G_a	ν_{calc}	ν_{exp}[b]	Character
T_{a+}	36	17	62		Inter-row diffusion
T_{a-}	9[c]	10	62		Reaction to [2+2] adduct
T_b	62	41	114		Intra-row diffusion
T_c	74[c]	22	238	200	Desorption

[a] All energy barriers in kJ mol^{-1} calculated with PBE-D3 (PAW). Vibrational frequencies in cm^{-1}. [b] Ref. [16]; spectral resolution: 16 cm^{-1}. [c] Hybrid functional (HSE06-D3) values: $E_a(T_{a-}) = 11$ kJ mol^{-1}, $E_a(T_c) = 81$ kJ mol^{-1}.

The low pre-exponential factor mentioned in the same publication cannot be explained by the immobile precursor we find here. Yet earlier, the reaction of vinyl bromide with Si(001) was experimentally investigated[18b] and results showed a similar energy barrier and reaction mechanism compared to ethylene and a pre-exponential factor of $1.5 \cdot 10^{13}$ s^{-1}.[11a,c,16,24] This value is comparable to data from desorption experiments[5a,b,25] and the estimates taken for reactions on silicon surfaces in general.[26] It is surprising that the substitution of a hydrogen

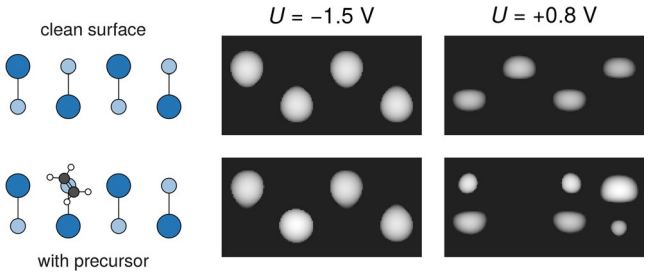

Figure 3. Simulated STM images of a clean row of surface dimers (top) with a row featuring adsorbed ethylene (bottom) for negative (center) and positive (right) bias voltage *U*. The adsorbate does not disturb the zig-zag pattern of bright spots from Si_{up} atoms (dark blue) for negative *U*, which probes occupied states. For positive *U*, probing unoccupied states, the pattern stemming from Si_{down} atoms (light blue) is broken mainly by quenching the signal from the Si atom to which the adsorbate is bound.

by a bromine atom should affect any property by eleven orders of magnitude if other properties (mechanism, barrier) remain similar. However, a pre-exponential factor of $10^{13}\ s^{-1}$ and an energy barrier of about 10 kJ mol^{-1} does not fit the experimental findings in Ref. [11a] that the precursor is stable for several days at 80 K. This discrepancy could indicate that the precursor model is not complete yet and needs to be investigated in the future—it will most probably help in the full understanding of this system.

Finally, the conclusion on mobility from the unusually high sticking coefficient at certain surface defects[11b] can be explained by the fact that those experiments were done at room temperature: Thermally excited ethylene molecules were found to have limited mobility on Si(001) and pass several dimers before reacting.[27] In addition, the impinging molecule will not always wind up directly at a binding site, but can also hit an electron-rich Si_{up} atom, which would result in repulsion due to Coulomb and Pauli repulsion and/or surface dimer flipping. Therefore, a short-ranged mobility can be expected and is not in conflict with our findings.

In conclusion, we have shown that the model of a mobile precursor cannot be generalized from metal to semiconductor surfaces in a way it has been done in the past. Precursors are not necessarily physisorbed, but can also be chemisorbed. The question whether or not a precursor is mobile is determined by the type of interaction between molecule and surface and the chemical reactivity of surface atoms. The fact that several precursors on silicon surfaces have already been observed experimentally[23,28] confirms that for silicon and presumably other semiconductors, too, the local atomic and electronic structure of individual surface atoms becomes crucial. This is well-known in the surface chemistry of semiconductors but has not yet been appreciated in the treatment of adsorption dynamics to the same extent. Our findings for the adsorbate ethylene should also be applicable to all adsorbates with functional groups that are able to form moderately strong donor–acceptor bonds to the surface (e.g. amines, ethers). However, some precursor states might be even stronger chemisorbed: Theoretical studies of acetylene on Si(001)[12c] show that already the precursor shows shared-electron binding to the surface. This does not contradict the experimentally findings,[5b] but instead underlines even more that these states are not necessarily physisorbed and can display a variety of chemical bonding motifs.

In summary, our study shows that the investigation of molecule–surface adsorption can highly benefit from taking a more chemically motivated point of view. Properties and mechanisms that might otherwise be overlooked become apparent and a new view on the interpretation of adsorption dynamics, surface reactivity and the way chemical bonds on surfaces form is opened up.

Computational Methods

All structures and energies were calculated using periodic density functional theory (DFT) with VASP[29] and the PAW formalism[30] (E_{cutoff} 400 eV), the PBE functional[31] and the DFT-D3 dispersion correction[32] applied. Hybrid functional calculations to confirm the PBE results were done using the HSE06 functional.[33] Electronic *k* space was sampled with Γ(241) for 4×2 cells and Γ(221) for 4×4 cells. A frozen double-layer model (6 layers) with vacuum >10 Å and cell sizes of 4×2 and 4×4 was taken for Si(001). Analysis with the pEDA method (PBE-D3/TZ2P, Γ-only) used a development version of ADF-BAND 2014.[9,20b] Gibbs energies ($T=300$ K, $p=1$ bar) and vibrational frequencies were obtained via finite differences in double harmonic approximation, transition-state structures via the climbing-image nudged elastic band method.[34] STM topographies (in Tersoff–Hamann approximation[35]) were obtained with bSKAN.[36] Further details are found in the Supporting Information.

Acknowledgements

This work was supported by Deutsche Forschungsgemeinschaft (DFG) via *SFB 1083 and TO 715/1-1. Computational resources were provided by HRZ Marburg, HLR Stuttgart and CSC-LOEWE Frankfurt. We thank Dr. Marc Raupach (Amsterdam) for support.*

Keywords: bonding analysis · dative bond · mobility · precursor · surface adsorption

[1] a) J. E. Lennard-Jones, *Trans. Faraday Soc.* **1932**, *28*, 333; b) D. A. King, *Crit. Rev. Solid State Mater. Sci.* **1978**, *7*, 167; c) G. Ertl, *Angew. Chem. Int. Ed.* **2008**, *47*, 3524; *Angew. Chem.* **2008**, *120*, 3578; d) M. Bowker, *J. Phys. Condens. Matter* **2010**, *22*, 263002.

[2] a) R. Gomer, *Discuss. Faraday Soc.* **1959**, *28*, 23; b) G. Ehrlich, F. G. Hudda, *J. Chem. Phys.* **1961**, *35*, 1421.

[3] a) E. S. Hood, B. H. Toby, W. H. Weinberg, *Phys. Rev. Lett.* **1985**, *55*, 2437; b) W. H. Weinberg in *Kinetics of Interface Reactions* (Eds.: M. Grunze, H. J. Kreuzer), Springer, Berlin, **1987**; c) D. J. Doren, J. C. Tully, *Langmuir* **1988**, *4*, 256; d) D. J. Doren, J. C. Tully, *J. Chem. Phys.* **1991**, *94*, 8428.

[4] a) C. T. Campbell, J. R. V. Sellers, *J. Am. Chem. Soc.* **2012**, *134*, 18109; b) C. T. Campbell, L. Árnadóttir, J. R. V. Sellers, *Z. Phys. Chem.* **2013**, *227*, 1435; c) J. F. Weaver, *Science* **2013**, *339*, 39; d) J. Gaberle, D. Z. Gao, M. B. Watkins, A. L. Shluger, *J. Phys. Chem. C* **2016**, *120*, 3913.

[5] a) L. Clemen, R. Wallace, P. Taylor, *Surf. Sci.* **1992**, *268*, 205; b) P. A. Taylor, R. M. Wallace, C. C. Cheng, W. H. Weinberg, M. J. Dresser, W. J. Choyke, J. T. Yates, Jr., *J. Am. Chem. Soc.* **1992**, *114*, 6754; c) C. S. Carmer, B. Weiner, M. Frenklach, *J. Chem. Phys.* **1993**, *99*, 1356; d) H. C. Flaum, D. J. D. Sullivan, A. C. Kummel, *J. Phys. Chem.* **1994**, *98*, 1719; e) X. H. Chen, Q. Kong, J. C. Polanyi, D. Rogers, S. So, *Surf. Sci.* **1995**, *340*, 224; f) M. C. Flowers, N. B. Jonathan, A. Morris, S. Wright, *Surf. Sci.* **1996**, *351*, 87.

[6] A. Groß, *Theoretical Surface Science: A Microscopic Perspective*, Springer, Berlin, Heidelberg, **2003**.

[7] a) P. W. Anderson, *Phys. Rev.* **1961**, *124*, 41; b) T. B. Grimley, *Proc. Phys. Soc. London* **1967**, *90*, 751; c) D. M. Newns, *Phys. Rev.* **1969**, *178*, 1123.

[8] R. Tonner, P. Rosenow, P. Jakob, *Phys. Chem. Chem. Phys.* **2016**, *18*, 6316.

[9] M. Raupach, R. Tonner, *J. Chem. Phys.* **2015**, *142*, 194105.

[10] J. Yoshinobu, *Prog. Surf. Sci.* **2004**, *77*, 37.

[11] a) C. H. Chung, W. J. Jung, I. W. Lyo, *Phys. Rev. Lett.* **2006**, *97*, 116102; b) G. Mette, C. H. Schwalb, M. Dürr, U. Höfer, *Chem. Phys. Lett.* **2009**, *483*, 209; c) M. A. Lipponer, N. Armbrust, M. Dürr, U. Höfer, *J. Chem. Phys.* **2012**, *136*, 144703.

[12] a) J.-H. Cho, L. Kleinman, *Phys. Rev. B* **2004**, *69*, 75303; b) X. L. Fan, Y. F. Zhang, W. M. Lau, Z. F. Liu, *Phys. Rev. B* **2005**, *72*, 165305; c) Q. J. Zhang, X. L. Fan, W. M. Lau, Z. F. Liu, *Phys. Rev. B* **2009**, *79*, 195303.

[13] In surface science, adsorption energy E_{ads} is commonly defined with inverse sign convention ($E_{ads}=-E_{bond}$).

[14] a) J. H. Cho, L. Kleinman, C. T. Chan, K. S. Kim, *Phys. Rev. B* **2001**, *63*, 73306; b) R. Miotto, A. C. Ferraz, G. P. Srivastava, *Surf. Sci.* **2002**, *507--510*, 12; c) M. Marsili, N. Witkowski, O. Pulci, O. Pluchery, P. L. Silvestrelli, R. D. Sole, Y. Borensztein, *Phys. Rev. B* **2008**, *77*, 125337; d) S. W. Kim, J. H. Lee, H. J. Kim, J. H. Cho, *Chem. Phys. Lett.* **2013**, *557*, 159.

[15] a) K. Morokuma, *J. Chem. Phys.* **1971**, *55*, 1236; b) T. Ziegler, A. Rauk, *Theor. Chim. Acta* **1977**, *46*, 1; c) F. M. Bickelhaupt, E. J. Baerends, in *Rev. Comput. Chem. Vol. 15* (Eds.: K. B. Lipkowitz, D. B. Boyd), Wiley-VCH, Inc., New York, **2000**, pp. 1; d) M. von Hopffgarten, G. Frenking, *WIREs Comput. Mol. Sci.* **2012**, *2*, 43.

[16] M. Nagao, H. Umeyama, K. Mukai, Y. Yamashita, J. Yoshinobu, *J. Am. Chem. Soc.* **2004**, *126*, 9922.

[17] The crystal orbital and its eigenvalue are given at the Γ point in *k* space.

[18] a) M. A. Filler, S. F. Bent, *Prog. Surf. Sci.* **2003**, *73*, 1; b) M. Nagao, K. Mukai, Y. Yamashita, J. Yoshinobu, *J. Phys. Chem. B* **2004**, *108*, 5703.

[19] H.-J. Freund, *Angew. Chem. Int. Ed. Engl.* **1997**, *36*, 452; *Angew. Chem.* **1997**, *109*, 444.

[20] a) M. P. Mitoraj, A. Michalak, T. Ziegler, *J. Chem. Theory Comput.* **2009**, *5*, 962; b) M. Raupach, *Ph.D. Thesis*, Philipps-Universität Marburg, **2015**.

[21] Deformation density $\Delta\rho_2$, with $\Delta E_2 = -88\ \mathrm{kJ\,mol^{-1}}$, represents back donation from σ(Si–Si) bonds at the surface into the π^* orbital of the molecule.

[22] a) M. Raupach, S. Dehnen, R. Tonner, *J. Comput. Chem.* **2014**, *35*, 1045; b) J.-N. Luy, S. A. Hauser, A. B. Chaplin, R. Tonner, *Organometallics* **2015**, *34*, 5099.

[23] a) M. Z. Hossain, Y. Yamashita, K. Mukai, J. Yoshinobu, *Phys. Rev. B* **2003**, *68*, 235322; b) G. Mette, M. Reutzel, R. Bartholomäus, S. Laref, R. Tonner, M. Dürr, U. Koert, U. Höfer, *ChemPhysChem* **2014**, *15*, 3725.

[24] Q. J. Zhang, J. L. Wang, Z. F. Liu, *J. Phys. Chem. C* **2007**, *111*, 6365.

[25] C. T. Campbell, J. R. V. Sellers, *Chem. Rev.* **2013**, *113*, 4106.

[26] a) L. Pirolli, A. V. Teplyakov, *J. Phys. Chem. B* **2005**, *109*, 8462; b) H. Guo, W. Ji, J. C. Polanyi, J. S. Y. Yang, *ACS Nano* **2008**, *2*, 699; c) K. R. Harikumar, L. Leung, I. R. McNab, J. C. Polanyi, H. Lin, W. A. Hofer, *Nat. Chem.* **2009**, *1*, 716; d) K. R. Harikumar, I. R. McNab, J. C. Polanyi, A. Zabet-Khosousi, C. Panosetti, W. A. Hofer, *Chem. Commun.* **2011**, *47*, 12101; e) M. Ebrahimi, S. Y. Guo, K. Huang, T. Lim, I. R. McNab, Z. Ning, J. C. Polanyi, M. Shapero, J. S. Y. Yang, *J. Phys. Chem. C* **2012**, *116*, 10129; f) X. Huang, R.-Y. Tian, X.-B. Yang, Y.-J. Zhao, *J. Phys. Chem. C* **2014**, *118*, 24603.

[27] a) K. R. Harikumar, J. C. Polanyi, A. Zabet-Khosousi, P. Czekala, H. Lin, W. A. Hofer, *Nat. Chem.* **2011**, *3*, 400; b) S. Y. Guo, S. J. Jenkins, W. Ji, Z. Ning, J. C. Polanyi, M. Sacchi, C. G. Wang, *J. Phys. Chem. Lett.* **2015**, *6*, 4093; c) K. Huang, O. MacLean, S. Y. Guo, I. R. McNab, Z. Ning, C.-G. Wang, W. Ji, J. C. Polanyi, *Surf. Sci.* **2016**, *652*, 312.

[28] a) D. E. Brown, D. J. Moffatt, R. A. Wolkow, *Science* **1998**, *279*, 542; b) B. Borovsky, M. Krueger, E. Ganz, *J. Vac. Sci. Technol. B* **1999**, *17*, 7; c) S. Yagi, N. Shirota, M. Taniguchi, E. Hashimoto, *Surf. Sci.* **2000**, *454*, 157; d) K. Huang, I. R. McNab, J. C. Polanyi, J. Yang, *Angew. Chem. Int. Ed.* **2012**, *51*, 9061; *Angew. Chem.* **2012**, *124*, 9195; e) D. Lock, S. Sakulsermsuk, R. E. Palmer, P. A. Sloan, *J. Phys. Condens. Matter* **2015**, *27*, 054003; f) M. Reutzel, G. Mette, P. Stromberger, U. Koert, M. Dürr, U. Höfer, *J. Phys. Chem. C* **2015**, *119*, 6018.

[29] a) G. Kresse, J. Hafner, *Phys. Rev. B* **1993**, *47*, 558; b) G. Kresse, J. Hafner, *Phys. Rev. B* **1994**, *49*, 14251; c) G. Kresse, J. Furthmüller, *Phys. Rev. B* **1996**, *54*, 11169; d) G. Kresse, J. Furthmüller, *Comput. Mater. Sci.* **1996**, *6*, 15.

[30] a) P. Blöchl, *Phys. Rev. B* **1994**, *50*, 17953; b) G. Kresse, D. Joubert, *Phys. Rev. B* **1999**, *59*, 1758.

[31] a) J. P. Perdew, K. Burke, M. Ernzerhof, *Phys. Rev. Lett.* **1996**, *77*, 3865; b) J. P. Perdew, K. Burke, M. Enzerhof, *Phys. Rev. Lett.* **1997**, *78*, 1396.

[32] a) S. Grimme, J. Antony, S. Ehrlich, S. Krieg, *J. Chem. Phys.* **2010**, *132*, 154104; b) S. Grimme, S. Ehrlich, L. Goerigk, *J. Comput. Chem.* **2011**, *32*, 1456.

[33] a) J. Heyd, G. E. Scuseria, M. Enzerhof, *J. Chem. Phys.* **2003**, *118*, 8207; b) J. Heyd, G. E. Scuseria, *J. Chem. Phys.* **2004**, *121*, 1187; c) J. Heyd, G. E. Scuseria, M. Enzerhof, *J. Chem. Phys.* **2006**, *124*, 219906.

[34] G. Henkelman, B. P. Uberuaga, H. Jónsson, *J. Chem. Phys.* **2000**, *113*, 9901.

[35] a) J. Tersoff, D. R. Hamann, *Phys. Rev. Lett.* **1983**, *50*, 1998; b) J. Tersoff, D. R. Hamann, *Phys. Rev. B* **1985**, *31*, 805.

[36] a) W. A. Hofer, *Prog. Surf. Sci.* **2003**, *71*, 147; b) K. Palotás, W. A. Hofer, *J. Phys. Condens. Matter* **2005**, *17*, 2705.

Manuscript received: October 18, 2016
Accepted Article published: November 7, 2016
Final Article published: November 18, 2016

CHEMPHYSCHEM

Supporting Information

Precursor States of Organic Adsorbates on Semiconductor Surfaces are Chemisorbed and Immobile

Josua Pecher and Ralf Tonner*[a]

cphc_201601129_sm_miscellaneous_information.pdf

Contents

1 Computational Details

All geometries and energies calculated in periodic density functional theory (DFT) using VASP[1] with PAW formalism[2] (plane wave cutoff energy 400 eV), the PBE functional[3] and the DFT-D3 dispersion correction[4] applied. Electronic *k* space was sampled using a Γ-centred Monkhorst-Pack grid, Γ(241) for 4×2 cells and Γ(221) for 4×4 cells. SCF and geometry convergence criteria were chosen as 10^{-6} eV and $5 \cdot 10^{-3}$ eV/Å, respectively. The surface was modelled as a six layer slab with the bottom two layers frozen in their optimized bulk geometries and the bottom layer saturated with hydrogen atoms. A vacuum layer of at least 10 Å in *z* direction was ensured. The cell size in *x* and *y* direction was chosen as 4×4 for structures describing motion along the *b* axis of the cell and 4×2 otherwise. The structures obtained were analysed by pEDA-NOCV calculations as implemented in a development version of ADF-BAND 2014[5] with PBE-D3/TZ2P, with a Γ-only *k* mesh. Closed-shell singlet fragments (precursor) and triplet fragments ([2+2] adduct) were used. Transition state structures were calculated using the climbing-image nudged elastic band method.[6] Gibbs energies were calculated with $T = 300$ K, $p = 1$ bar using the harmonic oscillator, rigid rotor and ideal gas approximations. Vibrational frequencies were derived using finite differences with displacements of 0.01 Å from the equilibrium structure. STM topographies were calculated in the Tersoff-Hamann approximation[7] using bSKAN.[8]

2 Calculation of all hindered motions in the precursor state

In addition to the hindered translation motions discussed in the main body text, we also calculated energy barriers for all hindered rotations in the precursor state as well as coupled motions with both translation and rotation. The definition of the rotation axes can be found in Figure S1. Results for all hindered motion calculations are given in Table S1.

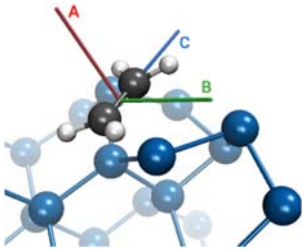

Figure S1. Definition of the rotation axes in the precursor state.

Table S1 Calculated energy (E_a) and Gibbs Energy (G_a) barriers and harmonic vibrational frequencies (ν) for all hindered translations and rotations as well as coupled motions.[a]

	E_a	G_a	ν_{calc}	ν_{exp}[b]	
Rotation					
R_A	3	6	66		Rotation in molecular plane
R_B	–[c]	–[c]	275		Rotation parallel to dimer row
R_C	48	24	589	642	Rotation parallel to dimer bond
Translation					
T_{a+}	36	17	62		Inter-row diffusion
T_{a-}	9	10	62		Reaction to [2+2] adduct
T_b	62	41	114		Intra-row diffusion
T_c	74	22	238	200	Desorption
Coupled motions					
$T_{a-} + R_B$	35	15			Inter-row diffusion + rotation
$T_b + R_A$	17	17			Reaction to *bridge* adduct[d]
$T_b + R_C$	63	41			Intra-row diffusion + rotation

[a] All energy barriers in kJ mol^{-1}, vibrational frequencies in cm^{-1}. Calculated with PBE-D3. Gibbs energies at T = 300 K, p = 1 bar. All rotation and diffusion motions end up in equivalent precursor configurations.
[b] Ref. [9]; spectral resolution: 16 cm^{-1}.
[c] No minimum energy path of R_B without a coupled translation could be found.
[d] See Ref. [10] for a description of the *bridge* adduct state across two surface dimers.

Rotation around the A axis is the only motion with a lower barrier in both E_a (3 kJ mol^{-1}) and G_a (6 kJ mol^{-1}) than the reaction barrier leading to the [2+2] adduct. This can be expected since this rotation axis is equivalent to the bond axis between the molecule's center of mass and the Si_{down} atom it is bound to, so a rotation would hardly diminish orbital overlap and chemical bonding. On the contrary, rotation around the B axis requires the molecule to be so far away from the Si_{down} atom that it becomes energetically more favourable to couple this motion with the hindered translation T_{a-}. No minimum energy path of R_B that would end up on the same surface atom could be found. Rotation around the C axis is able to end up on the same surface atom, but the energy barrier is very high (E_a: 48 kJ mol^{-1}, G_a: 24 kJ mol^{-1}). Furthermore, this motion has a very high computed harmonic frequency of 589 cm^{-1} and since there are no other frequencies in this range, it can clearly be assigned to the experimentally measured hindered motion at 642 cm^{-1}.[9]

Coupled motions have very similar energy barriers to their non-coupled translation counterparts. The only exception is the T_b + R_A motion, but this corresponds to the reaction to another covalently bound cycloadduct, the *bridge* state, in which the molecule is bound to two adjacent surface dimers. This state and the reaction to it have already been extensively described in the literature. [10]

3 Treatment of thermodynamic corrections to the electronic energy

To account for finite temperature and pressure effects in order to determine Gibbs energies, correction terms were applied to electronic energies using the harmonic oscillator, rigid rotor and ideal gas approximations from statistical thermodynamics. This is highly important due to the fact that the bonding energy of adsorbed molecules shifts with temperature[11] and the loss of molecular entropy is a crucial component in this.[12] These effects are completely neglected if only electronic energies are used. We calculated the Gibbs energy G using correction terms for the enthalpy (H_{corr}) and entropy (S) using the following equations:

$$G = E_{el} + H_{corr} + T\,S$$
$$H_{corr} = H_{vib} + H_{rot} + H_{trans}$$
$$S = S_{vib} + S_{rot} + S_{trans}$$

$$H_{\text{vib}} = R \sum_i^{3N} \left(\frac{h\nu_i}{k} \left(\frac{1}{2} + \frac{1}{e^{h\nu_i/kT} - 1} \right) \right)$$

$$H_{\text{rot}} = \frac{3}{2} RT \qquad H_{\text{trans}} = \frac{5}{2} RT$$

$$S_{\text{vib}} = R \sum_i^{3N} \left(\frac{h\nu_i}{kT} \frac{1}{e^{h\nu_i/kT} - 1} - \ln(1 - e^{-h\nu_i/kT} \right)$$

$$S_{\text{rot}} = R \left(\frac{3}{2} + \ln \left(\frac{\sqrt{\pi}}{\sigma} \left(\frac{8\pi^2 kT}{h^2} \right)^{\frac{3}{2}} \sqrt{I_1 I_2 I_3} \right) \right)$$

$$S_{\text{trans}} = R \left(\frac{5}{2} + \ln \left(V \left(\frac{2\pi mkT}{h^2} \right)^{\frac{3}{2}} \right) \right)$$

Here, T denotes the temperature, ν_i the computed vibrational frequencies, V the occupied volume of a single molecule, m the molecular mass, σ the symmetry number, and I_1, I_2 and I_3 the molecule's moments of inertia. These equations follow the harmonic oscillator, rigid rotor and ideal gas approximations for vibration, rotation and translation, respectively. The volume V in S_{trans} can be substituted by kT/p using the ideal gas law if constant pressure instead of constant volume conditions are to be used.

Since many experiments were done at room temperature, we chose a temperature of T = 300 K for our calculations. The choice of the pressure value p used in the calculation of the molecular translational entropy can be based on different arguments: Usually, theoretical Gibbs energies of adsorption are calculated using a Potential of Mean Field with Molecular Dynamics simulations[12] requiring long simulation times and therefore empirical force fields. Due to the lack of a reliable force field for our system and the system size, this approach is not feasible here. Those calculations define the Gibbs energy as a function of the molecule-surface distance, which is constrained during simulation while all other degrees of freedom are being sampled. The in-plane translation is therefore limited by the size of the cell, i.e. the area spanned by the cell vectors a and b and should behave like a one-molecule 2D ideal gas confined to an area of $A = |a| \cdot |b|$. From this we concluded that it is an appropriate approximation to treat the translational motion of the molecule as a one-molecule 3D ideal gas confined to the available volume of the unit cell which

is the total unit cell volume minus the volume occupied by the surface slab. Although this approximation is dependent on the system size, in our case this volume is only one order of magnitude different from the ideal gas value at 1 bar and 300 K which would correspond to the standard condition entropies usually given in experiments on surface adsorption.[13] Additionally, only the reference energy at infinite molecule-surface separation is dependent on this value and not the relative energies between different adsorption modes. So in order to be more consistent with experiment and less dependent on the choice of the cell size, we used a pressure value of 1 bar in all calculations.

Hindered rotation and translation can occur in weakly bound adsorption modes and might be described inaccurately in the harmonic oscillator approximation. Thus, we checked all structures for these motions. If a calculated frequency of a hindered motion was below 50 cm^{-1} or imaginary, we removed it from the vibrational partition function and treated this motion as a free translation or rotation. This was not the case in the precursor minimum, but in several of the calculated transition states. Now one could argue that a transition state with more than one imaginary frequency is not a first-order saddle point. However, in those cases, no nearby transition states where those frequencies would become real could be found, so we attributed these frequency values to the flat and free-molecule like potential energy surface and decided that a treatment as free motions would be appropriate. All transition state barriers with their corresponding imaginary frequencies and motions treated like a free molecule can be found in Table S2.

Table S2 Energy barriers (in kJ mol^{-1}) and transition state imaginary frequencies (in cm^{-1}) for each hindered motion considered. Also given are motions treated like a free molecule in the corresponding transition state partition function with their respective frequency values from the harmonic calculation.

	E_a	ν_{imag} (TS)	Free-molecule like motions (ν_{harm})
Rotation			
R_A	3	41	none
R_B	–	–	–
R_C	48	140	R_B (54*i*), T_b (10*i*)
Translation			
T_{a+}	36	54	R_A (12), T_b (25)
T_{a-}	9	138	none
T_b	62	41	R_A (22), T_a (10*i*)
T_c	74	–	No TS (desorption), free molecule
Coupled motions			
$T_{a-} + R_B$	35	82	R_A (40), T_b (47)
$T_b + R_A$	17	103	none
$T_b + R_C$	63	50	T_a (24)

4 References

[1] a) G. Kresse, J. Hafner, *Phys. Rev. B* **1993**, *47*, 558; b) G. Kresse, J. Hafner, *Phys. Rev. B* **1994**, *49*, 14251; c) G. Kresse, J. Furthmüller, *Phys. Rev. B* **1996**, *54*, 11169; d) G. Kresse, J. Furthmüller, *Comput. Mat. Sci.* **1996**, *6*, 15.

[2] a) P. Blöchl, *Phys. Rev. B* **1994**, *50*, 17953; b) G. Kresse, D. Joubert, *Phys. Rev. B* **1999**, *59*, 1758.

[3] a) J. P. Perdew, K. Burke, M. Ernzerhof, *Phys. Rev. Lett.* **1996**, *77*, 3865; b) J. P. Perdew, K. Burke, M. Enzerhof, *Phys. Rev. Lett.* **1997**, *78*, 1396.

[4] a) S. Grimme, J. Antony, S. Ehrlich, S. Krieg, *J. Chem. Phys.* **2010**, *132*, 154104; b) S. Grimme, S. Ehrlich, L. Goerigk, *J. Comput. Chem.* **2011**, *32*, 1456.

[5] a) M. Raupach, R. Tonner, *J. Chem. Phys.* **2015**, *142*, 194105; b) M. Raupach, *PhD thesis*, Philipps-Universität Marburg, **2015**.

[6] G. Henkelman, B. P. Uberuaga, H. Jónsson, *J. Chem. Phys.* **2000**, *113*, 9901.

[7] a) J. Tersoff, D. R. Hamann, *Phys. Rev. Lett.* **1983**, *50*, 1998; b) J. Tersoff, D. R. Hamann, *Phys. Rev. B* **1985**, *31*, 805.

[8] a) W. A. Hofer, *Prog. Surf. Sci.* **2003**, *71*, 147; b) K. Palotás, W. A. Hofer, *J. Phys. Condens. Mat.* **2005**, *17*, 2705.

[9] M. Nagao, H. Umeyama, K. Mukai, Y. Yamashita, J. Yoshinobu, *J. Am. Chem. Soc.* **2004**, *126*, 9922.

[10] a) J.-H. Cho, L. Kleinman, *Phys. Rev. B* **2004**, *69*, 75303; b) Q. J. Zhang, X. L. Fan, W. M. Lau, Z. F. Liu, *Phys. Rev. B* **2009**, *79*, 195303; c) R. Miotto, A. C. Ferraz, G. P. Srivastava, *Surf. Sci.* **2002**, *507-510*, 12; d) Y. T. Lee, J. S. Lin, *J. Comput. Chem.* **2013**, *34*, 2697.

[11] D. J. Doren, J. C. Tully, *Langmuir* **1988**, *4*, 256.

[12] J. Gaberle, D. Z. Gao, M. B. Watkins, A. L. Shluger, *J. Phys. Chem. C* **2016**, 3913.

[13] C. T. Campbell, J. R. V. Sellers, *Chem. Rev.* **2013**, *113*, 4106.

5 Cartesian coordinates and total energies

Molecule 4x2 cell: E(PBE-D3) = -32.03182160 eV, E(HSE06-D3) = -36.957235 eV

```
  1.00000000000000
    7.6622095108000003    0.0000000000000000    0.0000000000000000
    0.0000000000000000   15.3244190216000007    0.0000000000000000
    0.0000000000000000    0.0000000000000000   21.6720008849999992
  H    C
    4    2
Direct
  0.5128014398984094  0.6030008232869383  0.5537100493081262
  0.2702636435343849  0.6030012769834273  0.5537099076949994
  0.2702624980699749  0.4410843887664743  0.5537096292701257
  0.5128003851030172  0.4410841448243101  0.5537097098003814
  0.3915322557209402  0.5655382986171978  0.5537099063354624
  0.3915316099546608  0.4785468438966936  0.5537097981354203
```

Molecule 4x4 cell: E = -32.03185846 eV

```
  1.00000000000000
   15.3244190216000007    0.0000000000000000    0.0000000000000000
    0.0000000000000000   15.3244190216000007    0.0000000000000000
    0.0000000000000000    0.0000000000000000   21.6720008849999992
```

ChemPubSoc Europe

DOI: 10.1002/cphc.201601134

CHEMPHYSCHEM Articles

Site-Specific Reactivity of Ethylene at Distorted Dangling-Bond Configurations on Si(001)

Josua Pecher,[a] Gerson Mette,[b] Michael Dürr,*[b, c] and Ralf Tonner*[a]

Differences in adsorption and reaction energetics for ethylene on Si(001) are reported with respect to distorted dangling-bond configurations induced by hydrogen precoverage, as obtained by DFT calculations. This can help to understand the influence of surface defects and precoverage on the reactivity of organic molecules on semiconductor surfaces in general. The results show that the reactivity of surface dimers fully enclosed by hydrogen-covered atoms is essentially unchanged compared to the clean surface. This is confirmed by scanning tunneling microscopy measurements. On the contrary, adsorption sites with partially covered surface dimers show a drastic increase in reactivity. This is due to a lowering of the reaction barrier by more than 50% relative to the clean surface, which is in line with previous experiments. Adsorption on dimers enclosed by molecule (ethylene)-covered surface atoms is reported to have a strongly decreased reactivity, as a result of destabilization of the intermediate state due to steric repulsion; this is quantified through periodic energy decomposition analysis. Furthermore, an approach for the calculation of Gibbs energies of adsorption based on statistical thermodynamics considerations is applied to the system. The results show that the loss in molecular entropy leads to a significant destabilization of adsorption states.

1. Introduction

The chemistry of organic molecules on surfaces has been a major topic in materials science research for several years.[1] With respect to the development of new materials and electronic devices, the organic functionalization of Group 14 (aka. Group IV) semiconductor surfaces is of great interest.[2] Within this group, silicon is most interesting due to its widespread use and applications in the electronics industry and a great number of organic molecules reacting on silicon surfaces have already been investigated.[3] The Si(001) surface is especially suited for this because it is known to form dimers[4] that show pronounced chemical reactivity.[5]

Ethylene on Si(001) has already been studied extensively experimentally[6] and theoretically.[7] The reaction mechanism is uniformly agreed upon: Scheme 1 shows the weakly bound π complex, henceforth called precursor, which is the predominant structure at low temperatures and a short-lived intermediate at higher temperatures, and the two possible covalently bound structures to which the precursor can convert: "on-top" on a single dimer and "bridge" between two adjacent dimers. Although both products are accessible in the course of the reaction, calculations[7h,s] have shown the energy barrier from the precursor to the bridge structure to be significantly higher (11–16 kJ mol^{-1}) than that to the on-top structure (2–7 kJ mol^{-1}). In previous scanning tunneling microscopy (STM) measurements by some of the authors, the bridge structure was observed experimentally in addition to the predominant on-top structure.[6r] Although the existence of the bridge structure was then also confirmed by spectroscopic measurements,[6s] many former STM studies did not observe it.[6c,n,q] For

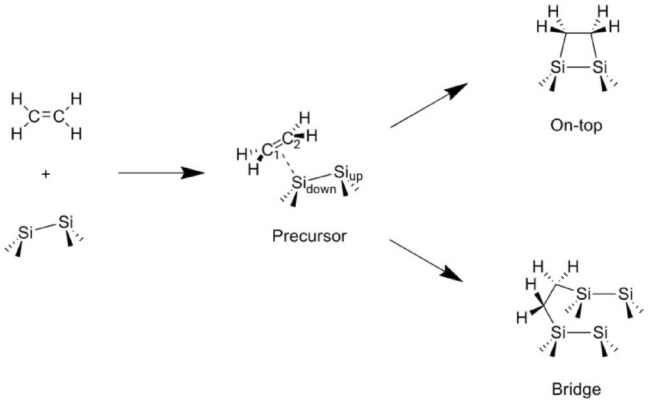

Scheme 1. Reaction pathway of ethylene on the Si(001) surface: adsorption into the π complex (precursor) on a single surface dimer at low temperatures, conversion into either the one- (on-top) or two-dimer (bridge) covalently bound states at elevated temperatures.

[a] J. Pecher, Dr. R. Tonner
Faculty of Chemistry and Material Sciences Centre
Philipps-Universität Marburg, Hans-Meerwein-Str. 4
35032 Marburg (Germany)
E-mail: tonner@chemie.uni-marburg.de

[b] Dr. G. Mette, Prof. Dr. M. Dürr
Faculty of Physics and Material Sciences Centre
Philipps-Universität Marburg, Renthof 5
35032 Marburg (Germany)

[c] Prof. Dr. M. Dürr
Institute of Applied Physics, Justus Liebig University Giessen
Heinrich-Buff-Ring 16, 35392 Giessen (Germany)
E-mail: michael.duerr@ap.physik.uni-giessen.de

Supporting Information and the ORCID identification number(s) for the author(s) of this article can be found under http://dx.doi.org/10.1002/cphc.201601134.

the low-temperature study,[6q] this can be attributed to the aforementioned significant difference in barriers. Furthermore, our experiments also showed increased reactivity towards bridge states in surface areas partially covered with hydrogen.[6r] This result is puzzling and was the driving force for the present study.

All theoretical studies up to now were restricted to the reactivity of ethylene with the clean surface. We now aim to analyze the influence of hydrogen precoverage to explain the increased reactivity observed experimentally. This is important for understanding how defects, impurities, and already adsorbed atoms or molecules affect the dynamics of the adsorption process. In doing so, DFT with semiempirical dispersion correction (DFT-D3) is used. Although the surface could be modeled by either a cluster or a periodic slab, we chose the latter option because it describes the electronic situation of the surface more accurately. The dispersion treatment is needed to correct for the known failure of most density functionals in describing these interactions.[8]

Furthermore, new experimental results for the reactivity of ethylene at isolated dimers (IDs) for high hydrogen and ethylene precoverage are presented and discussed. By using bonding analysis methods, the observed differences between the surface configurations can be easily explained.

Experimental Section

Computational Details

All calculations have been performed with periodic DFT as implemented in the Vienna Ab Initio Simulation Package (VASP),[9] version 5.3.5, by using the projector augmented-wave (PAW) formalism[10] and the exchange-correlation functional by Perdew, Burke, and Enzerhof (PBE).[11] To account for dispersive interactions, the semiempirical DFT-D3 correction by Grimme and co-workers was used.[12] The basis set consisted of plane waves up to a cutoff corresponding to a kinetic energy of 400 eV, whereas electronic k space was sampled by using a gamma-centered Monkhorst–Pack grid, in which a $\Gamma(241)$ grid was used for the 4×2-sized cells and a $\Gamma(221)$ grid for the 4×4 cells. Convergence criteria for the self-consistent field calculations and structural optimizations were chosen as 10^{-5} eV and 10^{-2} eV Å^{-1}, respectively, whereas, for structures to be used in frequency calculations, those values were chosen as 10^{-8} eV and 10^{-3} eV Å^{-1}. The conjugate gradient optimization algorithm[13] was used for structural optimizations. All obtained geometries are given in the Supporting Information.

The clean silicon surface (**Si**) was modeled in a slab approach with a thickness of six layers, in which the atoms in the bottom two layers were frozen to their bulk positions and saturated with hydrogen atoms, which pointed in the direction of the next bulk-layer atoms, at a distance of d(Si–H) = 1.480 Å; the experimental equilibrium Si–H bond length in silane.[14] The unit cell of the $c(4\times2)$ surface reconstruction with buckled dimers (Figure 1, left) was used for the on-top reactions, whereas a (1×2) supercell was used for the bridge reactions. This is equal to a coverage of $\theta = 0.25$ (on-top) and 0.125 (bridge) molecules per surface dimer, respectively. To minimize interactions with periodically repeated images of the slab in the c direction, a vacuum layer of at least 10 Å was ensured. The a and b cell constants were set to 15.324 and 7.662 Å, respectively, as derived from our optimized bulk lattice parameter of $a = 5.418$ Å. Hydrogen-precovered surfaces were obtained by adding hydrogen atoms to the slab structures and subsequent structural optimization. The **Si-ID** surface (Figure 1, center) was chosen to resemble an ID in an environment of hydrogen-saturated dimers, representing high hydrogen precoverage. The **Si-H4** surface (Figure 1, right; see Dürr et al.[15] for nomenclature) was constructed according to the observed features from our previous experiments.[6r] Adsorption energies, E_{ads}, are given as the difference between the energy of the optimized structure for the total system, E_{tot}, and the relaxed and isolated molecule and slab energies, E_{mol} and E_{slab}, respectively [Eq. (1)]:

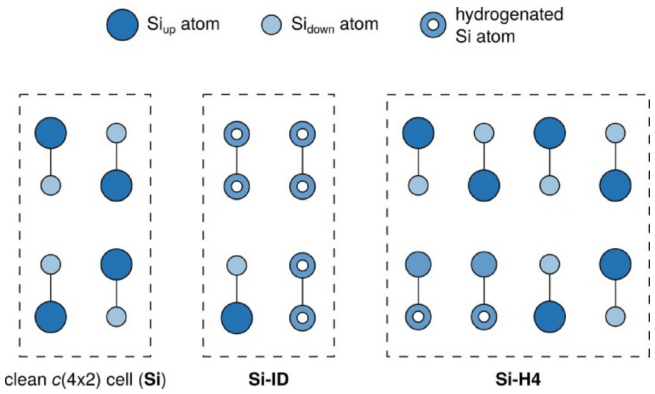

Figure 1. Unit cell of the clean Si(001) surface and the two hydrogen precovered H/Si(001) surfaces, **Si-ID** and **Si-H4**, investigated. Cell boundaries are shown in dashed lines.

$$E_{ads} = E_{tot} - E_{mol} - E_{slab} \quad (1)$$

Reaction pathways and their corresponding energy profiles were calculated by using the climbing-image nudged elastic band (NEB) method[16] in the VTST Tools extension to VASP.[17] All NEB calculations were performed by using the limited-memory Broyden–Fletcher–Goldfarb–Shanno optimization algorithm,[18] the most efficient algorithm for these kinds of calculations.[19] Interpolation in the energy profiles was achieved by using a cubic spline based on forces along the reaction coordinate.

Bonding analysis was performed with the PBE-D3 method, a TZ2P basis set, and sampling electronic k space at the Γ point by using ADF-BAND 2016.[20] A description of the periodic energy decomposition analysis (pEDA) method is found in Ref. [21].

Theoretical Treatment of Finite Temperature and Pressure Effects

Thermodynamic correction terms for enthalpy (H_{corr}) and entropy (S) were applied to the systems by using the well-known equations for the harmonic oscillator, rigid rotor, and ideal gas from statistical thermodynamics. This was necessary because entropy changes play a huge role in adsorption processes of molecules on surfaces[22] and are not described by usual DFT calculations, which only give the electronic energy, E_{el}. Accordingly, the Gibbs energy, G, was calculated for all structures by using Equations (2)–(9):[23]

$$G = E_{el} + H_{corr} + TS \quad (2)$$

$$H_{corr} = H_{vib} + H_{rot} + H_{trans} \quad (3)$$

$$S = S_{vib} + S_{rot} + S_{trans} \quad (4)$$

$$H_{vib} = R\sum_{i}^{3N}\left[\frac{h\nu_i}{k}\left(\frac{1}{2}+\frac{1}{e^{h\nu_i/kT}-1}\right)\right] \quad (5)$$

$$H_{rot} = \frac{3}{2}RT, \quad H_{trans} = \frac{5}{2}RT \quad (6)$$

$$S_{vib} = R\sum_{i}^{3N}\left[\frac{h\nu_i}{kT}\frac{1}{e^{h\nu_i/kT}-1} - \ln\left(1-e^{-h\nu_i/kT}\right)\right] \quad (7)$$

$$S_{rot} = R\left\{\frac{3}{2}+\ln\left[\frac{\sqrt{\pi}}{\sigma}\left(\frac{8\pi^2 kT}{h^2}\right)^{\frac{3}{2}}\sqrt{I_1 I_2 I_3}\right]\right\} \quad (8)$$

$$S_{trans} = R\left\{\frac{5}{2}+\ln\left[V\left(\frac{2\pi mkT}{h^2}\right)^{\frac{3}{2}}\right]\right\} \quad (9)$$

In Equations (2)–(9), T denotes the temperature; ν_i is the computed vibrational frequency; V is the occupied volume of a single molecule; m is the molecular mass; σ is the symmetry number; and I_1, I_2, and I_3 are the molecule's moments of inertia. In the case of constant pressure conditions instead of constant volume, V can be substituted by kT/p, assuming ideal gas behavior.

Harmonic frequencies were calculated from the Hessian matrix, which was constructed by using a finite difference approach with displacements of 0.01 Å from the equilibrium structure. For the isolated molecule, the optimized structure and vibrational frequencies were used from a calculation in a cell sized equally to the respective reaction (4×2 or 4×4). This was done to avoid artificial errors due to the change in basis set size and effects of the periodic boundary conditions.

The temperature was chosen to be $T = 300$ K to be comparable to experiments, which were mostly performed at room temperature. Nonetheless, we show electronic energies side-by-side with Gibbs energies to enable discussion of the temperature dependence of the energy values. Because experiments are usually performed under ultrahigh vacuum conditions, but the local pressure can vary by many orders of magnitude, multiple aspects have to be considered in the choice of a pressure value: state-of-the-art Gibbs energy calculations are often performed by using a potential of mean field (PMF) within molecular dynamics simulations.[24] To obtain reliable values and good sampling of all degrees of freedom, long simulation times are needed, which can only be achieved by using empirical force fields. Since there is currently no reliable force field available for the system described here, this approach cannot be pursued. Assuming the harmonic oscillator and rigid rotor approximations appropriately describe the behavior that is found in PMF calculations, translation was modeled in the following way: PMF calculations define the Gibbs energy as a function of the molecule–surface distance; this property is constrained during simulation. At large distances, translation in the other two directions should ideally behave similar to a one-molecule 2D ideal gas confined to an area, A, spanned by the cell vectors a and b. Consequently, we decided that an appropriate approximation of the translation would be to treat the molecule as a 3D ideal gas confined to the available volume, V_{avail}, of the cell with $V_{avail} = V_{cell} - V_{slab}$. Although this is dependent on the choice of the cell and slab size, the property V is included in a logarithmic expression, so only the order of magnitude should be relevant. In our case, the calculated volume was also very close to the ideal gas value at 1 bar and 300 K, at which standard condition entropies are usually given in surface adsorption experiments.[22b] Neglecting these small errors, we consistently chose $p = 1$ bar to be coherent with experiments.

In flat regions of the potential energy surface, hindered rotation and translation could become relevant and entropy terms might not be described accurately enough anymore in the harmonic oscillator approximation. Therefore, we checked our structures for these motions. Only one hindered rotation and no hindered translation were found to have an energy barrier smaller than the barriers leading to the covalently bound structures. The thermodynamic correction terms of this motion were calculated once by treating it as a harmonic oscillator and once as a free rotor, both limiting cases. The value of the real system should lie between these values. The results (Table S2 in the Supporting Information) showed the overall change to be only 2 kJ mol^{-1}, which was lower than that of other methodological errors, for example, general errors of DFT, so we decided to keep the harmonic oscillator approximation. The same approach was used in a detailed analysis of the precursor structure.[25]

Experimental Methods

The experiments were performed by using a commercial OMICRON VT scanning tunneling microscope in an ultrahigh vacuum chamber with a base pressure below 1×10^{-10} mbar. The n-doped Si(001) samples oriented within 0.25° along the (001) direction were prepared by degassing the sample at 700 K and repeatedly flashing to temperatures above 1450 K by means of direct current heating. Slow cooling to room temperature at rates of about 1 K s^{-1} then resulted in a clean and well-ordered Si(001) 2×1 reconstruction with a minimum of defects.[26] Hydrogen precovered surfaces were prepared by dosing highly purified H_2 gas (99.9999% purity) through a gas inlet system equipped with a liquid nitrogen trap to freeze out residual impurities. Molecular hydrogen was dissociated at a hot tungsten filament (≈2000 K), which was positioned 5 cm from the sample. Typical exposures were 2.5×10^{-6} mbar H_2 gas for 660 s. Ethylene with 99.95% purity was dosed through a second gas inlet system with exposures of 0.15 to 0.65 L of C_2H_4 gas (1 L = 1.33×10^{-6} mbar s). During ethylene exposure, the STM tip was withdrawn from the sample. All experiments were performed at room temperature; ion gauge readings were corrected for relative ionization probabilities.

2. Results and Discussion

2.1. Computational Results

Optimization of the isolated ethylene molecule resulted in structural parameters of $r_{CC} = 1.333$ Å, $r_{CH} = 1.092$ Å, $\alpha_{HCH} = 116.6°$, and $\alpha_{CCH} = 121.7°$, which are in excellent agreement with experimental data[27] (1.339/1.086 Å, 117.2/121.2°) and molecular DFT calculations at the similar PBE/TZVP level[28] (1.334/1.092 Å, 116.5/121.8°). To validate the quality of our frequency calculations, comparison with the literature showed that our values for the isolated molecule are in good agreement with experimental results[29] and PBE/TZVP calculations[28] (Table S1 in the Supporting Information), which give zero-point vibrational energies (ZPVEs) of 10785 (experiment) and 10888 cm^{-1} (theory), whereas our calculations yielded values of 10893 (4×2 cell) and 10889 cm^{-1} (4×4 cell).

Table 1 shows the individual adsorption energies, E_{ads}, and Gibbs energies, G_{ads}, for the precursor, transition state, and final state in all four reactions considered. Figure 2 shows an illustration of the different energy terms discussed for an exam-

Table 1. Electronic and Gibbs energies of bonding of the precursor (E_{prec}), transition state (E_{TS}), and final state (E_{final}) in the four reactions considered. The energies relative to the respective precursor (E^{rel}_{TS}, E^{rel}_{final}) are also given. See Figures 3 and 4 for the corresponding structures.[a]

		E_{prec}	E_{TS}	E_{final}	E^{rel}_{TS}	E^{rel}_{final}
on-top						
E_{ads}	**Si**	−74	−66	−201	9	−127
	Si-ID	−62	−54	−213	8	−151
G_{ads}	**Si**	−22	−12	−141	10	−119
	Si-ID	−13	−3	−156	10	−143
bridge						
E_{ads}	**Si**	−74	−57	−184	17	−110
	Si-H4	−79	−71	−238	8	−159
G_{ads}	**Si**	−22	−5	−117	17	−95
	Si-H4	−26	−19	−175	7	−148

[a] All values in kJ mol^{-1}, calculated by using PBE-D3/PAW. Gibbs energies at $T = 300$ K, $p = 1$ bar.

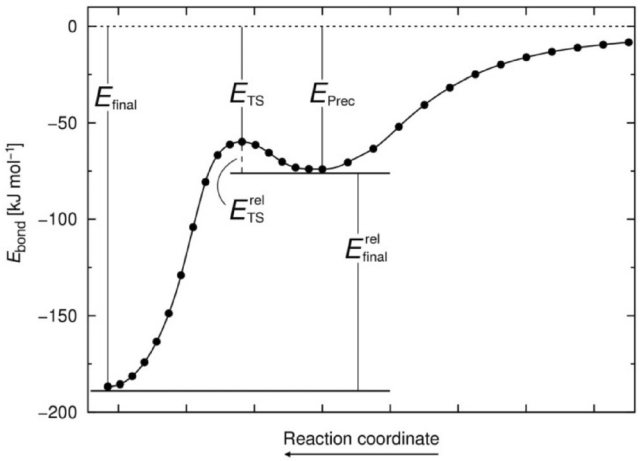

Figure 2. Potential energy curve of the adsorption of ethylene into the bridge structure on clean Si(001), calculated by the NEB method, introducing the energy terms discussed.

ple of a potential energy curve of adsorption, which depicts the actual energy profile for the adsorption into the bridge structure on the clean Si surface, as calculated by the NEB method. The large differences between electronic and Gibbs energies in Table 1 (ca. +45–65 kJ mol^{-1}) can mainly be attributed to the loss of translational and rotational entropy of the molecule due to adsorption on the surface ($\Delta TS_{trans} = -45$ kJ mol^{-1}, $\Delta TS_{rot} = -20$ kJ mol^{-1}, see also Table S3 in the Supporting Information); these are only partially compensated for by the increase in vibrational entropy ($\Delta TS_{vib} = +19$ kJ mol^{-1}). This example shows that using electronic energies can lead to a major overestimation of the adsorption and desorption energies for many surface adsorption reactions.

The nomenclature of the carbon and silicon atoms involved in the reaction, as used in the discussion of interatomic distances in the following section, is depicted in Scheme 1.

2.1.1. Precursor State

The three different precursor geometries are shown in Figures 3 a (**Si**), 3 d (**Si-ID**), and 4 d (**Si-H4**). There are no noticeable differences in the molecular orientation and, in all cases, the C–C bond is not in plane with the Si–Si dimer bond, but significantly rotated (see Figure 5 for a definition of the rotation angle): **Si** and **Si-ID**: 37°; **Si-H4**, 33°. This is in agreement with a previous ab initio molecular dynamics study that showed a maximum of the angular distribution at about 45°.[7w] As our calculated energy profile for the hindered rotation on the clean surface shows (Figure 5), the 0° orientation is actually

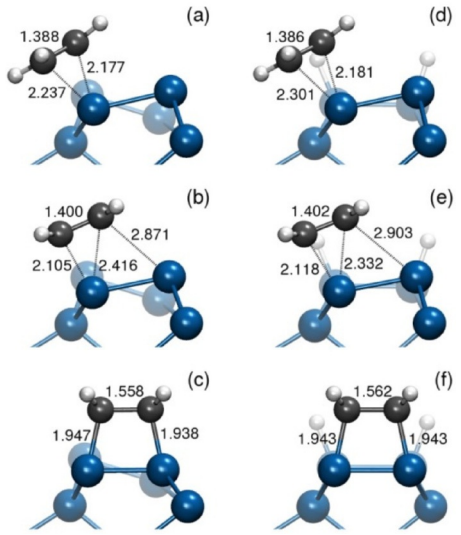

Figure 3. Pathway to the on-top structure: Precursor (a,d), transition-state (b,e), and final-state (c,f) structures for the reaction on the **Si** (a–c) and **Si-ID** (d–f) surfaces. Bond lengths are given in Å. Transition-state imaginary frequencies: 138*i* (b) and 153*i* cm^{-1} (e).

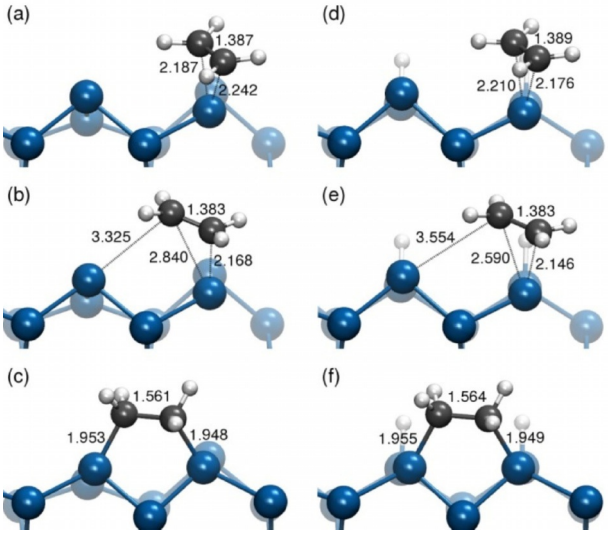

Figure 4. Pathway to the bridge structure: Optimized precursor (a,d), transition-state (b,e), and final-state (c,f) structures for the reaction on the **Si** (a–c) and **Si-H4** (d–f) surfaces. Bond lengths are given in Å. Transition-state imaginary frequencies: 103*i* (b) and 125*i* cm^{-1} (e).

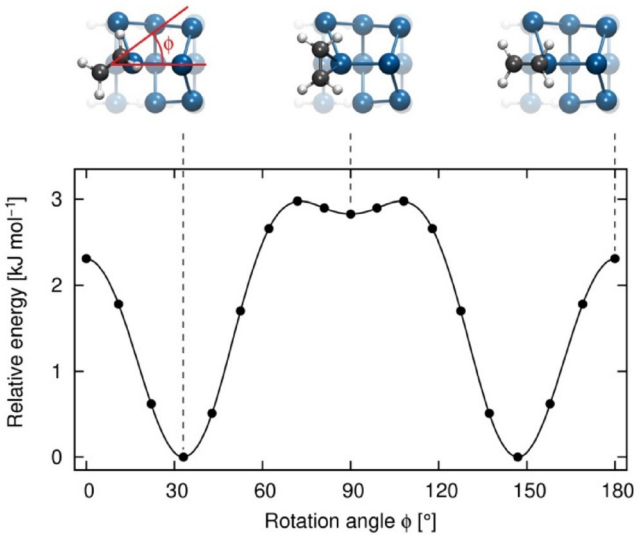

Figure 5. Energy profile of rotation for the precursor on the Si surface, as calculated by the NEB method. The zero point was set to the minimum energy orientation. ϕ denotes the angle between the *y* axis and the C–C bond axis projected onto the *xy* plane.[30]

a first-order saddle point ($\nu_{imag} = 60i\ cm^{-1}$), with a small energy difference of about 2 kJ mol^{-1} to the minimum, whereas the 90° orientation is a very shallow minimum at about 3 kJ mol^{-1}.

A look at the interatomic distances (Figures 3a, 3d, 4a, and 4d) shows that, in all cases, the C–C bond length is elongated from 1.333 Å in the gas phase to 1.386–1.389 Å in the precursor structures, indicating that this bond is already weakened in this state. Although symmetric coordination of the C–C bond to Si_{down} might be expected in the first place, different Si–C bond lengths show that, on **Si-H4**, the C_1 atom is closer to coordinated Si_{down}, compared with C_2, by 0.034 Å, whereas the **Si** and **Si-ID** precursors have the C_2 atom closer by 0.060/0.055 and 0.120 Å, respectively. These values also show that the **Si-ID** precursor is more asymmetrically bound with respect to the carbon atoms; this can be attributed to steric repulsion to the hydrogen atom on the adjacent dimer, which is missing for the other two surface configurations. Precursor bonding energies (Table 1) show a value of −74 kJ mol^{-1} on the clean surface for both reactions. Given that the only difference in those two calculations is the cell size, this implies that the 4×2 cell is large enough to properly describe the bonding situation in this system.

The **Si-H4** precursor is more strongly bound by 4–5 kJ mol^{-1}, whereas the **Si-ID** precursor is weaker by 9–12 kJ mol^{-1}; a trend that is reflected in the average C–Si bond lengths of 2.207/2.215 (**Si**), 2.241 (**Si-ID**), and 2.193 Å (**Si-H4**). Thermodynamic corrections on bonding energies ($G_{ads} - E_{ads}$) of the precursor are very similar for the precovered surface (+49/53 kJ mol^{-1}) and clean **Si** (+52 kJ mol^{-1}). The differences in bonding energies can be easily explained by the following effects of hydrogen precoverage: on the **Si-ID** surface: The molecule is thoroughly surrounded by hydrogen atoms that impose steric repulsion, especially along the dimer rows, where the distances are shorter than between the rows. This repulsion lowers the bond strength in that particular position. The **Si-H4** surface, which does not impose any steric pressure along the row, has a reduced tilting angle on both dimers (see also Figure 4a and d). Since the Si_{down} atom is slightly raised in the precursor on the clean surface (compare the height of the two visible Si_{down} atoms in Figure 4a), the displacement needed is reduced, and thus, the bonding energy gets more negative. These changes in the precursors should, however, have no effect for molecules approaching the surface from the gas phase. Adsorption into the precursor was always found to be direct and without any intermediate steps (see Figure 2 for the calculated adsorption profile on the clean 4×4 **Si** surface), so the initial sticking probability should be independent of the amount of hydrogen coverage.

A more detailed analysis of the precursor structure can be found elsewhere.[25]

2.1.2. Reactivity Towards Covalently Bound States

By comparing the energy barriers from the precursor to final state (E^{rel}_{TS} values in Table 1), it can be seen that, although the **Si-ID** precursor is more weakly bound than the one on the clean surface, the reaction barrier to the on-top structure does not change significantly through precoverage, changing merely from 9 to 8 kJ mol^{-1} (E_{ads}) and staying constant at 10 kJ mol^{-1} in Gibbs energy (G_{ads}). These differences are so small, because the reaction process is mainly dependent on the reacting dimer and surrounding dimers have no or only indirect influence. Since steric repulsion from neighboring hydrogen atoms on the precovered surface should be roughly the same in both precursor and transition-state structures, their relative energies should not change much in comparison to the clean surface; this is exactly what the results show.

In contrast, the barrier toward the bridge structure is drastically lowered through precoverage by more than 50% from 17 to 8 kJ mol^{-1} (E_{ads}) and 17 to 7 kJ mol^{-1} (G_{ads}), respectively. This can be explained similarly to the increased bonding energy of the precursor: during the course of the reaction, both reacting dimers have to distort and lower their tilting angle, which is an energy-consuming process. On the clean surface, this change is rather large (Figure 4a and c), whereas on the precovered surface the two dimers involved are already distorted by the hydrogen atoms attached and there is less displacement needed to reach a horizontal arrangement (Figure 4d and f). These results also match two of our previous experimental observations:[6r] First, the measured ratio of reacted sites on the clean surface, *N*(bridge)/*N*(on-top) of 0.062, is very well reproduced. This ratio can be estimated by assuming thermal equilibrium in the precursor and inserting the difference in Gibbs activation energies, $\Delta G_a = G_a(\text{bridge}) - G_a(\text{on-top})$, into a Boltzmann distribution at $T = 300$ K [Eq. (10)]:

$$N(\text{bridge})/N(\text{on-top}) = \exp(-\Delta G_a/kT) = 0.060 \quad (10)$$

Second, the increased site-selective reactivity towards covalently bound bridge states at the **Si-H4** reactive sites relative to that of unreacted dimers can be explained. Following the

same arguments as those outlined above, one can calculate the ratios of relative coverage for *c*(bridge)/*c*(**Si-H4**) and *c*(on-top)/*c*(**Si-H4**) to be 0.018 and 0.300, respectively, from the Gibbs activation energies. This is in excellent agreement with the experimental values (0.022 and 0.286).[6r]

Reaction energies (E^{rel}_{final}, Table 1) become significantly more negative by precoverage, changing from −127 (**Si**) to −151 kJ mol^{-1} (**Si-ID**) for the on-top reactions (G_{ads}: −119 to −143 kJ mol^{-1}) and −110 (**Si**) to −159 kJ mol^{-1} (**Si-H4**) for the bridge reactions (G_{ads}: −95 to −148 kJ mol^{-1}). This can be understood since full coverage is reached on **Si-ID** and strain in the surface is released when the system ends up on a completely symmetric arrangement. On **Si-H4**, the additional stability stems from the lowered deformation energy of the surface mentioned previously. For bridge adsorption on two clean dimers, both have to distort from their equilibrium geometry to form the bonds to the molecule. When a second molecule approaches this site, the distortion needed for bond formation has already been partially performed, so this destabilizing component vanishes from the reaction energy.

Differences between electronic and Gibbs energies of the final states ($G^{rel}_{final}-E^{rel}_{final}$: 8–15 kJ mol^{-1}) are more pronounced than those for the activation energies ($G^{rel}_{TS}-E^{rel}_{TS}$: 1–2 kJ mol^{-1}). This can mainly be attributed to the change in ZPVEs. While the precursor and transition-state structures feature low-frequency hindered translations and rotations, these motions are converted into fully vibrational modes in the final states with a higher frequency, which raises the ZPVE in the final state.

Structurally, the transition states of the on-top reactions (Figure 3b and e) show that the C–C bond is slightly elongated in both systems, but to the same degree. The value of $d(C_1-Si_{down})$ is also similar, 2.105 (**Si**) and 2.118 Å (**Si-ID**), but, on **Si-ID**, the C_2 atom is still closer to this silicon atom (2.332 Å) compared with the reaction on the clean **Si** surface (2.416 Å). Final-state structures for these reactions (Figure 3c and f) show very similar bond lengths and angles. The slight asymmetry in the C–Si bond lengths on the clean surface can be explained by the asymmetry of the adjacent tilted dimer relative to the completely symmetric hydrogen-saturated dimer on the **Si-ID** reactive site. The average C–Si value on the clean **Si** surface, however, perfectly fits the value for the **Si-ID** surface (1.943 Å).

In the bridge reaction, the transition-state structures (Figure 4b and e) show exactly the same C–C bond length, which is very close to the value in the precursor. This highlights that, in this reaction, the transition state occurs before this bond is further weakened. One distinct difference between the transition-state structures of the clean **Si** surface and the **Si-H4** one is that, in the latter case, it appears way closer to the precursor structure, as seen by comparing the C–Si bond lengths (2.146/2.590 Å) to those in the clean surface reaction (2.168/2.840 Å). In particular, the C_2 atom is much further away from Si_{down} in the latter case. This implies that the maximum energy is reached much earlier along the reaction coordinate, which also coincides with the lowered energy barrier (see Table 1). Final-state structures are again essentially the same, although on **Si-H4** not as symmetric as those on **Si-ID**, since the molecule arranges in a *gauche* conformation for both bridge reactions, which makes the two carbon atoms geometrically inequivalent.

2.1.3. Comparison with Data in the Literature

To estimate the reliability of our calculated values, a comparison to previous experimental and theoretical work is presented. Also, because no previous theoretical calculations investigating the reactivity used dispersion correction, it is of great interest to quantify the influence of this on the reactivity. So, for better comparison, we present our values with and without dispersion correction. Furthermore, all theoretical values are given as electronic energies only. All gathered data are found in Tables 2 (on-top reaction) and 3 (bridge reaction).

The most commonly reported value is E_{ads} of the on-top final state; the theoretical results without dispersion correction range from −180 to −203 kJ mol^{-1}. Our corresponding value of −183 kJ mol^{-1} fits very well to this. The precursor bonding energy has been calculated three times[7h,j,s] to be −45, −47, and −46 kJ mol^{-1}, and again our value of −46 kJ mol^{-1} fits excellently. Because most calculations have been performed in a 2×2 cell, it can be assumed that this cell size is sufficient for both precursor and on-top structural motifs. The study by Cho and co-workers[7h] showed a different precursor for the bridge reaction with the molecular axis oriented perpendicular to the dimer bond and 2 kJ mol^{-1} higher in energy (see Table 3), but as we have already shown in the calculated rotation profile (Figure 5), this second minimum is very shallow and should have a considerably shorter lifetime than the 37° orientation from which the reaction can also take place. Calculated energy barriers to the on-top state vary from 2 to 7 kJ mol^{-1}, which

Table 2. Comparison of our values obtained for the on-top reaction on clean Si(001) with periodic DFT calculations reported in the literature and with experimental results.[a]

Reference	Method (cell size)	E_{prec}	E_{TS}	E_{final}	E^{rel}_{TS}	E^{rel}_{final}
[7e]	PBE (2×2)			−186		
[7f]	PBE (2×2)			−203	5	
[7h]	PBE (2×2)	−45	−43	−187	2	−142
[7j]	PW91 (2×2)	−47	−41	−180	6	−133
[7q]	PW91 (2×2)			−199		
[7s]	PW91 (2×2)	−46	−39	−185	7	−139
[7v]	PBE (4×4)			−192		
[7v]	PBE + vdW-SCS (4×4)			−210		
this study	PBE (4×2)	−46	−39	−183	7	−137
	PBE-D3 (4×2)	−74	−66	−201	9	−127
[6b]	experiment		−12	−159		
[6q]	experiment				12	
[6t]	experiment		−14–19			

[a] All values in kJ mol^{-1}. Computational results list electronic energies, E_{ads}.

Table 3. Comparison of our obtained values for the bridge reaction on clean Si(001) with those reported in the literature.[a]

Reference	Method (cell size)	E_{prec}	E_{TS}	E_{final}	E^{rel}_{TS}	E^{rel}_{final}
[7f]	PBE (2×2)			−188		
[7h]	PBE (2×2)	−43	−32	−176	11	−133
[7q]	PW91 (2×2)			−187		
[7s]	PW91 (2×2)			−173	16	
this study	PBE (4×2)			−173		
	PBE (4×4)	−45	−30	−162	15	−117
	PBE-D3 (4×2)			−193		
	PBE-D3 (4×4)	−74	−57	−184	17	−110

[a] All values in kJ mol^{-1}. Computational results list electronic energies, E_{ads}.

emphasizes that small errors can have a huge influence here and that dispersion correction, although amounting to only 2 kJ mol^{-1} in our calculations, makes a large relative contribution. Differences between the functionals PBE and PW91 are, as expected, only marginal. A comparison between our PBE (without dispersion) values with those reported in the most recent PW91 study[7s] show exactly the same values, aside from a 2 kJ mol^{-1} change in the final-state energy. The study by Kim and co-workers[7v] emphasized the effect of different dispersion correction schemes on the bonding energy in these systems. Since the van der Waals self-consistently screened (vdW-SCS) correction, which is often considered to be superior to semi-empirical DFT-D corrections, yields a similar adsorption energy for the final on-top state compared with our PBE-D3 value (−210 vs. −201 kJ mol^{-1}), it appears that both methods describe this aspect similarly well. The inclusion of dispersion correction can sometimes make a significant difference: in our calculations of the bonding energy of the precursor state, E_{prec}, the value is lowered by almost 30 kJ mol^{-1} from −46 to −74 kJ mol^{-1}, which increases its absolute value by 61 %.

The bridge state and the reactivity towards it (Table 3) are less well documented than the on-top reaction. Bonding energies of the final state vary from −173 to −188 kJ mol^{-1}, whereas our value without dispersion yields only −162 kJ mol^{-1}. This can, however, be explained by the smaller cell size of 2×2 in all literature calculations compared with 4×4 in ours. To verify this assumption, we also performed calculations in a 4×2 cell, which had the same dimensions along the *b* axis of the cell as those reported in the literature, and the resulting value of −173 kJ mol^{-1} fits perfectly well. This emphasizes that a 4×2 or 2×2 cell is too small for this bonding motif and that non-physical interactions with images in neighboring cells become significant and artificially lower the bonding energy by about 10 kJ mol^{-1}. This effect can be expected to occur for any reaction with two dimers along a dimer row because, in a 4×2 or 2×2 cell, these are the only two dimers present in the row in this system.

The reactivity in this system has also been investigated by using finite cluster approaches for the surface.[7g,i,k–m] However, most of these calculations yield a diradical mechanism with a transition-state energy above the reference zero point. Because all experiments[6b,q,t] and periodic calculations report this energy to be negative, the cluster approach is probably not well suited for the questions investigated herein.

By comparing the on-top reaction with experimental results (Table 2), only one value for E_{final} is available: −159 kJ mol^{-1}.[6b] Although our Gibbs energy value of −141 kJ mol^{-1} is smaller, the deviation is in an acceptable range. The experimentally determined energy barrier[6q] fits well to our Gibbs energy value of 10 kJ mol^{-1}, although it should be noted that the Arrhenius analysis in the same study yielded an unusually low prefactor of 300 s^{-1}. The agreement in the transition-state energy, E_{TS}, is very good for the Gibbs energy (Table 1), whereas the absolute value of the electronic energy is far too high. This emphasizes again the importance of thermodynamic corrections to adsorption energies.

To summarize the review of the literature: First, although the 2×2 cell size is appropriate for the description of the on-top state, it is not large enough for the bridge state, since the periodic boundary conditions create a geometric arrangement that artificially lowers the bonding energy. Second, dispersion correction stabilizes the adsorption modes significantly and, since these forces are not described by conventional DFT functionals, they should be included in calculations of organic/semiconductor systems. The reaction barrier is also dependent on dispersion correction and, in combination with thermodynamic corrections, good agreement with the latest experimental values can be reached. In general, a direct comparison between electronic energy differences and experimental values should be taken with care because we have shown that dispersion- and Gibbs-corrected values are in much better agreement with experimental findings.

2.2. Experimental Results

Our calculations nicely confirm the previous experimental results for ethylene adsorption on the clean Si(001) surface and at low hydrogen precoverage.[6r] Herein, we additionally studied the site-selective reactivity of IDs at high hydrogen precoverage by means of STM. The IDs can be prepared by subsequent thermal annealing of a monohydride Si(001) surface. After thermal desorption of a few H_2 molecules and diffusion of atomic hydrogen on the surface,[26] one then yields a monohydride surface with IDs (majority) and isolated dangling bonds (minority), as shown in Figure 6a. Subsequent exposure to ethylene then leads to a distinct reduction in the number of IDs, whereas the number of single dangling bonds remains constant. Please note that the STM tip is removed during the experiment and the evaluation is not performed for the very same surface area, but by statistical analysis of the observed configurations. The decrease in IDs indicates the passivation of the two dangling bonds by adsorbed ethylene molecules. Within experimental error, the expected first-order adsorption kinetics represented by the solid line in Figure 6b reproduces the experimental data.

From the initial slope of the curve, the sticking coefficient of the IDs can be estimated to be close to unity. Thus, the site-specific reactivity of the IDs is very similar to the clean dimers, which is again in agreement with our calculations.

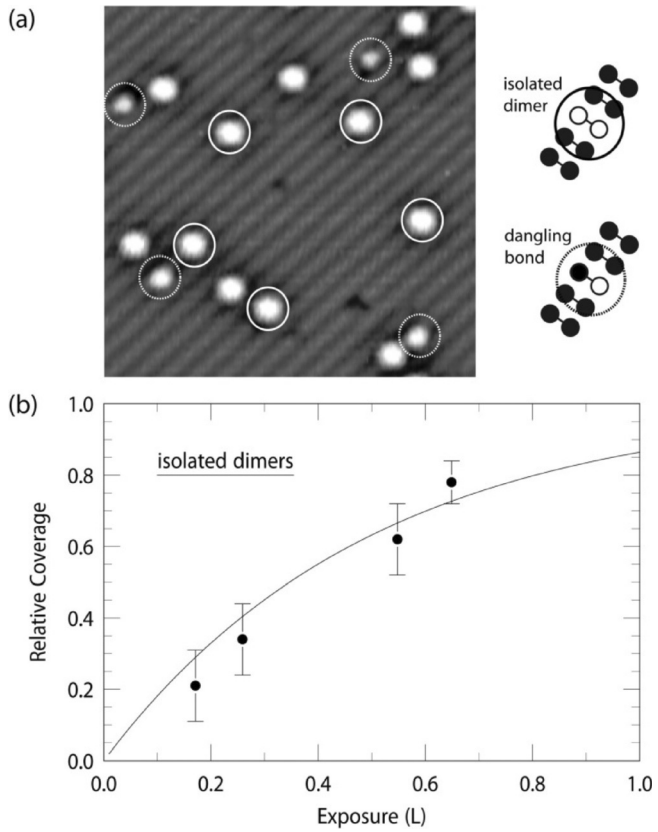

Figure 6. a) STM image (−1.9 V, 0.5 nA, 15×15 nm^2) of a monohydride Si(001) surface after thermal desorption of some hydrogen molecules. Bright configurations symmetric (some labeled by solid circles) and asymmetric (labeled by dashed circles) to the dimer rows are identified as IDs and single dangling bonds, respectively. Subsequent exposure to ethylene leads to a decrease in the number of IDs due to an on-top reaction, whereas the number of single dangling bonds is constant. b) Relative coverage of the IDs with respect to the exposure of ethylene. The solid line shows the relationship for first-order adsorption kinetics.

At this point, we would like to further compare our results with the observation that the reactivity of ethylene on ethylene-precovered Si(001) is strongly reduced at 0.5 monolayer coverage and above, when at least every second dimer is reacted with an ethylene molecule.[6c,t,7u] With respect to the surface electronic configuration, one does not expect a major difference for the dimers being reacted with either two hydrogen atoms or a covalently bonded ethylene molecule. Because neither our calculations nor experiments show a decrease in reactivity for the IDs between hydrogen-saturated dimers, the reduced reactivity on the ethylene-precovered surface is thus unlikely to result from electronic effects and has to be attributed to steric effects by the ethylene molecules on the neighboring dimers. This is confirmed by DFT calculations in a unit cell similar to that of **Si-ID**, but with on-top-bound ethylene molecules instead of hydrogen atoms occupying three of the four dimers (Figure S1 in the Supporting Information). The resulting precursor bonding energies, −52 (E_{prec}) and +2 kJ mol^{-1} (G_{prec}), show that, at room temperature, stabilization due to bond formation is not able to compensate for the loss in molecular entropy anymore and the state becomes thermodynamically unstable. The large difference compared with the **Si** precursor, +22 (E_{prec}) and +24 kJ mol^{-1} (G_{prec}), can be attributed to steric repulsion in two different ways. First, adsorbed molecules present in the same row have to deform to make space for the impinging molecule (Figure S1 in the Supporting Information). Second, even in this deformed structure, Pauli repulsion, as quantified with our recently developed pEDA method, is increased by 30 kJ mol^{-1} relative to that of the clean surface, whereas the orbital interaction is only marginally weakened (+5 kJ mol^{-1}) and a slight stabilization in electrostatics (−13 kJ mol^{-1}) and dispersion (−6 kJ mol^{-1}) is not able to compensate for the increased Pauli repulsion (Table S4 in the Supporting Information).

3. Conclusions

Our calculations and experiments complement each other well by showing that IDs in an environment of hydrogen-covered surface atoms show no significant change in reactivity, whereas the reactive site on the **Si-H4** surface lowers the energy barrier tremendously and enhances the reactivity, in accordance to our previous experiments. Additionally, the calculations showed that the precursor bonding energies shift slightly due to hydrogen precoverage and that reaction energies are enlarged as a result of the complete saturation of adjacent dimers. Gibbs energies of bonding were also presented and showed that, although temperature and pressure effects do not have a large influence on energy barriers and reaction energies, the bonding energies of adsorbed states are changed significantly; this emphasizes that the thermodynamic corrections are most certainly needed to appropriately describe these quantities. In the most pronounced case of a dimer fully enclosed by molecular coverage, the precursor becomes thermodynamically unstable at room temperature. The reason for this difference to the clean surface could clearly be attributed to the Pauli repulsion between the molecules, as our bonding analysis results showed.

Acknowledgements

We thank Prof. U. Höfer for most fruitful discussions. This work was supported by the Deutsche Forschungsgemeinschaft (DFG) within SFB 1083. Computational resources were provided by the Hochschulrechenzentrum Marburg, the HLR Stuttgart, and the LOEWE-CSC Frankfurt.

Keywords: density functional calculations · ethylene · scanning probe microscopy · silicon · surface analysis

[1] Z. Ma, F. Zaera, *Surf. Sci. Rep.* **2006**, *61*, 229.
[2] S. F. Bent, *Surf. Sci.* **2002**, *500*, 879.
[3] T. R. Leftwich, A. W. Teplyakov, *Surf. Sci. Rep.* **2007**, *63*, 1.
[4] R. E. Schlier, H. E. Farnsworth, *J. Chem. Phys.* **1959**, *30*, 917.
[5] J. Yoshinobu, *Prog. Surf. Sci.* **2004**, *77*, 37.
[6] a) J. Yoshinobu, H. Tsuda, M. Onchi, M. Nishijima, *J. Chem. Phys.* **1987**, *87*, 7332; b) L. Clemen, R. M. Wallace, P. A. Taylor, M. J. Dresser, W. J. Choyke, W. H. Weinberg, J. T. Yates, Jr., *Surf. Sci.* **1992**, *268*, 205; c) A. J. Mayne, A. R. Avery, J. Knall, T. S. Jones, G. A. D. Briggs, W. H. Weinberg,

Surf. Sci. **1993**, *284*, 247; d) C. C. Cheng, P. A. Taylor, R. M. Wallace, H. Gutleben, L. Clemen, M. L. Colaianni, P. J. Chen, W. H. Weinberg, W. J. Choyke, J. T. Yates, Jr., *Thin Solid Films* **1993**, *225*, 196; e) C. Huang, W. Widdra, W. H. Weinberg, *Surf. Sci.* **1994**, *315*, L953; f) H. Liu, R. J. Hamers, *J. Am. Chem. Soc.* **1997**, *119*, 7593 – 7594; g) F. Matsui, H. W. Yeom, A. Imanishi, K. Isawa, I. Matsuda, T. Ohta, *Surf. Sci.* **1998**, *401*, L413; h) F. Rochet, F. Jolly, F. Bournel, G. Dufour, F. Sirotti, J. L. Cantin, *Phys. Rev. B* **1998**, *58*, 11029; i) W. Widdra, A. Fink, S. Gokhale, P. Trischberger, D. Menzel, *Phys. Rev. Lett.* **1998**, *80*, 4269 – 4272; j) P. Baumgärtel, R. Lindsay, O. Schaff, T. Gießel, R. Terborg, J. T. Hoeft, M. Polcik, A. M. Bradshaw, M. Carbone, M. N. Piancastelli, R. Zanoni, R. L. Toomes, *New J. Phys.* **1999**, *1*, 20; k) F. Matsui, H. W. Yeom, I. Matsuda, T. Ohta, *Phys. Rev. B* **2000**, *62*, 5036; l) S. H. Xu, M. Keeffe, Y. Yang, C. Chen, M. Yu, G. J. Lapeyre, E. Rotenberg, J. Denlinger, J. T. Yates, Jr., *Phys. Rev. Lett.* **2000**, *84*, 939; m) M. Nagao, Y. Yamashita, S. Machida, K. Hamaguchi, F. Yasui, K. Mukai, J. Yoshinobu, *Surf. Sci.* **2002**, *513*, 413 – 421; n) M. Shimomura, M. Munakata, A. Iwasaki, M. Ikeda, T. Abukawa, K. Sato, T. Kawawa, H. Shimizu, N. Nagashima, S. Kono, *Surf. Sci.* **2002**, *504*, 19; o) M. Nagao, H. Umeyama, K. Mukai, Y. Yamashita, J. Yoshinobu, K. Akagi, S. Tsuneyuki, *J. Am. Chem. Soc.* **2004**, *126*, 9922; p) J. H. Seo, J. Y. Park, C. N. Whang, S. S. Kim, D. S. Choi, K. H. Chae, *Surf. Sci.* **2005**, *582*, L129; q) C. H. Chung, W. J. Jung, I. W. Lyo, *Phys. Rev. Lett.* **2006**, *97*, 116102; r) G. Mette, C. H. Schwalb, M. Dürr, U. Höfer, *Chem. Phys. Lett.* **2009**, *483*, 209; s) K. L. Kostov, R. Nathaniel, T. Mineva, W. Widdra, *J. Chem. Phys.* **2010**, *133*, 54705; t) M. A. Lipponer, N. Armbrust, M. Dürr, U. Höfer, *J. Chem. Phys.* **2012**, *136*, 144703.

[7] a) P. L. Cao, R. H. Zhou, *J. Phys. Condens. Matter* **1993**, *5*, 2887; b) A. J. Fisher, P. E. Blöchl, G. A. D. Briggs, *Surf. Sci.* **1997**, *374*, 298; c) W. Pan, T. Zhu, W. Yang, *J. Chem. Phys.* **1997**, *107*, 3981; d) U. Birkenheuer, U. Gutdeutsch, N. Rösch, A. Fink, S. Gokhale, D. Menzel, P. Trischberger, W. Widdra, *J. Chem. Phys.* **1998**, *108*, 9868; e) J. H. Cho, L. Kleinman, C. T. Chan, K. S. Kim, *Phys. Rev. B* **2001**, *63*, 73306; f) R. Miotto, A. C. Ferraz, G. P. Srivastava, *Surf. Sci.* **2002**, *507--510*, 12; g) X. Lu, *J. Am. Chem. Soc.* **2003**, *125*, 6384 – 6385; h) J. H. Cho, L. Kleinman, *Phys. Rev. B* **2004**, *69*, 75303; i) X. Lu, M. Zhu, *Chem. Phys. Lett.* **2004**, *393*, 124 – 127; j) X. L. Fan, Y. F. Zhang, W. M. Lau, Z. F. Liu, *Phys. Rev. B* **2005**, *72*, 165305; k) H. S. Lee, C. H. Choi, M. S. Gordon, *J. Phys. Chem. B* **2005**, *109*, 5067 – 5072; l) Y. Wang, J. Ma, S. Inagaki, Y. Pei, *J. Phys. Chem. B* **2005**, *109*, 5199 – 5206; m) G. Cantele, F. Trani, D. Ninno, M. Cossi, V. Barone, *J. Phys. Condens. Matter* **2006**, *18*, 2349; n) J. H. Cho, K. S. Kim, Y. Morikawa, *J. Chem. Phys.* **2006**, *124*, 24716; o) G. A. DiLabio, S. A. Dogel, R. A. Wolkow, *Surf. Sci.* **2006**, *600*, L209; p) I. Borriello, G. Cantele, D. Ninno, G. Iadonisi, M. Cossi, V. Barone, *Phys. Rev. B* **2007**, *76*, 35430; q) M. Marsili, N. Witkowski, O. Pulci, O. Pluchery, P. L. Silvestrelli, R. D. Sole, Y. Borensztein, *Phys. Rev. B* **2008**, *77*, 125337; r) M. Marsili, O. Pulci, M. Palummo, P. L. Silvestrelli, R. D. Sole, *Superlattices Microstruct.* **2009**, *46*, 240; s) Q. J. Zhang, X. L. Fan, W. M. Lau, Z. F. Lui, *Phys. Rev. B* **2009**, *79*, 195303; t) G. Fronzoni, G. Balducci, R. D. Francesco, M. Romeo, M. Stener, *J. Phys. Chem. C* **2012**, *116*, 18910; u) R. Coustel, Y. Borensztein, O. Pluchery, N. Witkowski, *Phys. Rev. Lett.* **2013**, *111*, 96103; v) S. W. Kim, J. H. Lee, H. J. Kim, J. H. Cho, *Chem. Phys. Lett.* **2013**, *557*, 159; w) Y. T. Lee, J. S. Lin, *J. Comput. Chem.* **2013**, *34*, 2697.

[8] a) A. Tkatchenko, L. Romaner, O. T. Hoffmann, E. Zojer, C. Ambrosch-Draxl, M. Scheffler, *MRS Bull.* **2010**, *35*, 435; b) S. Grimme, *WIREs Comput. Mol. Sci.* **2011**, *1*, 211.

[9] a) G. Kresse, J. Hafner, *Phys. Rev. B* **1993**, *47*, 558; b) G. Kresse, J. Hafner, *Phys. Rev. B* **1994**, *49*, 14251; c) G. Kresse, J. Furthmüller, *Comput. Mater. Sci.* **1996**, *6*, 15; d) G. Kresse, J. Furthmüller, *Phys. Rev. B* **1996**, *54*, 11169.

[10] a) P. Blöchl, *Phys. Rev. B* **1994**, *50*, 17953; b) G. Kresse, D. Joubert, *Phys. Rev. B* **1999**, *59*, 1758.

[11] a) J. P. Perdew, K. Burke, M. Enzerhof, *Phys. Rev. Lett.* **1996**, *77*, 3865; b) J. P. Perdew, K. Burke, M. Enzerhof, *Phys. Rev. Lett.* **1997**, *78*, 1396.

[12] a) S. Grimme, J. Antony, S. Ehrlich, S. Krieg, *J. Chem. Phys.* **2010**, *132*, 154104; b) S. Grimme, S. Ehrlich, L. Goerigk, *J. Comput. Chem.* **2011**, *32*, 1456.

[13] M. R. Hestenes, E. Stiefel, *J. Res. Natl. Bur. Stand.* **1952**, *49*, 409.

[14] D. R. J. Boyd, *J. Chem. Phys.* **1955**, *23*, 922.

[15] a) M. Dürr, M. B. Raschke, E. Pehlke, U. Höfer, *Phys. Rev. Lett.* **2001**, *86*, 123; b) M. Dürr, U. Höfer, *Surf. Sci. Rep.* **2006**, *61*, 465.

[16] a) H. Jónsson, G. Mills, K. W. Jacobsen in *Classical and Quantum Dynamics in Condensed Phase Simulations* (Eds.: B. J. Berne, G. Ciccotti, D. F. Coker), World Scientific, Singapore, **1998**, 385; b) G. Henkelman, B. P. Uberuaga, H. Jónsson, *J. Chem. Phys.* **2000**, *113*, 9901; c) G. Henkelman, H. Jónsson, *J. Chem. Phys.* **2000**, *113*, 9978.

[17] VTST Tools 3.1, Henkelman group, University of Texas, Austin, TX, USA, http://theory.cm.utexas.edu (accessed: 30.09.2016).

[18] J. Nocedal, *Math. Comput.* **1980**, *35*, 773.

[19] D. Sheppard, R. Terrell, G. Henkelman, *J. Chem. Phys.* **2008**, *128*, 134106.

[20] a) G. te Velde, E. J. Baerends, *Phys. Rev. B* **1991**, *44*, 7888; b) BAND2016, SCM, Theoretical Chemistry, Vrije Universiteit, Amsterdam, The Netherlands, http://www.scm.com (accessed: 30.09.2016).

[21] M. Raupach, R. Tonner, *J. Chem. Phys.* **2015**, *142*, 194105.

[22] a) C. T. Campbell, J. R. V. Sellers, *J. Am. Chem. Soc.* **2012**, *134*, 18109; b) C. T. Campbell, J. R. V. Sellers, *Chem. Rev.* **2013**, *113*, 4106; c) J. F. Weaver, *Science* **2013**, *339*, 39.

[23] F. Jensen, *Introduction to Computational Chemistry*, Wiley, New York, **2006**.

[24] a) D. Alfe, M. J. Gillan, *J. Chem. Phys.* **2007**, *127*, 114709; b) J. Gaberle, D. Z. Gao, M. B. Watkins, A. L. Shluger, *J. Phys. Chem. C* **2016**, *120*, 3913.

[25] J. Pecher, R. Tonner, *ChemPhysChem* **2017**, *18*, 34.

[26] C. H. Schwalb, M. Lawrenz, M. Dürr, U. Höfer, *Phys. Rev. B* **2007**, *75*, 085439.

[27] G. Herzberg, *Electronic Spectra and Electronic Structure of Polyatomic Molecules*, Van Nostrand, New York, **1966**.

[28] Ed. Russell D. Johnson III, NIST Computational Chemistry Comparison and Benchmark Database. NIST Standard Reference Database Number 101 Release 17b, **2015**, http://cccbdb.nist.gov (accessed: 30.09.2016).

[29] D. van Lerberghe, I. J. Wright, J. L. Duncan, *J. Mol. Spectrosc.* **1972**, *42*, 251.

[30] The angle ϕ represents by what amount the molecule, when viewed along the *z* axis, deviates from being parallel to the dimer bonds. Although the angle between the projected C–C and Si–Si bonds might seem more intuitive, the *y* axis is more consistent because the orientation of the Si–Si bond also changes when the molecule is rotating.

Manuscript received: October 28, 2016
Revised: November 28, 2016
Accepted Article published: November 29, 2016
Final Article published: January 16, 2017

CHEMPHYSCHEM

Supporting Information

Site-Specific Reactivity of Ethylene at Distorted Dangling-Bond Configurations on Si(001)

Josua Pecher,[a] Gerson Mette,[b] Michael Dürr,*[b, c] and Ralf Tonner*[a]

cphc_201601134_sm_miscellaneous_information.pdf

Contents

1 Additional Data

Table S1 Calculated harmonic frequencies (in cm^{-1}) of the isolated ethylene molecule in the 4×2 and 4×4 cells in comparison with literature data.

Symmetry	4×2 cell	4×4 cell	Experiment[25]	PBE/TZVP[24]
A_g	1345	1345	1342	1345
	1641	1640	1623	1645
	3081	3079	3026	3078
A_u	1037	1036	1023	1033
B_{1u}	1426	1425	1444	1426
	3068	3066	2989	3064
B_{2g}	936	936	940	932
B_{2u}	807	807	826	810
	3168	3166	3105	3165
B_{3g}	1202	1202	1217	1201
	3138	3137	3086	3137
B_{3u}	941	940	949	939

Table S2 Comparison of the harmonic oscillator and rigid rotor treatments in the clean surface precursor for the low-barrier hindered rotation shown in Figure 4 with respect to thermodynamic corrections. All values calculated at T = 300 K.

	Vibration	Rotation
ν [cm^{-1}]	74	
I [$kg \cdot m^2$]		$3.6 \cdot 10^{-46}$
H^{corr} [kJ mol^{-1}]	2.5	1.3
TS [kJ mol^{-1}]	5.4	6.2

Table S3 Example of the different contributions to the thermodynamic correction terms $H^{corr} - TS$ to the electronic energy yielding the Gibbs energy of bonding G_{ads} at $T = 300$ K, $p = 1$ bar for the ethylene precursor on the clean surface (see Figure 2(a) for the structure). All values in kJ mol^{-1}.

	H^{corr}_{trans}	H^{corr}_{rot}	H^{corr}_{vib}	$-TS_{trans}$	$-TS_{rot}$	$-TS_{vib}$	G^{corr}_{total}
Molecule	6	4	131	–45	–20	–1	75
Slab	0	0	287	0	0	–209	78
Precursor	0	0	432	0	0	–229	203
ΔE_{ads}	–6	–4	14	45	20	–19	49

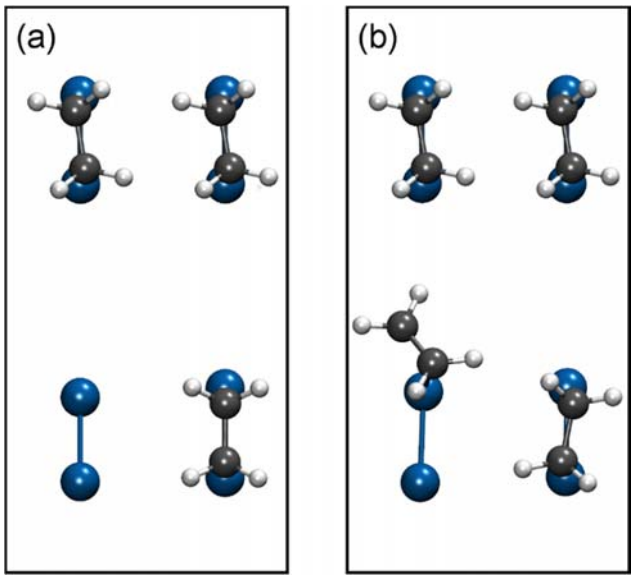

Figure S1 Top view of the silicon surface layer and adsorbed molecules in the molecule-covered surface (**IDmol**) mentioned in section 3.2 of the main article. (a) Optimized reference slab, (b) precursor of an adsorbed ethylene molecule, each in their respective unit cell. It can be seen that the molecule on the adjacent dimer in the same row has to deform.

Table S4 pEDA analysis of the precursor on both the clean **Si** surface and a molecule-covered surface as depicted in Figure S1. A description of the method can be found in Ref. [S1].[a]

	Si surface	**IDmol** surface
ΔE_{int}	–113	–97
ΔE_{Pauli}	707	737
ΔE_{disp}[b]	–28 (3%)	–34 (4%)
ΔE_{elstat}[b]	–366 (45%)	–379 (45%)
ΔE_{orb}[b]	–426 (52%)	–421 (51%)
ΔE_{prep}	34	45
E_{bond} (= $-E_{ads}$)	–79	–52
E_{bond} (PAW)[c]	–74	–52

[a] All values in kJ mol^{-1}, calculated with PBE-D3/TZ2P. Fragmentation: Closed-shell singlet.
[b] Percentage values give the relative contribution to the sum of all stabilizing interactions $\Delta E_{disp} + \Delta E_{elstat} + \Delta E_{orb}$.
[c] Bond dissociation energies computed with plane wave basis set for comparison.

2 References

[S1] M. Raupach, R. Tonner, *J. Chem. Phys.* **2015**, *142*, 194105.

3 Cartesian Coordinates and Total Energies

```
Molecule 4x2 cell: E = -32.03182 eV
  1.00000000000000
    7.6622095108000003    0.0000000000000000    0.0000000000000000
    0.0000000000000000   15.3244190216000007    0.0000000000000000
    0.0000000000000000    0.0000000000000000   21.6720008849999992
  H   C
  4   2
Direct
 0.5128014398984094  0.6030008232869383  0.5537100493081262
 0.2702636435343849  0.6030012769834273  0.5537099076949994
 0.2702624980699749  0.4410843887664743  0.5537096292701257
 0.5128003851030172  0.4410841448243101  0.5537097098003814
 0.3915322557209402  0.5655382986171978  0.5537099063354624
 0.3915316099546608  0.4785468438966936  0.5537097981354203
```

COMMUNICATION

Ethers on Si(001): A prime example for the common ground between surface science and molecular organic chemistry

Lisa Pecher, Slimane Laref,† Marc Raupach and Ralf Tonner*

Abstract: Using computational chemistry, we show that the adsorption of ether molecules on Si(001) under ultra-high vacuum conditions can be understood with textbook organic chemistry. The two-step reaction mechanism of (1) dative bond formation between the ether oxygen and a Lewis acidic surface atom and (2) a nucleophilic attack of a nearby Lewis basic surface atom is analyzed in detail and found to mirror the acid-catalyzed cleavage of ethers in solution. The O-Si dative bond is furthermore found to be the strongest of its kind and reactivity from this state defies the Bell-Evans-Polanyi (BEP) principle by having the lowest energy barrier leading to the product of highest energy. Electron rearrangement during the C-O bond cleavage is visualized using a newly developed bonding analysis method, which verifies that the reaction occurs as a single-step nucleophilic attack. This confirms that the mechanism of nucleophilic substitutions on semiconductor surfaces, which have been occasionally reported in recent years, is identical to molecular chemistry S_N2 reactions. Our findings thus illustrate how the fields of surface science and molecular chemistry can mutually benefit and unexpected insight can be gained.

In the last decades, material science and surface science have become research fields of ongoing importance pushing forward the development of new technologies and electronic devices. More recently, organic molecules began to be utilized, e.g. in the construction of organic light-emitting devices (OLED)[1] or the organic functionalization of semiconductors.[2] Chemical expertise is indispensable in describing bonding and reactivity phenomena in these fields.[3] Especially on semiconductor surfaces, where electronic states are usually more localized compared to delocalized states on metals, the surface often behaves like a molecular reagent and solution chemistry concepts can be very helpful in describing the system.[4]

The understanding and prediction of molecular reactivity has highly benefitted from the use of computational methods analyzing the chemical bond (See e.g. Ref. [5] for an overview). Many of these methods have been successfully transferred and applied to periodic systems, including (but not limited to) the Crystal Overlap Hamilton Population (COHP),[6] the Electron Localization Index (ELI),[7] Energy Decomposition Analysis (EDA),[8] Natural Bond Orbital (NBO) Analysis[9] and the Quantum Theory of Atoms In Molecules (QTAIM).[10] By applying bonding analysis methodology to the prime example of ether molecules on Si(001), we will highlight the ability of molecular organic chemistry to help in understanding surface science.

The Si(001) surface is a widely used substrate due to its relevance for application[11] and its high reactivity arising from both a nucleophilic and electrophilic character of individual surface atoms.[12] Ether molecules were previously found to show an unexpected reactivity on this surface: A surface-induced cleavage of the C-O bond[13] that underlies kinetic control and therefore allows controlled surface functionalization. In molecular chemistry, C-O bond cleavage is known to occur in several ways. One of the most prominent examples (Scheme 1) is ether activation by a strong Lewis acid[14] (e.g. $AX_3 = AlCl_3$) followed by a nucleophilic attack at C_α.[15]

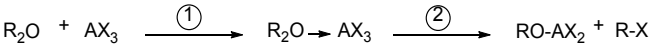

Scheme 1. Ether cleavage via Lewis acid (AX_3) activation and subsequent bond breaking.

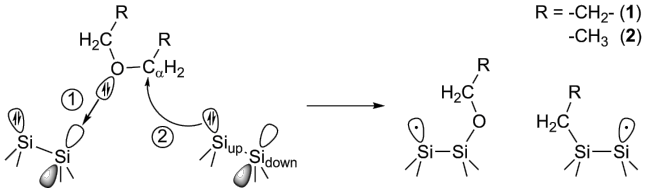

Scheme 2. Two-step reaction of ether molecules with the Si(001) surface: (1) Dative bond formation between the ether oxygen and a Si_{down} surface atom via donation into the empty *p* orbital; (2) Nucleophilic attack of a nearby Si_{up} atom at C_α. Dots indicate unpaired electrons (dangling bonds).

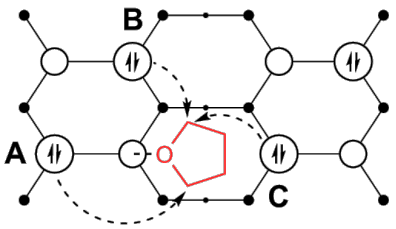

Scheme 3 Nucleophilic Si_{up} atoms **A**, **B** and **C** are close enough to initiate an attack at C_α of adsorbed tetrahydrofuran (**1**) (Scheme 2, step 2). The products will be denoted as A, B and C. Diethylether (**2**) shows the same reactivity.[16]

[a] Lisa Pecher, Dr. Slimane Laref, Dr. Marc Raupach, PD Dr. Ralf Tonner
Faculty of Chemistry and Material Sciences Center
Philipps-Universität Marburg
Hans-Meerwein-Str. 4, 35032 Marburg, Germany
E-mail: tonner@chemie.uni-marburg.de

† Current address: King Abdullah University of Science and Technology (KAUST), Physical Science and Engineering Division (PSE), Thuwal 23955, Saudi Arabia

Supporting information for this article is given via a link at the end of the document.

The well-known surface reconstruction of Si(001) sees the formation of buckled dimers with a localized electronic structure well approximated by an empty *p* orbital at the Lewis acidic Si_{down} dimer atom and a non-bonding electron pair at the Lewis basic and nucleophilic Si_{up} atom (Scheme 2).[12] Therefore, a mechanism analogous to the molecular reaction outlined above suggests itself: In the first step, a datively bonded intermediate (DB) is formed between the oxygen and Si_{down} atoms while in the second step, any nearby nucleophilic Si_{up} atom can attack a C_α atom to form a covalent Si-C bond (Scheme 2). This type of reaction has been reported in recent years for haloalkanes and other types of molecules on semiconductor surfaces[17] and was used to set up hypotheses regarding the surface reactivity of ethers on Si(001).[13a] Regioselectivity is another important aspect, since there are three Si_{up} atoms close enough to initiate the nucleophilic attack (Scheme 3) but only reaction via atom **C** is observed in experiment.[13a] Applying molecular chemistry concepts, one would expect the main product to occur for the reaction which is able to establish a transition state (TS) structure most closely to the trigonal bipyramidal structure of S_N2 reactions in gas phase and solution.[18] We will now apply computational analysis methods to the example of tetrahydrofuran (**1**) on Si(001) to verify that the reaction mechanism is identical to a molecular chemistry S_N2 reaction and furthermore gain a quantitative insight into bonding and reactivity. The findings for **1** are confirmed by equivalent investigations of diethylether (**2**), which rules out ring strain as the determining factor and shows that the results are more general for the compound class of ethers (see Supporting Information).

The bond between the ether oxygen atom and the surface in the DB intermediate (Scheme 2, step 1) can be analyzed using our recently developed periodic EDA (pEDA).[8a] The pEDA allows to decompose the interaction energy ΔE_{int} into dispersion and electronic effects and the latter part additionally into well-defined contributions from Pauli repulsion, electrostatics and orbital interaction.[19] The results (Table 1) show that electronic effects make up the majority (67%) of the interaction energy, underlining that this structure can be understood as being chemisorbed.[8b] Furthermore, electrostatic interaction dominates the attractive terms of the electronic interaction energy at 55% (orbital interaction: 45%). Such an outweighing of electrostatics in covalently bound systems has been shown to be a typical feature of a dative bond.[20] The orbital term can further be decomposed using the Natural Orbitals for Chemical Valence (NOCV) scheme[21] and the charge redistribution of the individual contributions visualized as deformation densities $\Delta\rho_i$. Visual inspection then allows to distinguish between different types of chemical bonding (e.g. σ/π, donation/back donation). The largest contribution for this system (Figure 1a) mainly shows charge flow from a *p* orbital shaped electron density at the oxygen atom (red lobes) into the bonding region between the O and Si_{down} atoms (blue lobes),[22] another typical feature of a dative bond.[8b,23]

Table 1. Bonding analysis (pEDA) of the molecule-surface interaction between THF and Si(001) for the dative bond (DB) intermediate and the transition state (TS) of the reaction from the DB intermediate to product C (see also Schemes 2 and 3).[a]

	DB intermediate (1)		TS(DB→C) (2)	
ΔE_{int}	–156		–235	
ΔE_{int}(disp)[b]	–51	(33%)	–52	(22%)
ΔE_{int}(elec)[b]	–105	(67%)	–183	(78%)
ΔE_{Pauli}	656		979	
ΔE_{elstat}[c]	–417	(55%)	–600	(52%)
ΔE_{orb}[c]	–344	(45%)	–562	(48%)
ΔE_{orb}(dative)[d]	–293	(85%)	–397	(71%)
ΔE_{orb}(S_N)[d]	0		–111	(20%)
ΔE_{prep}	22		157	
E_{bond}[e]	–134	(–132)	–78	(–79)

[a] All values in kJ mol^{-1}, calculated using PBE-D3/TZ2P. Fragments used are molecule and surface. Ground state (1) and transition state (TS) (2) structure analyzed. [b] Percentage values: Relative contributions of dispersion and electronic effects to the interaction energy ΔE_{int}. [c] Percentage values: Relative contributions between the attractive pEDA terms ΔE_{elstat} and ΔE_{orb}. [d] Percentage values: Relative contributions to the orbital interaction ΔE_{orb}. [e] Energies computed using a plane wave basis set given in parentheses.

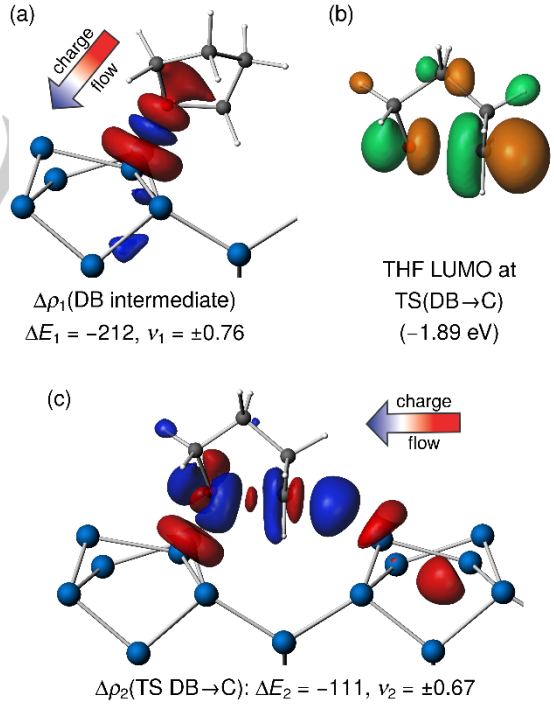

Figure 1. a) Bonding analysis (pEDA) deformation density $\Delta\rho_1$ at the DB structure of THF (step 1) showing electron density transfer mainly from a *p* orbital shaped density at the molecule (red lobes) to the O-Si bonding region (blue lobes). b) LUMO of the THF molecule in the TS(DB→C) geometry. c) pEDA deformation density $\Delta\rho_2$ at the TS(DB→C) geometry (step 2) showing mainly how a σ^*(C-O) type density (blue lobes) is populated by electrons from the opposing surface dimer row (red lobes). Energies ΔE_i in kJ mol^{-1}, eigenvalues ν_i in q_e.

Adding further minor contributions of dative bond character, the total stabilization due to dative bond formation can be determined as –293 kJ mol^{-1}, 85% of the orbital term ΔE_{orb}.[24] Hence, this structure undoubtedly represents a dative bond with σ and π donation of the non-bonding electron pairs at O toward the surface. This explains the high bonding energy E_{bond} of –134 kJ mol^{-1}, which is the strongest known oxygen dative bond on the Si(001) surface.[25]

To address the regioselectivity in step 2, reaction energies E_{react} and activation energies E_a were calculated for all three possible products (Table 2). While reaction via atom **A** results in the most stable product (E_{react} = –177 kJ mol^{-1}), the corresponding energy barrier (E_a) is actually the highest at 107 kJ mol^{-1}.[26] This is because **A** is located on the same dimer the molecule is bound to and thereby too close to attack the C_α from the back side. As a consequence, the attack has to occur from the side of the C-O bond, which is reflected in an acute angle α^{TS}(O-C-Si) of 65.6° and large bond lengths of d^{TS}(C-O) = 2.289 Å and d^{TS}(C-Si) = 3.374 Å at the TS geometry (Gas phase: d(C-O) = 1.441 Å, DB structure: 1.490 Å) In contrast to this, reactions via atoms **B** and **C** can occur from the back side. In case of **B** though, E_a is only marginally lower at 100 kJ mol^{-1}, which is again due to a far from ideal TS geometry with an angle of 117.2° and a high C-O bond length of 2.121 Å. In the attack of **C**, however, α^{TS} is much closer to linearity (157.4°), resulting in much shorter TS bond lengths (d^{TS}(C-O/C-Si) = 1.932/2.763 Å) and a drastically lowered E_a value of 53 kJ mol^{-1}. This confirms the initially made assumption that the main product occurs for the reaction with a TS structure that most closely resembles the linear/bipyramidal TS of S_N2 reactions.

Notably, the anticorrelation of E_{react} and E_a is an exception to the Bell-Evans-Polanyi (BEP) principle, which states that the reaction to the most stable product will have the lowest activation energy[27] and is widely applied in heterogeneous catalysis.[28] However, this anticorrelation was also found for other molecules adsorbing on Si(001), e.g. primary and secondary alkylamines,[29] so it might be a rather common phenomenon for adsorption on this surface. To our knowledge, this has not been highlighted before.

Table 2. Reaction energies E_{react}, activation energies E_a and optimized transition state (TS) distances d^{TS} and angle α^{TS} of the C-O bond being broken and the C-Si bond being formed in the S_N2 attack of surface atom **A**, **B** or **C** (see Scheme 3).[a]

Reaction via	E_{react} (G_{react})[b]	E_a (G_a)[b]	d^{TS}(C-O/Si)	α^{TS}(O-C-Si)
A	–177 (–176)	107 (94)	2.289/3.374	65.6
B	–163 (–162)	100 (94)	2.121/2.904	117.2
C	–144 (–139)	53 (50)	1.932/2.763	157.4

[a] All energies given relative to the energy of the dative bond structure in kJ mol^{-1}, calculated using PBE-D3(PAW). Gibbs energies G_{react} and G_a calculated at 300 K, 1 bar. Distances d^{TS} given in Å, angles α^{TS} in degrees. A detailed conformation analysis was performed to ensure the minimum energies are given in this table (see Supporting Information). [b] Hybrid functional values calculated using HSE06-D3, which showed no qualitative differences, can be found in the Supporting Information.

Finally, the TS geometry of the attack by atom **C** can be analyzed using pEDA to get insight into the change in bonding and the reaction mechanism. The results (Table 1) show that while dispersion contribution barely changes compared to the DB structure, electronic effects increase rapidly and orbital interaction has risen to a value (48% of the attractive terms) where it is almost equally as strong as electrostatics (52%). This is caused by a new orbital contribution with an energy of –111 kJ mol^{-1} (20% of ΔE_{orb}, Figure 1c) in addition to the persistent dative bond type interaction (–397 kJ mol^{-1}, 71% of ΔE_{orb}, see also Figure S14 in the Supporting Information). Using NOCV analysis, it can be assigned to a nucleophilic attack: The corresponding deformation density (Figure 1c) shows that the molecular LUMO (Figure 1b), an antibonding σ*(C-O) orbital, is populated by electrons from the occupied orbital at the opposing Si_{up} atom **C**.[30] Additionally, the largest electron-accepting region (blue lobe) is located between the attacking silicon and the attacked carbon atom, which highlights that the same electron rearrangement that forms this σ bond also breaks the C-O bond. This perfectly illustrates that the reaction occurs via a single-step nucleophilic substitution mechanism of type S_N2.[31]

In summary, our computational analysis has shown that bonding, reactivity and regioselectivity in this prime model system proceed very similarly to textbook organic chemistry reactions. This demonstrates that even under the conditions of ultra-high vacuum on surfaces, which might seem exotic to many chemists, simple chemical concepts are still applicable and allow predictability. Our applied computational analysis, however, additionally gives a quantitative insight that goes beyond the pure application of these concepts. The reported nucleophilic substitution reaction can be expected to occur for any molecule with a Lewis basic group and a nearby carbon atom that can be attacked, as previous studies of alcohols,[32] amines,[33] haloalkanes,[[17a,17b,17e] organophosphorus[17d] and organosulfur compounds[17c] on Si(001) and Ge(001) have shown. This establishes nucleophilic substitution as a common class of surface reaction on semiconductors analogous to organic chemistry along with the well-known cycloaddition, dative bond formation, dissociative addition and elimination reactions.[34] The fact that an insertion reaction has been reported as well[35] shows that there are many other bonding and reaction types between molecules and surfaces still waiting to be discovered. Molecular chemistry, however, can also benefit from knowledge gained in surface science: As a study has shown, the application of common acid-base theories to surfaces might lead to inconsistent conclusions regarding the acid-base character of a surface.[36] This might motivate chemists to devise a more general definition of acidity and basicity.

Computational Methods

All energies and structures were calculated using density functional theory with periodic boundary conditions as implemented in the Vienna ab initio simulation package (VASP)[37] with the PBE[38] and HSE06[39] functionals (optimizations done using PBE), the DFT-D3 dispersion correction[40] and the PAW formalism[41] (E_{cutoff} = 400 eV). The surface was modeled in frozen double layer approximation (six layers) with at least 10 Å vacuum and cell sizes of 4×2 (4×4 for reaction **B**). Electronic *k* space was sampled using a grid of Γ(221) for 4×4 and Γ(241) for 4×2 cells. Gibbs energies (T = 300 K, p = 1 bar) were calculated in an approach described elsewhere[42] using harmonic frequencies obtained numerically by cartesian displacements of 0.01 Å. TS structures were calculated using the Climbing-image Nudged Elastic Band[43] and Dimer[44] methods. The pEDA bonding analysis was done at PBE-D3/TZ2P, Γ only *k* point sampling using closed-shell singlet fragmentation as implemented in ADF-BAND 2016.[45] The approach outlined delivered accurate results for organic/semi-conductor systems in the past.[8b,42,46]

Acknowledgements

This work was supported by the Deutsche Forschungsgemeinschaft (DFG) within SFB 1083, GRK 1782 and TO 715/1-1. Computational resources were provided by HRZ Marburg, HLR Stuttgart and CSC-LOEWE Frankfurt. We thank Prof. Ulrich Koert, Prof. Ulrich Höfer (Marburg), Prof. Michael Dürr (Gießen), and Prof. Stacey Bent (Stanford) for discussions.

Keywords: bonding analysis • density functional theory • ether cleavage • surface chemistry • transfer of concepts

[1] J. Shinar, R. Shinar, *J. Phys. D: Appl. Phys.* **2008**, *41*, 133001.
[2] S. F. Bent, *Surf. Sci.* **2002**, *500*, 879.
[3] a) G. Ertl, *Angew. Chem. Int. Ed.* **2008**, 47, 3524; Angew. *Chem.* **2008**, *120*, 3578; b) R. Hoffmann, *Angew. Chem. Int. Ed.* **2013**, *52*, 93; *Angew. Chem.* **2013**, *125*, 99.
[4] M. A. Filler, S. F. Bent, *Prog. Surf. Sci.* **2003**, *73*, 1.
[5] G. Frenking, S. Shaik (Eds.) *The Chemical Bond: Bonding Across the Periodic Table*, Wiley-VCH, Weinheim, **2014**.
[6] a) R. Dronskowski, P. E. Blöchl, P. E. Blöchl, *J. Phys. Chem.* **1993**, *97*, 8617; b) V. L. Deringer, A. L. Tchougréeff, R. Dronskowski, *J. Phys. Chem. A* **2011**, *115*, 5461; c) A. Nandula, Q. T. Trinh, M. Saeys, A. N. Alexandrova, *Angew. Chem. Int. Ed.* **2015**, *54*, 5312; *Angew. Chem.* **2015**, *127*, 5402.
[7] a) M. Kohout, *Int. J. Quantum Chem.* **2004**, *97*, 651; b) A. I. Baranov, M. Kohout, *J. Comput. Chem.* **2011**, *32*, 2064; c) F. R. Wagner, A. I. Baranov, Y. Grin, M. Kohout, *Z. Anorg. Allg. Chem.* **2013**, *639*, 2025.
[8] a) M. Raupach, R. Tonner, *J. Chem. Phys* **2015**, *142*, 194105; b) J. Pecher, R. Tonner, *ChemPhysChem* **2017**, *18*, 34.
[9] a) B. D. Dunnington, J. R. Schmidt, *J. Chem. Theory Comput.* **2012**, *8*, 1902; b) B. D. Dunnington, J. R. Schmidt, *J. Catal.* **2015**, *324*, 50.
[10] a) R. F. W. Bader, *Chem. Rev.* **1991**, *91*, 893; b) A. Otero-de-la-Roza, E. R. Johnson, V. Luaña, *Comput. Phys. Commun.* **2014**, *185*, 1007; c) J.-H. Lee, N. C. Bristowe, P. D. Bristowe, A. K. Cheetham, *Chem. Commun.* **2015**, *51*, 6434.
[11] A. V. Teplyakov, S. F. Bent, *J. Vac. Sci. Technol. A* **2013**, *31*, 50810.
[12] J. Yoshinobu, *Prog. Surf. Sci.* **2004**, *77*, 37.
[13] a) G. Mette, M. Reutzel, R. Bartholomäus, S. Laref, R. Tonner, M. Dürr, U. Koert, U. Höfer, *ChemPhysChem* **2014**, *15*, 3725; b) M. Reutzel, G. Mette, P. Stromberger, U. Koert, M. Dürr, U. Höfer, *J. Phys. Chem. C* **2015**, *119*, 6018; c) M. Reutzel, M. A. Lipponer, M. Dürr, U. Höfer, *J. Phys. Chem. Lett.* **2015**, *6*, 3971; d) M. Reutzel, N. Münster, M. A. Lipponer, C. Länger, U. Hoefer, U. Koert, M. Dürr, *J. Phys. Chem. C* **2016**, *120*, 26284.
[14] Brønsted acids are common reagents for activation as well.
[15] a) R. L. Burwell, *Chem. Rev.* **1954**, *54*, 615; b) M. V. Bhatt, S. U. Kulkarni, *Synthesis* **1983**, 249.
[16] The scheme shows a *p*(2x2) surface reconstruction, which is necessary for a proper description of reaction C and only 2.2 kJ mol^{-1} higher in energy than the minimum *c*(4x2) reconstruction. At experimental conditions used for the investigation of ethers on Si(001),[13] the surface dimers are known to rapidly flip. More details are given in the Supporting Information.
[17] a) T. Lim, J. C. Polanyi, H. Guo, W. Ji, *Nat. Chem.* **2011**, *3*, 85; b) M. Ebrahimi, S. Y. Guo, K. Huang, T. Lim, I. R. McNab, Z. Ning, J. C. Polanyi, M. Shapero, J. Yang, *J. Phys. Chem. C* **2012**, *116*, 10129; c) K. T. Wong, S. N. Chopra, S. F. Bent, *J. Phys. Chem. C* **2012**, *116*, 26422; d) K. T. Wong, B. Shong, W. Sun, S. F. Bent, *J. Phys. Chem. C* **2013**, *117*, 26628; e) C.-G. Wang, K. Huang, W. Ji, *J. Chem. Phys.* **2014**, *141*, 174701.
[18] S. C. A. H. Pierrefixe, S. J. M. van Stralen, J. N. P. van Stralen, C. Fonseca Guerra, F. M. Bickelhaupt, *Angew. Chem. Int. Ed.* **2009**, *48*, 6469; *Angew. Chem.* **2009**, *121*, 6591.
[19] a) K. Kitaura, K. Morokuma, *Int. J. Quantum Chem.* **1976**, *10*, 325; b) T. Ziegler, A. Rauk, *Theor. Chim. Acta* **1977**, *46*, 1; c) F. M. Bickelhaupt, E. J. Baerends in *Rev. Comput. Chem., Vol. 15* (Eds.: K. B. Lipkowitz, D. B. Boyd), Wiley-VCH, New York, **2000**.
[20] a) H. V. R. Dias, C. Dash, M. Yousufuddin, M. A. Celik, G. Frenking, *Inorg. Chem.* **2011**, *50*, 4253; b) M. A. Celik, C. Dash, V. A. K. Adiraju, A. Das, M. Yousufuddin, G. Frenking, H. V. R. Dias, *Inorg. Chem.* **2013**, *52*, 729.
[21] a) M. P. Mitoraj, A. Michalak, T. Ziegler, *J. Chem. Phys.* **2009**, *5*, 962; b) M. Raupach, *Ph.D. thesis*, Philipps-Universität Marburg, **2015**.
[22] The deformation density also includes rearrangement of electrons in the surface slab.
[23] a) M. Raupach, S. Dehnen, R. Tonner, *J. Comput. Chem.* **2014**, *35*, 1045; b) J.-N. Luy, S. A. Hauser, A. B. Chaplin, R. Tonner, *Organometallics* **2015**, *34*, 5099.
[24] The remaining 15% can be attributed to back donation from the surface and polarization.
[25] J. S. Kachian, K. T. Wong, S. F. Bent, *Acc. Chem. Res.* **2010**, *43*, 346.
[26] The accuracy of the PBE functional was checked by repeating the calculations using the HSE06 hybrid functional, which showed no qualitative difference. More information can be found in the Supporting Information.
[27] a) R. P. Bell, *Proc. R. Soc. London A* **1936**, *154*, 414; b) M. G. Evans, M. Polanyi, *Trans. Faraday Soc.* **1938**, *34*, 11.
[28] a) J. K. Nørskov, T. Bligaard, B. Hvolbæk, F. Abild-Pedersen, I. Chorkendorff, C. H. Christensen, *Chem. Soc. Rev.* **2008**, *37*, 2163; b) R. A. van Santen, M. Neurock, S. G. Shetty, *Chem. Rev.* **2010**, *110*, 2005.
[29] a) C. Mui, G. T. Wang, S. F. Bent, C. B. Musgrave, *J. Chem. Phys.* **2001**, *114*, 10170; b) X. Cao, R. J. Hamers, *J. Vac. Sci. Technol. B* **2002**, *20*, 1614; c) A. J. Carman, L. Zhang, J. L. Liswood, S. M. Casey, *J. Phys. Chem. B* **2003**, *103*, 5491; d) J.-H. Cho, L. Kleinman, *Phys. Rev. B* **2003**, *68*, 245314; e) P. Prayongpan, C. M. Greenlief, *Surf. Sci.* **2009**, *603*, 1055.
[30] The deformation density also includes polarization at the O-Si bond.
[31] A mechanism via a radical intermediate, which can also occur in ether cleavage reactions, could be ruled out due to the high energy of the accepting orbital (see Supporting Information).
[32] a) P. L. Silvestrelli, *Surf. Sci.* **2004**, *552*, 17; b) J. G. E. Zhou, F. Hagelberg, *Int. J. Quantum Chem.* **2005**, *105*, 359.
[33] A. Naitabdi, F. Bournel, J. J. Gallet, A. Markovits, F. Rochet, Y. Borensztein, M. G. Silly, F. Sirotti, *J. Phys. Chem. C* **2012**, *116*, 16473.
[34] T. R. Leftwich, A. V. Teplyakov, *Surf. Sci. Rep.* **2007**, *63*, 1.
[35] Q. J. Zhang, X. L. Fan, W. M. Lau, Z. F. Liu, *Phys. Rev. B* **2009**, *79*, 195303.
[36] K. Mittal, F. M. Etzler, *Ann. Univ. Mariae Curie-Sklodowska, Sect. AA: Chem.* **2008**, *63*, 1.
[37] a) G. Kresse, J. Hafner, *Phys. Rev. B* **1993**, *47*, 558; b) G. Kresse, J. Hafner, *Phys. Rev. B* **1994**, *49*, 14251; c) G. Kresse, J. Furthmüller, *Phys.*

Rev. B **1996**, *54*, 11169; d) G. Kresse, J. Furthmüller, *Comput. Mat. Sci.* **1996**, *6*, 15.

[38] a) J. P. Perdew, K. Burke, M. Ernzerhof, *Phys. Rev. Lett.* **1996**, *77*, 3865–3868; b) J. P. Perdew, K. Burke, M. Enzerhof, *Phys. Rev. Lett.* **1997**, *78*, 1396.

[39] a) J. Heyd, G. E. Scuseria, M. Enzerhof, *J. Chem. Phys.* **2003**, *118*, 8207; b) J. Heyd, G. E. Scuseria, *J. Chem. Phys.* **2004**, *121*, 1187; c) J. Heyd, G. E. Scuseria, M. Enzerhof, *J. Chem. Phys.* **2006**, *124*, 219906.

[40] a) S. Grimme, J. Antony, S. Ehrlich, S. Krieg, *J. Chem. Phys.* **2010**, *132*, 154104; b) S. Grimme, S. Ehrlich, L. Goerigk, *J. Comput. Chem.* **2011**, *32*, 1456.

[41] a) P. Blöchl, *Phys. Rev. B* **1994**, *50*, 17953; b) G. Kresse, D. Joubert, *Phys. Rev. B* **1999**, *59*, 1758.

[42] J. Pecher, G. Mette, M. Dürr, R. Tonner, *ChemPhysChem* **2017**, *18*, 357.

[43] G. Henkelman, B. P. Uberuaga, H. Jónsson, *J. Chem. Phys.* **2000**, *113*, 9901.

[44] G. Henkelman, H. Jónsson, *J. Chem. Phys.* **1999**, *111*, 7010.

[45] a) G. te Velde, E. J. Baerends, *Phys. Rev. B* **1991**, *44*, 7888; b) BAND2016, SCM, Theoretical Chemistry, Vrije Universiteit, Amsterdam, The Netherlands, http://www.scm.com (accessed: 08.11.2016).

[46] J. Pecher, C. Schober, R. Tonner, *Chem. Eur. J.* **2017**, *23*, 5459.

Entry for the Table of Contents (Please choose one layout)

COMMUNICATION

The not-so-odd couple: Surface science and molecular chemistry show off their commonalities in this computational study of ethers on Si(001). Quantitative insight into bonding and reactivity demonstrates that these systems behave very similar to textbook organic chemistry.

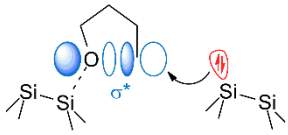

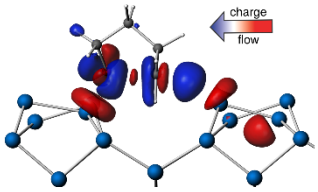

*Lisa Pecher, Slimane Laref, Marc Raupach, Ralf Tonner**

Page No. – Page No.

Ethers on Si(001): A prime example for the common ground between surface science and molecular organic chemistry

Supporting Information for:
Ethers on Si(001): A prime example for the common ground between surface science and molecular organic chemistry

Lisa Pecher, Slimane Laref,† Marc Raupach, Ralf Tonner*

Lisa Pecher, Dr. Slimane Laref, Dr. Marc Raupach, Dr. Ralf Tonner
Faculty Chemistry and Material Sciences Center, Philipps-Universität Marburg, Hans-Meerwein-Straße 4, 35032 Marburg, Germany
†Current address: King Abdullah University of Science and Technology (KAUST), Physical Science and Engineering Division (PSE), Thuwal 23955, Saudi Arabia

* Corresponding author Dr. Ralf Tonner. e-mail: tonner@chemie.uni-marburg.de

Contents

1. Conformational Analysis of Stable States of THF on Si(001)

Since for each adsorption state, at least two different conformations were found, we optimized every stable conformation and the transition states (TS) between them in order to be able to determine which conformation is the most stable and if transitions between them are possible at a given temperature. All barriers for conformational change were found to be lower than 50 kJ mol^{-1} and since the lowest reaction barrier was determined to be 53 kJ mol^{-1}, we assumed that in any temperature regime where the reaction takes place at an experimental time scale, the minimum conformation of each state can be expected.

An abbreviation scheme is introduced at this point for brevity in the SI. The dative bond (DB) intermediate structure is labeled with the letter *I*, while the products of the nucleophilic substitution reaction via surface atoms **A**, **B** and **C** are labeled with *A*, *B* and *C*, respectively. Since the conformations often resembled the chair, boat and twist structures of cyclohexane, a lowercase *c*, *b* or *t* is introduced. As an example, *Ib* denotes the intermediate in boat conformation, while *Ac* denotes the product of reaction A in chair conformation. All energies in the SI are calculated at PBE-D3/PAW(400 eV) if not stated otherwise.

1.1. Intermediate

Two conformations were found for the intermediate, *Ib* and *Ic* (Figure S1), of which the *Ib* structure is slightly more stable by 2 kJ mol^{-1}. There are three different ways of changing the conformation (Figure S1(b,c)): Ring inversion (*invert*), tilting of the molecule over the Si-Si dimer bond (*tilt*) and rotation around the O-Si axis (*rotate*). While the rotation has the highest energy barrier at 18 kJ mol^{-1}, the other two are very similar with the inversion having the lowest one (8 kJ mol^{-1}). This is in line with the finding for gas phase ring inversion of THF known to occur via a pseudorotation motion with energy differences and barriers below 1 kJ mol^{-1}.[1]

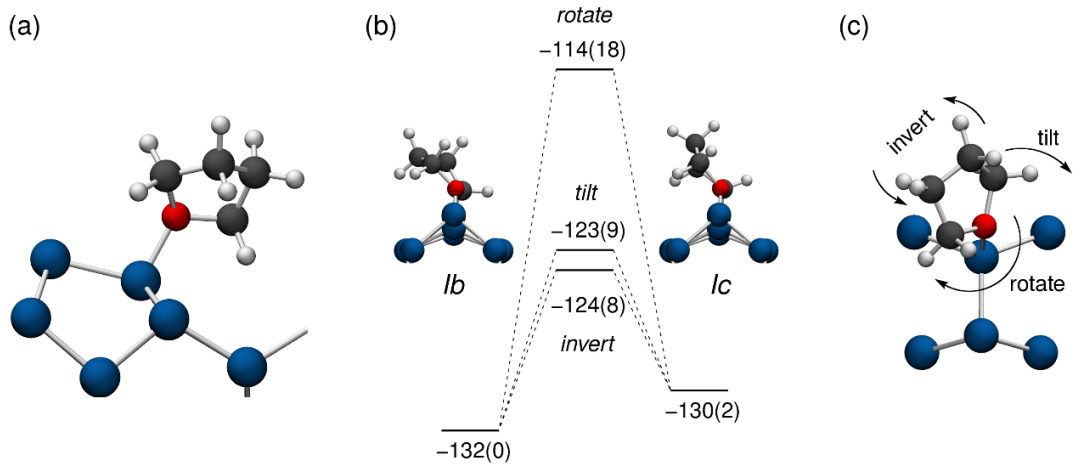

Figure S1 (a) Side view of the *Ib* conformation. (b) Energy diagram for the three different types of conformational change. (c) Depiction of the three different types of motion. Bonding energies between surface and molecule given in kJ mol^{-1}, relative energies (in parentheses) given with respect to the lowest energy conformation.

1.2. Final State of Reaction A

The product of reaction A features three different conformations (Figure S2), where *Ac* is the most stable one with a bonding energy of –309 kJ mol^{-1}.

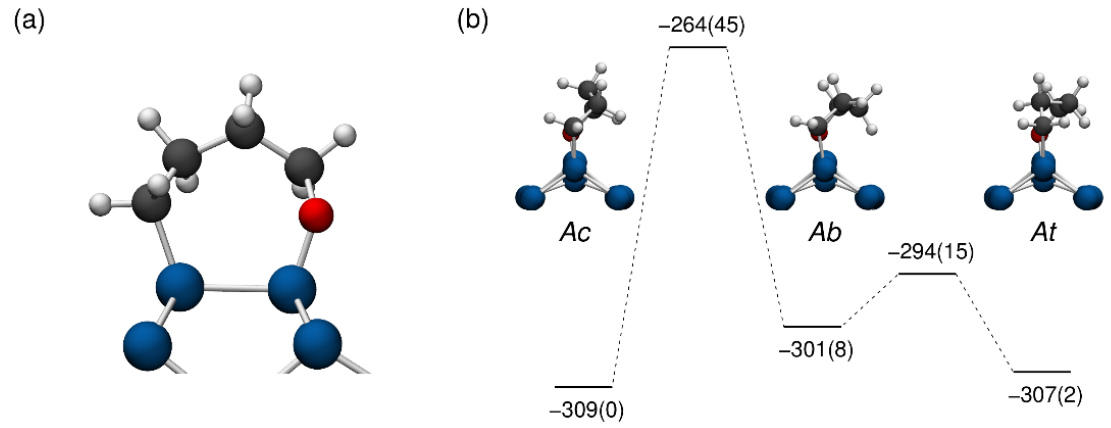

Figure S2 (a) Side view of the *Ac* conformation. (b) Energy diagram for conformational change of *A*. Bonding energies between surface and molecule given in kJ mol^{-1}, relative energies (in parentheses) given with respect to the lowest energy conformation.

1.3. Final State of Reaction B

In this case, eight different conformations were found in total. Since the qualitative differentiation is far more complicated than in the other cases, the conformations are simply numbered *B1*, *B2*, etc. with *B1* set to the conformation of lowest energy (see Figure S3). Two other conformations, *B4* and *B6*, are close in energy to *B1* albeit with considerable barriers towards formation. Furthermore, the low barrier of 1 kJ mol^{-1} for conversion from *B5* to *B4* could only be an artifact of the computational method and in reality, *B5* might not be a minimum structure at all.

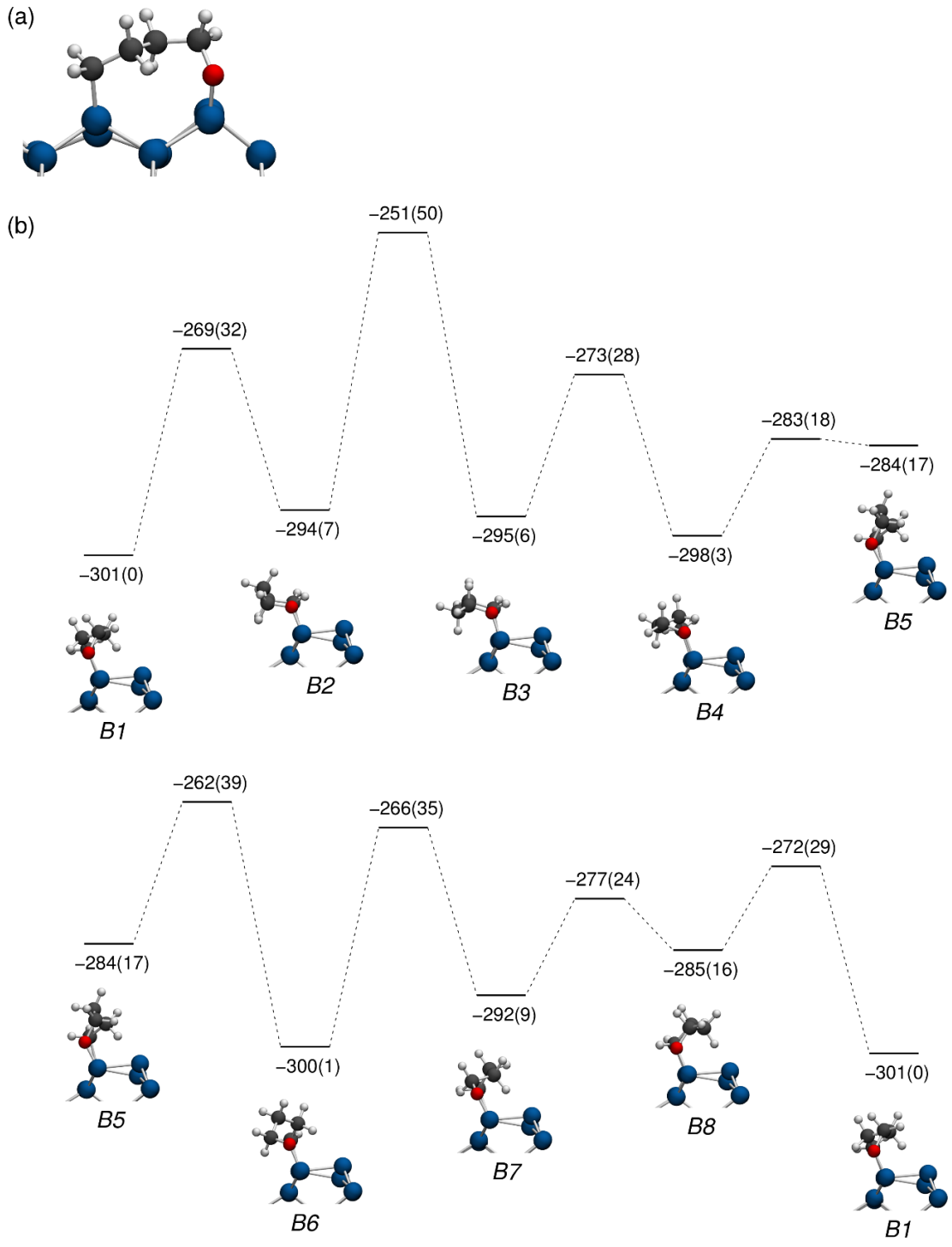

Figure S3 (a) Side view of the *B1* conformation. (b) Energy diagram for conformational change of *B*. Bonding energies between surface and molecule given in kJ mol^{-1}, relative energies (in parentheses) given with respect to the lowest energy conformation.

1.4. Final State of Reaction C

The product of reaction C only features a chair-type (*Cc*) and boat-type (*Cb*) conformation, of which the *Cb* structure is more stable by 5 kJ mol^{-1}.

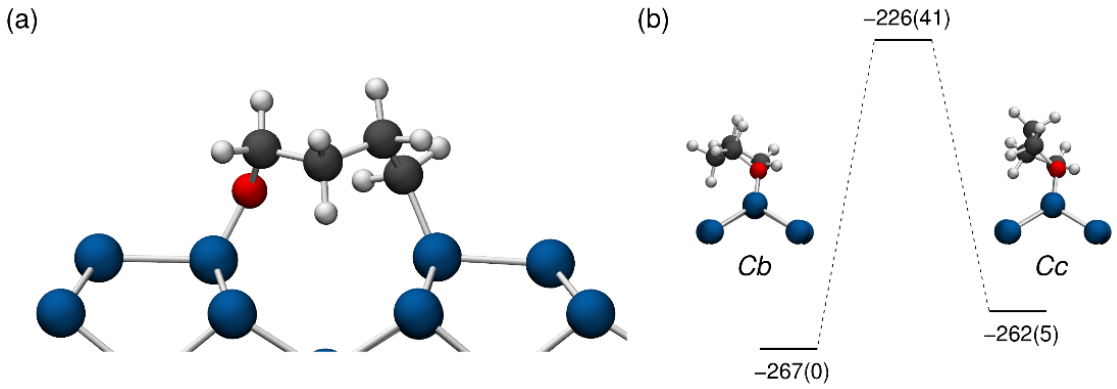

Figure S4 (a) Side view of the *Cb* conformation. (b) Energy diagram for conformational change of *C*. Bonding energies between surface and molecule given in kJ mol^{-1}, relative energies (in parentheses) given with respect to the lowest energy conformation.

2. Reactions from the THF/Si(001) Datively Bonded Intermediate (DB)

Since there are different transition states for each reaction, depending on the conformation of the initial and final state, all found reactions are listed here and the reader is given an explanation for the choice of the numbers that are given in the main text (Table 2).

2.1. DB To Final State A

There are two possible reactions from *I* to final state *A* (Figure S5): One from conformation *Ib* to product conformation *Ac* (a) and one from *Ic* to *At* (b). The lowest energy barrier is reached at the reaction *Ib*→*Ac*, which also leads to the lowest energy conformation product, so these are the numbers that are given in the main article.

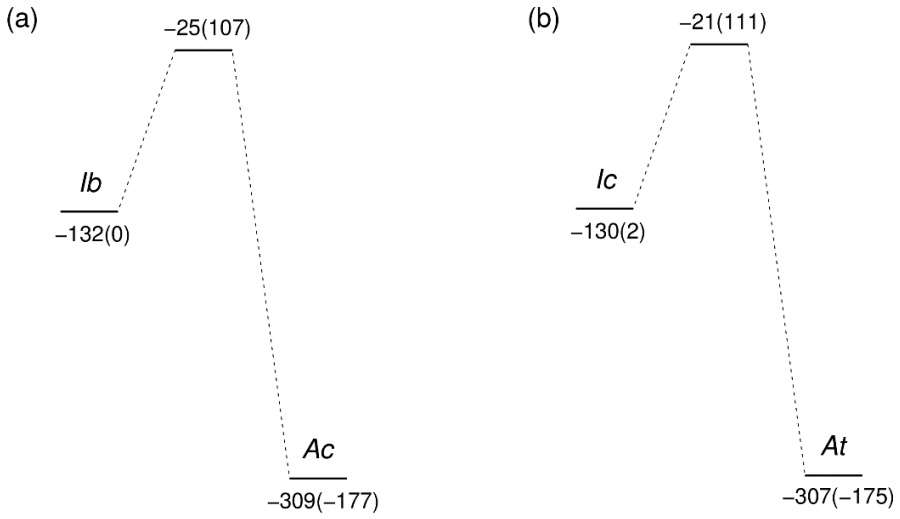

Figure S5 Reaction energy profiles for the attack of surface atom **A** in two different conformations of the intermediate, leading to two different conformations of product *A*. Bonding energies between surface and molecule given in kJ mol^{-1}, relative energies (in parentheses) given with respect to the energy of the minimum intermediate structure *Ib*. See also Figures S1 and S2.

2.2. DB To Final State B

Although there are eight conformations of final state B, only two are directly accessible from the intermediate (Figure S6). The lowest energy barrier is reached at the reaction *Ib*→*B2*, from which the system can easily convert to the lowest energy conformation, *B1*, by overcoming an energy barrier of 25 kJ mol^{-1} (Figure S3). Hence, the energies given in Table 2 of the main article are the activation energy of Figure S6(a) and the reaction energy to the *B1* state (Figure S3). Differences in *Ib* and *Ic* energies compared to the values given in Figures S1 and S5 can be attributed to the fact that these calculations had to be done in a 4×4 cell compared to the smaller 4×2 cell used for the other reactions, resulting in slightly different bonding energies for the same states.

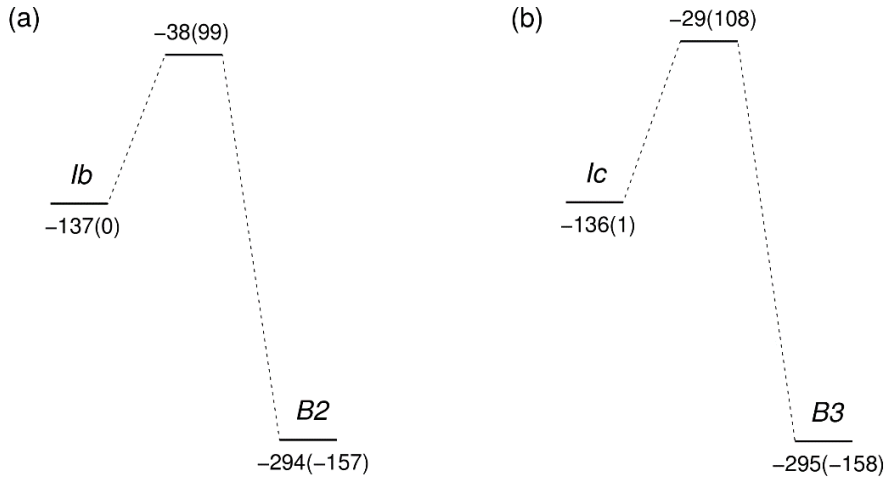

Figure S6 Reaction energy profiles for the attack of surface atom **B** in two different conformations of the intermediate, leading to two different conformations of product *B*. Bonding energies between surface and molecule given in kJ mol^{-1}, relative energies (in parentheses) given with respect to the energy of the minimum intermediate structure *Ib*. See also Figures S1 and S3.

2.3. DB To Final State C

Since the previous two reactions occurred within a surface dimer row, but this reaction between two rows (see main article, Scheme 3), the surface reconstruction becomes important. This is particularly evident in the reaction barriers (Figure S7), which drop from 75-76 kJ mol^{-1} for a 4×2 reconstruction to 53-56 kJ mol^{-1} for a 2×2 reconstruction. This reconstruction is only 2 kJ mol^{-1} higher in energy than 4×2 (Figure S8) and when the activation energy of 30 kJ mol^{-1} can be overcome, a significant percentage of the surface will be present as 2×2. The presence of a THF molecule in the intermediate structure has only minor effects on the energy barrier for flipping the dimers on the opposing row (Figure S8(b)), so it can be expected that most of the reactions will take place with the dimer flipping as an intermediate step.

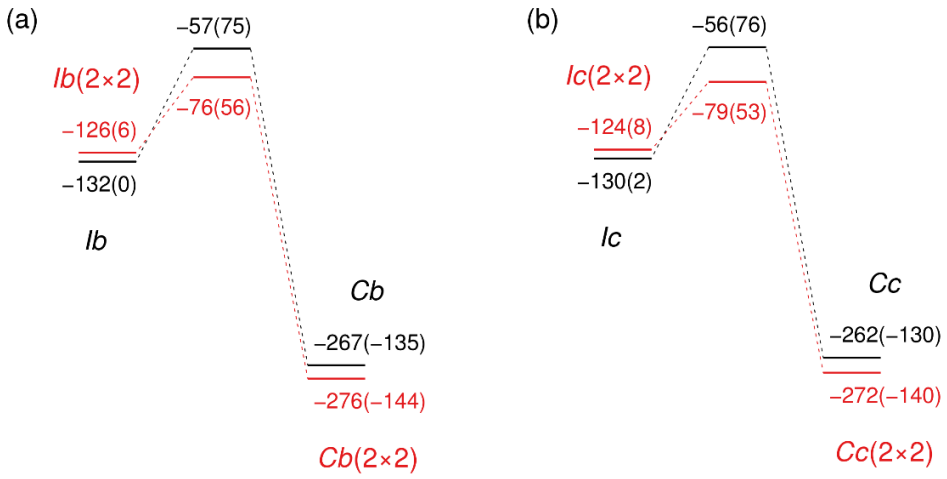

Figure S7 Reaction energy profiles for the attack of surface atom **C** in two different conformations of the intermediate and also two different kinds of surface reconstructions (4×2: black, 2×2: red). Bonding energies between surface and molecule given in kJ mol^{-1}, relative energies (in parentheses) given with respect to the energy of the minimum intermediate structure *Ib*. See also Figures S1, S4 and S8.

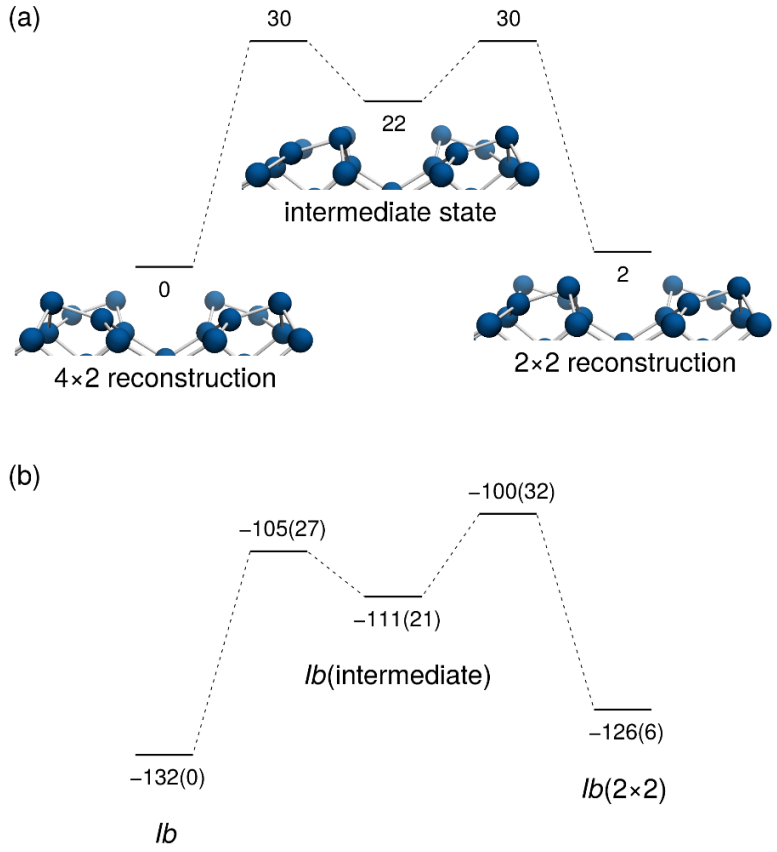

Figure S8 (a) Energy diagram for the change of the surface slab from 4×2 to 2×2 reconstruction. (b) Energy diagram for the same change if a THF molecule is present in the intermediate *Ib* structure and the reconstruction change is occuring on the opposing dimer row. Bonding energies in (b) between surface and molecule given in kJ mol^{-1}, relative energies (in parentheses) given with respect to the energy of the minimum intermediate structure *Ib.*

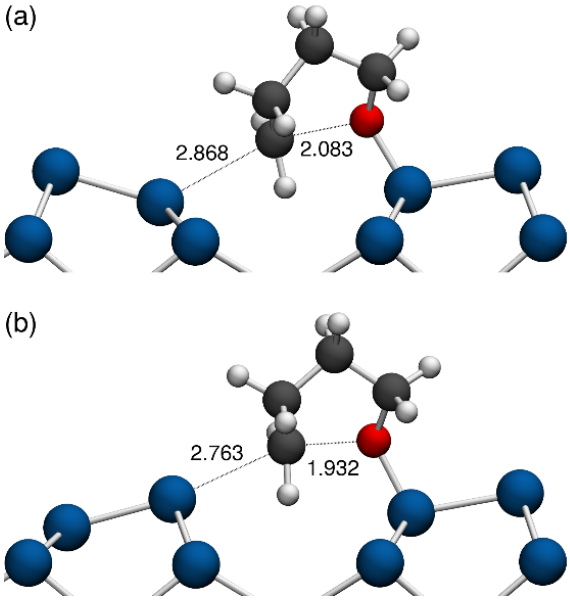

Figure S9 Comparison of the C-Si and C-O bond lengths at the transition state of the *Ic*→*Cc* reaction between (a) 4×2 and (b) 2×2 surface reconstruction.

The reason for the lowered energy barrier is expemplified by the transition state bond lengths of the C-Si and C-O bond (Figure S9): Due to the increased distance of the opposing Si atom, the C-O bond has to elongate significantly more (2.083 Å) than in the 2×2 reconstructed cell (1.932 Å) in order to reach the transition state. The reaction in the cell with 4×2 reconstruction can therefore be interpreted as the reaction in the 2×2 reconstructed cell plus an additional dimer flipping motion (Figure S8). This is underlined by the difference in activation energies between the two reconstructions, 19-23 kJ mol^{-1}, which is close to the energy needed to flip the opposing dimer, 30 kJ mol^{-1}.

The total reaction from the minimum intermediate structure *Ib* to the minimum structure of state C, *Cb*(2×2), therefore occurs in four steps (Figure S10): First, the surface reconstruction changes from 4×2 to 2×2, in the second step, the intermediate changes to the chair conformation *Ic*, in the third step, the actual reaction takes place and in the fourth and final step, the product changes its conformation to the minimum. For this minimum energy reaction pathway, the numbers were given in the main article in Table 2.

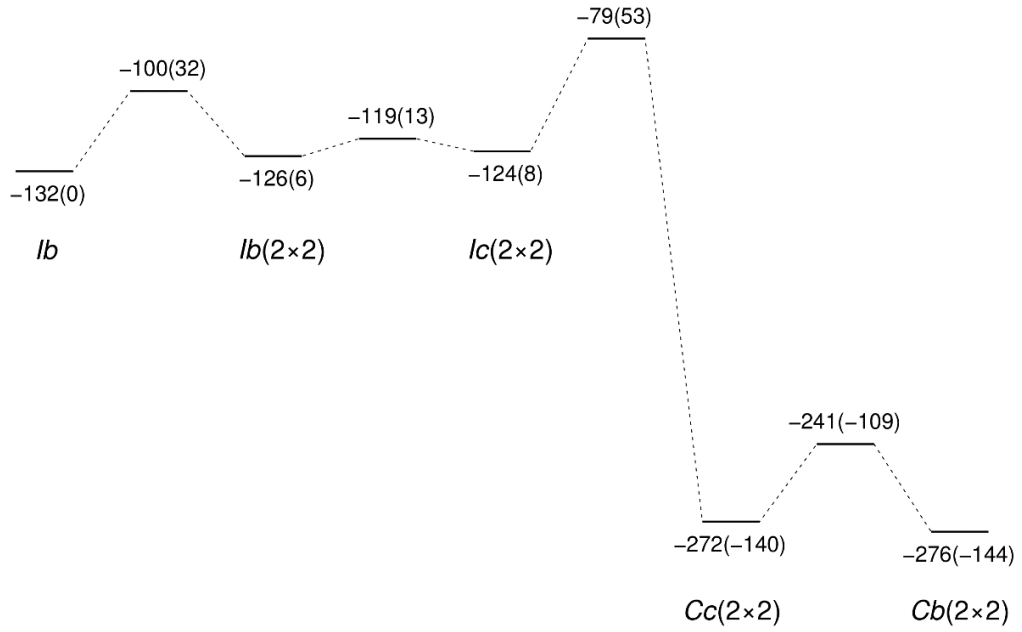

Figure S10 The full reaction path leading from the lowest energy intermediate structure (*Ib*) to the lowest energy product structure (*Cb*(2×2)), including surface reconstruction change (step 1), conformation change (step 2), the actual reaction (step 3) and product conformation change (step 4). Bonding energies between surface and molecule given in kJ mol^{-1}, relative energies (in parentheses) given with respect to the energy of the minimum intermediate structure *Ib*. See also Figures S1, S4, S7 and S8.

3. The σ*(C-O) Orbital in the Intermediate

In order to rule out an electron-transfer promoted mechanism of the ether cleavage, selected crystal orbitals (COs) of the intermediate structure *Ib* are displayed in Figure S16. To promote such a reaction, electrons have to be transferred from the occupied orbitals at the Si_{up} atoms of the opposing row to any orbital weakening the C-O bond. The highest occupied Si_{up} orbital of this row is found in the HOCO-4 (Figure S11, top) at –4.25 eV, while the lowest unoccupied orbital with a σ*(C-O) contribution is found in the LUCO+6 (Figure S11, bottom) at –2.50 eV. The energy difference between these two orbitals, i.e. the estimated energy required for an electron transfer, is 1.75 eV or 169 kJ mol^{-1}, which is much higher than the 53 kJ mol^{-1} of the thermally promoted nucleophilic substitution process (Figure S10). Therefore, we concluded that an electron-transfer promoted process is highly unlikely.

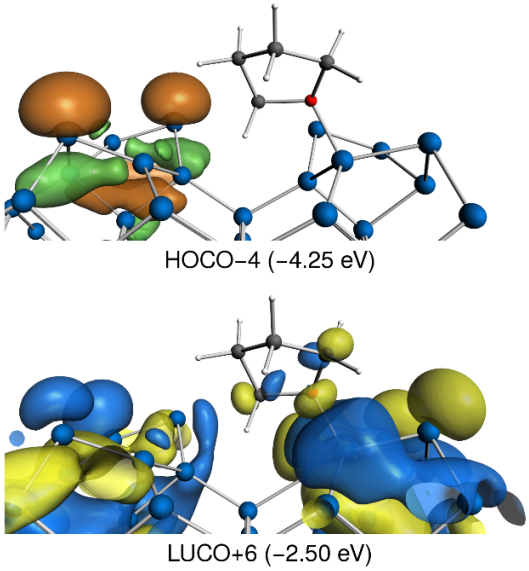

Figure S11 Two selected crystal orbitals of the *Ib* intermediate structure of THF on Si(001) shown at the Γ point in *k* space, calculated using PBE/TZ2P.

4. Accuracy of Computed Energy Differences

To check the accuracy of the GGA-type PBE functional, the reaction and activation energies from the dative bond structure (main article, Table 2) were also calculated using the HSE06-D3 range-separated hybrid functional. The results (Table S1) show that while the difference between reaction energies is higher and also activation energies are higher by 30-44%, the overall qualitative picture stays the same, i.e. the reaction via surface atom **C** is the most favored one and an anti-Bell-Evans-Polanyi behavior is observed.

Table S1 Reaction energies E_{react} and activation energies E_a for the nucleophilic attack of surface atom **A**, **B** or **C** (see main article, Scheme 3), calculated using both PBE-D3(PAW) and HSE06-D3(PAW).[a]

Reaction via	E_{react}(PBE-D3)	E_a(PBE-D3)	E_{react}(HSE06-D3)	E_a(HSE06-D3)
A	–177	107	–188	144
B	–163	100	–168	130
C	–144	53	–134	76

[a] All energies given relative to *Ib* in kJ mol^{-1}.

5. Diethylether on Si(001)

To rule out any influence of the ring strain in THF on the observed reactivity, selected calculations were performed with diethylether (**2**). Since experiments showed reaction via **C** to be the predominant feature as well,[2] only this reaction was considered (Figure S12). Again, the influence of the surface reconstruction is of major importance (compare Section S2.3) and the lowest energy barrier is reached in a cell of 2×2 reconstruction. While the intermediate (*I*) is more weakly bound by 16 kJ mol^{-1}, the activation energy is slightly higher at 61 kJ mol^{-1} compared to 53 kJ mol^{-1} in THF. The final state, however has a very similar bonding energy, –274 kJ mol^{-1}, compared to –276 kJ mol^{-1} in THF (see also Figures S7, S10).

pEDA results (Table S2) show a very similar picture in comparison to THF (main article, Table 1). With the exception of dispersion interaction, all pEDA terms are slightly smaller in the intermediate, leading to an interaction energy that is weaker by about 5 kJ mol^{-1} for diethylether. The second contribution leading to a slightly weaker bonding energy in this system is the increased preparation energy of 33 kJ mol^{-1} compared to 22 kJ mol^{-1} in THF, which can be attributed to the need of rotation of the ethylene groups for an ideal exposure of the oxygen atom.

The results for the transition state structure yield similar results again with the exception that the interaction is slightly stronger than in THF, which is reflected in an interaction energy of –248 kJ mol^{-1} (THF: –235 kJ mol^{-1}). This, however, is again overcompensated by a higher preparation energy of 192 kJ mol^{-1} (THF: 157 kJ mol^{-1}) which leads to a higher energy barrier in general for diethylether.

The two most important NOCV deformation densitites (Figure S13) show no qualitative and only minor numerical difference to the ones of THF (main article, Figure 1).

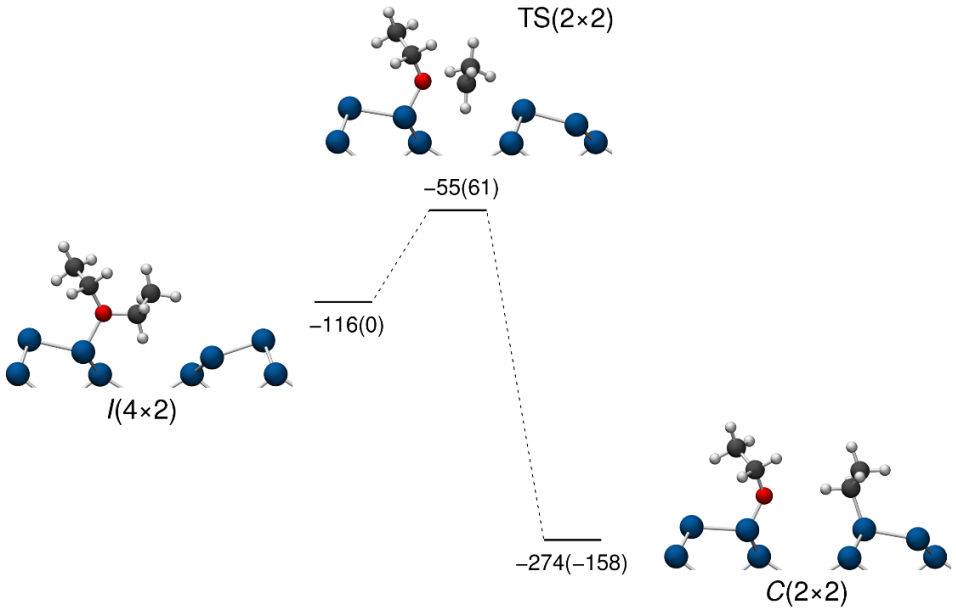

Figure S12 Reaction energy profile for the attack of surface atom **C** at a diethylether molecule on Si(001). The reaction also includes a change of the surface reconstruction from 4×2 to 2×2, which can be expected to occur similarly to the THF system (Figure S10) and is omitted in this diagram.

Table S1 Bonding analysis (pEDA) of the molecule-surface interaction between diethylether and Si(001) at the *I* and TS structures (See also Figure S12).[a]

	I(4×2 surface)	TS(2×2 surface)
ΔE_{int}	–151	–248
ΔE_{int}(disp)[b]	–54 (37%)	–58 (23%)
ΔE_{int}(elec)[b]	–97 (63%)	–190 (77%)
ΔE_{Pauli}	645	1001
ΔE_{elstat}[c]	–409 (55%)	–611 (51%)
ΔE_{orb}[c]	–334 (45%)	–580 (49%)
ΔE_{orb}(dative)[d]	–284 (85%)	–402 (69%)
ΔE_{orb}(S_N)[d]	0	–117 (20%)
ΔE_{prep}	33	192
E_{bond}[e]	–118 (–116)	–56 (–55)

[a] All values in kJ mol^{-1}, calculated using PBE-D3/TZ2P. [b] Percentage values: Relative contributions of dispersion and electronic effects to the interaction energy ΔE_{int}. [c] Percentage values: Relative contributions between the attractive pEDA terms ΔE_{elstat} and ΔE_{orb}. [d] Percentage values: Relative contributions to the orbital interaction ΔE_{orb}. [e] PBE-D3/PAW values calculated in VASP given for comparison (in parentheses).

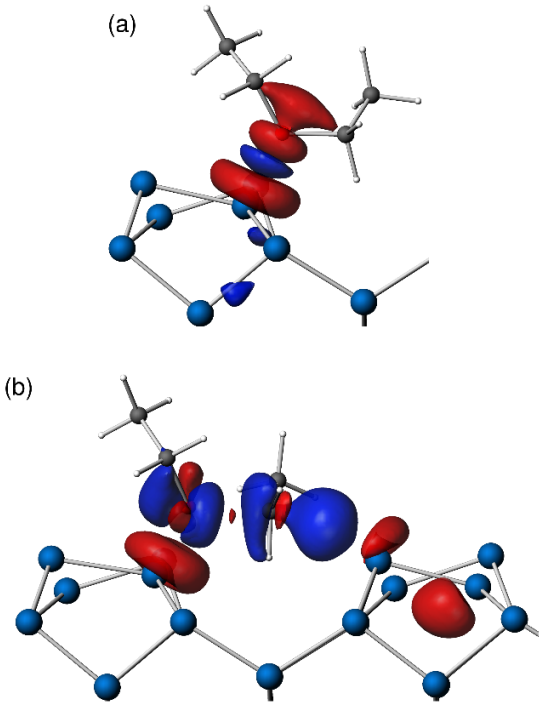

Figure S13 a) pEDA deformation densities $\Delta\rho_1$ at the *P*(4×2) structure of diethylether on Si(001). ΔE_1 = –202 kJ mol^{-1}, ν_1 = ±0.74 q_e. b) Deformation density $\Delta\rho_2$ at the TS(2×2) structure. ΔE_2 = –117 kJ mol^{-1}, ν_2 = ±0.72 q_e.

6. The Dative Bond in the Transition State Structure

The NOCV deformation densities, energies and eigenvalues at the transition state structures TS(DB→C) (THF) and TS(2×2) (diethylether) are given here to show that the dative bond between the oxygen atom and the surface is still the dominating contribution to the orbital energy. The difference of ΔE_1(THF) to the value of –397 kJ mol^{-1} mentioned in the main article arises from additional minor contributions of σ and π symmetry that are not shown here.

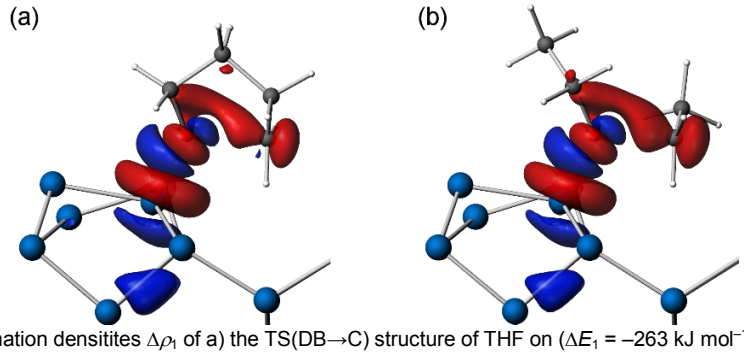

Figure S14 pEDA deformation densitites $\Delta\rho_1$ of a) the TS(DB→C) structure of THF on (ΔE_1 = –263 kJ mol^{-1}, ν_1 = ±1.00 q_e) and b) the TS(2×2) structure of diethylether (ΔE_1 = –256 kJ mol^{-1}, ν_1 = ±0.96 q_e)

7. References

[1] V. M. Rayón, J. A. Sordo, *J. Chem. Phys.* **2005**, *122*, 204303.

[2] M. Reutzel, G. Mette, P. Stromberger, U. Koert, M. Dürr, U. Höfer, *J. Phys. Chem. C* **2015**, *119*, 6018.; b) M. Reutzel, M. Lipponer, M. Dürr, U. Höfer, *J. Phys. Chem. Lett.* **2015**, *6*, 3971.

8. Cartesian Coordinates and Total Energies

8.1. THF Molecule

Molecule(4x2), E(PBE-D3/PAW) = -72.258583 eV, E(HSE06-D3/PAW) = -84.482333 eV, E(PBE-D3/TZ2P) = -72.2240 eV

```
  1.00000000000000
    7.6621999740000000    0.0000000000000000    0.0000000000000000
   -0.0000006700000000   15.3243999479999999    0.0000000000000000
   -0.0000007340000000   -0.0000007340000000   26.7875003810000010
  O   C   H
    1   4   8
Direct
  0.3255461681234662  0.2514518751367011  0.3362199606131157
  0.4477372206593573  0.2221834726808309  0.3734601807383408
  0.4825422779647897  0.3008834549682003  0.4068656170906052
  0.4748036469100440  0.3756269236357915  0.3688753000584534
  0.3282276542868693  0.3455628149840293  0.3340775151864024
  0.3890554454513212  0.1663869196302598  0.3931420542173253
  0.5694262747279585  0.1998739391581523  0.3551523569148410
  0.3779054111997033  0.3078154908406263  0.4347742172370820
  0.6078830050947910  0.2966494474050164  0.4266274923408809
  0.4483701865321350  0.4395963431694099  0.3857817290669660
  0.5992038880571301  0.3800727211057968  0.3483955235409401
  0.1998108561888148  0.3703032069325131  0.3465693462100117
  0.3480809482674512  0.3658921645156351  0.2950320801232018
```

Molecule(4x4), E(PBE-D3) = -72.239426 eV, E(HSE06-D3) = -84.429373 eV

```
  1.00000000000000
   15.3243999479999999    0.0000000000000000    0.0000000000000000
   -0.0000006700000000   15.3243999479999999    0.0000000000000000
   -0.0000007340000000   -0.0000007340000000   26.7875003810000010
  O   C   H
    1   4   8
Direct
  0.1631470172187455  0.2514422802965737  0.3360388692265114
  0.2237753088081962  0.2221215512914860  0.3734804735871088
  0.2414334717289528  0.3008976760164731  0.4068115544756246
  0.2373093154678405  0.3757157777546197  0.3688770707442474
  0.1641289547621470  0.3455616680584556  0.3340332809930538
  0.1940139441820521  0.1666306739360828  0.3932483524527034
  0.2845899797903025  0.1992459344544793  0.3553549879640346
  0.1893734251819932  0.3078378409145855  0.4348733324036980
  0.3042802888404489  0.2967141228978107  0.4264251334789905
  0.2238128429373217  0.4395215310695346  0.3859119338772624
  0.2994527129543408  0.3805607420158971  0.3484234473978778
  0.0998531794629957  0.3700243147689384  0.3464820419120507
  0.1741260503965827  0.3660246606880388  0.2950128948250205
```

8.2. Slab Configurations

Slab(4x2), E(PBE-D3/PAW) = -312.95109 eV, E(HSE06-D3/PAW) = -361.89223 eV, E(PBE-D3/TZ2P) = -300.5073 eV

ChemPubSoc Europe

DOI: 10.1002/chem.201605952

CHEMISTRY A European Journal Full Paper

Bonding Analysis |*Hot Paper*|

Chemisorption of a Strained but Flexible Molecule: Cyclooctyne on Si(001)

Josua Pecher,[a] Christoph Schober,[a, b] and Ralf Tonner*[a]

Abstract: The adsorption characteristics of a promising system for hybrid organic–inorganic interfaces, cyclooctyne on Si(001), is analyzed using density functional theory. The chemisorbed 'on-top' configuration, where a cycloadduct is formed between the ring triple bond and a surface dimer, is shown to be most stable. Less stable are 'bridge' and 'sublayer' modes featuring two molecule-surface bonds and the 'pedestal' mode with four bonds. Investigations with our recently proposed periodic energy decomposition analysis (pEDA) reveal that the four-bond configuration is destabilized by large deformation energies needed within molecule and surface as well as rather weak molecule–surface bonds. Dispersion interactions show significant influence on energy and structure of the configurations leading to an increased bending of the rather flexible molecules. Thus, features found in previous scanning tunneling microscopy experiments are conclusively explained with bent 'on-top' configurations and the 'pedestal' mode can be ruled out. A comparison to acetylene shows that the ring structure and the resulting strain of cyclooctyne are responsible for an increased reactivity of the larger adsorbate due to a pre-forming of the ring triple bond for surface bonding. In contrast, ring strain leads only to negligible electronic effects on the adsorbate–surface bonds. The computations highlight the need for in-depth theoretical analysis to understand adsorption characteristics of large, flexible molecules.

1. Introduction

Silicon devices are widely used in modern technology and the organic functionalization of silicon surfaces promises to enhance the application range of electronic devices, for example, in the construction of new sensors, organic electronics and nanostructures.[1] As a consequence, these hybrid organic-inorganic interfaces have become a major focus of research in both chemistry and physics in recent years.[2] Unsaturated organic molecules are particularly suited for the controlled build-up of interfaces, since they have been reported to form well-defined cycloaddition products with the Si(001) surface,[3] leading to stable, covalently linked (chemisorbed) structures. This reactivity results from the prevalent surface reconstruction of Si(001) (Figure 1) which features the formation of buckled dimers[4] that can act as both nucleophiles and electrophiles[5] and thus show high reactivity.

Although the adsorption of small molecules has already been extensively investigated,[6] the use of larger molecules is presenting exciting challenges. Cyclooctyne is the smallest cyclic alkyne stable under typical lab conditions. It is a formidable choice for semiconductor functionalization, since its enhanced reactivity due to the strained triple bond[7] has already made the molecule widely utilized as a building block in organic synthesis[8] and the in vivo modification of biological systems.[9] Moreover, the ability to attach functional groups to the ring makes the molecule an ideal candidate for the construction of organic/semiconductor interfaces.[10] Previous experimental studies have found a direct adsorption pathway leading to stable structures that form well-ordered patterns at high coverage.[11]

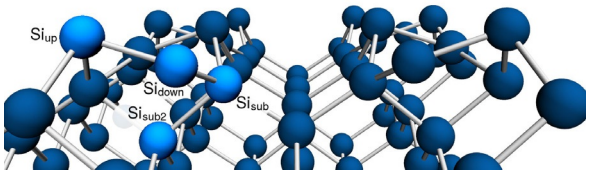

Figure 1. Structure of Si(001) in the most stable $c(4\times2)$ reconstruction with nomenclature for the highlighted surface and subsurface atoms.

A puzzling finding in the previous scanning tunneling microscopy (STM) results was the occurrence of two features of the surface-adsorbed molecule. The minority feature is readily identified as the 'on-top' mode (Figure 2a) but it only occurs for pairs of molecules. The majority feature appears symmetrically between two dimers and led to two hypotheses: Either the molecule forms formally four covalent bonds to the surface dimers (also termed 'tetra-σ mode') in a pedestal fashion (Fig-

[a] J. Pecher, C. Schober, Priv.-Doz. Dr. R. Tonner
Faculty of Chemistry and Material Sciences Center
Philipps-Universität Marburg
Hans-Meerwein-Str. 4, 35032 Marburg (Germany)
E-mail: tonner@chemie.uni-marburg.de

[b] C. Schober
Current address: Fakultät Chemie, TU München
Lichtenbergstr. 4, 85747 Garching (Germany)

Supporting information and the ORCID identification number(s) for the author(s) of this article can be found under http://dx.doi.org/10.1002/chem.201605952.

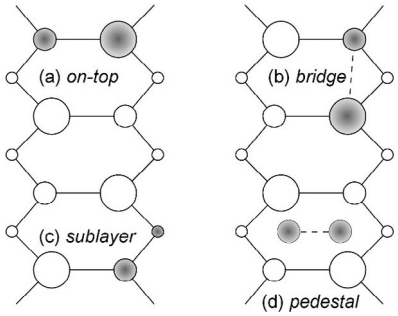

Figure 2. Possible adsorption modes for alkynes on Si(001). Circles represent Si surface atoms with the size being proportional to the height, shading denotes the horizontal position of the adsorbate's triple bond.

ure 2 d) or it shows "an asymmetric tilt".[11] This tilting has been found for cyclohexadiene before.[12] Also, a molecular analogue of the cyclooctyne/Si(001) system (a 1,2-disilacyclobut-3-ene) shows tilting in the X-ray structural analysis.[13]

We provide strong evidence for tilting as an explanation for the experimental observation and provide a rationale based on quantitative bonding analysis.[14] Furthermore, the inclusion of semiempirical dispersion correction methods is necessary to remedy the known failure of current density functionals, as it influences stability and structure of adsorbed states significantly. These results show the increased complexity of investigating a rather large molecule such as cyclooctyne in comparison to smaller adsorbates (e.g. influence of ring strain) and the consequences it has on the understanding of adsorption of organic molecules on semiconductor surfaces.

Computational Details

Molecular calculations

All calculations were done within the program packages Gaussian09 Rev.C01[15] and Turbomole 6.3.1.[16] Computation of electronic energies was carried out using the CCSD(T) method and the density functional by Perdew, Burke and Enzerhof (PBE)[17] with semi-empirical dispersion correction by Grimme (D3 with Becke-Johnson type damping)[18] applied. Structural optimizations and transition state search were done within density functional theory (DFT) using the Berny algorithm as implemented in Gaussian09. All calculations used the def2-TZVPP basis set.[19] Gibbs energies were calculated at $T=298.15$ K and $p=1$ bar.

Periodic calculations and convergence studies

All calculations with periodic boundary conditions were performed within the Vienna Ab-initio Simulation Package (VASP),[20] version 5.3.5, using the projector augmented wave (PAW) formalism[21] and the PBE functional with D3 dispersion correction. SCF calculations and structural optimizations were converged to values of 10^{-5} eV and 10^{-2} eV Å^{-1}, respectively, whereas for frequency calculations, the SCF convergence criterion was set to 10^{-8} eV. Optimizations were done using the conjugate gradient algorithm[22] and frequencies for derivation of Gibbs energies were calculated by numerical construction of the Hessian using Cartesian displacements of 0.01 Å. Gibbs energies, calculated in an approach described elsewhere,[23] are given at $T=298.15$ K and $p=1$ bar. The silicon surface was modeled as a slab in the frozen double layer approximation (i.e. the bottom two layers of the slab were kept in their bulk positions) with the bottom layer saturated with hydrogen atoms in tetrahedral arrangement at a distance of d(Si-H)$=$ 1.480 Å, the experimental bond length of silane.[24] Cell parameters in x and y direction were set to 15.324 Å, corresponding to a (4×4) cell with a computationally optimized bulk lattice parameter of 5.418 Å. The most stable surface reconstruction, c(4×2), was used.

Basis set size (plane wave cutoff energy), k point sampling, vacuum thickness and number of slab layers were benchmarked with convergence studies to avoid systematic errors in the computations. Estimates of the remaining errors are shown in Table 1. A full report on the convergence studies together with Cartesian coordinates and total energies of all structures is given in the Supporting Information.

Table 1. Choice of computational parameters and residual error estimates for all subsequent calculations as determined by convergence studies.[a]

	Value	Residual error[b]
plane wave energy cutoff	400 eV	<1 %
k point sampling[c]	Γ(221)	$\approx$0.2 kJ mol^{-1}
Δz (vacuum)	9 Å	$\approx$0.4 kJ mol^{-1}
No. of Si layers	6	<1 %

[a] All data on the convergence studies are given in the Supporting Information. [b] Deviation with respect to converged total energy (cutoff energy), adsorption energy (k point sampling, Δz (vacuum)) and surface energy (no. of Si layers). [c] k mesh suitable for a (4×4) cell of Si(001). For a (4×2) unit cell calculation, this corresponds to Γ(241).

Bonding energies E_{bond} were calculated as the difference between the energy E_{tot} of the relaxed total system and the relaxed and isolated surface and molecule energies E_{surf} and E_{mol} (surface science convention is the use of the adsorption energy E_{ads}, with inverted sign convention ($E_{ads}=-E_{bond}$)):

$$E_{bond} = E_{tot} - E_{surf} - E_{mol} \quad (1)$$

STM topographies were calculated in the Tersoff–Hamann approximation.[25]

Periodic energy decomposition analysis

Bonding analysis was done using the pEDA method[14] as implemented in ADF-BAND 2016.[26] The pEDA scheme begins with a partitioning of the bond energy E_{bond} into the intrinsic interaction energy ΔE_{int} and the preparation energies of molecule and surface, ΔE_{prep}(Mol) and ΔE_{prep}(Surf) (see also Figure 3):

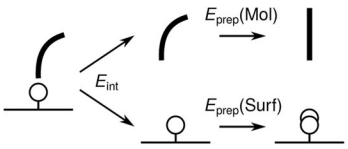

Figure 3. Schematic representation of the interaction and preparation energy contributions.

$$E_{bond} = \Delta E_{int} + \Delta E_{prep}(Mol) + \Delta E_{prep}(Surf) \quad (2)$$

ΔE_{int} can then be split up into contributions stemming from dispersion, ΔE_{int}(disp), and electronic effects, ΔE_{int}(elec):

$$\Delta E_{int} = \Delta E_{int}(disp) + \Delta E_{int}(elec) \quad (3)$$

The reader should note that the preparation energies ΔE_{prep} also consist of dispersion and electronic contributions, but a decomposition is not done here. After this step, the actual pEDA procedure takes place and the electronic interaction energy ΔE_{int}(elec) is split up into contributions from Pauli repulsion (ΔE_{Pauli}), electrostatics (ΔE_{elstat}) and orbital interaction (ΔE_{orb}):

$$\Delta E_{int}(elec) = \Delta E_{Pauli} + \Delta E_{elstat} + \Delta E_{orb} \quad (4)$$

2. Results and Discussion

2.1. The cyclooctyne molecule

Conformational analysis of the cyclooctyne molecule was performed to ensure that the lowest-energy conformer is used in adsorption studies. Due to the stiffness of the triple bond, the molecule can adopt the same conformations as cyclohexane: chair (C_2 symmetry) and twist-boat (C_1 symmetry) as stable minimum structures (Figure 4). We found the chair conformation to be more stable by 11.1 (PBE-D3/def2-TZVPP) and 11.2 kJ mol^{-1} (CCSD(T)/def2-TZVPP) in electronic energies and 12.5 kJ mol^{-1} (PBE-D3/def2-TZVPP) in Gibbs energies at standard conditions (Figure 5). The conversion energy barrier from twist-boat to chair was calculated to be 21.2 (PBE-D3) and 23.0 kJ mol^{-1} (CCSD(T)) in electronic energies and 20.2 kJ mol^{-1} (PBE-D3) in Gibbs energies. These values are in good agreement with a previous MP2/6-31G* study[27] that found 11.7 kJ mol^{-1} for the energy difference and 25.9 kJ mol^{-1} for the energy barrier. Furthermore, electron diffraction experiments,[28] force field calculations[29] and a ^{13}C NMR study showing only four signals[30] also suggest that the twist-boat conformation can be neglected over a wide temperature range including room temperature.

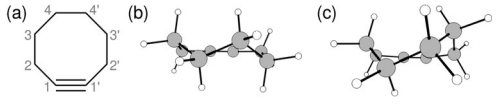

Figure 4. (a) Lewis structure of cyclooctyne with numbering used subsequently. (b) Chair conformation (C_2) and (c) twist-boat conformation (C_1), viewed along the direction corresponding to the symmetry axis of the chair conformation.

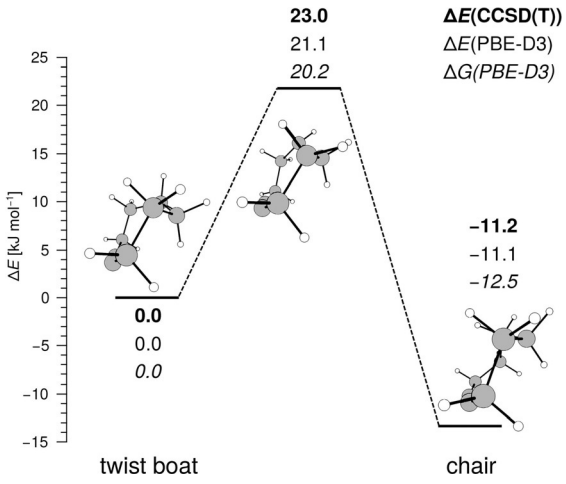

Figure 5. Relative energies of the two conformations of cyclooctyne and the corresponding transition state. Energies (in kJ mol^{-1}) calculated at CCSD(T)/def2-TZVPP and PBE-D3/def2-TZVPP on PBE-D3 structures.

Structural parameters of the optimized molecule in chair conformation are found in Table 2. The C–C bond lengths and C-C-C angles are in good agreement with previous calculations at the Hartree–Fock/6-31G* level[27] and experimental results.[28]

Table 2. Structural parameters of the carbon frame of optimized cyclooctyne in chair conformation.[a] Numbering according to Figure 4(a).

Method	Structural parameter				
	$r_{11'}$	r_{12}	r_{23}	r_{34}	$r_{44'}$
PBE-D3/def2-TZVPP[b]	1.215	1.455	1.553	1.547	1.560
HF/6-31G*[c]	1.188	1.466	1.547	1.549	1.561
Exp.[d]	1.232	1.459	1.491	1.584	1.584
	$\alpha_{1'12}$	α_{123}	α_{234}	$\alpha_{344'}$	
PBE-D3/def2-TZVPP[b]	157.5	107.0	115.6	118.4	
HF/6-31G*[c]	159.9	106.5	114.0	115.1	
Exp.[d]	158.5	110.1	109.6	110.3	

[a] Bond lengths r in Å, angles α in degrees. [b] This study. [c] Ref. [27]. [d] Ref. [28], measured by electron diffraction in gas phase. Uncertainty: ±0.012 Å (r), ±0.9° (α). A constrained structural model was used in the refinement.

Differences, the largest ones to experiment being 0.062 Å and 8.1°, can be attributed to missing temperature and anharmonicity effects that have not been considered in our calculations as well as the simplified structural model assumed in the data refinement of the experimental study.

The triple bond C≡C–C angle $\alpha_{1'12} = 157.5°$ nicely illustrates the concept of ring strain as it strongly deviates from the ideal value of 180°. For cyclooctyne, however, the ring closure forces the triple bond to bend and a deformation energy corresponding to ring strain is stored within the molecule. This ring strain energy is not an observable due to the lack of an unstrained reference molecule of same chemical composition. Estimates

based on hydration energies or cyclization energies using fragmentation schemes lead to a value of around 80 kJ mol^{-1}.[7] Effects of ring strain are found, for example, in the increased reactivity of strained alkynes in comparison to linear ones.[7,31]

2.2. Chemisorption of cyclooctyne on Si(001)

2.2.1. Adsorption modes

Four chemisorbed modes were found (Figure 6, also see Figure 2): In the 'on-top' mode (a), the molecule is bound to two atoms of a single surface dimer (Figure 1, Si_{up} and Si_{down}),

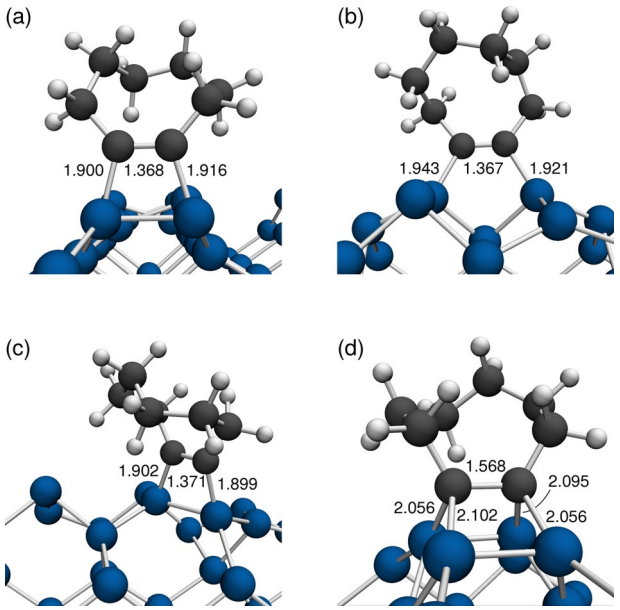

Figure 6. Adsorption modes (PBE-D3) of cyclooctyne on Si(001): (a) 'on-top', (b) 'bridge', (c) 'sublayer', (d) 'pedestal'. *d*(C–Si) and *d*(C–C) given in Å.

whereas in the 'bridge' motif (b) it is rotated by 90° and forms bonds to one atom each of two adjacent dimers. These are also known as the predominant bonding motifs reported for acetylene on Si(001).[32] The 'sublayer' mode mirrors a structure proposed in a theoretical study on acetylene adsorption[33] which has not yet been experimentally observed but could be a relevant intermediate state at low temperatures. In this case, the covalent bonds are formed to a silicon dimer atom and a neighboring atom (Figure 1, Si_{sub}) of the next lowest layer. The 'pedestal' mode is similar to 'on-top', but instead of being bound to a single surface dimer, the molecule forms four covalent bonds to two adjacent dimers. Based on the number of covalent C–Si bonds being formed in the adsorption process, the terms di-σ and tetra-σ are frequently used in the literature as mentioned above. The term di-σ will be used in the following to refer to the group of 'on-top', 'bridge', and 'sublayer' modes.

The number of covalent bonds to the surface is also reflected in the C–C distance of the former triple bond: While the di-σ structures show values of 1.368 ('on-top'), 1.367 ('bridge') and 1.371 Å ('sublayer'), typical values for C=C double bonds, this bond is significantly longer in the 'pedestal' mode (1.568 Å), indicating a C–C single bond. This underlines that in order to form bonds to the surface, one (di-σ) or both ('pedestal') of the molecular π systems have to be broken, resulting in sp^2 (di-σ) or sp^3 ('pedestal') hybridized carbon atoms.

Carbon–silicon bond lengths are in a similar range for all di-σ structures: The shortest bonds are present in the 'sublayer' structure (1.899/1.902 Å), in 'on-top' they are marginally longer (1.900/1.916 Å), whereas 'bridge' features the longest C–Si bonds (1.921/1.943 Å). In contrast, bond lengths in the 'pedestal' mode are significantly longer (2.056–2.102 Å). This is caused by the formation of four equivalent bonds, the lengths of which are limited by the distance of the two surface dimers to each other, which is 3.831 Å in the relaxed slab. Although these two dimers deform to get closer to the molecule during bond formation (distance in 'pedestal': 3.018 Å), the gain in energy by covalent bond formation is at some point compensated by the strain energy caused by this surface deformation.

The values for the di-σ structures are in good agreement with the X-ray structural analysis of the molecular analogue disilacyclobut-3-ene featuring *d*(C–C') = 1.357(3) and *d*(C–Si) = 1.882(2)/1.881(2) Å.[13]

Bonding energies of the four structures investigated are given in Table 3. To determine effects of the cell size in *y* direction on these quantities, calculations were done in a (4×2) and a (4×4) sized cell. This comparison has been done before for ethylene on Si(001), where results showed that significant errors remain with a (4×2) cell for the 'bridge' structure.[23] This is confirmed for cyclooctyne: Whereas the 'on-top' and 'pedestal' modes do not show large differences, the 'bridge' and 'sublayer' structures are artificially stabilized in the smaller cell by 16–17 kJ mol^{-1}. These findings underline that for types of adsorption structures that include bonding to more than one dimer of a row, the cell size in the *y* direction has to be increased in order to get reliable results. An explanation for this is: when the chemical environment of two adjacent dimers in a row is changed in a (4×2) cell, the system depicts a whole row being structurally changed. In contrast, in a (4×4) cell there are still two relaxed dimers in addition to the reaction site. The effect should in principle also be apparent for the 'pedestal' mode, but the bonding energies in both cells are

Table 3. Bonding energies E_{bond} of all adsorption modes of cyclooctyne and acetylene on the Si(001) surface investigated. Calculations done in both a (4×2) unit cell and a (4×4) sized supercell.[a]

	'On-top'	'Bridge'	'Sublayer'	'Pedestal'
cyclooctyne				
(4×2) cell	−306	−279	−235	−124
(4×4) cell	−308	−263	−218	−123
acetylene				
(4×2) cell	−267	−263	−129	−104
(4×4) cell	−268	−249	−120	−97

[a] All values in kJ mol^{-1}, calculated using PBE-D3/PAW.

very similar. This issue will be addressed in Section 2.2.3, when comparison to acetylene is made. From this point on, only energies of the (4×4) cell will be discussed.

The 'on-top' structure is clearly the most stable one with a bonding energy of −306 kJ mol^{-1} in electronic energies (E_{bond}) and −238 kJ mol^{-1} in Gibbs energies (G_{bond}, Table 4), followed by 'bridge' (E_{bond}: −263 kJ mol^{-1}, G_{bond}: −198 kJ mol^{-1}) and 'sublayer' (E_{bond}: −218 kJ mol^{-1}, G_{bond}: −149 kJ mol^{-1}). The most weakly bound mode is 'pedestal' (E_{bond}: −123 kJ mol^{-1}, G_{bond}: −54 kJ mol^{-1}), which results from the high deformation energies in both surface and molecule to form the four bonds (see also Section 2.2.3). The differences in E_{bond} within the di-σ structures ('on-top', 'bridge', 'sublayer') can mainly be explained by the surface deformation energy (compare Figure 3): For 'on-top', only one dimer has to deform, for 'bridge' two dimers and for 'sublayer', bonds within the surface have to rearrange additionally.

Table 4. Gibbs bonding energies G_{bond} and dispersion contribution to the electronic bonding energy E_{bond} of all binding motifs investigated of cyclooctyne and acetylene on Si(001).[a]

	'On-top'	'Bridge'	'Sublayer'	'Pedestal'
cyclooctyne				
G_{bond}(PBE-D3)	−238	−198	−149	−54
E_{bond}(PBE-D3)	−308	−263	−218	−123
E_{bond}(PBE)[b]	−261	−213	−149	−75
E_{bond}(D3) [b]	−47	−50	−69	−48
acetylene				
G_{bond}(PBE-D3)	−204	−187	−66	−36
E_{bond}(PBE-D3)	−268	−249	−120	−97
E_{bond}(PBE)[b]	−253	−231	−92	−91
E_{bond}(D3) [b]	−15	−18	−28	−6

[a] All values in kJ mol^{-1}, calculated using PBE-D3/PAW in a (4×4) cell. [b] The bonding contributions from PBE and the dispersion correction scheme are given separately to enable discussion about the respective influence on the bonding energy.

The dispersion contribution to the bonding energy, E_{bond}(D3), can also be found in Table 4. Whereas 'on-top', 'bridge' and 'pedestal' have similar contributions of 47–50 kJ mol^{-1}, in 'sublayer' it is higher by about 20 kJ mol^{-1}, because the molecule is closer to other surface atoms by bonding to an atom of the sub-surface layer. In that case, dispersion makes up 32% of the total bonding energy, unusually high compared to small organic molecules like ethylene or acetylene,[34] but expectable since adsorption of large organic molecules like benzene shows an even higher contribution of dispersion.[34b,35] In addition to the influence on the bonding energy, the inclusion of dispersion also has an effect on the structure of adsorbed states: Figure 7 shows a side view of the optimized 'on-top' and 'pedestal' modes with the molecule tilted sideways over the surface. The vertical difference Δz between the highest carbon atom of the molecule and the adjacent Si_{up} atom, an indicator for the amount of tilting, is lowered by 0.333 Å ('on-top') and 0.161 Å ('pedestal') when including dispersion forces during optimization, a decrease by 8 and 4%, respectively. This highlights the importance of describing dispersion effects properly when investigating the adsorption of large molecules on semiconductors as has been shown before for metal surfaces.[36]

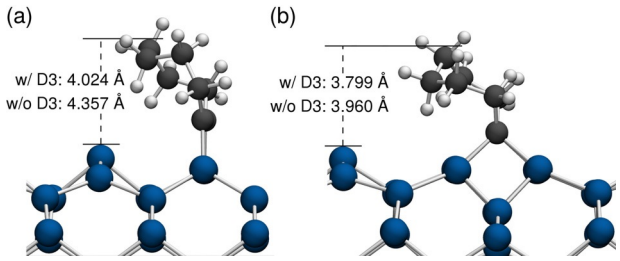

Figure 7. Tilting of adsorbed cyclooctyne with (w/) and without (w/o) dispersion correction: (a) 'on-top', (b) 'pedestal' mode. The distance given is the vertical difference Δz between the topmost carbon atom of the molecule and the adjacent Si_{up} atom.

2.2.2. Comparison with experiment

In a previous experimental study on the adsorption of cyclooctyne on Si(001),[11] STM images at low coverage showed all signals to be symmetric with respect to the dimer rows and the vast majority have a maximum between two dimers of a row. 'Bridge' and 'sublayer' structures can thus easily be ruled out based on symmetry considerations. Asymmetric signals were observed in STM studies of 'bridge'-bound ethylene and acetylene on Si(001)[32b,37] and predicted by theory for 'sublayer'-bound acetylene.[33] The question whether the signals observed represents a molecule in 'pedestal' or a tilted 'on-top' mode remains, since both modes would result in similar features. Analyzing these findings in the light of our theoretical results from the last section, it can be concluded that those signals correspond to the 'on-top' structure: Comparing the two structures, it becomes clear that the 'on-top' structure is tilted in a way that the maximum height of the adsorbed molecule would lie between two dimers, whereas in the 'pedestal' structure, it would lie on top of one of the dimers the molecule is bound to (Figure 7). Therefore, a signal with a maximum between two dimers and no other features corresponds to the bent 'on-top' structure. Furthermore, this mode is much more strongly bound to the surface than 'pedestal', providing the additional argument of thermodynamic stability.

Measurements at higher coverages revealed that the adsorbed molecules form non-statistical chains with an average distance of 1.5 to 2 dimers per molecule.[11] This can be understood by the effect of higher coverages on the amount of tilting in the molecules, as our STM simulation of four molecules in a (4×8) cell (Figure 8) shows: When three molecules adsorb next to each other in a row (dimers 2, 3 and 4), the outer ones tend to tilt similarly to an isolated molecule (dimer 7), resulting in a maximum height appearing between two dimers (feature A). In contrast, the central molecule cannot tilt due to the limited space and its maximum appears on top of a dimer (feature B). Therefore, in a three-molecule chain, the distance between the molecules would appear to be 1.5 dimers, whereas

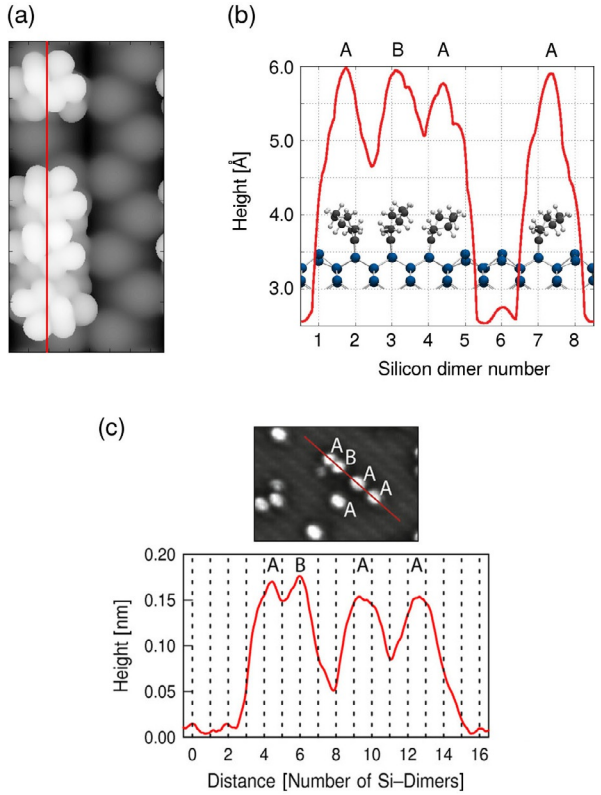

Figure 8. (a) Simulated STM topography ($U=-3$ V) of four cyclooctyne molecules adsorbed 'on-top' in a (4×8) cell of Si(001). (b) Height profile along the red line in (a) with superimposed structure. A: Maximum between two dimers, B: Maximum on top of a dimer. (c) Experimentally measured STM topography ($U=-2.0$ V) reproduced with permission from Ref. [11].

they are all adsorbed next to each other. This can be generalized to longer chains by imagining another molecule binding to dimer 6 in Figure 8(b), which would, again due to limited space, not be able to tilt extensively, resulting in a B feature for this molecule and an A-B-A-B-A arrangement of the whole chain. As a consequence, the row would be almost completely covered and approaching molecules unable to bind to dimers 1, 5 and 8 due to the tilted molecules blocking the adsorption sites. This arrangement would correspond to a coverage of 5/8 or 0.63 monolayers (ML) and an average distance between adsorbed molecules of 1.6 dimers, both in good agreement with the experimental values of 0.57 ML coverage and 1.5–2 dimers separation for maximum coverage. Further investigations on high-coverage effects, for example, changes in adsorption dynamics,[23] are currently underway.

2.2.3. Bonding analysis of the 'on-top' and 'pedestal' modes

The reason why the 'pedestal' mode is so much weaker bound compared to the 'on-top' mode although it features two more covalent bonds to the surface can be addressed by applying the pEDA bonding analysis scheme to the structures. The results (Table 5) show that whereas the 'pedestal' mode shows intrinsically stronger bonding, which is reflected in higher values for all pEDA terms (ΔE_{int}(elec), ΔE_{Pauli}, ΔE_{elstat}, ΔE_{orb}), all

Table 5. pEDA analysis of cyclooctyne and acetylene adsorbed on Si(001) in the 'on-top' and 'pedestal' modes.[a]

	'On-top'	'Pedestal'
cyclooctyne		
ΔE_{int}	−658	−958
ΔE_{int}(disp)[b]	−43 (7%)	−41 (4%)
ΔE_{int}(elec)[b]	−615 (93%)	−917 (96%)
ΔE_{Pauli}	1468	2045
ΔE_{elstat}[c]	−936 (45%)	−1281 (43%)
ΔE_{orb}[c]	−1148 (55%)	−1680 (57%)
ΔE_{prep}(Mol)	313	608
ΔE_{prep}(Surf)	26	206
E_{bond}[d]	−319 (−308)	−144 (−123)
acetylene		
ΔE_{int}	−668	−997
ΔE_{int}(disp)[b]	−12 (2%)	−1 (0%)
ΔE_{int}(elec)[b]	−656 (98%)	−996 (100%)
ΔE_{Pauli}	1323	1959
ΔE_{elstat}[c]	−828 (42%)	−1202 (41%)
ΔE_{orb}[c]	−1152 (58%)	−1753 (59%)
ΔE_{prep}(Mol)	364	677
ΔE_{prep}(Surf)	25	204
E_{bond}[d]	−279 (−268)	−116 (−97)

[a] All values in kJ mol^{-1}, calculated at PBE-D3/TZ2P. Fragments: Molecule and surface. Fragmentation: Triplet ('on-top') and quintet ('pedestal'). [b] Percentage values give electronic and dispersion contributions to the interaction energy ΔE_{int}. [c] Percentage values give the contribution to attractive interactions in the pEDA Scheme $\Delta E_{elstat}+\Delta E_{orb}$. [d] PAW values (in parentheses) given for comparison.

stabilizing contributions except ΔE_{int}(disp) are only 37–46% stronger compared to 'on-top'. If all four bonds in the 'pedestal' mode were as strong as the two in the 'on-top' mode, the stabilizing terms would see an increase of 100%. This means that each 'pedestal' bond is actually 30% weaker than an 'on-top' bond. This decrease in stabilization is due to the forced increase in C–Si bond length (Figure 6) that has been mentioned before. In addition to that, the molecular preparation energy for 'pedestal' is about twice as large as for the 'on-top' mode and the surface preparation energy is eight times as high due to the large deformation mentioned before and visible in Figure 7. These preparation energies destabilize the system much more than the formation of two additional bonds is able to stabilize it and they are the main reason why this mode is much more weakly bound than the 'on-top' mode.

2.2.4. Comparison to the adsorption of acetylene on Si(001)

The comparison to acetylene, the prototype alkyne, is of particular interest in these investigations, since it allows us to determine the influence of the strained triple bond and the additional CH_2 groups of the ring on the adsorption. Moreover, acetylene adsorption on Si(001) has been extensively studied in experiment[32,38] and theory.[33,34,39] Since there is no previous theoretical study on the adsorption of cyclooctyne, investigation of acetylene allows us to compare and evaluate the reliability of our approach.

Bonding energies in small (4×2) and large (4×4) cells show that for this molecule, too, the (4×2) cell is not large enough to describe the 'bridge' and 'sublayer' modes properly (Table 3). The 'bridge' mode even appears to be almost as strongly bound to the surface as the 'on-top' mode, which might lead to false conclusions regarding relative thermodynamic stability. In contrast to cyclooctyne, a larger difference of 7 kJ mol^{-1} is also apparent for the 'pedestal' mode. Since surface deformation should be similar in both systems, the difference must be a result of the large cyclooctyne molecule interacting with images of itself in neighboring cells. This is confirmed by calculation of the molecular preparation energy (Supporting Information, Table S2), where the stabilization due to the smaller cell size is 5 kJ mol^{-1} stronger for cyclooctyne than for acetylene.

The (4×4) cell bonding energies of acetylene (Table 4) show first of all that the dispersion contribution in this system is, as expected, significantly smaller due to the smaller size of the molecule. Moreover, the 'on-top' mode is again the most stable structure with −268 kJ mol^{-1} in electronic energies (G_{bond}: −204 kJ mol^{-1}), where literature values range from −253 to −297 kJ mol^{-1}[33,34,39]. This is 40 kJ mol^{-1} less than the bonding energy of cyclooctyne and can be attributed to a difference of 32 kJ mol^{-1} in dispersion contribution and 8 kJ mol^{-1} in electronic contribution. The nature of this becomes apparent in pEDA analysis (Table 5):[40] The intrinsic interaction energy ΔE_{int} of acetylene to Si(001) is actually stronger than the one of cyclooctyne, even with the inclusion of the large difference in dispersion. This, however, is compensated by the preparation energy which is 51 kJ mol^{-1} higher in acetylene. Because the cyclooctyne triple bond is already bent and therefore preformed for bonding to the surface, the need for deformation is decreased, since part of the deformation energy of linear alkynes is already contained in the ring strain. Furthermore, pEDA analysis shows that covalent bonding contributions (ΔE_{orb}) are equally strong in both systems and the differences result from the other terms. These values also show that the weaker interaction energy of cyclooctyne is due to the heightened Pauli repulsion ΔE_{Pauli}, since all stabilizing components are either the same (ΔE_{orb}) or more stabilizing (ΔE_{int}(disp), ΔE_{elstat}) than in the acetylene system.

The bonding energies of the 'bridge' and 'pedestal' modes (Table 4) are weaker than the ones of cyclooctyne with values of −249 ('bridge', literature: −236 to −253 kJ mol^{-1},[33,34a,39] G_{bond}: −187 kJ mol^{-1}) and −97 kJ mol^{-1} ('pedestal', literature: −63 to −124 kJ mol^{-1}[34a,39a], G_{bond}: −36 kJ mol^{-1}), but only due to the lower dispersion energy caused by the smaller size of the molecule. The PBE bonding energies are even stronger by 16–18 kJ mol^{-1}, showing that this molecule better fits to electronically interact with the surface in these modes. Comparison of pEDA values between 'on-top' and 'pedestal' are similar to cyclooctyne: although all terms except dispersion are about 50% stronger, the larger preparation energies of molecule and surface compensate this and destabilize the system. The difference in molecular preparation energies is even more pronounced than for 'on-top' at 69 kJ mol^{-1}.

Finally, the 'sublayer' structure shows the largest difference in bonding energy compared to cyclooctyne with a value of −120 kJ mol^{-1} (Literature: −97 kJ mol^{-1},[33] G_{bond}: −66 kJ mol^{-1}) compared to −218 kJ mol^{-1}. Although this is again partly caused by the higher contribution of dispersion interactions, the arrangement of surface atoms is actually different in both structures: whereas the acetylene 'sublayer' sees a Si_{down}—Si_{sub} bond broken (see Figure 1 for nomenclature) and the molecule inserting into it,[33] for cyclooctyne, this bond stays intact, but a Si_{sub}—Si_{sub2} bond is broken and the Si_{sub2} atom regains this bond by attaching to the Si_{down} atom of the adjacent dimer. This surface might be energetically more stable than the one of the acetylene insertion, thus stabilizing the whole system.

Although the final state adsorption structures and energies of acetylene and cyclooctyne are comparable, the adsorption dynamics leading to these states might be different. Experiments found the adsorption of acetylene to occur via a precursor intermediate state,[38] which might be the 'sublayer' structure,[33] whereas the adsorption of cyclooctyne was found to be direct without any intermediates.[10] This topic is currently under investigation.

3. Conclusion

We have presented four possible adsorption modes of cyclooctyne on Si(001), 'on-top', 'bridge', 'sublayer' and 'pedestal', and calculated their electronic and Gibbs energies of bonding. The 'on-top' mode is the thermodynamically most stable and the 'pedestal' mode the most unstable one. Major influence of dispersion interactions has been found for structures as well as bonding energies. With the aid of our calculated structures and STM simulations, experimental features are well explained by a tilted 'on-top' adsorption structure. Using bonding analysis, we have shown that the 'pedestal' mode, although featuring four covalent bonds to the surface, is much more weakly bound to the surface than the other states due to a major increase in preparation energies of both molecule and surface. Comparing the bonding of cyclooctyne to Si(001) with acetylene, the lowered deformation energy of the molecule resulting from the strained triple bond makes cyclooctyne adsorption more favorable, although the intrinsic interaction energy is actually larger for acetylene.

In summary, our results have shown that although adsorption of cyclooctyne on Si(001) proceeds similar to acetylene, the conformational flexibility of the molecule and dispersion interaction between molecule and surface complicate analysis of experimental results. DFT studies provide insight into interplay of ring strain and flexibility of the large adsorbates and provide a rationale for the observed final states in terms of bonding analysis.

Acknowledgements

This work was supported by Deutsche Forschungsgemeinschaft within SFB 1083. Computational resources were provided by HRZ Marburg, HLR Stuttgart and CSC-LOEWE Frankfurt.

We thank Dr. Marc Raupach (Amsterdam) for support and Prof. Michael Dürr (Gießen), Prof. Ulrich Höfer (Marburg), Prof. Ulrich Koert (Marburg) for discussions. We thank Prof. Felix Studt (Karlsruhe) for discussions regarding a consistent definition of dispersion contributions in the context of pEDA.

Keywords: bonding analysis · density functional calculations · dispersion · silicon · surface analysis

[1] A. V. Teplyakov, S. F. Bent, *J. Vac. Sci. Technol. A* **2013**, *31*, 50810.
[2] a) H. Neergaard Waltenburg, J. T. Yates Jr., *Chem. Rev.* **1995**, *95*, 1589; b) R. A. Wolkow, *Annu. Rev. Phys. Chem.* **1999**, *50*, 413; c) S. F. Bent, *Surf. Sci.* **2002**, *500*, 879.
[3] R. J. Hamers, S. K. Coulter, M. D. Ellison, J. S. Hovis, D. F. Padowitz, M. P. Schwartz, C. M. Greenlief, J. N. Russell, Jr., *Acc. Chem. Res.* **2000**, *33*, 617.
[4] R. E. Schlier, H. E. Farnsworth, *J. Chem. Phys.* **1959**, *30*, 917.
[5] J. Yoshinobu, *Prog. Surf. Sci.* **2004**, *77*, 37.
[6] T. R. Leftwich, A. V. Teplyakov, *Surf. Sci. Rep.* **2008**, *63*, 1.
[7] R. D. Bach, *J. Am. Chem. Soc.* **2009**, *131*, 5233.
[8] D. Heber, P. Rösner, W. Tochtermann, *Eur. J. Org. Chem.* **2005**, 4231.
[9] a) N. J. Agard, J. A. Prescher, C. R. Bertozzi, *J. Am. Chem. Soc.* **2004**, *126*, 15046; b) S. T. Laughlin, J. M. Baskin, S. L. Amacher, C. R. Bertozzi, *Science* **2008**, *320*, 664; c) M. F. Debets, S. S. van Berkel, J. Dommerholt, A. J. Dirks, F. P. J. T. Rutjes, F. L. van Delft, *Acc. Chem. Res.* **2011**, *44*, 805.
[10] M. Reutzel, N. Münster, M. A. Lipponer, C. Länger, U. Höfer, U. Koert, M. Dürr, *J. Phys. Chem. C* **2016**, *120*, 26284.
[11] G. Mette, M. Dürr, R. Bartholomäus, U. Koert, U. Höfer, *Chem. Phys. Lett.* **2013**, *556*, 70.
[12] K. Akagi, S. Tsuneyuki, Y. Yamashita, K. Hamaguchi, J. Yoshinobu, *The Ninth International Conference on the Formation of Semiconductor Interfaces* **2004**, *234*, 162–167.
[13] J. Belzner, H. Ihmels, B. O. Kneisel, R. Herbst-Irmer, *J. Chem. Soc. Chem. Commun.* **1994**, 1989–1990.
[14] M. Raupach, R. Tonner, *J. Chem. Phys.* **2015**, *142*, 194105.
[15] Gaussian09 Revision C.01, Gaussian Inc. Wallingford CT, **2009**.
[16] TURBOMOLE V6.3.1, a development of University of Karlsruhe and Forschungszentrum Karlsruhe GmbH, 1989–2007, TURBOMOLE GmbH, since 2007; available from http://www.turbomole.com, **2010**.
[17] a) J. P. Perdew, K. Burke, M. Enzerhof, *Phys. Rev. Lett.* **1996**, *77*, 3865; b) J. P. Perdew, K. Burke, M. Enzerhof, *Phys. Rev. Lett.* **1997**, *78*, 1396.
[18] a) S. Grimme, J. Antony, S. Ehrlich, S. Krieg, *J. Chem. Phys.* **2010**, *132*, 154104; b) S. Grimme, S. Ehrlich, L. Goerigk, *J. Comput. Chem.* **2011**, *32*, 1456.
[19] F. Weigend, R. Ahlrichs, *Phys. Chem. Chem. Phys.* **2005**, *7*, 3297.
[20] a) G. Kresse, J. Hafner, *Phys. Rev. B* **1993**, *47*, 558; b) G. Kresse, J. Hafner, *Phys. Rev. B* **1994**, *49*, 14251; c) G. Kresse, J. Furthmüller, *Phys. Rev. B* **1996**, *54*, 11169; d) G. Kresse, J. Furthmüller, *Comput. Mater. Sci.* **1996**, *6*, 15.
[21] a) P. Blöchl, *Phys. Rev. B* **1994**, *50*, 17953; b) G. Kresse, D. Joubert, *Phys. Rev. B* **1999**, *59*, 1758.
[22] M. R. Hestenes, E. Stiefel, *J. Res. Natl. Bur. Stand.* **1952**, *49*, 409.
[23] J. Pecher, G. Mette, M. Dürr, R. Tonner, *ChemPhysChem* **2017**, *18*, DOI:10.1002/cphc.201601134.
[24] D. R. J. Boyd, *J. Chem. Phys.* **1955**, *23*, 922.
[25] a) J. Tersoff, D. R. Hamann, *Phys. Rev. Lett.* **1983**, *50*, 1998; b) J. Tersoff, D. R. Hamann, *Phys. Rev. B* **1985**, *31*, 805.
[26] BAND 2016, SCM, Theoretical Chemistry, Vrije Universiteit, Amsterdam, The Netherlands, can be found under http://www.scm.com.
[27] I. Yavari, F. Nasiri, H. Djahaniani, A. Jabbari, *Int. J. Quantum Chem.* **2006**, *106*, 697.
[28] J. Haase, A. Krebs, *Z. Naturforsch. A* **1971**, *26*, 1190.
[29] M. Trætteberg, W. Lüttke, R. Machinek, A. Krebs, H. J. Hohlt, *J. Mol. Struct.* **1985**, *128*, 217.
[30] R. Bartholomäus, *Ph.D. thesis*, Philipps-Universität Marburg, **2013**.
[31] N. Münster, P. Nikodemiak, U. Koert, *Org. Lett.* **2016**, *18*, 4296.
[32] a) F. Matsui, H. W. Yeom, a. Imanishi, K. Isawa, I. Matsuda, T. Ohta, *Surf. Sci.* **1998**, *401*, L413; b) W. Kim, H. Kim, G. Lee, J. Chung, S. Y. You, Y. K. Hong, J. Y. Koo, *Surf. Sci.* **2002**, *514*, 376.
[33] Q. J. Zhang, X. L. Fan, W. M. Lau, Z. F. Liu, *Phys. Rev. B* **2009**, *79*, 195303.
[34] a) P. T. Czekala, H. Lin, W. A. Hofer, A. Gulans, *Surf. Sci.* **2011**, *605*, 1341; b) S. W. Kim, J. H. Lee, H. J. Kim, J. H. Cho, *Chem. Phys. Lett.* **2013**, *557*, 159.
[35] H.-J. Kim, A. Tkatchenko, J.-H. Cho, M. Scheffler, *Phys. Rev. B* **2012**, 85.
[36] R. J. Maurer, V. G. Ruiz, J. Camarillo-Cisneros, W. Liu, N. Ferri, K. Reuter, A. Tkatchenko, *Prog. Surf. Sci.* **2016**, *91*, 72.
[37] G. Mette, C. H. Schwalb, M. Dürr, U. Höfer, *Chem. Phys. Lett.* **2009**, *483*, 209.
[38] P. A. Taylor, R. M. Wallace, C. C. Cheng, W. H. Weinberg, M. J. Dresser, W. J. Choyke, J. T. Yates, Jr., *J. Am. Chem. Soc.* **1992**, *114*, 6754.
[39] a) D. C. Sorescu, K. D. Jordan, *J. Phys. Chem. B* **2000**, *104*, 8259; b) P. L. Silvestrelli, O. Pulci, M. Palummo, R. Del Sole, F. Ancilotto, *Phys. Rev. B* **2003**, *68*, 235306; c) J.-H. Cho, L. Kleinman, *Phys. Rev. B* **2004**, *69*, 75303; d) N. Takeuchi, *Surf. Sci.* **2007**, *601*, 3361; e) M. Marsili, O. Pulci, M. Palummo, P. Luigi, R. Del, *Superlattices Microstruct.* **2009**, *46*, 240.
[40] pEDA analysis of the acetylene/Si(001) 'on-top' structure has also been published in Ref. [14]. The minor numerical differences can be attributed to the different computational setup (e.g. smaller cell size).

Manuscript received: December 21, 2016
Accepted Article published: January 24, 2017
Final Article published: February 16, 2017

CHEMISTRY
A European Journal

Supporting Information

Chemisorption of a Strained but Flexible Molecule: Cyclooctyne on Si(001)

Josua Pecher,[a] Christoph Schober,[a, b] and Ralf Tonner*[a]

chem_201605952_sm_miscellaneous_information.pdf

Supporting Information

Contents

1 Convergence Studies

To ensure reliability of results in computational studies, several technical parameters have to be chosen carefully. This allows for consistency and comparability with other computational work and furthermore makes sure that the errors caused by the choice of these technical parameters are insignificantly small for the results described by the methods. The accuracy of a given parameter can be checked by conducting variational convergence studies. i.e. a series of calculations where one parameter is varied and all other parameters are kept fixed. This is presented in the following for all relevant parameters of bulk silicon and additional parameters for adsorption studies on a Si(001) slab.

1.1 Bulk Silicon

Convergence studies of the bulk material are necessary, since the surface slab is based on the bulk lattice constant, which again is dependent on the number of k points sampling the Brillouin zone and the plane wave energy cutoff determining the size of the basis set. Hence, these are the three parameters varied in the calculation of a unit cell (diamond structure, eight atoms) of bulk silicon.

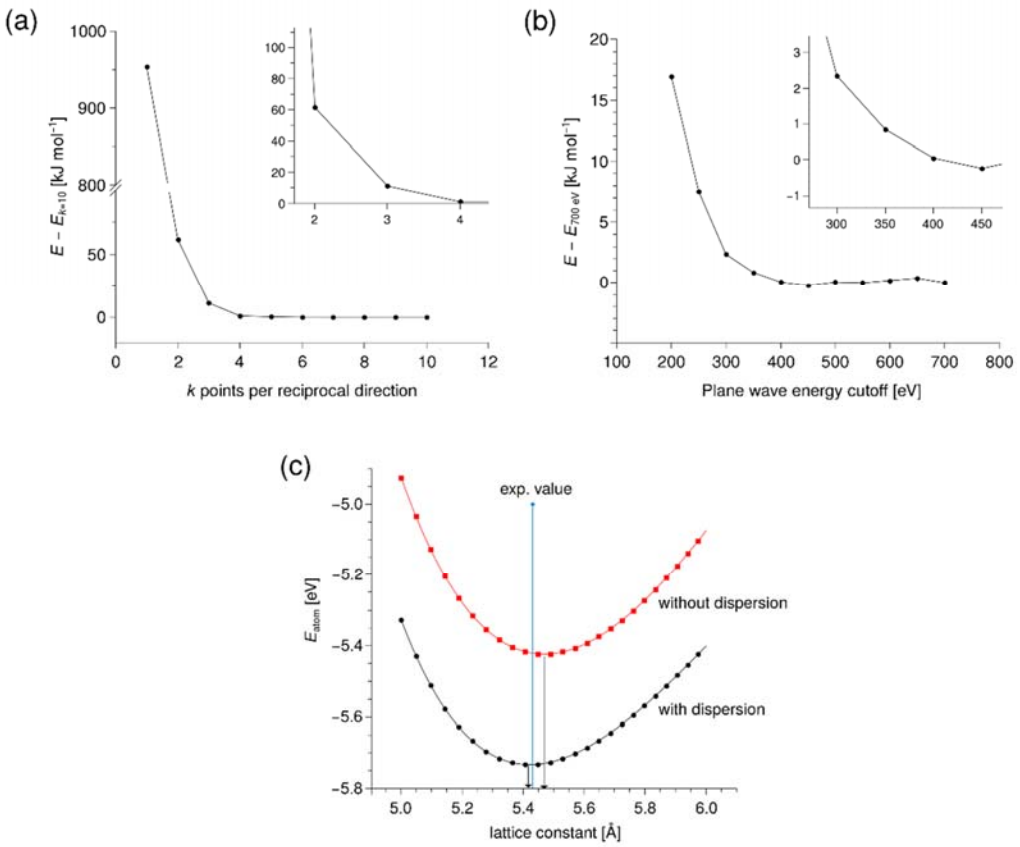

Figure S1 Variation of a) the number of k points in the Monkhorst-Pack grid, b) the plane wave energy cutoff and c) the lattice constant in the calculation of a silicon bulk unit cell (diamond structure). Choice of the other parameters: a) a = 5.500 Å, E_{cut} = 350 eV, b) a = 5.500 Å, Monkhorst-Pack(444) mesh, c) E_{cut} = 400 eV, Monkhorst-Pack(444) mesh.

The results (Figure S1) show that for values of four *k* points per reciprocal direction and a plane wave energy cutoff of 350 eV, a deviation of less than 1 kJ mol^{-1} per unit cell is reached in comparison to the calculations with the respective highest values. For the lattice constant, calculations were done with and without the D3 dispersion correction. The energy diagram (c) shows that with inclusion of D3, the energy minimum obtained at a lattice constant of a = 5.418 Å is much closer to the zero-point energy corrected[1] experimental value[2] of 5.415 Å in comparison to the value obtained without using dispersion correction (5.469 Å). This shows that even in the calculation of bulk material, the inclusion of dispersion corrections leads to better agreement with experiment. Thus, a lattice constant of 5.418 Å was used in the construction of the slab.

1.2 Si(001) Slab

Besides the *k* point sampling and the plane wave energy cutoff, two additional parameters arise for surface slabs: Due to the finite thickness, a number of atomic layers has to be chosen and additionally, the vacuum layer thickness in *z* direction of the periodic cell should be large enough to avoid interaction of the system with images of itself in that direction.

The plane wave energy cutoff showed the same behavior as in the bulk calculation, i.e. convergence to 1 kJ mol^{-1} at E_{cut} = 350 eV, therefore the data of the convergence study is not listed here.

Convergence of *k* point sampling was checked by calculating the adsorption energy of a cyclooctyne molecule in *on-top* geometry (see manuscript) in a (4×4) cell with a six-layer slab, a plane wave cutoff of 400 eV and a vacuum layer of 9 Å. The results are given in Table S1.

Table S1 Cyclooctyne *on-top* adsorption energy (in kJ mol^{-1}) as a function of the size of the *k* mesh sampling the Brillouin zone. Monkhorst-Pack (MP) and Gamma-centered (Γ) meshes were used.

mesh	E_{ads}(MP)	E_{ads}(Γ)
1 1 1	–314.4	–314.4
2 2 1	–307.6	–308.0
3 3 1	–307.8	–307.8
4 4 1	–307.8	–307.8
6 6 1	–307.8	–307.8

A residual error below 1 kJ mol^{-1} is reached at both a Monkhorst-Pack and a Gamma-centered 2×2×1 *k* mesh. Since the top of the valence band, an important part of the surface electronic structure, is located at the Gamma point for silicon(001),[3] we chose a Gamma-centered Γ(221) mesh for all subsequent calculations. For calculations in smaller (4×2) cells, a Γ(241) mesh was used analogously.

The convergence of the slab with respect to the number of atomic layers was determined by calculation of the surface energy σ, where the following equation of Fiorentini and Methfessel[4] was used:

$$\sigma = E_N - N\,E_{bulk}^{extrapolated}$$

Here, N denotes the number of layers, E_N the energy of an N-layer slab and $E_{\text{bulk}}^{\text{extrapolated}}$ the bulk energy of a single layer, which is taken in this case from the difference between the two slabs of highest thickness in this study, 12 and 14 layers:

$$E_{\text{bulk}}^{\text{extrapolated}} = \frac{1}{2}(E_{14} - E_{12})$$

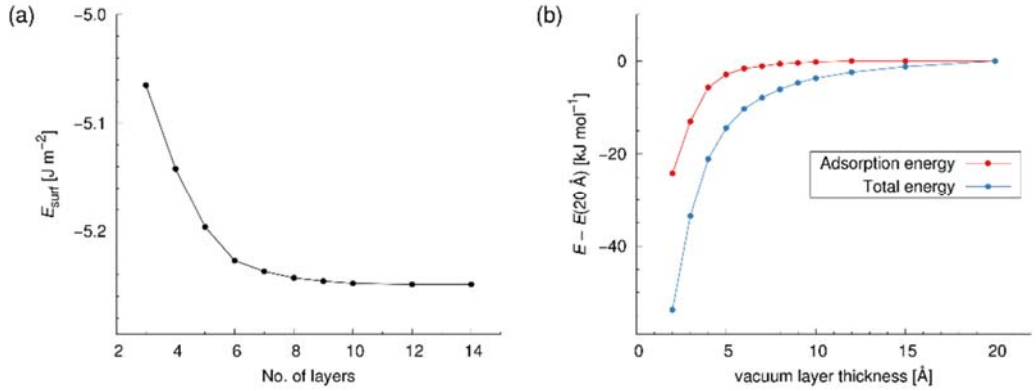

Figure S2 Convergence studies of a Si(001) surface slab: a) Surface energy E_{surf} as a function of the number of atomic layers, b) adsorption energy and total energy of a cyclooctyne molecule adsorbed *on-top* on a (4×4) Si(001) slab as a function of the vacuum layer thickness. Choice of the other parameters: E_{cut} = 400 eV and k mesh Γ(221) (both studies), a) Δz_{vacuum} = 12 Å, b) six layer slab.

The results (Figure S2(a)) show that the surface energy is converged to more than 99% accuracy at six silicon layers. Thus, a slab of this thickness was used in all calculations.

Effects of the vacuum layer thickness (Figure S2(b)) can be measured through two different quantities: The total energy of a system and an energy difference, as in this case, the adsorption energy of a cyclooctyne molecule *on-top* to the surface. While the total energy of an adsorbed molecule on the surface is not converged below 1 kJ mol^{-1} even at a vacuum layer thickness of 15 Å, the adsorption energy reaches this convergence already at 5 Å. However, in order to allow calculations with a larger molecule-surface distance to have the same accuracy, a value of 9 Å with respect to this structure was chosen in all subsequent calculations (corresponding to a cell size of 21.672 Å in z direction).

2 Molecular Preparation Energies in the *Pedestal* Mode

In order to explain why the energies of the *pedestal* structure do not differ in different cell sizes for cyclooctyne (ΔE = 1 kJ mol^{-1}), but for acetylene (ΔE = 7 kJ mol^{-1}), molecular preparation energies were calculated. The results (Table S2) show that the adsorbed cyclooctyne molecule gets stabilized by 10 kJ mol^{-1} in the smaller cell, while for acetylene, this stabilization is only 5 kJ mol^{-1}. This can be explained by the larger size of the cyclooctyne molecule, leading to a more pronounced interaction with images of itself in neighboring cells.

Table S2 Molecular preparation energies of cyclooctyne and acetylene in the *pedestal* structure in a (4×2) and (4×4) cell, calculated at PBE-D3/PAW in VASP. All values in kJ mol^{-1}.[a]

	Cyclooctyne	Acetylene
4×2 cell	412	515
4×4 cell	402	510

[a] Due to differences in methodology and the electronic state of the molecule, the preparation energies of the 4×4 cell differ from those given in Table 5 of the main article.

3 References

[1] a) A. B. Alchagirov, J. P. Perdew, J. C. Boettger, R. C. Albers, C. Fiolhais, *Phys. Rev. B* **2001**, *63*, 224115; b) V. N. Staroverov, G. E. Scuseria, J. Tao, J. P. Perdew, *Phys. Rev. B* **2004**, *69*, 075102; c) V. N. Staroverov, G. E. Scuseria, J. Tao, J. P. Perdew, *Phys. Rev. B* **2008**, *78*, 239907; d) P. Haas, F. Tran, P. Blaha, *Phys. Rev. B* **2009**, *79*, 085104.

[2] D. Windisch, P. Becker, *Phys. Status Solidi A* **1990**, *118*, 379.

[3] J. Yoshinobu, *Prog. Surf. Sci.* **2004**, *77*, 37.

[4] V. Fiorentini, M. Methfessel, *J. Phys.: Condens. Matter* **1996**, *8*, 6525.

Modeling the complex adsorption dynamics of large organic molecules: Cyclooctyne on Si(001)

*Lisa Pecher, Sebastian Schmidt, and Ralf Tonner**

Faculty of Chemistry and Material Sciences Center, Philipps-Universität Marburg, Hans-Meerwein-Straße 4, 35032 Marburg, Germany

ABSTRACT: We present a computational protocol for the description of the adsorption dynamics of large molecules (i.e. more than two non-hydrogen atoms) on surfaces at the example of the system cyclooctyne/Si(001). The system size prohibits the use of established accurate methods and approximations have to be made and validated. Our approach combines potential energy surface scans, reaction path determination methods, statistical thermodynamics and *ab initio* molecular dynamics simulations based on density functional theory (DFT). This leads to a conclusive picture of adsorption dynamics in this system in the limits of DFT accuracy. Surprising insight is gained regarding the adsorption pathways which are shown to be either direct or pseudo-direct in contrast to common precursor-mediated surface reactions. This shows how a thoughtful selection of DFT methods can comprehensively describe the adsorption dynamics of a system that might seem too complex for *ab initio* approaches at first glance.

1. Introduction

In the previous century, the study of the interaction between molecules and solid surfaces has become a highly relevant topic for chemists, physicists, and material scientists alike. Notable examples in this field are heterogeneous catalysis,[1] atomic layer deposition[2] and the organic functionalization of semiconductors.[3] Understanding the dynamical aspects of surface adsorption is of particular importance,[4,5] since it allows for a control, e.g. via temperature, of the adsorption process that leads to the formation of well-ordered structures and interfaces. Here, theory has made valuable contributions in recent decades and it is now possible to make reliable predictions for many questions in surface science.[6] State-of-the-art methods for simulating these processes make use of high-dimensional potential energy surfaces,[7] which can be constructed, e.g., by using effective medium theory[8–10] or neural networks.[11–13] The dynamics of nuclei on the PES is then described either by classical mechanics (Born-Oppenheimer molecular dynamics)[14] or quantum dynamical methods like the time-dependent wave-packet method.[15,16] For nonadiabatic processes, one might additionally need to include electron transfer, as it is done in the independent electron surface hopping algorithm.[17–19] Alternatively, if the adsorption dynamics is governed by a few processes, transition state theory or kinetic Monte Carlo[20] can be used to describe the system over longer timescales. Although many current applications of these methods deal with the adsorption of "small" molecules, a proper description is already complex and challenging. To investigate the adsorption dynamics of "large" molecules these methods are currently not applicable. The main reason is the rapid increase of degrees of freedom, leading to a higher dimensionality of the PES and consequently a huge increase in necessary computing time. Thus, "large" already comprises molecules with more than two non-hydrogen atoms.

Recent activities to apply machine-learning and big data approaches to surface and material science questions might be a future solution but are not widely applicable, yet.[21–24]

However, the adsorption of larger molecules brings in several exciting features: This includes the increased influence of dispersion interactions on structure and energy,[25–28] conformational freedom,[29,30] and the ability to functionalize the surface and build interfaces.[3,31,32] An exemplary system here is cyclooctyne on Si(001): This smallest cyclic alkyne stable under typical lab conditions forms dense and well-ordered structures upon adsorption[33] and the attachment of additional functional groups in synthesis was previously mastered,[34–37] so it can be used as a covalent linker between the substrate and other molecules or materials. Experiments furthermore indicate a direct adsorption channel into the final state, a [2+2] cycloadduct,[38] which is unusual, since unsatured molecules like ethylene usually adsorb via a precursor intermediate (Scheme 1). Understanding the origin of this difference might give important insight into the adsorption dynamics of organic molecules on semiconductors in general. Furthermore, it promises to enable the chemical design of adsorbates to reliably yield a desired surface structure under a wide range of conditions. Therefore, we selected this system as a prototype to develop an approach on how to investigate the complex adsorption dynamics of larger molecules on surfaces.

The usual approach of simulating large systems, i.e. by using force fields, is not applicable here due to the intricate electronic structure of the Si(001) surface[39] and the formation of covalent bonds in the adsorption process. While there have been studies of adsorption on Si(001) using the reactive force field ReaxFF,[40–44] none of them featured the characteristic buckling of the surface dimers.[39] This buckling is a decisive factor for a correct description of the reactivity with unsaturated organic molecules,[3] thus rendering the approach unsuitable for our investigations.

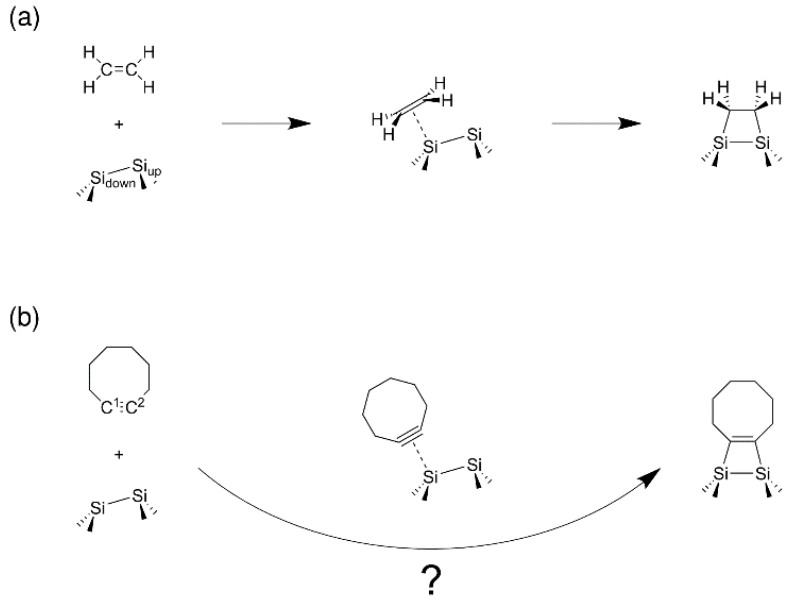

Scheme 1. Comparison between (a) the common precursor-mediated adsorption of ethylene and (b) the proposed direct adsorption of cyclooctyne on Si(001). A single surface dimer is shown to represent the surface.

Here, we present an approach on how to investigate such a complex system with computationally feasible DFT methodology. First, decisive regions on the PES will be identified by performing scans. Within these regions, the influence of selected degrees of freedom (molecule location and orientation) on the energy profile and trajectory of the system will be analyzed. In a third step, the effect of thermal excitation within molecule and surface will be studied. Throughout the study, results will be compared to previous experimental work to validate our approach.

2. Computational Methods

2.1. Structural Optimization

All calculations were done in the Vienna *Ab initio* Simulation Package (VASP)[45–48] version 5.3.5 using the exchange-correlation functional by Perdew, Burke and Enzerhof (PBE)[49,50] and the semiempirical D3(BJ) dispersion correction by Grimme and co-workers.[51,52] A plane wave basis set with a kinetic energy cutoff of 400 eV was used within the projector augmented wave (PAW) formalism,[53,54] while electronic *k* space was sampled using a gamma-centered Γ(221) Monkhorst-Pack grid. Self-consistent field (SCF) calculations were converged to an accuracy of 10^{-6} eV and structural optimization was performed using the Conjugate Gradient (CG) algorithm[55] with a convergence criterion of 10^{-2} eV Å^{-1}. Reaction paths were calculated using the Nudged Elastic Band (NEB) method,[56,57] optionally using the climbing-image modification[58] in case of the presence of transition states. Gibbs energies were calculated at $T = 300$ K and $p = 1$ bar in an approach described elsewhere[59] and harmonic frequencies were obtained by numerical construction of the Hessian using Cartesian displacements of 0.01 Å. All obtained minimum and transition state geometries are given in the Supporting Information.

The silicon(001) surface was modeled as a six-layer slab with the two bottom layers frozen in their bulk position and saturated with hydrogen atoms in the direction of the next layer bulk atoms. The Si-H distance was set to 1.480 Å, the experimental equilibrium distance in silane.[60] Cell constants *a* and *b* were both set to 15.324 Å, corresponding to a (4×4) cell with a lattice parameter of 5.418 Å. The surface structure was set to the most stable reconstruction, *c*(4×2).[39] To avoid artificial interaction with images of the slab in c direction, a vacuum layer of at least 10 Å was ensured. An extensive study on the convergence of these values was done previously.[61]

Bonding energies E_{bond} are given as the difference between the relaxed energy of the total system, E_{tot}, and the relaxed isolated surface and molecule energies, E_{surf} and E_{mol} (Equation 1). Please note that surface science convention is the use of the adsorption energy E_{ads} with inverse sign convention ($E_{\mathrm{ads}} = -E_{\mathrm{bond}}$).

$$E_{\mathrm{bond}} = E_{\mathrm{tot}} - E_{\mathrm{surf}} - E_{\mathrm{mol}} \qquad (1)$$

Bonding analysis was performed with periodic Energy Decomposition Analysis (pEDA)[62] in ADF-BAND 2016[63] using the PBE functional with D3 dispersion correction, a TZ2P basis set and a Γ-only sampling of electronic *k* space. Reaction rates were calculated using quasi-quantum harmonic transition state theory (qq-hTST), which uses the quantum-mechanical partition function for vibrations within the rate equation of classical transition state theory.[64,65]

2.2. Ab initio Molecular Dynamics

All AIMD simulations were performed in VASP using the same parameters as the structural optimizations except for a reduced SCF convergence accuracy of 10^{-5} eV. Trajectories were calculated using the velocity Verlet algorithm[66,67] with a time step of $\Delta t = 1$ fs which ensured proper sampling of the highest-frequency vibrations (C-H stretching modes at ~3000 cm^{-1}). A canonical ensemble (*NVT*) was simulated by using the Nosé thermostat[68–70] with a Nosé mass chosen so that the periodicity of energy oscillation was equal to the lowest energy vibrations of the system (slab phonons at ~55 cm^{-1}).

Initially, molecule and slab were simulated separately for 20 ps starting from their static DFT minimum structure to approach thermodynamic equilibrium. After this, every 3 ps, a set of

coordinates and velocities was written out to yield molecule and slab in qualitatively different states of thermal excitation. In total, twenty different states were generated this way.

The two systems were then combined by placing the molecular center of mass 5.5 Å above the equilibrium position of the highest surface atom and displacing it randomly in *x* and *y* direction using a true random number generator.[71] Additionally, a translational velocity vector **t** was added to the molecule to simulate the effect of a gas escaping from a nozzle into an ultra-high vacuum chamber. The absolute value of the vector |**t**| was chosen to be equal to the mean speed <*v*> of a Maxwell-Boltzmann distribution (Equation 2), while the direction was again chosen randomly by using a true random number generator. The value of |**t**| is only a function of the temperature *T* and the molecular mass *m*. Additionally, the *z* component was ensured to point into the direction of the surface. The bash script that was used to combine molecule and slab, displace the molecule and add the translational velocity is given in the Supporting Information.

$$|\mathbf{t}| = < v > = \sqrt{\frac{8k_{\mathrm{B}}T}{\pi m}} \qquad (2)$$

3. Results

3.1. Static DFT Calculations

Since the fully analytical description of the adsorption PES (> 50 degrees of freedom) is currently not feasible for a molecule the size of cyclooctyne, investigations will be focused on certain regions of the PES that are of importance to the adsorption process. One way to identify these regions is to perform a PES scan, i.e. to calculate the bonding energy as a function of a set of variables, for example the molecular position or internal coordinates. In our case, we chose the

position of the molecule as it will most probably have a larger influence on the interaction than internal degrees of freedom. There are two ways to perform a PES scan: A “frozen” or “rigid” scan, where all coordinates except the ones being sampled are fixed, and a relaxed scan, where an energy minimization of the other coordinates is performed at each point. Due to the highly increased computational cost of relaxed scans, we limit our study to frozen scans at this point. However, we will address the influence of relaxation of internal degrees of freedom at a later point.

Since the distance between molecule and surface is the decisive variable for the interaction strength, but not the character (e.g. bonding to different adsorption sites), we performed the first PES scans by displacing the molecule parallel the surface in *x* and *y* direction while keeping the *z* coordinate fixed. For this, the molecule was put in an upright position, so that the reactive triple bond atoms were oriented towards the surface and the molecular C_2 symmetry axis was aligned parallel to the *z* axis. The rotational orientation was set to two values: One where the triple bond atoms were aligned parallel to the *y* axis (abbreviated *par-y* in the following) and one where they were aligned parallel to the *x* axis (*par-x*, see also Scheme 2). This choice was made because of the symmetry of the surface reconstruction, where the dimer bonds are oriented parallel to the *y* axis, while the dimer rows are spreading in *x* direction. Furthermore, the two most stable chemisorbed states, *on-top* and *bridge* (Scheme 2), see the triple bond oriented *par-y* and *par-x*, respectively.[61] The vertical *z* position of the molecule had to be set to a value where interaction is apparent, but the system is still not in the potential well of a chemisorbed state. We chose the position so that the vertical difference between the triple bond carbon atoms and the uppermost surface atoms Si_{up} is 3 Å. This is more than 50% longer than the equilibrium C-Si bond lengths

in the chemisorbed states[61] and fulfils the previously mentioned criterion of negligible covalent interaction.

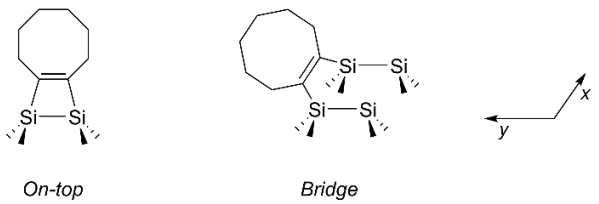

Scheme 2. Schematic representation of the two most stable chemisorbed states in the cyclooctyne/Si(001) system, *on-top* and *bridge*, and definition of the *x* and *y* axis with respect to the surface dimers.

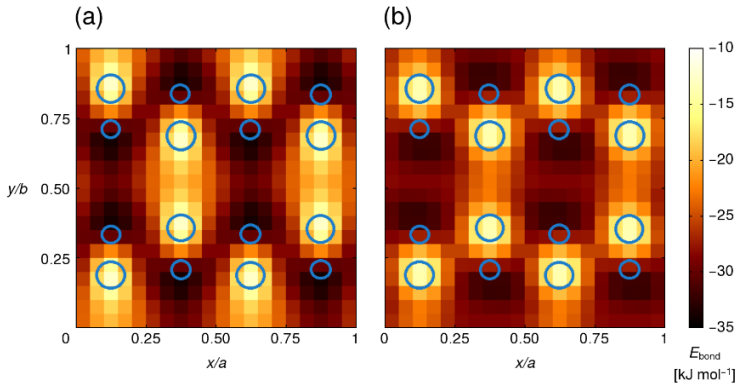

Figure 1. Rigid potential energy scan of a cyclooctyne molecule above the Si(001) surface in upright orientation, calculated at PBE-D3/PAW. The scan is given with respect to the center of the triple bond, whose atoms are aligned parallel to (a) the *y* axis and (b) the *x* axis (see Scheme 2). $\Delta z(C_{triple\text{-}bond}\text{-}Si_{up})$ = 3 Å. The blue circles denote the positions of the Si_{up} (larger circles) and Si_{down} (smaller circles) atoms.

The computed scans (Figure 1) show that, regardless of rotational orientation, regions above the electrophilic Si_{down} atoms (smaller blue circles) are energetically favored in comparison to regions above the nucleophilic Si_{up} atoms (larger blue circles). At this Δz value, the energy difference can be up to 25 kJ mol^{-1}, so that the molecule is considerably more strongly attracted to a Si_{down} atom (E_{bond} = –35 kJ mol^{-1}) compared to a Si_{up} (E_{bond} = –10 kJ mol^{-1}). Therefore, it is most likely that during the adsorption process, the triple bond will be attracted to a Si_{down} atom. This is not surprising since the electron-rich triple bond experiences electrostatic attraction at these electrophilic sites, and repulsion at nucleophilic Si_{up} atoms, which can be understood to exhibit occupied orbitals.[39] Additionally, the energy range confirms that the scan was performed at a distance between molecule and surface where covalent interactions are negligible, since chemisorbed structures in this system occur at an energy range below E_{bond} = –200 kJ mol^{-1}.[61] As already mentioned in the introduction, the adsorption of alkenes on Si(001) even sees a stable precursor intermediate arising at a geometry where the molecular π system is coordinated to a Si_{down} atom.[59,72–78] Hence, even if such a structure is not a minimum in this system, this part of the PES is still decisive during the adsorption process and will be investigated in more detail.

To address the influence of structural relaxation and changes in internal coordinates, the system was optimized from five distinct starting positions where the triple bond was placed above a Si_{down} atom (Figure 2a): One starting with the triple bond *par-y* and its center located vertically above the Si_{down} (2), one displaced in *y* direction so that it was located above the center of the dimer bond (3, Δy = 1.127 Å) and one displaced by the same amount in the opposite direction (1). All three structures see the triple bond atoms in-plane with the two silicon dimer atoms. In addition, two starting structures with the triple bond in *par-x* orientation were generated: One equivalent to (1), but with the molecule rotated by 90° around its symmetry axis

(4) and another by displacing structure 4 in *x* direction by half the distance between two dimers (5, Δx = 1.916 Å). To avoid large forces at the beginning of the adsorption path, the $\Delta z(C_{\text{triple-bond}}\text{-}Si_{up})$ value was increased to 4 Å.

We will focus on two aspects here: First, the trajectory of the molecule which might lead to insight regarding the mechanism of chemical bond formation, and second, the corresponding energy profile. Because the energy profile might be biased by the choice of the optimization algorithm (here: CG), we additionally performed NEB calculations, since these converge to the Minimum Energy Path (MEP) by construction.[56] For these NEB calculations, the final image was set to the final structure of the CG optimization, while the starting geometry was set as the initial image. Comparing both energy profiles (Fig. 2b and 2c), it becomes clear that the CG optimization shows no qualitative differences to the more accurate NEB calculation. The results are given in Figure 2. Due to the nature of the CG algorithm, which includes trial steps, only every second step is plotted in the energy profile.

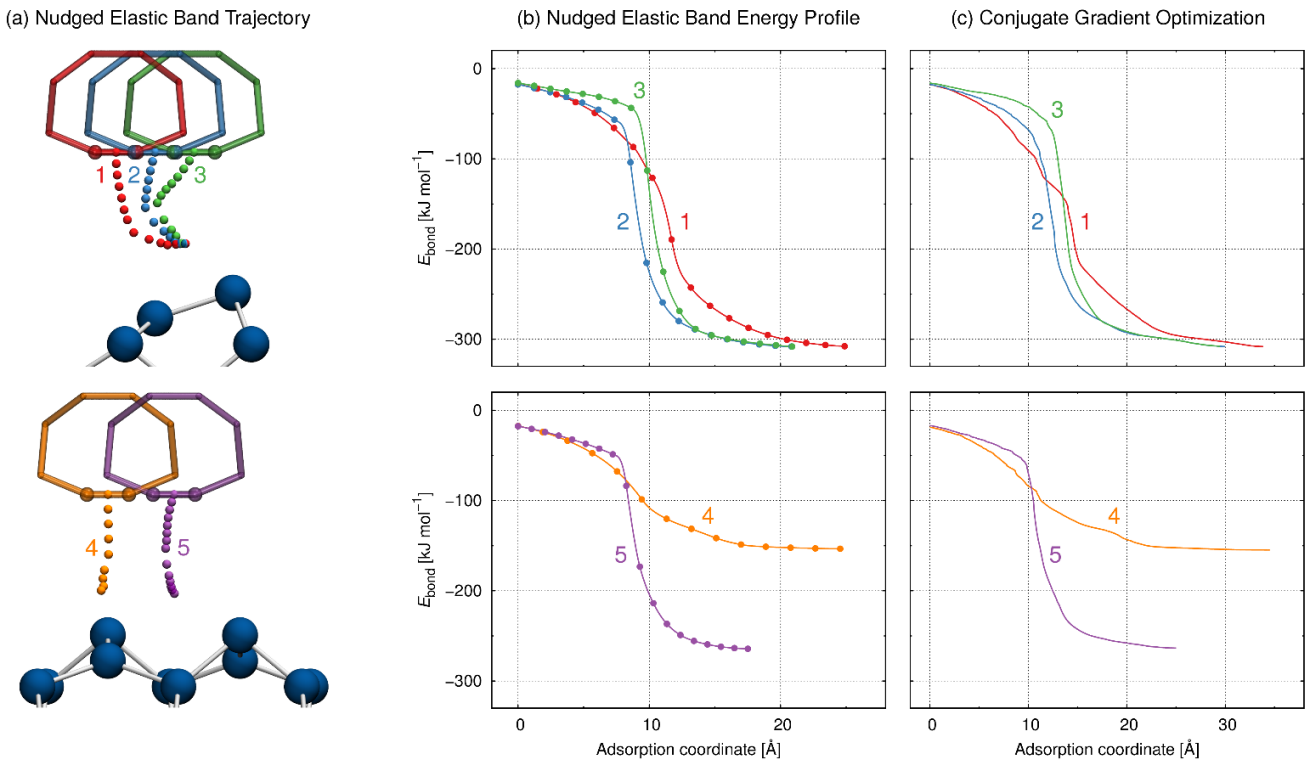

Figure 2. (a) NEB adsorption trajectories starting at five different positions and orientations (1-5) of the cyclooctyne molecule. For clarity, only the trajectory of the triple bond center is shown. (b) Corresponding energy profiles. (c) Energy profiles obtained by CG optimization of the starting geometries.

Paths 1-3 all end up directly in the *on-top* configuration, which was identified by the final state bonding energy of E_{bond} = –308 kJ mol^{-1} and visual inspection of the structure (see Ref. 61 for a detailed description of all final states). The corresponding NEB trajectories (Figure 2a, top) are in line with the previous assumption that the adsorption proceeds via coordination of the triple bond to the Si_{down} atom: Whereas in path 1, the triple bond center moves almost vertically in the first part of the trajectory, paths 2 and 3 show it making a slight "left turn" to achieve better interaction with the Si_{down}. Therefore, it appears that starting position 1 is closer to the optimal

adsorption path. This is underlined in the energy profiles (Figure 2b and c): Even though the initial energies of paths 1-3 are almost identical, path 1 shows a steeper gradient along the adsorption coordinate in the first third of the profile. This indicates larger forces and therefore stronger attraction. Apart from this, all three profiles look qualitatively very similar. The only mentionable aspect is a wider drop in the center of profile 1 compared to 2 and 3. This drop is caused by the formation of the two shared-electron bonds between molecule and surface. The reason why it appears more narrowly in profiles 2 and 3 is presumably because the triple bond is a little closer to the Si_{up} atom in comparison to path 1 and the molecule does not need to move as much between the formation of the first and second bond. The CG optimization profiles (Figure 2c) show almost no qualitative differences to the NEB profiles. The only visible difference is a small bump in the center of path 1, which could either be an artifact of the CG algorithm or a part of the profile that the NEB method missed, since it has a much lower resolution along the adsorption coordinate. Either way, it is not important for the features of the curve described before (the gradient in the first part and the width of the energy drop in the center). This means that the cheap CG optimization is sufficient to describe all qualitative features of an energy profile of direct adsorption. For adsorption pathways proceeding via an intermediate, however, one is limited to using Climbing-Image NEB to determine the energy profile between the stationary states or, alternatively, determining the transition state using, e.g., the Dimer method[79] and tracing out the energy profile from the transition states in both directions of the imaginary mode using an optimizer afterwards.

If the molecule is oriented *par-x* (paths 4 and 5), one can expect the adsorption to end up in the similarly oriented *bridge* configuration. However, this only happens in path 5, apparent by the final state bonding energy of $E_{bond} = -263$ kJ mol^{-1} (compare Ref. 61) and identified by visual inspection of the structure. Path 4 ends up in a stationary point resembling the common precursor structure for unsaturated organic adsorbates on Si(001) at $E_{bond} = -155$ kJ mol^{-1}. Since the presence of a precursor intermediate is in apparent contradiction to the experimental findings,[38] we will examine it critically and study its implications in detail in the following sections. In contrast to paths 2 and 3, the trajectory of path 5 sees the molecule moving almost without any horizontal displacement towards the closest Si_{down} atom. This has to do with the increased distance to both the Si_{down} atom, to which the triple bond is attracted, and the closest Si_{up} atom, from which it is repelled for electrostatic reasons. Due to the placement of the molecule, the drop in the energy profile is, as in paths 2 and 3, very narrow. Again, the reason for this is a reduced need for molecular translation between the formation of the two bonds. On the contrary, the energy profile of path 4 has a wide energy drop, because there are no shared-electron bonds being formed (see next paragraph and Supporting Information) and there is just a steady increase in interaction. Additionally, the latter half of the profile shows that the system is in a flat part of the PES. The qualitative differences between the NEB and CG optimization energy profiles are, as for paths 1-3, negligible.

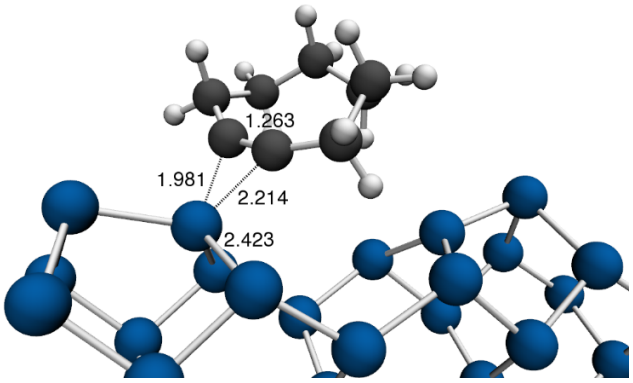

Figure 3. Structure of the precursor-like stationary point, optimized using PBE-D3/PAW. Bond lengths given in Å.

The structure in Figure 3 resembles the datively bonded precursor of ethylene on Si(001) in the way that both triple bond atoms are coordinated to the Si_{down} atom (distances: 1.976/2.214 Å, ethylene precursor:[59] 2.177/2.237 Å), albeit more asymmetrically, and a slightly elongated triple bond compared to the isolated molecule (1.215[61]→1.263 Å, ethylene double bond:[59] 1.333→1.388 Å). Additionally, the small elongation of the Si_{down}-Si_{sub} surface bond (2.340→2.423 Å) indicates back donation from this bond to the molecule and therefore orbital interaction, which is confirmed by our pEDA bonding analysis (see Supporting Information). The analysis furthermore reveals that the bonding character between molecule and surface in this structure is very similar to the ethylene precursor, i.e. a dative bond with the molecular π system donating into an empty orbital at the Si_{down}. The finding that the bonding energy here (–155 kJ mol^{-1}) is twice as high compared to the ethylene precursor (–74 kJ mol^{-1})[78] can be understood due to the increased size of the molecule which leads to both a higher amount of dispersion forces and hyperconjugation effects (see also Table S1 and Figure S1 in the Supporting Information). Moreover, a value of 100 to 200 kJ mol^{-1} is typical for organic molecules of similar size, like methyl- or ethylamines, that are datively bonded to Si(001). [29,80,81]

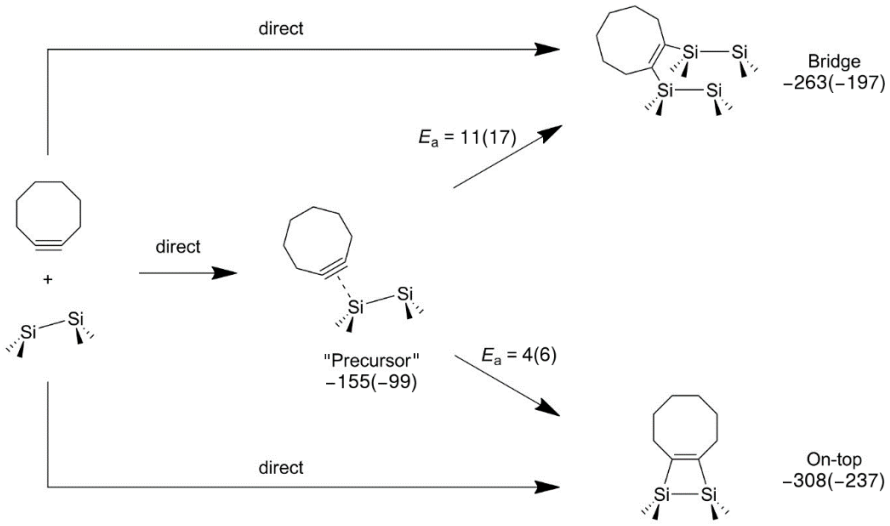

Figure 4. Adsorption and surface reactivity map of cyclooctyne on Si(001). Bonding energies E_{bond} and activation energies E_a calculated at PBE-D3/PAW, given in kJ mol^{-1}. Gibbs energies (in parentheses) calculated at T = 300 K, p = 1 bar.

As for ethylene, conversion from the intermediate state into the final *on-top* and *bridge* states is possible. We calculated the energy barriers and the results are given in Figure 4. The barrier into *on-top* is particularly low at E_a = 4 and G_a = 6 kJ mol^{-1}, and close to the residual errors of our chosen parameters[61] and the general accuracy of GGA functionals. Hence, this energy barrier might vanish in a more accurate calculation. We repeated the calculation of the energy barrier by using the hybrid functional HSE06-D3[82] and the result saw only minimal changes with values of E_a = 3 and G_a = 5 kJ mol^{-1} (the PBE-D3 frequencies were used in the calculation of G_a). Therefore, we assume that the presence of this energy barrier is not an artifact of the chosen methodology. As we will show later, this is perfectly in line with the experimental results. The energy difference between the barriers (E_a: 4 vs. 11, G_a: 6 vs. 17 kJ mol^{-1}) indicate a preferred conversion into the *on-top* final state, which is what experiments showed.[33,61] However, since all three states can be reached directly (Figures 2 and 4), there is no way to estimate how the adsorption path via the "precursor" competes with the direct ones. This is in contrast to ethylene

on Si(001), where reaction proceeds exclusively via the precursor, since the transition state for direct adsorption has a positive E_{bond} value of +23 kJ mol^{-1},[73] whereas computed values for the transition state of the precursor-mediated reaction range between E_{bond} = –66 and –39 kJ mol^{-1}.[59,72,73,76,83]

At this point, the commonly used methods for determination of adsorption pathways have been applied, but the results are not able to predict in which states the system will preferably end up. This makes a refinement of methodology necessary. In particular, the influence of the molecular orientation on the adsorption has to be investigated, since it appears to be a determining factor here. This is in contrast to systems where the adsorption proceeds via an intermediate and thermodynamic equilibrium can be assumed, which also affects the orientation of the molecule.[59] For this system, the influence of orientation can be determined by performing a more detailed series of structural optimizations similar to those presented in Figure 2. In specific, rotational orientations of 30 and 60° with respect to the *y* axis were introduced, another starting point in the *xy* plane was added (Point 6 in Figure 5) and every rotational orientation was sampled for each starting point. This allows us to figure out which starting position and orientation leads to which final state. Results are given in Table 1.

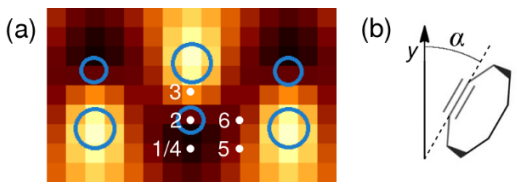

Figure 5. (a) Depiction of the starting point locations 1-6 within an excerpt of Figure 1a. (b) Definition of the orientation angle α.

Table 1. Final states of a CG optimization as a function of the starting point and orientation (see Figure 5 for nomenclature). Abbreviations of final states: O: *on-top*, I: Intermediate, H: β-H abstraction, B: *bridge*.

Starting point	Orientation angle α			
	0°	30°	60°	90°
1/4	O	I	I	I
2	O	I	I	H
3	O	I	I	H
5	I	O	B	B
6	O	O	B	B

It can be seen that the system ends up in *bridge* (B) only at points 5 and 6 and an angle of α = 60 and 90°. Since these locations are higher in energy on the PES scan compared to points 1 and 2 by ~10 kJ mol^{-1} (see Figure 1), we can assume that the molecule has a much lower probability of presence here and the paths are less relevant. In contrast, paths starting from points 1 and 2 end up in the intermediate (I) in most cases and only go directly to *on-top* (O) for an orientation of α = 0°. As these locations are lower in energy on the PES scan, one can expect them to be more relevant. At point 2 and 90°, a final state structure appears that has not been observed before: The abstraction of a hydrogen atom in *β* position to the triple bond by a nearby Si_{up} atom (H, see also the Supporting Information). Since this occurred only two times (points 2 and 3, 90°) and was not observed in experiment, we assume that this reaction is not relevant. Summarizing all results up to now, we conclude that the most probable final state is the

intermediate and occasionally, direct adsorption into the *on-top* state might occur. However, the validity of these conclusions is limited, since only a small number of starting configurations was sampled, its selection could be biased based on how one expects the reaction to proceed (e.g. triple bond pointing towards the surface) and thermal effects have only been considered at the stationary points. To resolve these issues, we performed *ab initio* molecular dynamics simulations of the adsorption process. Due to the high computational cost, the number of simulations had to be limited and the first issue (small number of configurations/trajectories) might not be compromised, but the other two points are covered more properly in this approach.

3.2. *Ab initio* Molecular Dynamics Simulations

We performed 20 AIMD simulations of a thermally excited cyclooctyne molecule adsorbing onto a thermally excited Si(001) surface at 300 K. The setup is described in Section 2.2. Aside from the identification of the final state by visual inspection, distinction was made between direct adsorption and adsorption via the intermediate. This is now illustrated by examining data from two exemplary trajectories (Figure 6).

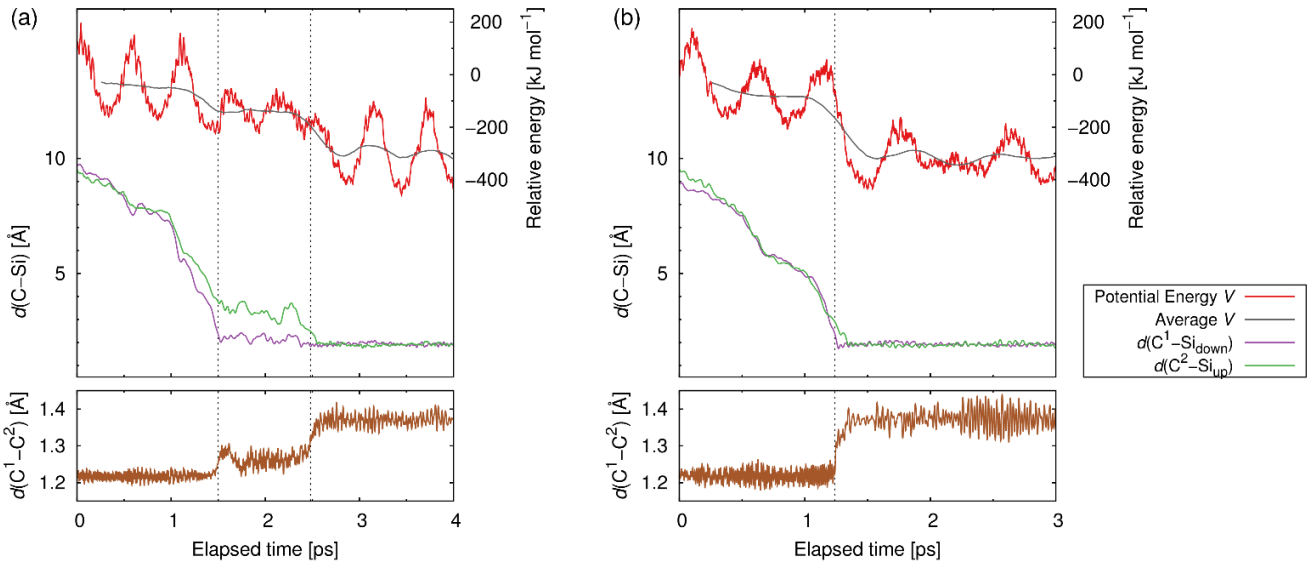

Figure 6. Potential energy V and selected interatomic distances indicative for the progress of the adsorption, taken from two exemplary AIMD trajectories. (a) Adsorption via intermediate, (b) direct adsorption. Averaging of V done over 600 fs, the approximate oscillation periodicity of the Nosé thermostat. The atomic nomenclature is given in Scheme 1. The zero point of the potential energy was set to the sum of the averaged (over 6 ps) potential energies of separated molecule and slab simulations in equilibrium.

The presence of the intermediate in a trajectory (Figure 6a) is apparent from three features:

1. An energy plateau with an average potential energy around –150 kJ mol^{-1},
2. Asymmetric C-Si interatomic distances, d(C^1-Si$_{down}$) close to 2 Å,
3. A slight elongation of the C-C triple bond with a value still below 1.3 Å.

The beginning and end of intermediate residence was marked with two vertical dashed lines. These points were defined as the midpoint of the most pronounced changes in the d(C^1-C^2) bond length. Neither of the three features can be found in Figure 6b, which depicts direct adsorption.

Here, only one vertical line was drawn, since the average $d(C^1\text{-}C^2)$ increases straight from the gas phase value of 1.21 Å to the final state value of 1.37 Å (see also Ref. 61). In this way, all 20 trajectories were analyzed (the full data sets are given in the Supporting Information). The number of occurrences of each final state is given in Table 2. For simulations ending up in *on-top*, distinction between direct adsorption and adsorption via the intermediate was made as well.

Table 2. Number of AIMD trajectories that ended up in the respective O (*on-top*), B (*bridge*) and H (β-H abstraction) states. In case of O, differentiation between direct adsorption and adsorption via the intermediate (I) is made. The full data sets are given in the Supporting Information.

Final state	No. of trajectories
O via I	15
O direct	2
B direct	3
H	0

The results show that 15 of the 20 simulations proceeded via the intermediate and ended up in *on-top*, while only 2 ended up directly in *on-top* and 3 in *bridge*. A β-H abstraction could not be observed, supporting the previous assumption that this reaction is not relevant. In general, these results support the conclusions of the previous section: While direct adsorption into *on-top* and

bridge is possible, the majority of molecules will adsorb via the intermediate, from which the system will most likely convert to *on-top* due to the much lower energy barrier.

Using the three criteria for intermediate residence, one can also assign an intermediate lifetime for each trajectory. Averaging this number for all 15 simulations that feature the intermediate, one arrives at a value of

$$\Delta t(\text{intermediate}) = 1.0 \pm 0.7\ \text{ps} = \tau(300\ \text{K}) \approx k^{-1}(300\ \text{K}) \qquad (3)$$

which can be approximated in first order to be the life time τ of an Arrhenius equation or the inverse of the rate constant k at the simulation temperature (300 K). Although τ is usually defined as the point in time when the reaction has occurred in $e^{-1} \approx 37\%$ of the system, only the order of magnitude is of interest here, so the potential error will not affect the results in a qualitative way. One can then insert the value for k derived this way and the Gibbs energy barrier G_a for conversion (Figure 4) into the Arrhenius equation to yield the pre-exponential factor A_0:

$$k(T) = A_0 \exp\left(-\frac{G_a}{k_B T}\right) \rightarrow A_0 = 12 \pm 8\ \text{THz} \qquad (4)$$

This A_0 value and the temperature-dependent G_a can then be used to extrapolate the lifetime of the intermediate to lower temperatures assuming A_0 to be independent of temperature. The results are given in Table 3.

Table 3. Estimation of the lifetime τ of the intermediate at different temperatures T using the Gibbs activation energy G_a and the Arrhenius pre-exponential factor A_0 (in THz) taken from the AIMD calculations (MD results) or, alternatively, qq-hTST. For comparison, all values are also given using the HSE06-D3 activation energies.

		PBE-D3		HSE06-D3	
T [K]	A_0 [THz]	G_a [kJ mol^{-1}]	τ [ps]	G_a [kJ mol^{-1}]	τ [ps]
MD results					
50	12±8	3.8	720±500	2.7	60±40
150	12±8	4.5	3.0±2.0	3.4	1.3±0.9
300	12±8	6.2	1.0±0.7	5.1	0.7±0.5
qq-hTST					
50	1.8	3.8	4700	2.7	400
150	2.2	4.5	17	3.4	7.3
300	2.6	6.2	4.5	5.1	3.0

Even at 50 K, the lifetime is only in the nanosecond range. The reason for this is the very low energy barrier at room temperature (6.2 kJ mol^{-1}), which is even decreased due to thermal effects at lower temperatures (3.8 kJ mol^{-1} at 50 K). This means that the system does not proceed via the typical precursor-mediated pathway but instead shows either direct adsorption or pseudo-direct adsorption via an ultra-short-lived stationary state. Although we used the term "intermediate" up to now for clarity of presentation, this transient species on the potential energy surface does not fulfill the common definition of an intermediate state that is understood to show a lifetime

"appreciably longer than a molecular vibration".[84] Thus, our findings of direct and pseudo-direct pathways are perfectly in line with the experimental findings of direct adsorption over a wide temperature range, since the lifetime of the state is too low to allow isolation under typical experimental conditions.

Finally, two critical issues shall be addressed: First, the PBE functional has a tendency to underestimate reaction barriers[85] and second, as previously mentioned, the statistical significance of a set of 15 simulations is low. This could lead, for example, to a considerable overestimation of the pre-exponential factor A_0. To address the first issue, we calculated the energy barrier again using the HSE06 hybrid functional.[82] As it turns out (Table 3), G_a becomes even smaller, resulting in a lifetime of 60±40 ps at 50 K if the pre-exponential factor from the PBE AIMD simulations is used. The second issue was addressed using quasi-quantum harmonic transition state theory (qq-hTST).[64,65] This method assumes thermodynamic equilibrium and Boltzmann statistics at the intermediate within the usual approximation of harmonic vibrations. As a consequence, the statistics is more properly sampled than in the previous approach. While this yields, as expected, a smaller pre-exponential factor A_0 (Table 3), the value is only one order of magnitude lower than the previous one. As a result of this, calculation of the lifetime at 50 K yields 4.7 ns (PBE-D3) and 400 ps (HSE06-D3), still in line with the transient nature of the intermediate state. The qq-hTST method cannot capture anharmonicity within vibrations, which could be important, since the PES is flat in the proximity of the intermediate (see Figure 2, path 4). However, this is treated properly in the AIMD approach, while the qq-hTST approach treats the drawbacks of the AIMD approach properly as outlined above. Therefore, we assume that these two approaches complement each other and give a consistent overall picture.

4. Conclusion

Using a careful selection of DFT methods, we have shown that the adsorption dynamics of the complex and large system cyclooctyne/Si(001) can consistently be described and shows surprising behavior that could only be revealed by theoretical analysis. Since a fully analytical description of the potential energy surface is not feasible for a system of this size, well calibrated approximations are unavoidable. The choice and combination of methods turned out to be crucial in our case, since a meaningful and reliable conclusion could only be reached by combining PES scans, structural optimization, AIMD simulations and statistical thermodynamics. Neglecting only one of these four approaches, the conclusiveness would be severely weakened. Additionally, the influence of the molecular orientation has to be investigated carefully and in detail, since in systems with direct and pseudo-direct adsorption paths like this, the effect is much more significant than in systems where the adsorption proceeds via an intermediate state.

Based on our investigations on the prime model system presented here, we propose the following approach for investigating the adsorption dynamics of larger systems without clearly defined intermediate and/or final states:

1. Determination of energetically relevant regions on the PES with respect to the molecule position and orientation (PES scans with static DFT methods)
2. Investigation of adsorption trajectories and energy profiles within these regions as a function of molecular position and orientation (NEB or CG optimization)
3. If stationary points appear: Investigation of transition states, application of statistical thermodynamics (NEB, Dimer method, vibrational analysis)
4. AIMD simulations and qq-hTST to estimate lifetimes

The results could be refined by performing a high number of long MD simulations. Since the Si(001) surface is too complex to be adequately modeled by a force field, the development of highly parallel DFT and/or wavefunction implementations could pave a road for the future. Together with Potential of Mean Field (PMF) calculation this could deliver a detailed Gibbs energy profile of adsorption, as has been done for large organic molecules on KCl(001) using force fields.[30] Additionally, approximate DFT methods like Density Functional based Tight Binding (DFTB)[86] might be able to properly describe the Si(001) surface and speed up calculations significantly. Now that this system has been properly studied at an *ab initio* level of accuracy, it can be used to test or validate less accurate but faster methods for investigating the adsorption of larger molecules on surfaces.

ASSOCIATED CONTENT

Supporting Information.

The following files are available free of charge.

Supporting Information (PDF)

AUTHOR INFORMATION

Corresponding Author

* PD Dr. Ralf Tonner. e-mail: tonner@chemie.uni-marburg.de

Author Contributions

All calculations were performed by LP except the PES scans (Figure 1), which were performed by SS. The first version of the manuscript was written by LP and subsequently refined in collaboration between LP and RT. All authors have given approval to the final version of the manuscript.

Funding Sources

This work was supported by Deutsche Forschungsgemeinschaft (DFG) within SFB 1083.

Notes

The authors declare no competing financial interest.

ACKNOWLEDGMENT

Computational resources were provided by HRZ Marburg, CSC-LOEWE Frankfurt and HLR Stuttgart. We thank Prof. Ulrich Höfer (Marburg) and Prof. Michael Dürr (Gießen) for discussions.

ABBREVIATIONS

AIMD, *ab initio* molecular dynamics; B, *bridge*; CG, conjugate gradient; DFT, density functional theory; DFTB, density-functional based tight binding; GGA, generalized gradient approximation; H, β-hydrogen abstraction; I, intermediate; MEP, minimum energy path; NEB, nudged elastic band; O, *on-top*; par-x; parallel to the *x* axis; par-y, parallel to the *y* axis; PAW, projector augmented wave; pEDA, periodic energy decomposition analysis; PES, potential energy surface; qq-hTST, quasi-quantum harmonic transition state theory; SCF, self-consistent field; VASP, Vienna *ab initio* simulation package.

REFERENCES

(1) Schlögl, R. Heterogeneous catalysis. *Angew. Chem. Int. Ed.* **2015**, *54*, 3465.

(2) Johnson, R. W.; Hultqvist, A.; Bent, S. F. A brief review of atomic layer deposition: From fundamentals to applications. *Mater. Today* **2014**, *17*, 236.

(3) Bent, S. F. Organic functionalization of group IV semiconductor surfaces: Principles, examples, applications, and prospects. *Surf. Sci.* **2002**, *500*, 879.

(4) Rettner, C. T.; Auerbach, D. J.; Tully, J. C.; Kleyn, A. W. Chemical Dynamics at the Gas−Surface Interface. *J. Phys. Chem.* **1996**, *100*, 13021.

(5) *Dynamics of Gas-Surface Interactions;* Díez Muiño, R.; Busnengo, H. F., Eds.; Springer: Berlin Heidelberg, 2013.

(6) Groß, A. *Theoretical Surface Science*; Springer: Berlin Heidelberg, 2003.

(7) Bukas, V. J.; Meyer, J.; Alducin, M.; Reuter, K. Ready, Set and no Action: A Static Perspective on Potential Energy Surfaces commonly used in Gas-Surface Dynamics. *Z. Phys. Chem.* **2013**, *227*, 1523.

(8) Nørskov, J. K.; Lang, N. D. Effective-medium theory of chemical binding. *Phys. Rev. B* **1980**, *21*, 2131.

(9) Nielsen, U.; Halstead, D.; Holloway, S.; Nørskov, J. K. The dissociative adsorption of hydrogen: Two-, three-, and four-dimensional quantum simulations. *J. Chem. Phys.* **1990**, *93*, 2879.

(10) Janke, S. M.; Auerbach, D. J.; Wodtke, A. M.; Kandratsenka, A. An accurate full-dimensional potential energy surface for H-Au(111): Importance of nonadiabatic electronic excitation in energy transfer and adsorption. *J. Chem. Phys.* **2015**, *143*, 124708.

(11) Lorenz, S.; Groß, A.; Scheffler, M. Representing high-dimensional potential-energy surfaces for reactions at surfaces by neural networks. *Chem. Phys. Lett.* **2004**, *395*, 210.

(12) Behler, J.; Parrinello, M. Generalized neural-network representation of high-dimensional potential-energy surfaces. *Phys. Rev. Lett.* **2007**, *98*, 146401.

(13) Behler, J. Neural network potential-energy surfaces in chemistry: A tool for large-scale simulations. *Phys. Chem. Chem. Phys.* **2011**, *13*, 17930.

(14) Tuckerman, M. E. Ab initio molecular dynamics: Basic concepts, current trends and novel applications. *J. Phys.: Condens. Matter* **2002**, *14*, R1297.

(15) Kosloff, R. Time-Dependent Quantum-Mechanical Methods for Molecular Dynamics. *J. Phys. Chem.* **1988**, *92*, 2087.

(16) Kroes, G.-J. Six-dimensional quantum dynamics of dissociative chemisorption of H2 on Cu(100). *Prog. Surf. Sci.* **1999**, *60*, 1.

(17) Shenvi, N.; Roy, S.; Tully, J. C. Nonadiabatic dynamics at metal surfaces: Independent-electron surface hopping. *J. Chem. Phys.* **2009**, *130*, 174107.

(18) Cooper, R.; Bartels, C.; Kandratsenka, A.; Rahinov, I.; Shenvi, N.; Golibrzuch, K.; Li, Z.; Auerbach, D. J.; Tully, J. C.; Wodtke, A. M. Multiquantum vibrational excitation of NO scattered from Au(111): Quantitative comparison of benchmark data to Ab initio theories of nonadiabatic molecule-surface interactions. *Angew. Chem. Int. Ed.* **2012**, *51*, 4954.

(19) Krüger, B. C.; Bartels, N.; Bartels, C.; Kandratsenka, A.; Tully, J. C.; Wodtke, A. M.; Schäfer, T. NO Vibrational Energy Transfer on a Metal Surface: Still a Challenge to First-Principles Theory. *J. Phys. Chem. C* **2015**, *119*, 3268.

(20) Jónsson, H. Theoretical Studies of Atomic-Scale Processes Relevant to Crystal Growth. *Annu. Rev. Phys. Chem.* **2000**, *51*, 623.

(21) Li, Z.; Kermode, J. R.; De Vita, A. Molecular Dynamics with On-the-Fly Machine Learning of Quantum-Mechanical Forces. *Phys. Rev. Lett.* **2015**, *114*, 96405.

(22) Caccin, M.; Li, Z.; Kermode, J. R.; De Vita, A. A Framework for Machine-Learning-Augmented Multiscale Atomistic Simulations on Parallel Supercomputers. *Int. J. Quantum Chem.* **2015**, *115*, 1129.

(23) Ghiringhelli, L. M.; Vybiral, J.; Levchenko, S. V.; Draxl, C.; Scheffler, M. Big Data of Materials Science: Critical Role of the Descriptor. *Phys. Rev. Lett.* **2015**, *114*, 105503.

(24) Ghiringhelli, L. M.; Vybiral, J.; Ahmetcik, E.; Ouyang, R.; Levchenko, S. V.; Draxl, C.; Scheffler, M. Learning physical descriptors for materials science by compressed sensing. *New J. Phys.* **2017**, *19*, 23017.

(25) Ruiz, V. G.; Liu, W.; Zojer, E.; Scheffler, M.; Tkatchenko, A. Density-functional theory with screened van der Waals interactions for the modeling of hybrid inorganic-organic systems. *Phys. Rev. Lett.* **2012**, *108*, 146103.

(26) Kim, S. W.; Lee, J. H.; Kim, H. J.; Cho, J. H. Contribution of van der Waals interactions to the adsorption energy of C2H2, C2H4, and C6H6 on Si(100). *Chem. Phys. Lett.* **2013**, *557*, 159.

(27) Liu, W.; Tkatchenko, A.; Scheffler, M. Modeling Adsorption and Reactions of Organic Molecules at Metal Surfaces. *Acc. Chem. Res.* **2014**, *47*, 3369.

(28) Tonner, R.; Rosenow, P.; Jakob, P. Molecular structure and vibrations of NTCDA monolayers on Ag(111). *Phys. Chem. Chem. Phys.* **2016**, *18*, 6316.

(29) Naitabdi, A.; Bournel, F.; Gallet, J. J.; Markovits, A.; Rochet, F.; Borensztein, Y.; Silly, M. G.; Sirotti, F. Triethylamine on Si(001)-(2×1) at 300 K: Molecular adsorption and site configurations leading to dissociation. *J. Phys. Chem. C* **2012**, *116*, 16473.

(30) Gaberle, J.; Gao, D. Z.; Watkins, M. B.; Shluger, A. L. Characterizing the Entropy Loss on Adsorption of Organic Molecules at Insulating Surfaces. *J. Phys. Chem. C* **2016**, *120*, 3913.

(31) Hovis, J.S.; Liu, H.; Hamers, R.J. Cycloaddition chemistry and formation of ordered organic monolayers on silicon(001) surfaces. *Surf. Sci.* **1998**, *402-404*, 1.

(32) Ma, Z.; Zaera, F. Organic chemistry on solid surfaces. *Surf. Sci. Rep.* **2006**, *61*, 229.

(33) Mette, G.; Dürr, M.; Bartholomäus, R.; Koert, U.; Höfer, U. Real-space adsorption studies of cyclooctyne on Si(001). *Chem. Phys. Lett.* **2013**, *556*, 70.

(34) Agard, N. J.; Baskin, J. M.; Prescher, J. A.; Lo, A.; Bertozzi, C. R. A Comparative Study of Bioorthogonal Reactions with Azides. *ACS Chem. Biol.* **2006**, *1*, 644.

(35) Codelli, J. A.; Baskin, J. M.; Agard, N. J.; Bertozzi, C. R. Second-Generation Difluorinated Cyclooctynes for Copper-Free Click Chemistry. *J. Am. Chem. Soc.* **2008**, *130*, 11486.

(36) Sun, Y.; Ma, X.; Cheng, K.; Wu, B.; Duan, J.; Chen, H.; Bu, L.; Zhang, R.; Hu, X.; Deng, Z. *et al.* Strained Cyclooctyne as a Molecular Platform for Construction of Multimodal Imaging Probes. *Angew. Chem. Int. Ed.* **2015**, *54*, 5981.

(37) Münster, N.; Nikodemiak, P.; Koert, U. Chemoselective layer-by-layer approach utilizing click reactions with ethynylcyclooctynes and diazides. *Org. Lett.* **2016**, *18*, 4296.

(38) Reutzel, M.; Münster, N.; Lipponer, M. A.; Länger, C.; Hoefer, U.; Koert, U.; Dürr, M. Chemoselective Reactivity of Bifunctional Cyclooctynes on Si(001). *J. Phys. Chem. C* **2016**, *120*, 26284.

(39) Yoshinobu, J. Physical properties and chemical reactivity of the buckled dimer on Si(100). *Prog. Surf. Sci.* **2004**, *77*, 37.

(40) Pamungkas, M. A.; Joe, M.; Kim, B. H.; Lee, K. R. Reactive molecular dynamics simulation of early stage of dry oxidation of Si(100) surface. *J. Appl. Phys.* **2011**, *110*, 53513.

(41) Pamungkas, M. A.; Kim, B.-H.; Lee, K.-R. Reactive molecular dynamic simulations of early stage of wet oxidation of Si(001) surface. *J. Appl. Phys.* **2013**, *114*, 73506.

(42) Cao, H.; Srivastava, P.; Choi, K.; Kim, S.; Lee, K. R. Early stage oxynitridation process of Si(001) surface by NO gas: Reactive molecular dynamics simulation study. *J. Appl. Phys.* **2016**, *119*, 125305.

(43) Psofogiannakis, G.; van Duin, A. C. T. Development of a ReaxFF reactive force field for Si/Ge/H systems and application to atomic hydrogen bombardment of Si, Ge, and SiGe (100) surfaces. *Surf. Sci.* **2016**, *646*, 253.

(44) Sun, Y.; Liu, Y.; Chen, X.; Zhai, Z.; Xu, F.; Liu, Y. Micromechanism of oxygen transport during initial stage oxidation in Si(100) surface: A ReaxFF molecular dynamics simulation study. *Appl. Surf. Sci.* **2017**, *406*, 178.

(45) Kresse, G.; Hafner, J. Ab initio molecular dynamics for liquid metals. *Phys. Rev. B* **1993**, *47*, 558.

(46) Kresse, G.; Hafner, J. Ab initio molecular-dynamics simulation of the liquid-metal–amorphous-semiconductor transition in germanium. *Phys. Rev. B* **1994**, *49*, 14251.

(47) Kresse, G.; Furthmüller, J. Efficient iterative schemes for ab initio total-energy calculations using a plane-wave basis set. *Phys. Rev. B* **1996**, *54*, 11169.

(48) Kresse, G.; Furthmüller, J. Efficiency of ab-initio total energy calculations for metals and semiconductors using a plane-wave basis set. *Comput. Mat. Sci.* **1996**, *6*, 15.

(49) Perdew, J. P.; Burke, K.; Ernzerhof, M. Generalized Gradient Approximation Made Simple. *Phys. Rev. Lett.* **1996**, *77*, 3865.

(50) Perdew, J. P.; Burke, K.; Enzerhof, M. Erratum: Generalized Gradient Approximation Made Simple. *Phys. Rev. Lett.* **1997**, *78*, 1396.

(51) Grimme, S.; Antony, J.; Ehrlich, S.; Krieg, S. A consistent and accurate ab initio parametrization of density functional dispersion correction (DFT-D) for the 94 elements H-Pu. *J. Chem. Phys.* **2010**, *132*, 154104.

(52) Grimme, S.; Ehrlich, S.; Goerigk, L. Effect of the damping function in dispersion corrected density functional theory. *J. Comput. Chem.* **2011**, *32*, 1456.

(53) Blöchl, P. Projector augmented-wave method. *Phys. Rev. B* **1994**, *50*, 17953.

(54) Kresse, G.; Joubert, D. From ultrasoft pseudopotentials to the projector augmented-wave method. *Phys. Rev. B* **1999**, *59*, 1758.

(55) Hestenes, M. R.; Stiefel, E. Methods of conjugate gradients for solving linear systems. *J. Res. Natl. Bur. Stand.* **1952**, *49*, 409.

(56) Jónsson, H.; Mills, G.; Jacobsen, K. W. Nudged elastic band method for finding minimum energy paths of transitions. In *Classical and Quantum Dynamics in Condensed Phase Simulations*; Berne, B. J., Ciccotti, G., Coker, D. F., Eds.; World Scientific, 1998; p 385.

(57) Henkelman, G.; Jónsson, H. Improved tangent estimate in the nudged elastic band method for finding minimum energy paths and saddle points. *J. Chem. Phys.* **2000**, *113*, 9978.

(58) Henkelman, G.; Uberuaga, B. P.; Jónsson, H. A climbing image Nudged elastic band method for finding saddle points and minimum energy paths. *J. Chem. Phys.* **2000**, *113*, 9901.

(59) Pecher, J.; Mette, G.; Dürr, M.; Tonner, R. Site-Specific Reactivity of Ethylene at Distorted Dangling-Bond Configurations on Si(001). *ChemPhysChem* **2017**, *18*, 357.

(60) Boyd, D. R. J. Infrared Spectrum of Trideuterosilane and the Structure of the Silane Molecule. *J. Chem. Phys.* **1955**, *23*, 922.

(61) Pecher, J.; Schober, C.; Tonner, R. Chemisorption of a Strained but Flexible Molecule: Cyclooctyne on Si(001). *Chem. Eur. J.* **2017**, *23*, 5459.

(62) Raupach, M.; Tonner, R. A periodic Energy Decomposition Analysis (pEDA) method for the Investigation of Chemical Bonding in Extended Systems. *J. Chem. Phys.* **2015**, *142*, 194105.

(63) *BAND 2016, SCM, Theoretical Chemistry, Vrije Universiteit, Amsterdam, The Netherlands*. http://www.scm.com/.

(64) Henkelman, G.; Arnaldsson, A.; Jónsson, H. Theoretical calculations of CH4 and H2 associative desorption from Ni(111): Could subsurface hydrogen play an important role? *J. Chem. Phys.* **2006**, *124*, 44706.

(65) Árnadóttir, L.; Stuve, E. M.; Jónsson, H. Adsorption of water monomer and clusters on platinum(111) terrace and related steps and kinks: II. Surface diffusion. *Surf. Sci.* **2012**, *606*, 233.

(66) Verlet, L. Computer "Experiments" on Classical Fluids: I. Thermodynamical Properties of Lennard-Jones Molecules. *Phys. Rev.* **1967**, *159*, 98.

(67) Swope, W. C.; Andersen, H. C.; Berens, P. H.; Wilson, K. R. A computer simulation method for the calculation of equilibrium constants for the formation of physical clusters of molecules: Application to small water clusters. *J. Chem. Phys.* **1982**, *76*, 637.

(68) Nosé, S. A unified formulation of the constant temperature molecular dynamics methods. *J. Chem. Phys.* **1984**, *81*, 511.

(69) Nosé, S. Constant Temperature Molecular Dynamics Methods. *Prog. Theor. Phys. Suppl.* **1991**, *103*, 1.

(70) Bylander, D. M.; Kleinman, L. Energy fluctuations induced by the Nosé thermostat. *Phys. Rev. B* **1992**, *46*, 13756.

(71) *Random Decimal Fraction Generator*. http://www.random.org/decimal-fractions.

(72) Cho, J.-H.; Kleinman, L. Adsorption kinetics of acetylene and ethylene on Si(001). *Phys. Rev. B* **2004**, *69*, 75303.

(73) Nagao, M.; Umeyama, H.; Mukai, K.; Yamashita, Y.; Yoshinobu, J. Precursor Mediated Cycloaddition Reaction of Ethylene to the Si(100)c(4×2) Surface. *J. Am. Chem. Soc.* **2004**, *126*, 9922.

(74) Nagao, M.; Mukai, K.; Yamashita, Y.; Yoshinobu, J. The Precursor Mediated Chemisorption of Vinyl Bromide on Si(100)c(4×2). *J. Phys. Chem. B* **2004**, *108*, 5703.

(75) Cho, J.-H.; Kleinman, L. Dissociative adsorption of vinyl bromide on Si(001): A first-principles study. *Phys. Rev. B* **2005**, *71*, 125330.

(76) Zhang, Q. J.; Fan, X. L.; Lau, W. M.; Liu, Z. F. Sublayer Si atoms as reactive centers in the chemisorption on Si(100): Adsorption of C2H2 and C2H4. *Phys. Rev. B* **2009**, *79*, 195303.

(77) Akagi, K.; Yoshinobu, J. The chemistry of simple alkene molecules on Si(100)c(4x2): The mechanism of cycloaddition and their selectivities. *Surf. Sci.* **2016**, *652*, 304.

(78) Pecher, J.; Tonner, R. Precursor States of Organic Adsorbates on Semiconductor Surfaces are Chemisorbed and Immobile. *ChemPhysChem* **2017**, *18*, 34.

(79) Henkelman, G.; Jónsson, H. A dimer method for finding saddle points on high dimensional potential surfaces using only first derivatives. *J. Chem. Phys.* **1999**, *111*, 7010.

(80) Cao, X.; Hamers, R. J. Silicon surfaces as electron acceptors: Dative bonding of amines with Si(001) and Si(111) surfaces. *J. Am. Chem. Soc.* **2001**, *123*, 10988.

(81) Cho, J.-H.; Kleinman, L. Contrasting structural and bonding properties of trimethylamine and dimethylamine adsorbed on Si(001). *Phys. Rev. B* **2003**, *68*, 245314.

(82) Krukau, A. V.; Vydrov, O. A.; Izmaylov, A. F.; Scuseria, G. E. Influence of the exchange screening parameter on the performance of screened hybrid functionals. *J. Chem. Phys.* **2006**, *125*, 224106.

(83) Fan, X. L.; Zhang, Y. F.; Lau, W. M.; Liu, Z. F. Violation of the symmetry rule for the [2+2] addition in the chemisorption of C2H4 on Si(100). *Phys. Rev. B* **2005**, *72*, 165305.

(84) Muller, P. Glossary of terms used in physical organic chemistry (IUPAC Recommendations 1994). *Pure Appl. Chem.* **1994**, *66*, 1077.

(85) Cohen, A. J.; Mori-Sanchez, P.; Yang, W. Challenges for Density Functional Theory. *Chem. Rev.* **2012**, *112*, 289.

(86) Seifert, G.; Joswig, J. O. Density-functional tight binding - an approximate density-functional theory method. *WIREs Comput. Mol. Sci.* **2012**, *2*, 456.

FOR TABLE OF CONTENTS USE ONLY

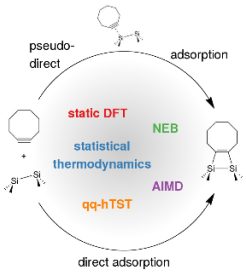

Modeling the complex adsorption dynamics of large organic molecules: Cyclooctyne on Si(001)

Lisa Pecher, Sebastian Schmidt, and Ralf Tonner

Supporting Information for:
Modeling the complex adsorption dynamics of large organic molecules: Cyclooctyne on Si(001)

Lisa Pecher, Sebastian Schmidt, Ralf Tonner*

Lisa Pecher, Sebastian Schmidt, PD Dr. Ralf Tonner
Faculty of Chemistry and Material Sciences Center, Philipps-Universität Marburg, Hans-Meerwein-Straße 4, 35032 Marburg, Germany

* Corresponding author PD Dr. Ralf Tonner. e-mail: tonner@chemie.uni-marburg.de

Contents

1. Bash Script for Combining the Separated Slab and Molecule MD Simulations, Displacing the Molecule and Adding Thermal Velocity

```
#!/bin/bash

# CHECK IF INPUTS EXIST
if [[ -a $1 ]]
then
if [[ -a $2 ]]
then
echo ""
echo "          ************************************************************"
echo "          *    This script combines two MD simulation CONTCARs     *"
echo "          * and adds thermal translational motion to the molecule  *"
echo "          ************************************************************"
echo ""
echo "   Slab CONTCAR: " $1
echo "   Molecule CONTCAR: " $2
echo ""
echo "   *** Attention! Any POSCAR in this folder will be overwritten! ***"
echo ""
echo ""
echo -n "Enter fractional x,y and z displacements for displacing the molecule in the cell: "
read rx ry rz

echo ""
echo ""

# INPUT VELOCITY VARIABLES
echo "     ************************************"
echo "     * Calculation of the velocity vector *"
echo "     ************************************"
echo ""
echo -n "Enter molecular weight in g/mol: "
read m_molecule

echo -n "Enter the desired temperature in K: "
read temp
```

```
echo ""
echo "   *** According to the Maxwell-Boltzmann mean speed equation ***"
echo -n "   *** your molecule has a translational velocity of "
speed=$(echo "sqrt(8*8.3144621*"$temp"*1000/(3.14159265359*"$m_molecule"))" | bc -l)
printf "%.2f " $speed
echo "m/s ***"
echo ""

# CONVERSION OF SPEED TO ANGSTROM/FS
speed_angfs=$(echo $speed"/100000" | bc -l)

echo -n "Enter x, y and z vector components for the direction of the velocity vector: "
read dvx_u dvy_u dvz_u # UNSCALED VECTOR COMPONENTS
echo ""
echo ""

if (( $(echo "sqrt("$dvx_u"^2 + "$dvy_u"^2 + "$dvz_u"^2) == 0"| bc -l) ))
then
echo "   You entered a vector of length zero! No translational velocity will be added to the
molecule."
echo ""
echo ""
dvx=0
dvy=0
dvz=0

else

echo -n "   Normalizing vector... "
vabs=$(echo "sqrt("$dvx_u"^2+"$dvy_u"^2+"$dvz_u"^2)" | bc -l)
scaling=$(echo $speed_angfs"/"$vabs | bc -l)

dvx=$(echo $dvx_u"*"$scaling | bc -l)
dvy=$(echo $dvy_u"*"$scaling | bc -l)
dvz=$(echo $dvz_u"*"$scaling | bc -l)

echo "Done!"
fi

echo -n "   Writing the coordinates into the POSCAR... "

# REMOVE MOLECULE PREDICTOR-CORRECTOR COORDINATE .TMP FILE IF EXISTS (THIS IS GENERATED AT A
LATER POINT)
if [ -a pc-coords-mol.tmp ]
then
rm pc-coords-mol.tmp
fi

# WRITE SLAB COORDINATES INTO POSCAR
firstemptyline_slab=$(grep -n '^[[:space:]]*$' $1 | awk '{print $1}' | sed -n -e 1p | rev | cut -
c 2- | rev)
endslabcoords=$((firstemptyline_slab - 1))
head -n $endslabcoords $1 > POSCAR

# GET NUMBER OF MOLECULE ATOMS
natoms=$(sed -n -e 7p $2 | awk '{for(i=1;i<=NF;i++)x+=$i;print x}')

# CHECK IF COORDINATES START IN LINE 9 OR 10 (DIFFERENCE VASP4/VASP5 POSCAR FORMAT)
line9=$(sed -n -e 9p $2 | awk '{print $1}' | cut -c 1)

if [ $line9 == 0 ]
  then
  i=9
  else
  i=10
fi

# READ AND DISPLACE MOLECULE COORDINATES
```

```
firstemptyline_mol=$(grep -n '^[[:space:]]*$' $2 | awk '{print $1}' | sed -n -e 1p | rev | cut -c
2- | rev)

while [ $i -lt $firstemptyline_mol ]
do
read x_old y_old z_old <<<$(sed -n -e "$i"p $2)

x_new=$(echo $x_old" + "$rx | bc -l | awk '{printf "%.8f", $0}')
y_new=$(echo $y_old" + "$ry | bc -l | awk '{printf "%.8f", $0}')
z_new=$(echo $z_old" + "$rz | bc -l | awk '{printf "%.8f", $0}')

# MOVE ATOMS INTO UNIT CELL IF FRACTIONAL COORDINATES BECOME <0 or >1
if (( $(echo $x_new" > 1" | bc -l) ))
then
x_new=$(echo $x_new" - 1" | bc -l | awk '{printf "%.8f", $0}')
fi
if (( $(echo $y_new" > 1" | bc -l) ))
then
y_new=$(echo $y_new" - 1" | bc -l | awk '{printf "%.8f", $0}')
fi
if (( $(echo $z_new" > 1" | bc -l) ))
then
z_new=$(echo $z_new" - 1" | bc -l | awk '{printf "%.8f", $0}')
fi

if (( $(echo $x_new" < 0" | bc -l) ))
then
x_new=$(echo $x_new" + 1" | bc -l | awk '{printf "%.8f", $0}')
fi
if (( $(echo $y_new" < 0" | bc -l) ))
then
y_new=$(echo $y_new" + 1" | bc -l | awk '{printf "%.8f", $0}')
fi
if (( $(echo $z_new" < 0" | bc -l) ))
then
z_new=$(echo $z_new" + 1" | bc -l | awk '{printf "%.8f", $0}')
fi

# WRITE MOLECULE COORDINATES INTO POSCAR
echo "  "$x_new"   "$y_new"   "$z_new"   T   T   T" >> POSCAR

# WRITE TEMPORARY FILE FOR PREDICTOR-CORRECTOR COORDINATES
printf "  %.8E" $x_new $y_new $z_new >> pc-coords-mol.tmp
printf "\n" >> pc-coords-mol.tmp

((i=i+1))
done
echo "Done!"

########################################
# EXTRACTION AND CHANGING OF VELOCITIES #
########################################

echo " " >> POSCAR

echo -n "   Writing the velocities into the POSCAR... "

secondemptyline_slab=$(grep -n '^[[:space:]]*$' $1 | awk '{print $1}' | sed -n -e 2p | rev | cut
-c 2- | rev)
secondemptyline_mol=$(grep -n '^[[:space:]]*$' $2 | awk '{print $1}' | sed -n -e 2p | rev | cut -
c 2- | rev)

vstart=$((firstemptyline_slab + 1))
vend=$((secondemptyline_slab - 1))

# WRITE SLAB VELOCITIES
sed -n -e "$vstart","$vend"p $1 >> POSCAR

# READ MOLECULE VELOCITIES
i=$((firstemptyline_mol + 1))
```

```
while [ $i -lt $secondemptyline_mol ]
do
read vx_old vy_old vz_old <<<$(sed -n -e "$i"p $2)

# CONVERT FORMAT: EXPONENTIAL TO DECIMAL
printf -v vx_old "%.12f" "$vx_old"
printf -v vy_old "%.12f" "$vy_old"
printf -v vz_old "%.12f" "$vz_old"

vx_new=$(echo $vx_old" + "$dvx | bc -l)
printf -v vx_new "%.7E\n" "$vx_new"
vy_new=$(echo $vy_old" + "$dvy | bc -l)
printf -v vy_new "%.7E\n" "$vy_new"
vz_new=$(echo $vz_old" + "$dvz | bc -l)
printf -v vz_new "%.7E\n" "$vz_new"

# WRITE MOLECULE VELOCITIES
echo '  '$vx_new'  '$vy_new'  '$vz_new >> POSCAR

(( i=i+1 ))
done

echo "Done!"
echo -n "   Writing the Predictor-Corrector coordinates into the POSCAR... "

# COMBINATION OF THE PREDICTOR-CORRECTOR (PC) COORDINATES OF SLAB AND MOLECULE
# GET NUMBER OF SLAB ATOMS
slabatoms=$(sed -n -e 7p $1 | awk '{for(i=1;i<=NF;i++)x+=$i;print x}')

pcblock_slab=$((slabatoms * 3 + 3))

# WRITE SLAB PC COORDINATES PART 1 INCL. TWO LEADING LINES
echo " " >> POSCAR
tail -n $pcblock_slab $1 | head -n $((slabatoms+3)) >> POSCAR

# WRITE MOLECULE PC COORDINATES PART 1
cat pc-coords-mol.tmp >> POSCAR
rm pc-coords-mol.tmp

# WRITE SLAB PC COORDINATES PART 2
tail -n $((slabatoms*2)) $1 | head -n $slabatoms >> POSCAR

# WRITE MOLECULE PC COORDINATES PART 2
tail -n $((natoms*2)) $2 | head -n $natoms >> POSCAR

# WRITE SLAB PC COORDINATES PART 3
tail -n $slabatoms $1 >> POSCAR

# WRITE MOLECULE PC COORDINATES PART 3
tail -n $natoms $2 >> POSCAR

echo "Done!"
echo ""
echo "   Finished writing the POSCAR."

echo ""
echo ""
echo "   !!! ATTENTION !!!"
echo "   !!! Please adjust the atom types and number of atoms (lines 6-7) in your POSCAR.  !!!"
echo "   !!! This has not been implemented yet and just copies over from the slab CONTCAR. !!!"
echo "   !!! ATTENTION !!!"
echo ""

# ERROR MESSAGES IF NO CONTCARS ARE GIVEN
else
echo ""
echo "Slab CONTCAR: " $1
echo ""
echo "       **********************************"
echo "       * Molecule CONTCAR not specified! *"
```

```
echo "       **********************************"
echo ""
echo "Usage: combine-mdruns.sh slab.CONTCAR molecule.CONTCAR"
echo ""
fi
else
echo ""
echo "       ******************************"
echo "       * Slab CONTCAR not specified! *"
echo "       ******************************"
echo ""
echo "Usage: combine-mdruns.sh slab.CONTCAR molecule.CONTCAR"
echo ""
fi
```

2. pEDA Bonding Analysis of the Intermediate

Table S1. pEDA bonding analysis of the cyclooctyne/Si(001) intermediate (main article, Figure 3) and the ethylene/Si(001) precursor.[a]

	Cyclooctyne intermediate	Ethylene precursor
ΔE_{int}	−226	−113
ΔE_{int}(disp)[b]	−75 (33%)	−28 (25%)
ΔE_{int}(elec)[b]	−151 (67%)	−85 (75%)
ΔE_{Pauli}	993	706
ΔE_{elstat}[c]	−528 (46%)	−368 (47%)
ΔE_{orb}[c]	−615 (54%)	−423 (53%)
ΔE_{orb}(M→S)	−421 (68%)	−293 (69%)
ΔE_{orb}(S→M)	−115 (19%)	−89 (21%)
ΔE_{prep}(Mol.)	28	12
ΔE_{prep}(Surf.)	31	21
E_{bond}[d]	−167 (−155)	−80 (−74)

[a] All values in kJ mol^{-1}, calculated at PBE-D3/TZ2P. Fragments: Molecule (M) and surface (S). Fragmentation: Closed-shell singlet. For better comparability, the ethylene precursor calculation was repeated in ADF-BAND 2016 and therefore shows minor numerical differences to the values presented in Ref. 72 of the main article. [b] Percentage values give the relative contribution of dispersion and electronic effects to the interaction energy ΔE_{int}. [c] Percentage values give the relative contribution between the attractive pEDA terms ΔE_{elstat} and ΔE_{orb}. [d] PAW values calculated in VASP (in parentheses) given for comparison.

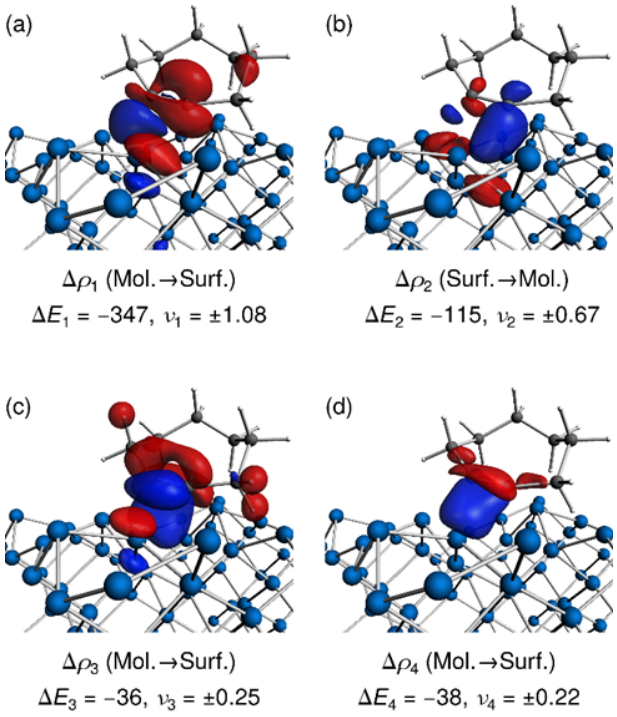

Figure S1. pEDA deformation densities $\Delta\rho_i$ visualizing individual contributions to the orbital interaction ΔE_{orb}. Red: Depletion of electron density, blue: Accumulation of electron density. Energy contributions ΔE_i in kJ mol^{-1}, eigenvalues ν in q_e.

Hyperconjugation is visible in deformation densities $\Delta\rho_1$ (red lobe at a nearby σ(C-C) bond) and $\Delta\rho_3$ (red lobes at hydrogen atoms).

3. Optimized Structure of the β-H Abstraction

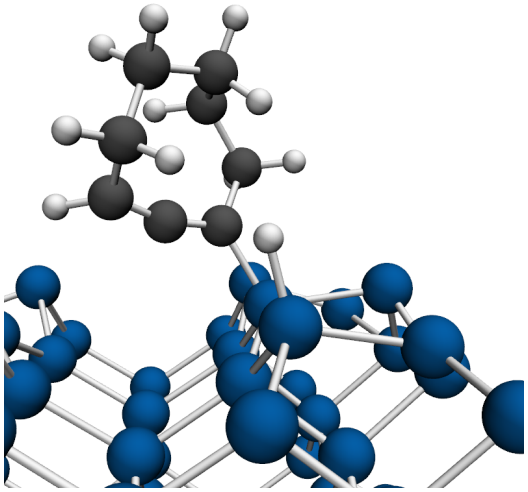

Figure S2. Final state of the β-H abstraction (compare Table 1 in the main article). E_{bond} = –217 kJ mol^{-1}.

4. AIMD Simulation Data

Simulation 1, final state: *bridge*

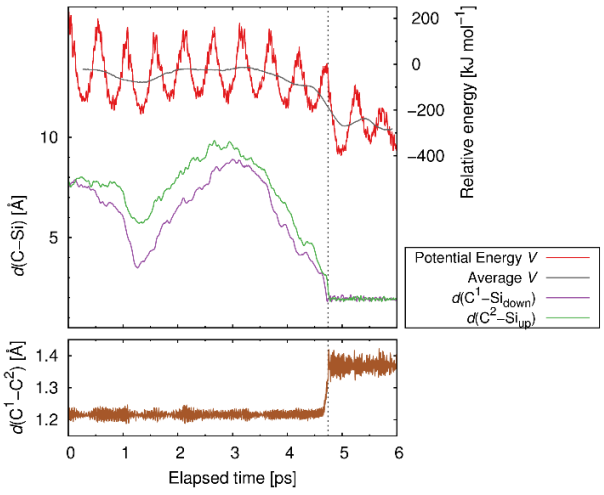

Simulation 2, final state: *on-top*

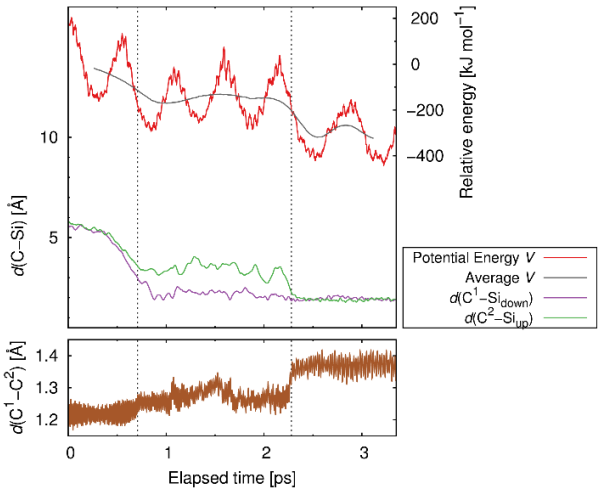

Simulation 3, final state: *on-top*

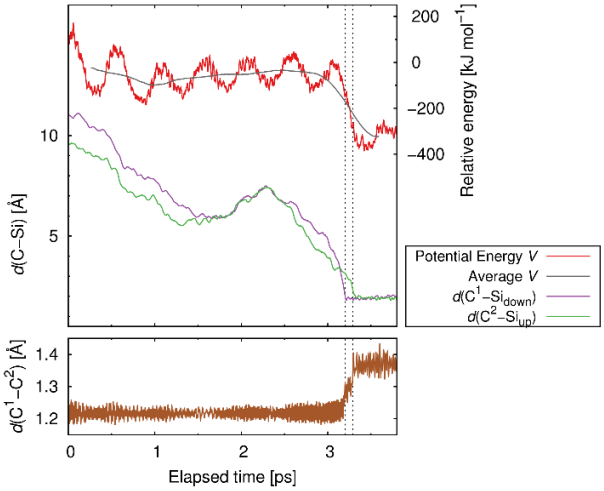

Simulation 4, final state: *on-top*

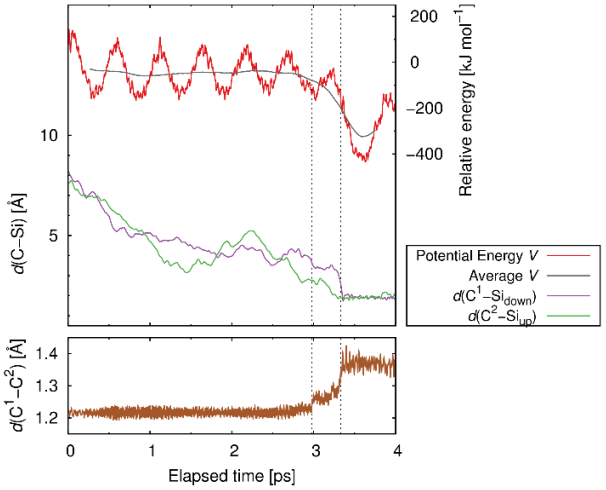

Simulation 5, final state: *on-top*

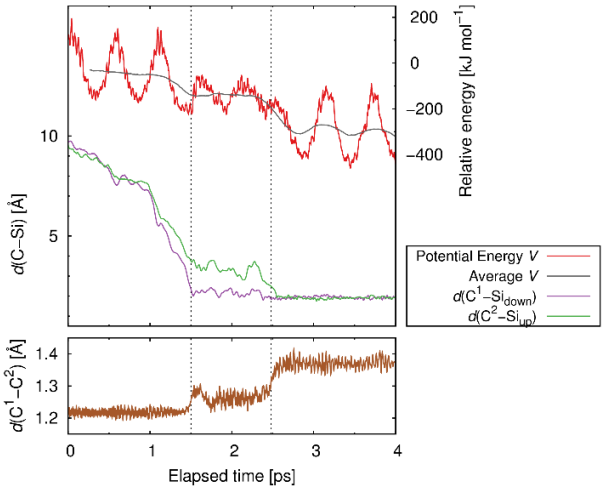

Simulation 6, final state: *on-top*

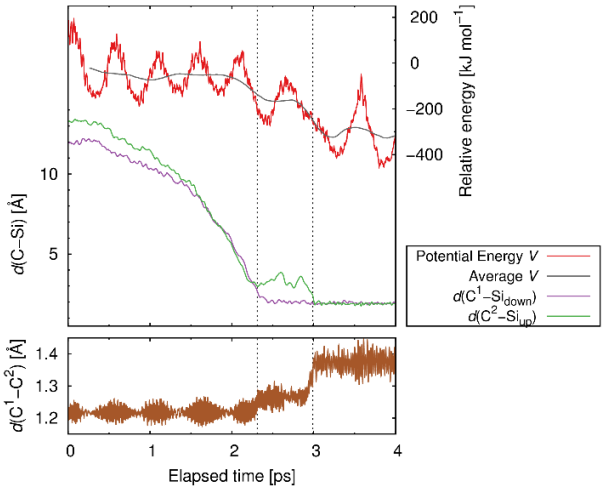

Simulation 7, final state: *on-top*

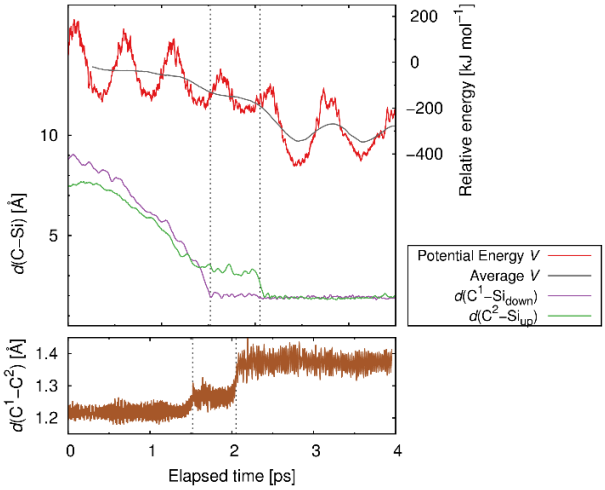

Simulation 8, final state: *bridge*

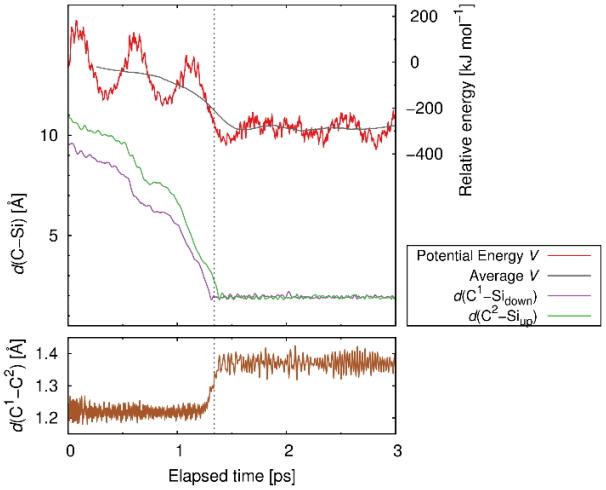

Simulation 9, final state: *on-top*

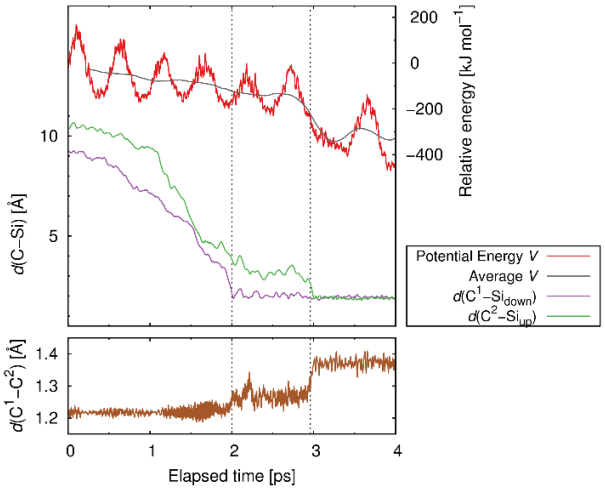

Simulation 10, final state: *bridge*

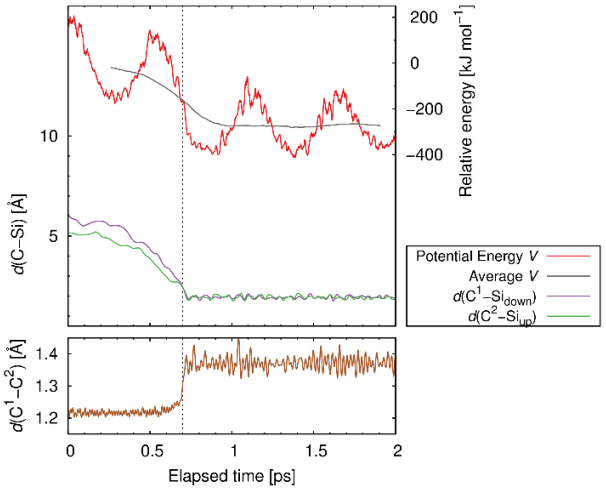

Simulation 11, final state: *on-top*

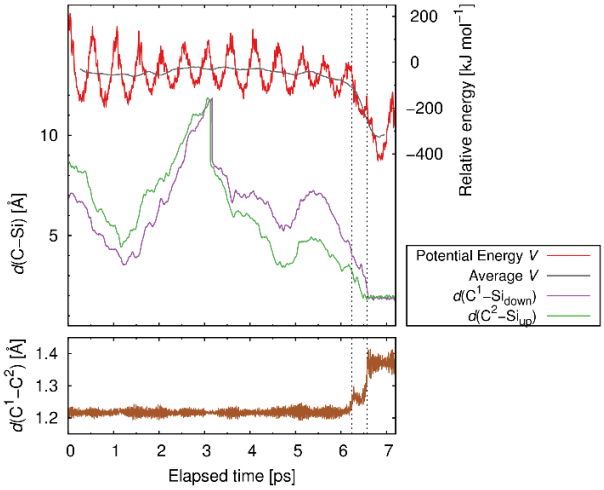

Simulation 12, final state: *on-top*

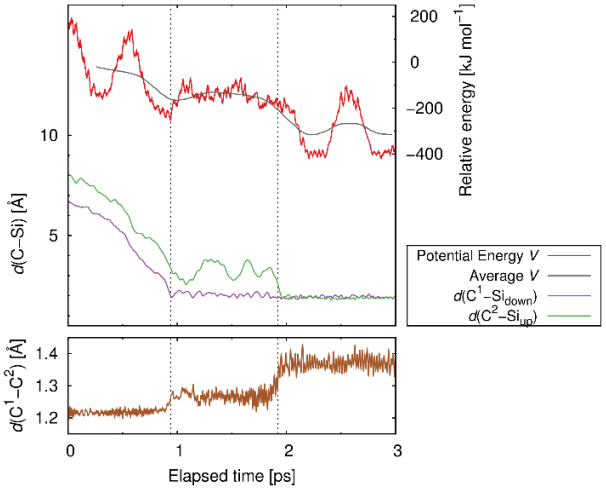

Simulation 13, final state: *on-top*

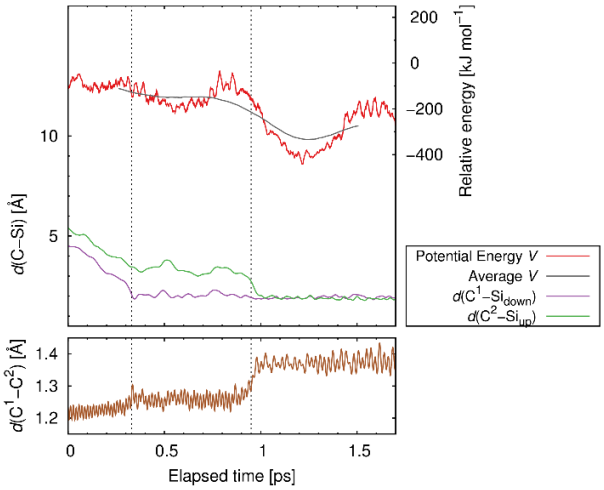

Simulation 14, final state: *on-top*

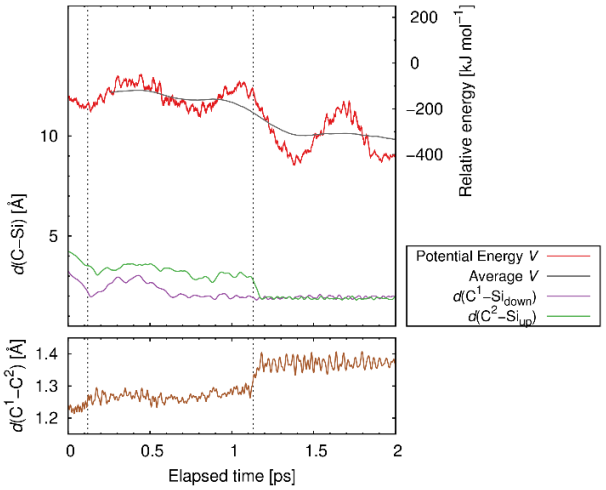

Simulation 15, final state: *on-top*

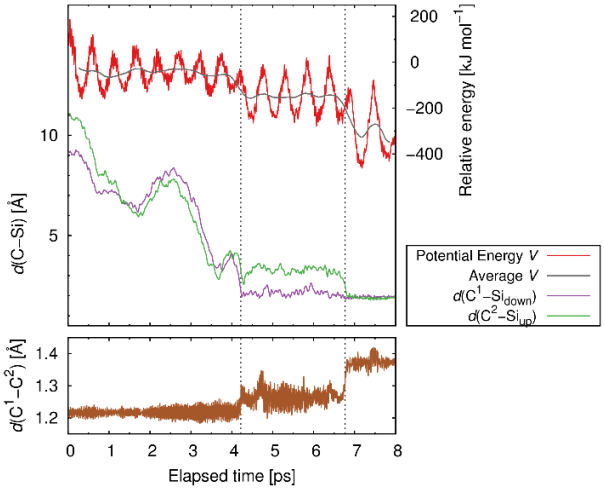

Simulation 16, final state: *on-top*

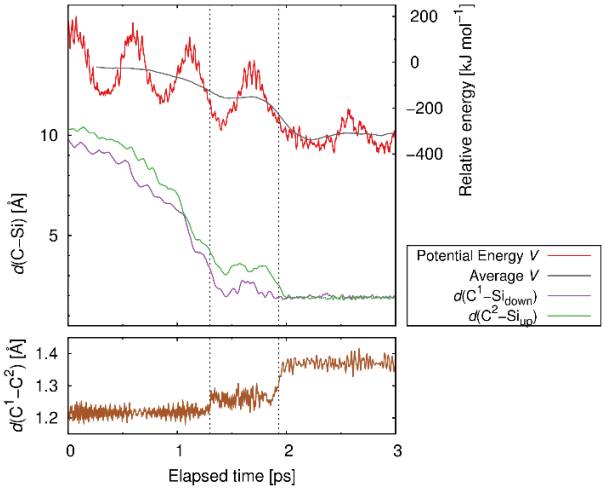

Simulation 17, final state: *on-top*

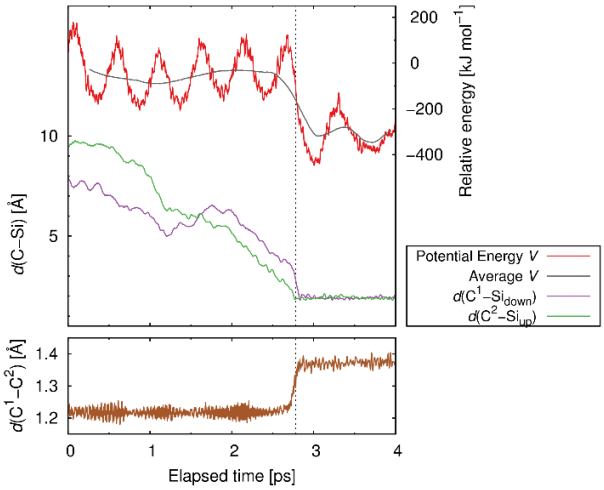

Simulation 18, final state: *on-top*

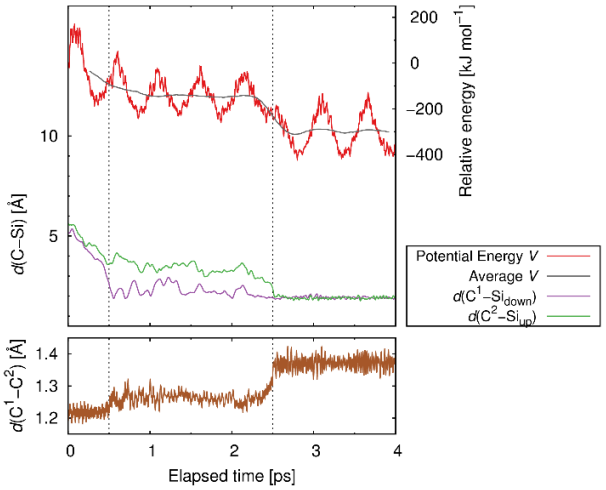

Simulation 19, final state: *on-top*

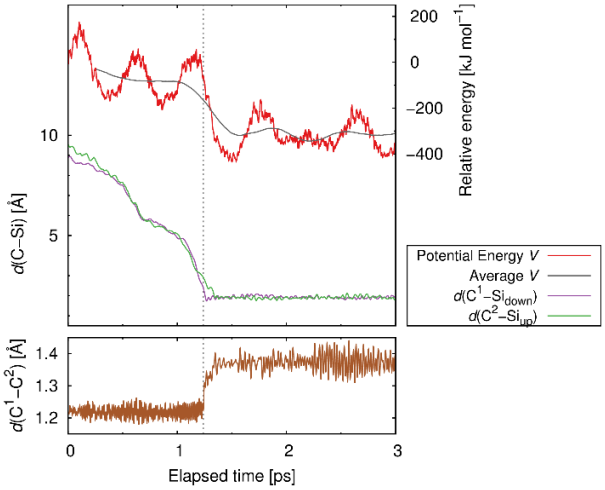

Simulation 20, final state: *on-top*

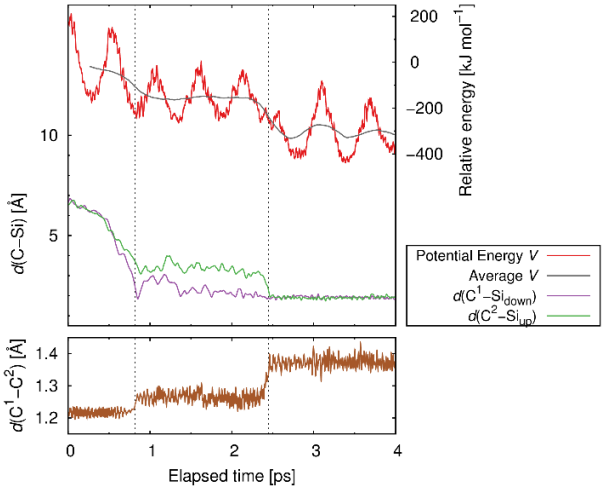

5. Cartesian Coordinates and Total Energies

Cyclooctyne molecule: E = -115.01046 eV

1.00000000000000

15.3244190216000007 0.0000000000000000 0.0000000000000000

0.0000000000000000 15.3244190216000007 0.0000000000000000

0.0000000000000000 0.0000000000000000 21.6720008849999992

H C

12 8

Direct

0.1163292027615839 0.6075905129068531 0.6489572235432988

0.0432877432463101 0.6285424276006779 0.5883106440942782

0.1499959959152122 0.4908745064372297 0.5880627771758000

0.2288209192430060 0.5660420583681045 0.5611408236228854

0.0578964740925230 0.5117902870342448 0.4973925222925502

0.1904054750395119 0.8220361050279124 0.4822764132445130

0.1561410273173252 0.7463691841605851 0.6429950518866505

0.2195764077142996 0.7174582486771399 0.5786903955150677

0.0306393927154573 0.7771647276382865 0.5621253712003664

0.0791274400424058 0.8380471554892495 0.4638629576123918

0.1128068282114540 0.8550615537008071 0.5778717888148819

0.1657336841321140 0.4932807017369711 0.4714541689074920

0.1222223218395584 0.7051062349559629 0.4653092188627923

0.1133722423679444 0.6269314805172215 0.6000332349693096

0.1580897035959765 0.5531165957501614 0.5631557335818798

0.1244806956188427 0.7941845194493524 0.4882726092733662

0.1011920815474809 0.7899406237531252 0.5578110578395723